TU Delft

Delft University of Technology

Development of Flexure-Driven Eversion Mechanisms for Confined-Space Grasping

Huisjes, A.E.

DOI
10.4233/uuid:49c156a4-2dd8-4cc3-a1fb-ec2cb855568f

Publication date
2026

Document Version
Final published version

Citation (APA)
Huisjes, A. E. (2026). *Development of Flexure-Driven Eversion Mechanisms: for Confined-Space Grasping*. [Dissertation (TU Delft), Delft University of Technology]. https://doi.org/10.4233/uuid:49c156a4-2dd8-4cc3-a1fb-ec2cb855568f

Important note
To cite this publication, please use the final published version (if applicable).
Please check the document version above.

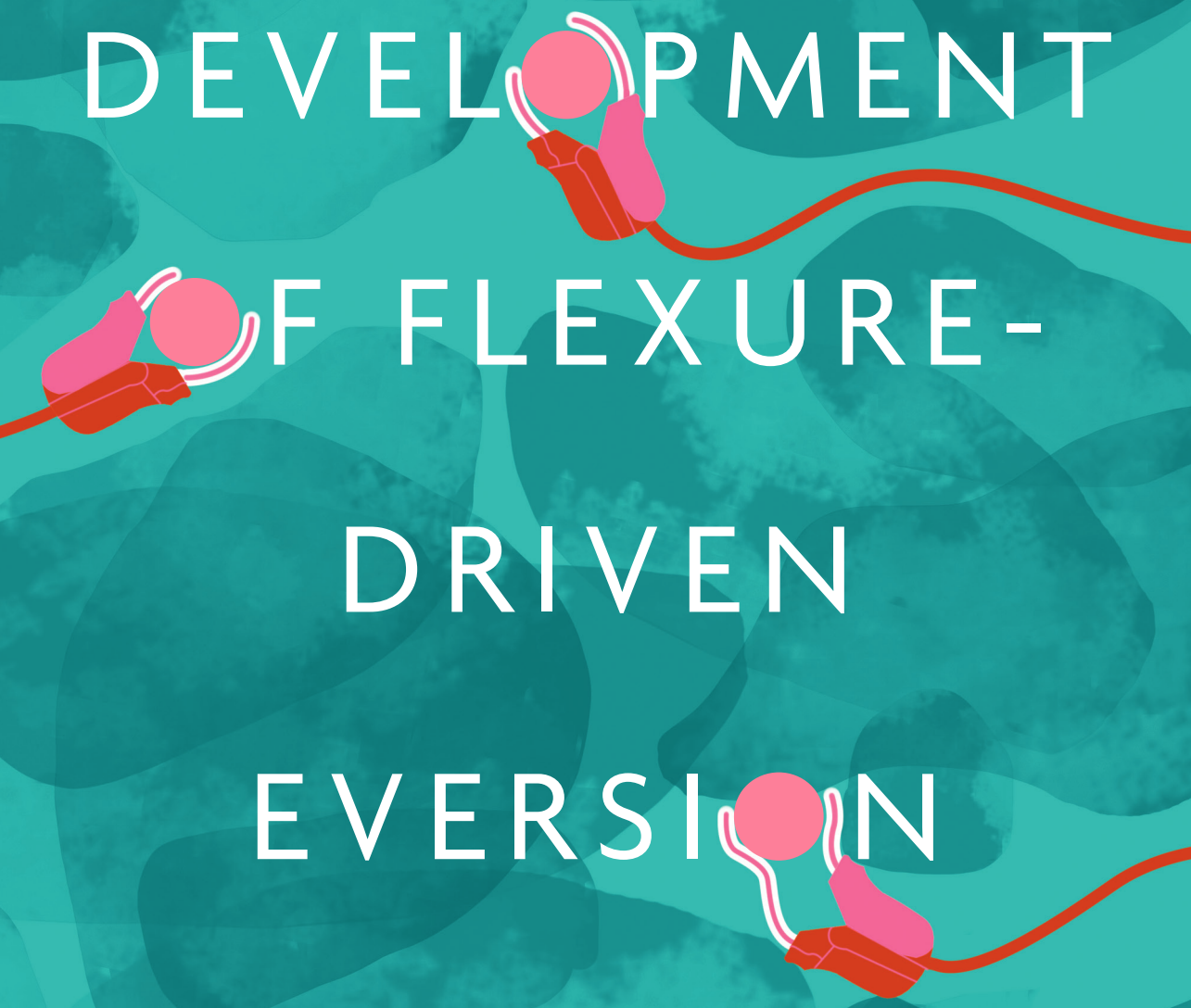
Copyright
Other than for strictly personal use, it is not permitted to download, forward or distribute the text or part of it, without the consent of the author(s) and/or copyright holder(s), unless the work is under an open content license such as Creative Commons.

Takedown policy
Please contact us and provide details if you believe this document breaches copyrights.
We will remove access to the work immediately and investigate your claim.

This work is downloaded from Delft University of Technology.
For technical reasons the number of authors shown on this cover page is limited to a maximum of 10.

Ad Huisjes

DEVELOPMENT OF FLEXURE-DRIVEN EVERSION MECHANISMS



for Confined-Space Grasping

Development of Flexure-Driven Eversion Mechanisms

for Confined-Space Grasping

Development of Flexure-Driven Eversion Mechanisms

for Confined-Space Grasping

Dissertation

for the purpose of obtaining the degree of doctor
at Delft University of Technology,
by the authority of the Rector Magnificus Prof.dr.ir. T.H.J.J. van der Hagen,
chair of the Board for Doctorates,
to be defended publicly on,
Friday 09 January 2026 at 12:30 o'clock

by

Albert Eddy HUISJES

Master of Science in Mechanical Engineering,
Delft University of Technology, The Netherlands
born in Hardenberg, The Netherlands.

This dissertation has been approved by the promotor and the copromotor.

Composition of the doctoral committee:

Rector Magnificus,	Chairperson
Prof. dr. ir. J. L. Herder,	Delft University of Technology, promotor
Dr. ir. V. van der Wijk,	Delft University of Technology, copromotor
Independent members:	
Prof.dr.ir. P. Breedveld,	Delft University of Technology
Prof.dr.ir. D.L. Schott,	Delft University of Technology
Prof.dr. G. Berselli,	U. of Geneva
Prof.dr. L.E. Birglen,	PolyMTL
Dr. G.W. Kootstra,	Wageningen University & Research

This work was conducted within the FlexCRAFT project (P17-01), funded by the Dutch Research Council (NWO).

Keywords: Flexure-Driven Eversion Mechanisms, Compliant Mechanisms, Eversion Mechanisms, Curved Flexures, Pseudo-Rigid-Body Modeling (PRBM), Event-Based Contact Modeling, Clutter Navigation, Food Handling Robotics, Confined-Space Grasping.

Printed by: ProefschriftMaken

Cover Design: Simone Golob
Front: Artistic impression of grippers with fingers designed as flexure-driven eversion mechanisms, operating in confined spaces and grasping objects by progressively extending self-searching fingers that navigate along the object's surface.
Inside: Ad Huisjes, the chapter fronts are original article images edited with the assistance of ChatGPT.

Copyright © 2025 by A. E. Huisjes

ISBN 978-94-6534-099-9

An electronic version of this dissertation is available at: http://repository.tudelft.nl

TU Delft Delft University of Technology

NWO

'Good design makes a product understandable. It clarifies the product's structure.
Better still, it can make the product talk.
At best, it is self-explanatory.'

Dieter Rams

Contents

Summary xi

Samenvatting xiii

Preface xv

1 Introduction 1
1.1 Motivation . . . 2
1.2 Gripper systems for food handling . . . 2
1.3 Problem statement . . . 7
1.4 Approach: Tangential finger motion . . . 9
1.5 Proposed finger concept . . . 9
1.6 Research objective . . . 11
1.7 Thesis outline . . . 12

I Theory 15

From Design Concept to the Modeling Framework 17

2 Pseudo-Rigid-Body Modeling of Advancing Interacting Flexures 19
2.1 Introduction . . . 21
2.2 Method. . . . 22
2.2.1 Case study . . . 23
2.2.2 Model development . . . 24
2.2.3 Phase I . . . 25
2.2.4 Phase II . . . 25
2.2.5 Phase III . . . 28
2.3 Experimental validation . . . 36
2.3.1 Test setup . . . 36
2.3.2 Test procedure . . . 37
2.4 Results . . . 38
2.4.1 Kinematic results. . . . 38
2.4.2 Interaction force results . . . 40
2.5 Discussion . . . 42
2.5.1 Results . . . 42
2.5.2 Case study: phase transitions. . . . 43
2.5.3 Case study: extendability. . . . 43
2.5.4 Methodology: contributions and restrictions . . . 44
2.6 Conclusion . . . 46

II Design **49**

Towards Finger Design **50**

3 Gripper with Dual-Belt Curved-Flexure Eversion Mechanism Fingers **53**
3.1 Introduction . . . 55
3.2 Method. . . . 55
3.2.1 Conceptual gripper design . . . 55
3.2.2 Use case: task and design requirements . . . 59
3.2.3 Mechanical design and manufacturing . . . 59
3.3 Experimental performance validation . . . 61
3.3.1 Tangential object-following finger motion . . . 61
3.3.2 Tangential disturbances at contact interfaces . . . 61
3.3.3 Pull-out force . . . 62
3.3.4 Net disturbance force on the object. . . . 63
3.3.5 Grasp success rate in a practical robotic set-up . . . 63
3.4 Results and implications . . . 65
3.4.1 Tangential object-following finger motion . . . 65
3.4.2 Tangential disturbances at contact interfaces . . . 65
3.4.3 Pull-out force . . . 66
3.4.4 Net disturbance force on the object during grasping . . . 67
3.4.5 Grasp success rate in a practical robotic set-up . . . 67
3.5 Discussion . . . 67
3.5.1 Damage and limitations . . . 68
3.5.2 Holding force requirements . . . 68
3.5.3 Future directions and broader applications . . . 69
3.6 Conclusion . . . 70

4 Gripper with Sleeved Concentric-Flexures Eversion Mechanism Fingers **73**
4.1 Introduction . . . 75
4.2 Method. . . . 76
4.2.1 Performance metrics . . . 76
4.2.2 Finger concept and design rationale . . . 77
4.2.3 Use case: task and design requirements . . . 79
4.2.4 Mechanical design and manufacturing . . . 80
4.2.5 Operating principles . . . 84
4.3 Experimental performance validation . . . 85
4.3.1 Grasp success rate for confined-space grasping. . . . 85
4.3.2 Disturbance forces . . . 87
4.3.3 Pull-out force . . . 92
4.4 Results and implications . . . 92
4.4.1 Grasp success rate for confined-space grasping. . . . 92
4.4.2 Disturbance forces . . . 94
4.4.3 Pull-out force . . . 98

4.5 Discussion . . . 100
4.5.1 Reflection on concept and methods . . . 100
4.5.2 Versatility, gentle handling through flexural caging . . . 101
4.5.3 Durability, hygiene, and holding force considerations . . . 102
4.5.4 Mechanical (flexure) driven eversion mechanism . . . 102
4.6 Conclusion . . . 103

5 Discussion **107**
5.1 Overview of contributions and sub-goal achievements . . . 108
5.2 Positioning DBCF- and SCF-EM gripper performance . . . 109
5.2.1 Relating to the state-of-the-art in gripper designs . . . 110
5.2.2 Trend-based comparison between DBCF-/SCF-EM grippers . . . 110
5.3 Implications for the gripper field . . . 111
5.3.1 Cohesive design process and practical evaluation . . . 111
5.3.2 Mechanical gripper design . . . 112
5.3.3 Gripper design theory . . . 113
5.4 Implications for axially advancing mechanisms . . . 114
5.4.1 Positioning DBCF-/SCF-EM in eversion mechanism research . . . 114
5.4.2 Base-driven flexures in interactive navigation . . . 115
5.4.3 Base-driven flexures combined with eversion mechanisms . . . 116
5.4.4 Manufacturing aspects of flexure-driven eversion mechanisms . . . 118
5.4.5 Concluding Remarks . . . 119

6 Conclusion **121**

A Supplementary Video Material **125**
A.1 Video recordings of DBCF-EM gripper . . . 126
A.2 Video recordings of SCF-EM gripper . . . 126

B Pull-Out Force Models **127**
B.1 Pull-out force of precurved flexure fingers via PRBM . . . 128
B.1.1 Problem introduction . . . 128
B.1.2 Methodology . . . 128
B.1.3 Results and conclusion . . . 129
B.2 Pull-out force by DBCF-EM eversion belt pretension . . . 131
B.2.1 Problem introduction . . . 131
B.2.2 Methodology . . . 131
B.2.3 Results and conclusion . . . 132

C Design Reasoning **135**
C.1 Design rationale towards proposed concept . . . 136
C.1.1 Strategies to set form-closed grasps in dense environments . . . 136
C.1.2 Strategies to reduce friction . . . 137
C.1.3 Feasible strategies integrable for a conceptual finger . . . 137

References **141**

Overview of Author Contributions 155

Contextual Exploratory Studies 157

Acknowledgments 173

MSc Projects Supervised 177

Curriculum Vitæ 179

List of Publications 181

Summary

This dissertation explores the development and evaluation of mechanical grippers with flexure-driven eversion mechanism fingers, designed to address the challenges of grasping objects in confined spaces—a common issue in the agri-food and food processing industry that hinders robotic automation. Conventional mechanical grippers face significant difficulties in dense environments, such as within piles or plants, as their grasping process relies on positioning fingers around the object performing inward-outward movements from its sides. This approach requires considerable clearance, often obstructed by neighboring obstacles. To overcome this challenge, this research introduces in Chapter 1 a novel grasping approach in which the gripper fingers move tangentially along the surface of the object, utilized as flexure-driven eversion mechanisms, to set or release the grasp while reducing environmental disturbances. This approach significantly reduces the required space, as well as unwanted displacements and forces in the surroundings, and leverages environmental interactions to aid finger navigation.

The main objective is to develop and evaluate flexure-driven eversion mechanism fingers for mechanical grippers, aimed at grasping food in confined spaces, as presented in Chapter 1. The finger design incorporates a curved flexure as the structural backbone, which navigates along the object's surface—displacing adjacent obstacles if necessary—and securely holds it once enclosed. The flexure is combined with the principles of eversion mechanisms to reduce friction forces during operation by ensuring zero relative speed differences with the environment.

This thesis is divided into two parts. The first part, presented in Chapter 2, investigates the applicability of flexures within the proposed finger concept by analyzing their ability to navigate predictably through multiple obstacles when driven from the base. A case study was conducted, modeling the kinematics and kinetics of a straight base-driven flexure, which bends and moves through two consecutive circular obstacles when pushed forward, using a pseudo-rigid-body modeling (PRBM) approach. This analysis required an extension of existing PRBM techniques, enabling the analysis of flexures in event-based scenarios (e.g., abrupt load changes) and with multiple loads at unknown locations along their length. This was achieved by systematically switching and stitching PRBM-topologies while maintaining the system's potential energy within reasonable bounds. Experimental validation confirmed the compatibility of base-driven flexures with the proposed finger concept, demonstrating their ability to navigate through obstacles in a predictable manner, with both trajectory and interaction forces modeled with high accuracy for design purposes.

In the second part of this thesis, two finger designs were developed and manufactured as prototype grippers, which were experimentally validated based on defined performance criteria. Chapter 3 presents a preliminary gripper design with three fingers, each implemented as a Dual-Belt Curved-Flexure Eversion Mechanism (DBCF-EM)—a single curved base-driven flexure, with its inner and outer contours covered by two everting (outwardly unrolling) belts guided through rollers. Chapter 4 presents an evolved gripper design

featuring Sleeved Concentric-Flexure Eversion Mechanisms (SCF-EM) as fingers—a base-driven channeled backbone comprising two concentric curved flexures, fully enclosed along its circumference by a latex sleeve with engineered stretchability, which everts from the channel. The design is completed by a cable-pulley system that synchronizes both movements.

The results showed that both grippers operated as intended, following the object's surface and navigating adjacent obstacles, and successfully validated the proposed grasping method, enabling form-closed grasps of densely packed objects. Practical tests involving integration into a robotic set-up tasked with emptying a crate of tomatoes, one at a time, demonstrated an exceptionally high grasp success rate, previously unobserved. While the gripper with DBCF-EM fingers occasionally encountered issues such as misgrasps, object damage, and hygiene concerns due to its open structure, the gripper with SCF-EM fingers achieved a 100% success rate in picking and placing tomatoes without damaging them or the surroundings. Additionally, the SCF-EM fingers offered improved hygiene compliance, durability, and robustness due to the enclosed eversion sleeve creating a barrier and a reduction in the number of mechanical components. Technical tests of both designs measured relatively low disturbance forces and sufficient holding forces. Comparative studies showed that the integration of the eversion mechanism reduced friction forces by around 90%, reducing both damage and misgrasps.

In general, these findings demonstrate the effectiveness of the proposed finger designs for grasping objects in confined spaces and their suitability to gently and securely handle fragile agri-food products while accommodating natural variations, although additional engineering, testing, and refinement are required to ensure industrial readiness.

Ultimately, the most important outcome is that this dissertation introduces flexure-driven eversion mechanisms for the first time and convincingly demonstrates their exceptional potential for navigation in complex and confined environments. This breakthrough constitutes the central scientific contribution of this work, arising from the need for alternative gripper methods for grasping tasks in tight spaces. This contribution provides a solid foundation for further applications in domains such as medical devices, search-and-rescue robotics, and inspection systems for hard-to-reach environments.

Samenvatting

Deze dissertatie richt zich op de ontwikkeling en evaluatie van mechanische grijpervingers, ontworpen om de uitdagingen aan te pakken bij het grijpen van objecten in krappe ruimtes. Dit scenario komt veel voor in de landbouw- en voedselverwerkingsindustrie en vormt een belangrijke belemmering voor robotautomatisering van taken in deze sector. Conventionele grijpers ondervinden moeilijkheden wanneer ze in dichte omgevingen moeten opereren, zoals bijvoorbeeld in een stapel of in een plant, omdat hun grijpproces doorgaans afhankelijk is van het positioneren van de vingers rondom het object, gevolgd door een beweging naar de zijkanten van het object toe of juist ervan weg. Dit vereist aanzienlijke vrije ruimte rondom het object, die door naburige obstakels vaak ontbreekt, waardoor de sluitende beweging van de vinger niet kan worden uitgevoerd. Om deze uitdaging te overwinnen, introduceert dit onderzoek in Hoofdstuk 1 een innovatieve grijpmethode waarbij de grijpervingers tangentieel langs het oppervlak van het object bewegen om de greep te zetten of los te laten. Hierdoor hebben de vingers aanzienlijk minder bewegingsruimte nodig, wat ongewenste verplaatsingen en krachten in de omgeving sterk vermindert. Tegelijkertijd worden de aanwezige interacties benut voor het navigeren van de vingers.

Het hoofddoel van dit onderzoek is het ontwikkelen en evalueren van grijpervingers gebaseerd op een met bladveren aangedreven eversie-mechansimen-concept, om het grijpen van voedsel in krappe ruimtes mogelijk te maken, zoals gepresenteerd in Hoofdstuk 1. Het vingerontwerp omvat onder andere een gebogen bladveer die fungeert als structurele ruggengraat. Deze beweegt langs het objectoppervlak, schuift aangrenzende objecten opzij om het doelobject te omsluiten en maakt het mogelijk om het object met een robot uit de stapel te tillen. De bladveer is gecombineerd met een eversiemechanisme om de wrijvingskrachten tijdens de beweging te verminderen, aangezien dit mechanisme voorkomt dat er een relatieve snelheid ontstaat ten opzichte van de omgeving.

Het vervolg van dit proefschrift bestaat uit twee delen. Het eerste deel is gepresenteerd in Hoofdstuk 2, waarin de toepasbaarheid van bladveren wordt onderzocht binnen het voorgestelde vingerconcept door te analyseren of ze op een voorspelbare manier door een omgeving met meerdere obstakels navigeren wanneer ze vanaf hun basis naar voren worden bewogen. Hiervoor is een proefsituatie uitgewerkt waarin de kinetica en kinematica van een rechte bladveer worden gemodelleerd. Deze bladveer wordt naar voren geschoven, komt opeenvolgend in contact met twee cirkelvormige obstakels en moet tussen beide door bewegen door middel van buiging. De modellering is uitgevoerd op basis van de pseudo-rigid-body model (PRBM)-methode, die een uitbreiding van de bestaande kennis vereiste om de analyse van bladveren in gebeurtenisgestuurde scenario's, zoals abrupte veranderingen in belasting, evenals bladveren met meerdere belastingen op onbekende locaties langs hun lengte, mogelijk te maken. Dit is bereikt door systematisch te schakelen tussen PRBM-topologieën en deze met elkaar te verbinden, waarbij de potentiële systeemenergie binnen acceptabele grenzen bleef. Experimentele validatie bevestigde de compatibiliteit van basis-aangedreven bladveren met het voorgestelde vingerconcept, waarbij ze langs

de obstakels konden navigeren en dat zowel het traject als de interactiekrachten met een hoge nauwkeurigheid konden worden voorspeld met behulp van het model.

In het tweede deel worden twee vingerontwerpen ontwikkeld en als prototype-grijpers vervaardigd, die experimenteel zijn gevalideerd op basis van gedefinieerde prestatiecriteria.

Hoofdstuk 3 presenteert een eerste grijperontwerp met drie vingers, elk uitgevoerd als een Dual-Belt Curved-Flexure Eversion Mechanism (DBCF-EM), bestaande uit een voorgekromde bladveer (CF) waarvan de binnen- en buitencontouren zijn bedekt met twee everterende banden (Dual-Belt) en vanuit de basis wordt aangedreven. De banden worden door rollers begeleid en rollen vanuit het midden van de vinger naar beide buitenzijden af, d.w.z. 'everting', en tezamen vormen ze een eversie-mechanisme (EM).

Hoofdstuk 4 introduceert een vervolgontwerp van een grijper met Sleeved Concentric-Flexure Eversion Mechanisms (SCF-EM) als vingers. Elke vinger bestaat uit twee co-radiaal geplaatste, voorgekromde bladveren (CF) die samen de ruggengraat vormen en volledig worden omsloten door een eversiemouw. Deze mouw (S), vergelijkbaar met een afgeknipt stukje fietsband, is gemaakt van latex waarvan de rekbare eigenschappen per richting zijn afgestemd op het functioneren van het ontwerp. Het ontwerp wordt aangevuld met een kabel-katrolsysteem dat beide bewegingen synchroniseert.

De resultaten toonden aan dat beide grijpers functioneerden zoals bedoeld, de vingers volgden het objectoppervlak en passeerden langs nabijgelegen obstakels. Daarbij is aangetoond dat grijpen in krappe ruimtes mogelijk is gemaakt op basis van de voorgestelde grijpmethode. Experimenten waarbij de grijpers werden geïntegreerd in een robotsysteem dat een krat met een stapel tomaten één voor één moest leegmaken, toonden een ongekend hoge grijpsuccesratio. Hoewel het DBCF-EM-vingerontwerp soms problemen vertoonde, zoals misgrijpen, beschadiging van objecten en hygiëneproblemen door de open structuur van het ontwerp, behaalde het SCF-vingerontwerp daarentegen een succesratio van 100% met volledig onbeschadigde tomaten. Dit ontwerp biedt bovendien verbeterde hygiëne, duurzaamheid en robuustheid dankzij de vermindering van het aantal mechanische componenten die volledig omsloten zijn door de eversiemouw. Tijdens aanvullende technische experimenten werden relatief kleine verstoringskrachten en voldoende grijpkrachten gemeten voor beide ontwerpen. In vergelijkende studies werd aangetoond dat de integratie van het eversiemechanisme de wrijvingskrachten met ongeveer 90% verminderde, wat zowel schade aan objecten als misgrijpen aanzienlijk reduceert.

Deze bevindingen bevestigen de effectiviteit van beide vingerontwerpen voor het grijpen van objecten in krappe ruimtes en hun geschiktheid om kwetsbare landbouwproducten op een zachte en veilige manier te hanteren, terwijl natuurlijke variaties worden opgevangen. Aanvullende tests en verdere verfijning zijn echter nodig om industriële gereedheid te waarborgen. Dit wordt onder andere besproken en geconcludeerd in Hoofdstuk 5 en 6, evenals in andere hoofdstukoverstijgende aspecten van het onderzoek.

Kortom, het belangrijkste is dat dit proefschrift voor het eerst met bladveren aangedreven eversiemechanismen introduceert en het uitzonderlijke potentieel ervan overtuigend aantoont voor navigatie in complexe en krappe ruimtes. Deze doorbraak vormt de centrale wetenschappelijke kernbijdrage van dit werk, ontstaan vanuit de noodzaak voor alternatieve grijpermethoden voor grijptaken in krappe omgevingen. Deze bijdrage legt een solide basis voor verdere toepassingen in domeinen zoals medische instrumenten, zoek- en reddingsrobots en inspectiesystemen voor moeilijk toegankelijke omgevingen.

Preface

It is a great pleasure for me to present this work, which introduces the first flexure-driven eversion mechanisms and demonstrates how they can be applied to food-gripper finger designs that enable reliable grasping in confined spaces. This dissertation marks the completion of my PhD journey at Delft University of Technology, and because it has resulted in outcomes that differ significantly from the original proposal, it reflects one of the most motivating aspects—and perhaps the true beauty—of scientific research in general. I would therefore like to share the context in which this journey took place, which helped shape the work presented here and continually motivated and energized me, especially because the chapters of this dissertation represent only a selective reflection of the broader journey behind this PhD.

A key enabler of this work was its embedding in the FlexCRAFT programme (Cognitive Robotics for Flexible Agro-Food Technology), complemented by the privilege of supervising a large group of MSc students whose contributions provided valuable insights to the project. The FlexCRAFT consortium brought together academic partners and numerous industrial collaborators to develop robotic technologies with flexibility as a central guiding principle to address the unique challenges of the agri-food sector. Approximately twenty researchers worked full-time on this programme, representing multiple robotics disciplines across five Dutch universities (TU Delft, TU Eindhoven, University of Twente, University of Amsterdam, and Wageningen University & Research). Their efforts were organized into four research lines: (RL1) active perception, (RL2) probabilistic world modelling, (RL3) semantic task planning and control, and (RL4) gripping and smart manipulation, the line in which I was involved.

A strong emphasis was placed on active collaboration among researchers and industrial partners. To ensure both the generic applicability of the developed robotic capabilities and their continued relevance to industrial challenges, results from all research lines were integrated and tested within three representative use cases, each addressing a distinct stage of the agri-food chain. Each case featured a dedicated robotic setup that evolved throughout the programme, serving as a testbed in which newly developed technologies were combined and validated to perform increasingly complex tasks over time: (P5) the greenhouse case focusing on selective fruit harvesting (typically tomatoes), (P6) the food-processing case handling chicken pieces, and (P7) the packaging case addressing high-speed product handling.

Within the three FlexCRAFT use cases, one challenge surfaced again and again across all robotic setups: grasping objects in confined spaces. Although this issue had been studied in other robotics domains, it remained relatively underexplored from a gripper-design perspective. Our problem analysis—built on interdisciplinary discussions, literature study, and the work of multiple MSc students—made one thing clear: many contemporary agri-food manipulation challenges stem not from the objects themselves, but from their surroun-

ding environment. This repeatedly prevented us from easily implementing promising state-of-the-art industrial grippers on any of our three robotic setups.

While robotics research frequently highlights clutter, chaos, and variability, gripper design has traditionally remained centred on the object—its shape, fragility, or diversity—as was also reflected in the original project proposal, which implicitly assumed top-table conditions. Many papers showcase grippers holding (or supporting) a wide range of objects—impressive results achieved through dedicated work. However, this focus overlooks a fundamental step: before we can hold an object, we must first be able to grasp it.

This emphasis may partly stem from the ingrained definitions of form-closed and force-closed grasps, which fundamentally describe conditions for holding an object once contact has been fully established. These definitions say little about the actual process of grasping—the transition from having no attachment or interaction with the object to reaching a state in which the object is securely retained.

Recognizing this gap motivated me to rethink gripper architectures and to treat the environment as an integral part of the grasping process. Rather than viewing environmental contact as an obstacle to be avoided or worked around, this dissertation explores how it can be exploited—using interaction with the surroundings to guide, stabilize, and ultimately enable successful grasping in confined spaces.

This shift in perspective led to a new design philosophy: moving away from perpendicularly closing fingers toward fingers that follow trajectories close to the object's surface, enabling grasps to be established more naturally in dense environments. Such motions require less clearance and allow the fingers to gently displace nearby obstacles instead of colliding with them. Through countless sketches and concept explorations, this idea gradually crystallized into the notion of compliant, base-driven curved fingers that advance tangentially along the surface and minimize sliding forces within the environment by integrating the principles of eversion mechanisms.

What began as a task to design flexible grippers for agricultural products thus evolved into a more fundamental question of how a gripper should move through clutter, rather than what it should grasp. Once we design a gripper system that can reliably encage objects—even in cluttered environments—the subsequent steps of holding the object and integrating the gripper into robotic systems become far less problematic, or can be readily addressed using the wealth of existing robotics research already available for these stages.

Following this paradigm shift, the development of flexure-driven eversion mechanisms emerged as the core technology of this thesis. Although not grippers in the traditional sense, these mechanisms introduce a new motion principle that enables gentle and effective grasping in cluttered environments. It was a technically demanding and unconventional direction—considered high-risk at the time—but profoundly rewarding to watch the concept evolve step by step: from abstract sketches, including the one depicted on the thesis cover, to behavioral models and mechanical prototypes that validated the feasibility of this approach.

I have aimed to make this dissertation accessible to a diverse audience by presenting both modelling work and tangible prototypes, so that you can engage with the parts you find most interesting—whether the mathematical insights, the illustrations and videos, or the experimental validation. Although the first part may at first glance seem far removed from gripper design, it was essential for establishing a foundation strong enough to pursue this new direction: it provides the initial proof of principle through a modelling-based study of flexures navigating along object surfaces and obstacles. The second part builds directly on these insights by translating them into practical gripper designs validated through extensive experiments. Naturally, the work is not complete; time constraints always limit how deeply one can explore a topic, and in my case the later stages prioritized design and manufacturing over extensive modelling. Still, when we integrated our first gripper prototype relatively straightforwardly into the robotic setup—and it performed tasks that commercial grippers had not achieved there before—a FlexCRAFT colleague remarked, "So perception wasn't the problem here" - that moment confirmed that this alternative gripper design could simplify robotic systems and offer the long-sought flexibility. This progress was possible only because flexibility was embraced not just within the robotic systems themselves, but also within the FlexCRAFT environment: the principal investigators and industrial partners gave me the freedom and trust to pursue this new idea, even when it required patience before concrete results emerged.

Ultimately, this journey has given me much more than the technical challenges it set out to solve. It made me realize that a deep and collaborative problem analysis is essential when attempting to tackle a fundamental challenge in a new way. Such analysis requires not only a multidisciplinary academic approach but also the practical insights of industrial partners. Without this foundation, one might achieve short-term results, but fail to create the long-term change that research can truly bring about. To me, this has become one of the core contributions of science—and it is what gave me the energy and motivation to drive this work forward and to lay down the many conceptual pillars on which this new line of gripper technology can continue to grow. I hope the mechanisms and prototypes developed here are tangible and self-explanatory, and that they inspire you as much as earlier designs within my research group inspired me. Whether you choose to read, browse, or simply look at the figures, illustrations, or videos of this work, I hope it encourages you to explore, build, and create something new.

Enjoy,
Ad

1

Introduction

This chapter introduces the motivation for the research and its primary objective: developing flexure-driven fingers for mechanical grippers to grasp food in confined spaces. It provides background on current gripper systems, highlighting their benefits and the challenges they face in agri-food applications. Furthermore, it addresses the key problem that limits existing grippers - and, by extension, robotic systems - from functioning in the dense unstructured environments typical of this sector. The purpose of this work is to bridge the gap between existing technologies and the specific needs of the food industry by proposing a new grasping approach and a conceptual mechanical finger design, which will be developed throughout the thesis. This chapter also outlines the research's main objective and subgoals and presents the thesis structure, showing how each chapter progressively contributes to achieving the overarching objective.

1

1.1 Motivation

The global agri-food sector is under growing pressure to increase food production, improve food quality, and enhance production efficiency [1, 2]. Population growth, coupled with increasing prosperity, has driven the demand for higher yields and better quality food, while simultaneously facing the challenges of climate change [3].

Meeting these demands is increasingly difficult because human labor remains essential in many stages of the food production chain. This includes repetitive tasks in greenhouses, slaughterhouses, and packaging lines, such as harvesting tomatoes, sorting chicken and fish pieces, packaging sandwiches, or boxing bags of soup, as shown in Fig. 1.1(a–d). Many of these jobs are difficult to fill due to low wages, physically demanding work, and monotonous tasks [4, 5]. Labor shortages, further exacerbated by crises such as the COVID-19 pandemic, have shown how disruptions can severely affect the continuity of the food supply chain [6]. Temporary solutions such as immigration have alleviated labor shortages, but have also created political tensions in the Netherlands [7–10].

Moreover, human involvement in the food production chain reduces yield efficiency, introduces contamination risks, and increases food waste due to the need for open processing environments. As a result, robot-driven automation of human tasks has become an increasingly compelling solution [11] to reduce dependence on human labor, improve production efficiency, and enhance the sustainability of food systems.

Despite the successful implementation of robotics in other sectors, the comprehensive integration of robotics in the agri-food sector remains limited due to its unique challenges [12–16]. Most successful applications of robotics consist of fixed solutions for repetitive tasks in controlled environments. The natural agri-food environment is dense and unstructured, complicating the detection and mapping of the target object and its surroundings and leading to difficulties in robot task planning and motion control [17], as illustrated in Fig. 1.1. To address these challenges, research labs are developing cognitive robotic systems along several research lines, including active perception methods [18, 19], improved world modeling [20], semantic task planning and control [21], and smart manipulation systems.

1.2 Gripper systems for food handling

The robot gripper system faces unique challenges when handling delicate food items, which limits overall robot performance and hinders progress toward fully autonomous agri-food systems [22–24]. The variability of food objects—such as size, shape, surface properties, deformability, and fragility—makes them difficult to handle without causing damage [25]. These object-related challenges are well recognized in industry and academia, driving extensive research into gripper technologies tailored to specific food-handling problems [26]. In practice, constraints such as cycle time, cost, compactness, reliability, and food-safety approval further complicate the design and deployment of effective grippers.

Numerous gripper designs have been developed, ranging from standalone mechanical devices to integrated mechatronic systems with sensing and actuation. Early work focused on suction cups and mechanical grippers with parallel jaws or multi-DoF fingers, while more recent approaches—such as granular [27], soft robotic [28], compliant, and origami-based grippers—have gained prominence. The wide variety of designs is commonly classified by operating principles, application domains, or gripper types [25, 29–36].



(a) Harvested tomatoes stacked in a crate, ready for transport.



(b) A cluster of kiwis hanging from a tree, awaiting harvest [37].



(c) Human labor harvesting tomatoes in a greenhouse [38].



(d) Human workers packing chicken products from a pile onto trays in a slaughterhouse [39].



(e) Academic robot harvesting bell peppers in a greenhouse [40].



(f) Industrial robot packing individual chicken products from a conveyor belt onto trays [16].

Figure 1.1: The agri-food sector: examples showcasing the variety of food items, environmental scenarios, and tasks performed at different stages of the food supply chain. In response to societal demands, scientists and industry are working to automate these tasks using robotics to reduce reliance on human labor, with varying degrees of success. Depending on the complexity of the task and the environment, robots face technological challenges due to the dense, unstructured agri-food settings and the need to handle food items of different sizes, shapes, deformability, fragility, and surface properties.

1

In the literature, grasping an object can be described either as constraining its motion through a set of contacts [41] or as exerting forces and moments that move the object or maintain it in stable equilibrium. These two perspectives are dual to one another. A grasp achieves form-closure when all motions of the object (translations and rotations) are prevented by the geometric arrangement and shape of the contacts. In such grasps, geometry alone immobilizes the object by blocking every possible direction of movement, even in the absence of friction [42, 43]. A grasp achieves force-closure when the contacts can generate wrenches—through normal forces and friction—that allow the grasp to resist any combination of external forces and moments acting on the object. An equilibrium of forces and moments can be established that counteracts all external disturbances.

Figure 1.2 presents a categorized overview, offering a broad perspective on the available gripper technologies. Although not exhaustive, the technologies highlighted represent approaches with the potential and flexibility to address the diverse challenges posed by a wide range of food items. This framework builds upon existing overviews [25, 29–36, 44], providing a more effective basis for comparing their suitability and performance in the agri-food sector. It serves as a guide for selecting technologies with the characteristics and flexibility needed to address the broader challenges of the agri-food industry, while also providing valuable background knowledge and preliminary design insights for this thesis. The overview begins by classifying grippers based on the used grasping principles, form- or force-closure. Further subclassifications are indicated in Fig. 1.2 and labeled as *(a)* to *(j)*.

Form-closed grippers use geometric constraints to secure objects without the need to constantly apply external force to the object [36, 55–61]. These grippers either physically enclose the object or lock it within a cavity, preventing movement through mechanical contact. Most designs feature mechanically driven fingers [36], but alternative approaches include grippers equipped with puncturing needles *(a)* [48], or grippers that stiffen upon activation, such as pneumatically actuated granular pouches *(b)* [49], among others. The mechanical finger gripper typically consists of a serial arm, which can be underactuated with multiple degrees of freedom (DoF) - implemented as rigid linkage *(h)* [52], compliant mechanisms *(i)* [53], or soft robotics *(j)* [54] - or fully actuated, with multiple DoFs *(f)* [50], or with scoops *(g)* [51], or spatially shaped jaws.

Force-closed grippers, on the contrary, rely on the continuous application of external forces, such as negative pressure or squeezing, to secure an object by counteracting forces that could displace it, often maintaining grip through friction at the contact points [44, 59–62]. Common examples include pneumatic grippers, such as suction cups *(c)* [45] or Bernoulli grippers, mechanical pinch grippers *(d)* [46], and others like, for instance, the Flexshape DHEF gripper *(e)* [47], which operates based on principles similar to a chameleon's tongue.

Form-closed grippers offer a more flexible and reliable approach to address the challenges posed by the wide variety of properties appearing in food products, such as varying shapes, sizes, surface textures, and structural stiffness than force-closed grippers [36, 63]. Their holding capabilities are independent of surface properties, such as texture or friction; they have a lower risk of damaging delicate products because the grasping forces are generally lower [36, 62, 64], which also results in a more stable grasping of deformable products since they are less squeezed [25, 44, 60]. Furthermore, form-closed grippers are less likely to transmit bacterial contamination between products compared to gripper types

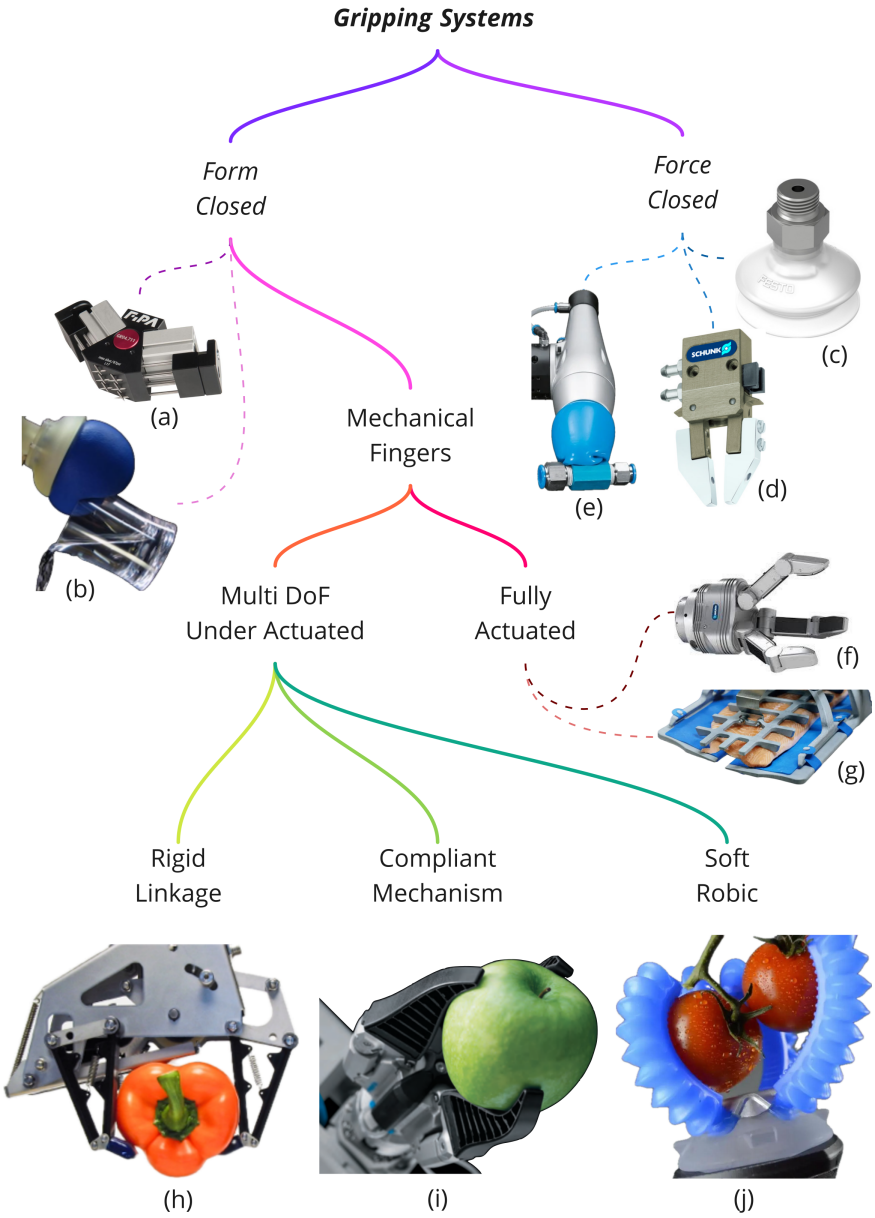


Figure 1.2: Categorized overview of gripper systems relevant for agri-food product handling. Systems are divided into two main approaches: Form-closure and force-closure. Force-closure designs include pneumatic grippers (c), mechanical pinch grippers (d), and other designs (e), such as the Flexshape DHEF gripper. Form-closure designs primarily feature mechanical fingers but also include examples like puncturing grippers (a) and granular jamming grippers (b). Mechanical fingers are further categorized into fully actuated hands with multi-DoF fingers (f) or 1-DoF scoops (g), and multi-DoF under-actuated fingers designed as rigid linkages (h), compliant mechanisms (i), or soft robotic bellows (j). Gripper images retrieved from [45–50, 50–54], and edited.

driven by open-air flow, such as suction cups or Bernoulli grippers [25, 59]. However, they must enclose the object at its widest cross-section and therefore require more freely accessible surface area than force-closure grippers. In practice, when lifting a round object from a table, the structure must wrap around the object at more than three contact regions and exceed 90° of circumferential coverage to constrain vertical motion and lift the object securely.

Among form-closed systems, designs with multi-DoF underactuated fingers show the greatest potential for application in the agri-food industry, as these fingers automatically adapt to various shapes by design [33, 36, 64, 65]. Unlike puncture grippers, they do not damage the object, and compared to granular pouch grippers, they offer lighter, more maneuverable designs that perform better in dense or harsh environments [59, 66]. Fully actuated hands, while precise, are expensive, difficult to control, and overly sensitive for the use of agri-food, especially compared to the simpler mechanical designs of underactuated fingers [63, 67]. The depicted scooping gripper has shown strong performance in relatively predefined and controlled applications, such as grasping individual fish products on conveyor belts [51]. However, this technology lacks the flexibility required for broader applications in the agri-food supply chain. Its design necessitates complete positioning of its (flat) jaws beneath the product, and the grip is inherently unstable in the sideways directions. This instability demands advanced robotic hand control to reorient the plate or a binding system to securely strap the product [55, 68, 69]. Therefore, form-closed grippers with underactuated multi-DoF fingers stand out as the most promising and adaptable solution for handling diverse and delicate products encountered in the food industry [55, 64, 67, 70–72].

Form-closed grippers with multi-DoF fingers designed as rigid linkage *(h)* consist of phalanges made of hard solid materials with hinged connections [34, 63, 67, 73–76]. Force distribution technologies can be integrated into their design to ensure that the same force is applied across the phalanges of the finger [75]. Those designed as soft bellow robotic gripper fingers *(j)* are flexible, air-filled (or fluid-filled) actuators that allow the fingers to bend and conform to the shape of the object being grasped [28, 77]. They are made of soft materials such as silicone or rubber and have a bellowed structure, which expands and contracts when pneumatic or hydraulic pressure is applied [28]. Those designed as compliant mechanisms *(i)* are flexible, elastic structures that achieve motion through the elastic deformation of their material. The varying stiffness and compliance of the design determine their movement and bending direction. These fingers grasp and conform to the shape of an object through localized bending at joints or distributed compliance along the length of the finger. All three types are used in industrial or academic robotic setups, although with varying degrees of success [12].

Fingers designed as compliant mechanisms offer advantageous characteristics for grasping food compared to rigid linkage and soft robotic designs [78]. Unlike rigid linkages, they have fewer moving parts, lower mass, do not require lubrication, and distribute the grasp forces more evenly across the surface [79, 80]. This reduces the risk of contamination and damage, making them ideal for ultra-clean environments. In contrast to soft robotic mechanisms—which are bulkier, require continuous pressurization to maintain load capacity, and wear out more quickly due to softer materials—compliant mechanisms offer superior durability, grasp stability, practicality [78, 81, 82], and passive load-carrying

capacity enabled by their structural stiffness.

Thus, we selected a mechanical gripper with fingers designed as compliant mechanisms to secure objects using form-closed grasps. The literature presented various trends and preferences for specific technologies, with efforts aimed at identifying the best or most generalizable gripper solution, but a universal solution remains elusive; no single technology unequivocally dominates the current field. Each technology offers unique advantages, but among these, we believe compliant mechanisms stand out as the most promising path forward.

Compliant mechanisms - whether designed as underactuated fingers with lumped compliant joints [83–86], or structures with distributed compliance [87–90] - provide a beneficial combination of flexibility and structural rigidity [91–93]. This makes them particularly well-suited for the food industry, where they enable gentle yet secure handling of delicate objects and effectively address object-related challenges. In addition, they offer robustness, reliability, hygiene, and force transparency - attributes that support continuous operation in harsh environments, minimize damage to objects, and simplify control efforts [94, 95]. These features give compliant mechanisms a significant competitive edge over alternative designs [89, 95]. Despite the substantial advances made in this field, there remains considerable potential to explore innovative compliant finger designs for form-closed grippers. In doing so, a broader applicability and more effective solutions can be achieved for agri-food applications.

1.3 Problem statement

Despite the demonstrated success of grippers with mechanical fingers in grasping food objects [96–98], their practical application in the agri-food industry remains limited [12, 99, 100]. The primary challenge arises from objects located in dense and cluttered environments, a common and persistent issue in agri-food automation [101–107]. In such settings, limited space around the target object prevents conventional grippers from establishing a secure grasp. Current systems often attempt to resolve this challenge through complex grasp-planning strategies of the robotic system [19, 108–110], rather than addressing the root of the problem: the closing motion of the gripper design itself.

Conventional grippers designs require sufficient clearance around an object to operate effectively. They rely on positioning wide-open fingers around the object before closing inward to secure it, regardless of whether they are designed as rigid linkages, compliant mechanisms, or soft robotics [36]. Although this approach works well in controlled, or table-top environments with ample clearance [108], such as shown in Figs. 1.3 (a) and (b), it faces significant challenges in more dense, cluttered and unstructured environments, depicted in (c) - (e). In these scenarios, the presence of adjacent obstacles around the target object obstructs the placement and inward movement of the gripper's fingers, leading to misgrasps, disturbances, or even damage, as illustrated in Fig. 1.4.

To overcome the limitations posed by confined spaces, an alternative grasping approach is required to make form-closed mechanical grippers viable in the agri-food industry, bringing automation by flexible robots closer to reality.

1

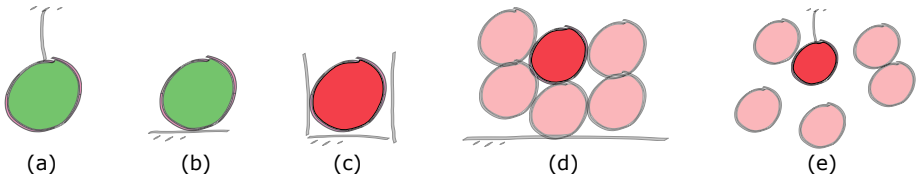


Figure 1.3: Schematic representation of five scenarios commonly appearing in the agri-food sector in which conventional form-closed grippers can (shown in green) and cannot (shown in red) operate, identified by observing the allowable and obstructed sides for grasping, as well as immovable directions. The five classified scenarios include: (a) free-hanging object (e.g., on a branch), (b) object on a flat surface (e.g., table or conveyor belt), (c) object in a tight box (e.g., packed products), (d) object in a pile or heap, and (e) object hanging in a cluster (e.g., a bunch on a plant or surrounded by leaves). In scenarios (a) and (b) conventional grippers can grasp and release the object, as the object is singulated and accessible from the sides, as shown in Fig. 1.1f. In contrast, in scenarios (c)-(e) they cannot establish or release their grasp on the target object (dark red), as they require sufficient clearance around the object for the placement and motion of their fingers as shown in Fig. 1.4 due to walls or neighboring objects (light red), hence an alternative grasping approach is needed.

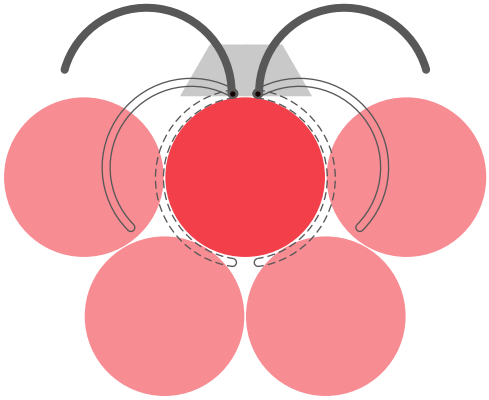


Figure 1.4: The problem of conventional grippers: they set their grasp by moving their fingers towards it to set an encompassing grasp. This method is ineffective in confined spaces due to adjacent objects that obstruct this motion.

1.4 Approach: Tangential finger motion

To enable form-closed grasping in confined spaces, we envision a gripper concept as shown in Fig. 1.5, with fingers that advance tangentially along the object's surface to set and release the grasps, reducing environmental disturbances. These disturbances include both displacements and forces exerted by the fingers on the target and adjacent objects. Effective grasping requires that these forces remain below damaging thresholds for both the object and its surroundings, while the displacements must remain small to avoid misgrasping.

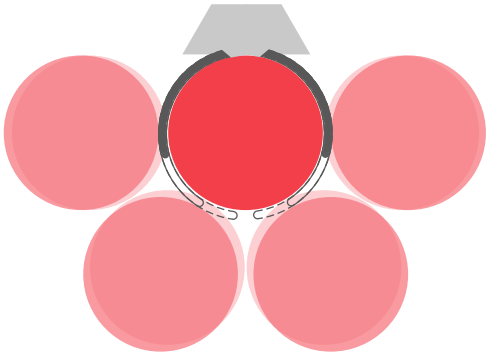


Figure 1.5: Proposed grasping strategy to overcome the limitations of conventional grippers: enabling form-closed grasping in confined spaces by advancing the gripper's fingers tangentially along the object's surface, navigating between adjacent obstacles, aiming to minimize disturbance and space requirements. In this dissertation, we aim to investigate if this solution enables form-closed grasping of food objects in dense environments by developing finger concepts and mechanical gripper designs.

1.5 Proposed finger concept

To operationalize this new grasping approach, we postulate a concept of advancing fingers designed as a flexure-driven eversion mechanism, of which a 2D cross-sectional sketch is shown in Fig. 1.6. The design combines advancing flexures, driven by force F_A from the base, with an eversion mechanism that reduces sliding forces on surrounding surfaces; the elements and working principle are explained next.

The thin, flexible sleeve (e.g. a belt or fabric) is attached at point A, covering the flexures and folding inward over the tip. During operation, the flexures advance with velocity v_t and the tip presses against the inner side of the sleeve, pulling it forward at velocity v_i and unrolling it outward, enclosing the exterior of the finger. This minimizes friction by maintaining a zero relative velocity ($v_e = 0$) with the object and surroundings. A minor tension force F_T controls the backward movement and a snug fit.

The flexures act as structural backbones for navigating clutter, advancing and retracting through curved guides in the gripper housing, and holding the object. They passively follow a predetermined path parallel to the object's contour and exploit environmentally induced bending for steering and adapting to variations in object shape within the intended design envelope, enabled by its lateral flexibility. However, direct sliding along the object

can generate shear forces that risk pushing or damaging the object or hinder the forward motion.

To address this, we incorporate principles from conventional pressure-driven eversion mechanisms to minimize friction during advancement [111–115]. Such mechanisms typically consist of a pressurized tubular structure with one end folded inward, forming a half-toroidal tip. Upon pressurization, the inverted segment rolls outward at the tip, advancing the inward-folded sleeve and continuously everting it until it transitions into the outer wall. This produces a circumferentially stationary outer surface with negligible shear, enabling low-disturbance traversal through confined spaces. The resulting longitudinal motion—advancing without relative sliding—is conceptually similar to the stationary outer layer of a party blower, though in that case the tube is rolled sideways rather than folded inward, yielding only a single stationary surface rather than a circumferentially stationary one.

Combined, the Flexure-Driven Eversion Mechanism enables tangential motion along the object's surface, realizing the proposed finger-closing approach while minimizing environmental disturbances.

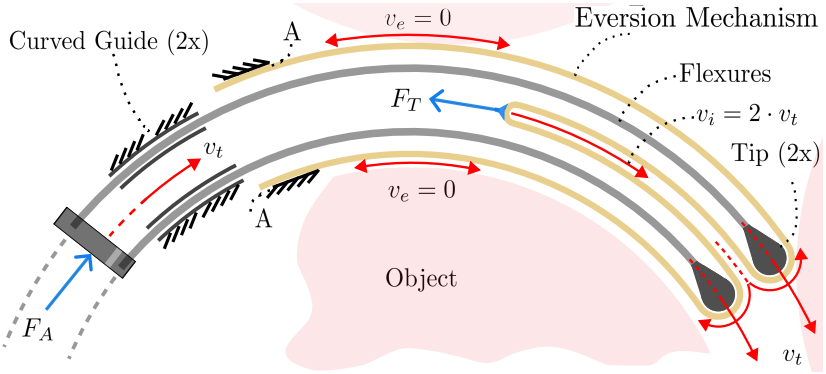


Figure 1.6: 2D cross-section of the proposed Flexure-Driven Eversion Mechanism finger, illustrating the operating principle that enables motion tangential along the object's surface, while minimizing environmental disturbance. The design integrates advancing curved flexures (grey) with an eversion mechanism sleeve (yellow), wrapped inside-out around the tip, reducing traction forces with both the target and adjacent objects during propagation. The flexures are driven forward by force F_A from the base, which extrudes and retracts them through curved guides, aligning them parallel to the object's surface. The eversion mechanism, fixed at point A, is driven by the flexures, which push against its inner surface, pulling the internal part of the sleeve outward along the finger, covering its outer sides. A tension (spring) force F_T is applied at the interior end to control backward motion.

1.6 Research objective

The main objective of this thesis is to develop and evaluate flexure-driven eversion mechanism technology for application in gripper finger designs to enable the grasping of food in confined spaces.

To achieve this, subgoals have been defined that lead to the design, analysis, refinement, and performance evaluation of flexure-driven gripper fingers equipped with an eversion mechanism. The development process begins with establishing performance metrics and creating a model, followed by the introduction and evaluation of finger concepts that embody the proposed design shown in Fig. 1.6. The subgoals are formulated as follows:

1. Define performance metrics validated through technical and practical tests. These metrics drive the design process and assess the gripper's effectiveness in confined, dense environments, including the contribution of finger components to overall performance.

2. Model the kinematics and kinetics of a base-driven flexure navigating sequential obstacles through contact to analyze its trajectories and interaction forces. This evaluation will help assess the applicability of base-driven flexures to execute grasps using the proposed approach and provide insights into their behavior.

3. Design and construct a preliminary gripper with three fingers, each implemented as a Dual-Belt Curved-Flexure Eversion Mechanism (DBCF-EM)—a single curved, base-driven flexure with its inner and outer contours covered by two everting belts guided through rollers. This prototype serves as a proof of concept, validating the key working principles: flexure-based navigation for grasping and holding, and friction reduction at two surfaces through eversion mechanisms. Performance metrics will be evaluated to assess its effectiveness.

4. Redesign and construct an improved gripper to enhance performance and applicability in the agri-food sector. The fingers are designed as Sleeved Concentric-Flexure Eversion Mechanisms (SCF-EM)—a base-driven channeled backbone featuring two concentric curved flexures, which is fully enclosed by a latex eversion sleeve with engineered stretchability, with motions synchronized by a cable-pulley system. This iteration addresses limitations of the DBCF-EM by minimizing finger deviation to prevent misgrasps, increasing holding force, and incorporating a circumferential everting sleeve to enhance durability, hygiene, and reduce the risk of object damage.

The grippers developed in this dissertation are designed to efficiently empty crates of stacked tomatoes by grasping them individually. However, the technology developed is intended to be applicable to handle various foods, dense environments, and tasks.

1

1.7 Thesis outline

This thesis is divided into two main parts: theory and design, each chapter addressing subgoals, contributing to the overall research objective.

Part I (**Chapter 2**) primarily addresses the second sub-goal by introducing a Pseudo-rigid-body model for flexures in event-based scenarios and with multiple loads along their length. Through a case study, it presents the kinetostatic modeling of a base-driven flexure navigating two sequential circular obstacles by bending when obstructed, with each obstruction inducing a new event. The accuracy of the model in predicting the flexure's motion and interactions is validated through experimental testing.

Part II focuses on the development and evaluation of two finger designs, covering subgoals 1, 3, and 4. **Chapter 3** introduces a preliminary gripper design with three fingers, each implemented as a Dual-Belt Curved-Flexure Eversion Mechanism (DBCF-EM)—a single curved, base-driven flexure with its inner and outer contours covered by two everting belts guided through rollers. **Chapter 4** advances with introducing an improved gripper design, with fingers implemented as Sleeved Concentric-Flexure Eversion Mechanisms (SCF-EM)—a base-driven channeled backbone featuring two concentric curved flexures, which is fully enclosed by a latex eversion sleeve with engineered stretchability, with motions synchronized by a cable-pulley system. In addition to introducing these finger designs, both chapters provide details on the mechanical design and manufacturing of the grippers, as well as the experimental setup and testing methods used for their evaluation.

Chapters 5 and 6 discuss and summarize the key findings of this work, comparing the performance metrics with the state of the art and among both presented designs, offering recommendations for future design improvements and grasp strategies to advance the development of effective agri-food grippers, and place the technology and results in a broader context, highlighting their potential impact. from all sides by a stretchable latex eversion sleeve.

'I find out what the world needs. Then I go ahead and try to invent it.'

Thomas Edision

I

Theory

From Design Concept to the Modeling Framework

In Chapter 1, we introduced the advancing finger concept based on a flexure-driven eversion mechanism, intended for form-closed grasping in dense environments. In such settings, the flexure acts as a compliant backbone, navigating around obstacles—both by design and through interaction-induced bending—while advancing forward to guide the finger along the object. This demands an understanding of how flexures behave when interacting with their surroundings, as well as the ability to predict their resulting trajectory and interaction forces to assess their suitability for the design.

In Chapter 2, we develop a kinetostatic model of advancing flexures using the Pseudo-Rigid-Body Model (PRBM) approach, supported by experiments, to assess their applicability for navigation through clutter. The model is developed around a deliberately selected case study: a straight, base-driven flexure navigating between two circular obstacles under frictionless contact. Although the envisioned finger must follow a curved trajectory—making the choice to model a straight rather than a curved flexure seem counterintuitive—beginning with a straight flexure is an intentional and advantageous first step. Also, the frictionless-contact assumption may appear abstract at first sight, it is consistent with the intended finger design, as the eversion mechanism naturally removes surface friction through its unrolling motion.

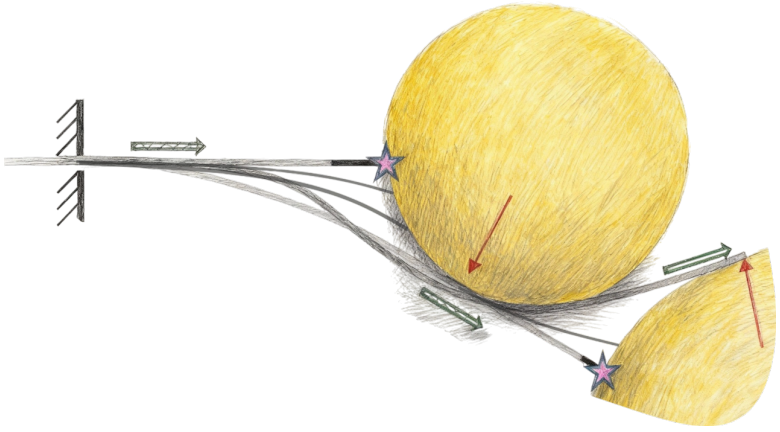
An important argument for using a straight flexure is that PRBM theory is an insightful parametric modeling method with several validated formulations for straight beams under different bending modes and tip loads. This makes straight flexures a robust and analytically transparent starting point, enabling us to begin with simple cases and incrementally add complexity. It allows us to focus on the core mechanics of navigation—bending under obstruction, switching contact points, progressing through clutter, and the resulting interaction forces—phenomena that also arise when designing curved flexures. A PRBM of a curved flexure, however, is a more complex starting point because it inherently requires a multi–degree-of-freedom topology. Nonetheless, we see no reason why such a model could not be implemented once the straight-flexure case is fully understood and established.

A second argument for using a straight flexure is that it enables far more accurate experimental validation of the model. Straight flexures made from flat spring steel provide highly repeatable geometry and material properties at industrial precision, meaning that the design parameters used in the model can be reproduced with high accuracy in the experiments. In contrast, curved flexures must be manually formed, introducing significant variability and uncertainty, which makes reliable validation of the model impractical at this stage.

These choices allow the model to be developed step-by-step while remaining analytically tractable, yet rich enough to capture the essential mechanics of navigational behavior and to enable proper experimental validation of the model itself.

2

Pseudo-Rigid-Body Modeling of Advancing Interacting Flexures



Chapter 2 develops and validates a kinetostatic model of an advancing flexure navigating sequential obstacles using a Pseudo-Rigid-Body Modeling (PRBM) approach. Building on Chapter 1, we focus on how a base-driven flexure bends, switches contact points, and progresses through clutter to assess its suitability for confined-space grasping. The modeling framework will build upon a deliberately simplified case study: a straight advancing flexure interacting with frictionless circular obstacles. The method extends PRBM by accommodating multiple loads at unknown positions and managing event-based topology changes through a phase-based analysis that avoids nonphysical behavior. Experiments show repeatable advancement between closely spaced obstacles with 98% trajectory accuracy and 90% force accuracy, forming a foundation for continuing evaluating advancing flexures in the proposed finger design.

This chapter was resubmitted as: Huisjes, A.E., van der Wijk, V., and Herder, J.L., (2025). Pseudo-rigid-body modeling of flexures in event-based scenarios with multiple loads along their length. Journal of Mechanisms and Robotics.

2

Pseudo-Rigid-Body Modeling of Flexures in Event-based scenarios with Multiple Loads along their length

Abstract *This paper extends the Pseudo-Rigid-Body Modeling (PRBM) of kinematics and kinetostatic force and moment analysis of flexures to cover event-based scenarios and cases where flexures endure multiple loads at various unknown locations along their length. Events signify crucial junctures requiring a sudden change to another PRB model like, for example, the addition or removal of an external load. The phase between events is analyzed by performing three subsequent steps: 1) selecting a representative PRBM accounting for the flexure deformation and the load; 2) performing a kinematic analysis via vector loop equations; and 3) kinetostatic force and moment computation using equilibrium equations associated with the PRBM. A smooth phase transition was ensured by keeping the potential energy in the system within reasonable bounds at events. Additionally, we enable the analysis of flexures with multiple loads along its length by serially combining different PRBMs and minimizing the system's potential energy. The two aspects of the method were developed using a case study; the kinetostatic modeling of a flexure advancing from its base forward, encountering two subsequent circular objects, and passing between them by bending when obstructed. Here, two events are identified once hitting a new obstacle, separating the problem into three distinct phases for the analysis. Our model was validated through experiments, demonstrating accurate motion prediction between the flexure and the obstacles and a highly nonlinear evolution of the interaction forces while moving forward, with errors of 1.5% in the kinematics and 10% in the interaction forces.*

2.1 Introduction

Compliant mechanisms offer advantages over rigid-body mechanisms, as they provide repeatable motion, lower part count, reduced mass, and cost-effectiveness due to their reliance on elastic deformation instead of rigid joints [94, 116–118]. Moreover, compliant mechanisms do not require lubrication, which makes them ideal for ultra-clean environments in precision mechatronics, food handling, and medical industries. Flexures are widely used as lumped joints or as flexure-beam elements with distributed compliance in applications such as motion stages, robotic devices, and surgical instruments, where they provide precise motion guidance or force transmission [93, 119–121]. They are also increasingly realized as fully monolithic compliant structures, either directly by design or through topology optimization.

Several methods exist for the kinetostatic modeling of compliant mechanisms for both small and large deflections, aiming to analyze their force-deflection behavior. For example, methods such as Finite Element Analysis (FEA), Timoshenko's beam theory, free-body diagram (FBD) and constraint-force-based (CFB) methods, the circle-arc method, energy-based approaches, compliance matrix methods, numerical and closed-form analytical solutions, and the Pseudo-Rigid-Body Modeling (PRBM) approach are presented in the literature [122–129], each having their advantages and disadvantages as shown by several overview articles [130, 131].

The PRBM method is a parametric modeling method that uses conventional rigid-body linkage kinematics to approximate the nonlinear, large-deflection behavior of compliant mechanisms. In this approach, a compliant joint or flexure defined by its geometry and load case is replaced by a simplified pseudo-rigid linkage with torsional pseudo-springs at its revolute joints, enabling rapid computation of its bending stiffness and the associated force–deflection and tip-motion response, while providing an insightful representation of the deflection behavior with only a few meaningful parameters and enabling rapid design exploration and optimisation [132, 133].

PRBM theory provides several validated fundamental formulations for basic elements—most notably lumped compliant joints and thin flexural beams—each represented by a specific serial pseudo-linkage topology with corresponding torsional spring stiffness values derived from their bending mode, tip loading, and geometry [91, 134–139]. These models support detailed kinetostatic and dynamic analyses across a wide variety of flexures with different initial shapes, deformation patterns, and loading conditions, offering engineers a straightforward and insightful method for analyzing compliant elements of comparable geometry and load case.

For more complex compliant structures, dedicated PRBM models have also been developed. These are either assembled directly from existing fundamental formulations—using analytically computed torsional stiffnesses based solely on hinge geometry, as in spatial mechanical metamaterials [140]—or constructed by defining custom pseudo-rigid-linkage topologies whose spring stiffness values must be identified empirically through FEA or experiments, as seen in soft robotic fingers based on the Fin Ray effect [53] or in variable-stiffness mechanisms using snap-fit reconfiguration, where each configuration requires its own PRBM representation [141].

However, the standard fundamental PRBM formulations for flexures encounters two primary limitations. Firstly, scenarios that necessitate modifying the pseudo-linkage

topology during the analysis have not been addressed. This situation occurs when there is an instantaneous alteration in the flexure's initial or deformed shape or when the imposed load case undergoes an abrupt change, requiring a switch to another PRB model for more precise and accurate modeling, i.e., an *event* happens (1). Secondly, the methodology exclusively addresses flexures subjected to loads at their endpoints, omitting flexures experiencing *multiple load cases along their length* (2). This limitation becomes evident when dealing with flexures exposed to individual forces, moments, or their combinations at different locations along their span, such as when they have multiple contact points with their environment.

The goal of this article, therefore, is to present and validate experimentally the PRB modeling of flexures in event-based scenarios with multiple loads along their length. We will develop our method using a challenging yet illustrative case study that addresses both of these two aspects: flexures in event-based scenarios and flexures with multiple load cases along their length.

The case study involves the kinetostatic modeling of a flexure advancing from its base forward, encountering two subsequent circular objects, and passing between them by bending when obstructed. This case study is illustrative for analyzing the kinetostatic behavior of slender devices that move forward through an environment using interaction with objects and self-searching for navigation. Practical examples include a catheter moving through tissue, a soft rescue robot navigating urban settings, or a compliant gripper finger maneuvering down a pile of objects to grasp one.

In the case study, an event (1) occurs every instance when the advancing flexure hits a new obstacle, initiating a new load at the contact point and a significant morphing of the flexure's deflectional shape, requesting a change in the PRB model for further analysis. We present a method that deals with these sudden alterations in the pseudo-linkage topology and enables smooth switching between different PRB models at events by keeping the potential energy in the system within reasonable bounds. Multiple contact forces (2) are established when passing between the objects as the flexure's side slides over the first one while its tip follows the contour of the second one. Here, we perform the kinetostatic analysis by serially combining different PRB models, setting up multiple vector loops, and minimizing the system's potential energy to compute the pose of the serially connected pseudo-linkage.

First, in section 2.2, the general steps of the method will be explained and subsequently developed within the defined use case. Following this, in section 2.3, the experimental setup that has been built for model validation and accuracy assessment is presented, followed by the presentation of the results in section 2.4. In section 2.5, a comprehensive discussion of the results, the method, and suggestions for future research will be provided. Finally, the conclusions of this article are presented in section 2.6.

2.2 Method

The methodology for PRB modeling of flexures in an event-based scenario involves a systematic approach. First, instances when specific events occur within the problem at hand must be identified.

Events signify crucial junctures requiring a sudden change to another PRB model, i.e., a different pseudo-linkage topology, to ensure accurate further modeling. Such transitions become necessary because the previous model is no longer capable of accurately representing the evolving scenario.

A typical example of an event is the addition or removal of an external load as the deflectional shape of the flexure morphs significantly. This becomes evident when the flexure, for instance, makes contact or loses contact with an external object, such as when the flexure hits an object or when an object falls onto it. In addition, instantaneous changes in the initial or deflectional shape of the flexure without the case of addition or removal load can be examples of events. This includes buckling a flexure or the snap-through of a prestressed S-shaped deformed flexure toward a C-shaped deformed flexure. Each of these example scenarios identifies an event as they necessitate a swift transition to another pseudo-linkage model to model the kinetostatic behavior of the flexure accurately within the newly evolved conditions.

Phases are the periods between events, during which the pseudo-linkage topology remains unchanged until the next event. The difference from an event is that during a phase, only the pose of the linkage changes instead of the topology. During a phase, the deflective shape of the flexure gradually reduces or increases by a continuous decline or incline of the magnitude of the load case.

Three sequential steps must subsequently be performed per phase to analyze the kinetostatic behavior of flexures in event-based scenarios. In step (1), a representative PRB model topology must be selected to account for the flexures's deformation and the load case during that phase. In step (2), using an incremental procedure, the kinematic analysis is performed by incrementally calculating the linkage's pose from its initial to its final state within the defined phase duration. In step (3), a kinetostatic force and moment analysis is conducted by substituting the obtained pose values of the pseudo-linkage into the force-balance equations of the chosen PRB model. These three steps result in the development of the force that governs the behavior of the flexure during the specific phase, and by subsequently combining them, the entire problem is analyzed.

Smooth phase transition is ensured by keeping the potential energy in the system within reasonable bounds at events. The topology change results in alterations in the number, the length, and often the pose of links, and the number of springs and their stiffness. Consequently, in the first increments after an event occurs, the system's potential energy tends to change suddenly, and the mechanism becomes stretched unnaturally to satisfy the kinematic equations. This can potentially yield physically invalid outcomes. The first increments of a new phase are removed to keep the system's potential energy within reasonable bounds at events, i.e. near the value of the end of the previous phase, ensuring a more consistent and valid transition between phases.

2.2.1 Case study

The theory of the event-based PRBM method is presented through a carefully selected case study that involves the planar setup depicted in Fig. 2.1. This case study consists of a straight flexure driven linearly forward from its base, encountering two subsequent circular rigid objects. The base of the flexure is positioned at coordinates $(x, y) = (0, 0)$ and the flexure has a thickness $t[m]$, a width $w[m]$, and a Young modulus $E[Pa]$. The flexure length

protruding from the base is l and increases incrementally with Δl as $l^{i+1} = l^i + \Delta l$. The objects have radii R_A and R_B, centered at Q_A and Q_B, respectively. They were positioned such that the flexure passed between them by bending when obstructed. The contact between the flexure and the objects was considered frictionless, and the contact forces at the respective contact points are denoted as F_A and F_B, respectively.

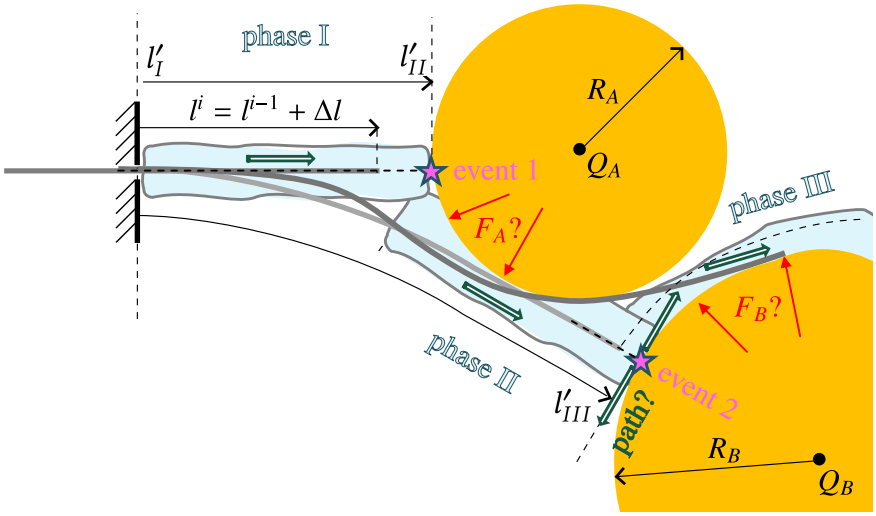


Figure 2.1: The examined case study: A straight flexure advances forward from its base, encountering two subsequent circular rigid objects, A and B, and passing between them by bending when obstructed. Here, two events occur when the flexure hits a new object, separating the problem into three distinct phases: phase I, until its tip hits object A; phase II, first, its tip following object's A contour and subsequently leaving it till it hits object B; phase III, its tip following object's B contour until leaving it, with the end of phase III intentionally chosen. The flexure is loaded by contact force F_A and F_B while interacting with the objects.

2.2.2 Model development

As illustrated in Fig. 2.1, two events can be identified that occur when the flexure encounters a new obstacle. The first event occurs when the tip of the flexure hits object A, and the second event occurs when the tip hits object B. The events separate the problem into three distinct phases: Phase I, the period from the start of the problem to event one; phase II, the period between events one and two; phase III, the period from event two until the flexure's tip leaves object B.

The end of phase III was intentionally chosen for the brevity of this article; otherwise, the flexure would have transversed further until it hit another object. However, this part has been excluded because the analysis of this aspect is already covered in phase II when the flexure approaches object B.

The duration of a phase is expressed in terms of the length of the flexure. The start and end of a specific phase are indicated as ($'$) and ends ($''$), respectively, plus the phase number. For example, l'_I, l'_{II}, and l'_{III} mark the length of the flexure when phase I, phase II,

and phase III starts, while l_I'', l_{II}'', and l_{III}'' designate the flexure length when each of those phases, respectively, ends.

2.2.3 Phase I

In phase I, the flexure freely approaches object A without experiencing any contact forces until it comes into contact with object A. At first, the flexure length is $l_I' = 0$; at the end, it reaches length l_I''. Forces are not experienced during this phase, so $F_A = 0$ and $F_B = 0$. To determine the value of length l_I'', the Matlab function *linecirc* was utilized to find the intersection point between the flexure and the object located closest to the slit. For this calculation, the flexure was modeled as a straight line with a slope $m = 0$, while the object was represented as a circle with a center at Q_A and a radius of R_A.

2.2.4 Phase II

In phase II, contact with object A is established, obstructing the linear path of the flexure, leading to a C-shaped deformation and contact force F_A. Phase II begins the first increment after hitting object A, so at flexure length $l_{II}' = l_I'' + \Delta l$. First, the flexure's tip follows the contour of object A, tracing a circular path with a radius R_A around the object's center. Hereafter, its tip leaves the surface and starts approaching object B. This occurs when the longitudinal axis through the end of the deflected flexure becomes perpendicular to the normal vector of the object's surface at the contact location, at a length denoted as $l_{II}^{\perp}$. Continuing, the flexure slides over object A, and the contact point shifts along its side. Now, the flexure has a deformed part between its base and object A and an undeformed part that has passed object A. This segment lengthens incrementally in a straight line toward object B until it hits object B, reaching a total flexure length l_{II}''.

Step 1: PRBM

The flexure's deformation and load during phase II were modeled using the PRBM formulation presented in Section A.1.3 of [91], known as "deflecting a fixed–free beam with a force at its end," and shown in Fig. 2.2. In this model, the flexure of length l^i is represented by a pseudo-link l_2 pinned to a fixed link l_1. As the flexure length is incremented, $l^{i+1} = l^i + \Delta l$, the corresponding link lengths l_1 and l_2 increase proportionally according to their defined ratios. Consequently, link l_2 rotates by an angle θ_2 about a pseudo-joint equipped with a torsional spring of stiffness K_1 [Nm/rad], which represents the flexure's bending resistance and is used in Step 3 to compute the contact force on the flexure, F_A^{II}, during Phase II.

The stiffness K_1 was obtained using

$$K_1 = \gamma K_\Theta \frac{EI}{l^i}, \tag{2.1}$$

where $I = wt^3/12$ is the flexure's second moment of area about its neutral axis, with t the flexure thickness and w its width, and $K_\Theta = 2.65$ is taken from [91]. Assuming frictionless contact, the contact force F_A^{II} acts normal to the object's surface at the contact point N. The corresponding angle is denoted ϕ in [91] and here referred to as θ_3, defined as the clockwise angle from the horizontal axis to the point of contact with the flexure, as shown in Fig. 2.3. The components of this contact force in the horizontal and vertical directions

are indicated as nP and P, respectively. As given in [91], the angle θ_0 represents the exit angle of the flexure tip and is equal to $\theta_2 c_0$, with c_0 being a constant.

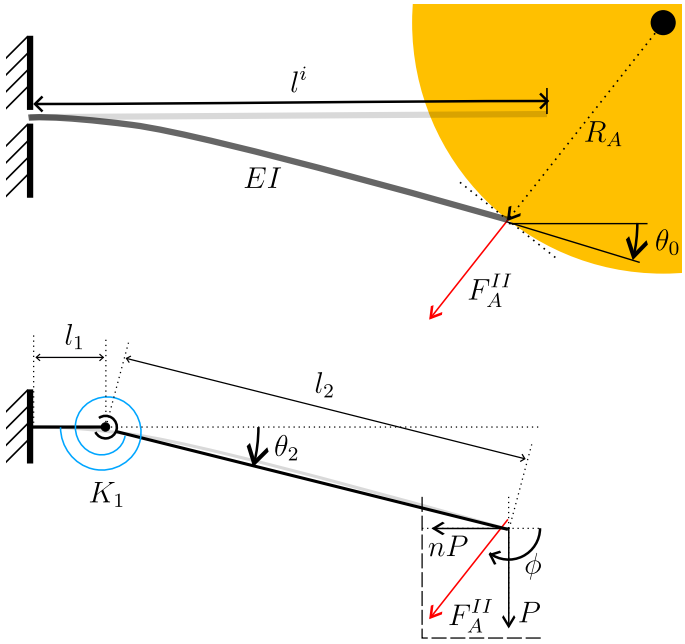


Figure 2.2: Phase II: at the top, the flexure deflection while interacting with object A; at the bottom, the selected corresponding PRB model [91]. This pseudo-linkage comprises a fixed link l_1 pinned to link l_2 via a torsional spring that permits rotation by an angle θ_2. The flexure is subjected to a force F_A^{II} at the contact point, consistently oriented normal to the object's surface.

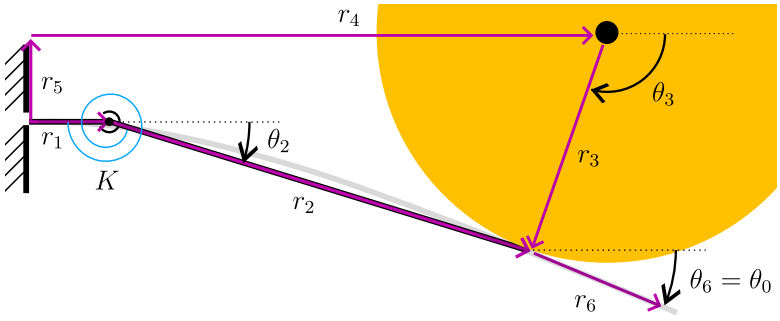


Figure 2.3: Vector-loop of phase II, with vector r_1 and r_2 being the links of the pseudo-linkage, r_3 representing the distance from the object's origin to the point of contact with the flexure, and r_4 and r_5 denoting the relative positions of the object's origin concerning the base of the flexure. Notably, vector r_6 is excluded from this loop, representing the part of the flexure that had passed object A at an exit angle θ_6, equalling the deflected flexure's tip orientation θ_0 [91].

Step 2: Kinematic analysis

The kinematic analysis was performed using the vector loop shown in Fig. 2.3 and solved using (2.2):

$$\vec{\mathbf{r_1}} + \vec{\mathbf{r_2}} = \vec{\mathbf{r_3}} + \vec{\mathbf{r_4}} + \vec{\mathbf{r_5}}, \tag{2.2}$$

where the positions and orientations of the fixed link l_1 and the pseudo-link l_2 are represented by the vectors $\vec{\mathbf{r_1}}$ and $\vec{\mathbf{r_2}}$, respectively. Their lengths increase incrementally by $(1-\gamma)l^i$ and γl^i, with $\gamma = 0.85$ as defined ratio taken from [91]. The angle of $\vec{\mathbf{r_1}}$ is fixed, whereas the direction of $\vec{\mathbf{r_2}}$ relative to the positive x-axis is given by the angle θ_2.

The vector $\vec{\mathbf{r_3}}$ describes the circular trajectory of the flexure's tip around Q_A, with constant length $l_3 = R_A$, rotating around the center of object A by the angle θ_3. The tip of $\vec{\mathbf{r_3}}$ is connected to the tip of $\vec{\mathbf{r_2}}$, and the two vectors may rotate relative to each other until they become perpendicular to the flexure length $l_{II}^{\perp}$. The vector loop of the deformed portion of the flexure is completed by the vectors $\vec{\mathbf{r_4}}$ and $\vec{\mathbf{r_5}}$, whose fixed lengths and angles define the x- and y-distances from the base to the point Q_A. The remaining vector, $\vec{\mathbf{r_6}}$, represents the undeformed flexure length l_6 that has passed object A under exit angle θ_6 and is not included in the vector-loop equations.

To solve (2.2), all five vectors were substituted by their complex-number expressions, separated into their x- and y-components, and combined with the known parameters (l_3, l_4, l_5, θ_1, θ_4, θ_5), yielding the set of two equations shown in (2.3):

$$\begin{aligned} l_1 + l_2 c_2 - l_3 c_3 - l_4 &= 0, \\ l_2 s_2 - l_3 s_3 - l_5 &= 0, \end{aligned} \tag{2.3}$$

where the shorthand notations $c_i = \cos\theta_i$ and $s_i = \sin\theta_i$ (for $i = 1, \ldots, 6$) are used throughout this work. For each incremental flexure length, the unknown angles θ_2 and θ_3 were obtained by substituting l^i into (2.3) and solving the resulting system using the *fsolve* command in MATLAB for length values ranging from l'_{II} to $l_{II}^{\perp}$.

Before solving these equations, the specific flexure lengths l''_{II} and $l_{II}^{\perp}$ must be determined. The flexure length $l_{II}^{\perp}$ corresponds to the moment at when the flexure tip leaves object A. This occurs when the tip direction becomes perpendicular to the surface normal at the contact point, meaning that vectors $\mathbf{r_2}$ and $\mathbf{r_3}$ are orthogonal. This orthogonality condition is imposed using (2.4):

$$\vec{\mathbf{r_2}} \cdot \vec{\mathbf{r_3}} = c_2 l_2 \, c_3 l_3 + s_2 l_2 \, s_3 l_3 = 0. \tag{2.4}$$

The length $l_{II}^{\perp}$ was obtained by substituting $l_1 = (1-\gamma)l_{II}^{\perp}$ and $l_2 = \gamma l_{II}^{\perp}$ into (2.3) and (2.4) and solving the resulting system simultaneously, yielding $l_{II}^{\perp}$, $\theta_2^{\perp}$, and $\theta_3^{\perp}$.

The flexure length l''_{II} corresponds to the moment when the tip comes into contact with object B. This length was computed using the MATLAB function *linecirc* by modeling the protruding part of the flexure as a straight line with slope $m = -\tan(\theta_0)$ and intercept $b = r_{2,y} - m\, r_{2,x}$, and finding its closest intersection with the circle centered at Q_B with radius R_B. Here, $r_{2,x}$ and $r_{2,y}$ denote the coordinates of the tip of the vector $\vec{\mathbf{r_2}}$, and $\theta_0 = \theta_6 = \theta_2^{\perp} c_0$ is the terminal angle, with $c_0 = 1.24$ taken from [91].

The kinematic analysis of phase II was then performed by substituting $l_1 = (1-\gamma)l^i$ and $l_2 = \gamma l^i$ for each incremental flexure length l^i from l'_{II} to $l_{II}^{\perp}$ into (2.3) and solving the

resulting system. This yielded the evolution of the pseudo-linkage pose, the direction angle θ_3 of the contact force, and the location of the contact point for all lengths between l'_{II} and $l^{\perp}_{II}$. The remaining portion of phase II was completed by noting that the pseudo-linkage pose remained constant from $l^{\perp}_{II}$ to l''_{II}, such that $l_1 = l^{\perp}_1$, $l_2 = l^{\perp}_2$, $l_6 = l^i - l^{\perp}_1 - l^{\perp}_2$, $\theta_2 = \theta^{\perp}_2$, $\theta_3 = \theta^{\perp}_3$, and $\theta_6 = \theta^{\perp}_2 c_0$.

Step 3: Kinetostatic force and moment analysis

The magnitude of the force F^{II}_A for a flexure of length l^i was calculated using the PRBM force relations shown in (2.5)–(2.7). The force magnitude is given by:

$$F^{II}_A = P\sqrt{1+n^2}, \tag{2.5}$$

where P is the lateral force component acting on the flexure and is obtained using:

$$P = \frac{K_1\theta_2}{\gamma l(c_2 + n s_2)}, \tag{2.6}$$

and where n is the ratio of the horizontal to vertical components of F^{II}_A, defined as:

$$n = -\tan(\phi) = -\tan(\theta_2). \tag{2.7}$$

The torsional stiffness K^i and the force ratio n^i were first determined by substituting the values of l^i and θ^i_2 into (2.1) and (2.7). The lateral force component P^i was then computed by inserting l^i, θ^i_2, K^i, and n^i into (2.6). Finally, the magnitude of the force $F^{II,i}_A$ was obtained by substituting P^i and n^i into (2.5), and the force components in the x- and y-directions were computed using:

$$\overrightarrow{\mathbf{F}^{\mathbf{II}}_{\mathbf{A}}} = \begin{bmatrix} F_{A,x} \\ F_{A,y} \end{bmatrix} = \begin{bmatrix} c_2|F^{II}_A| \\ s_2|F^{II}_A| \end{bmatrix}. \tag{2.8}$$

2.2.5 Phase III

In phase III, the flexure remains in sliding contact with object A while simultaneously establishing contact with object B, resulting in two interaction forces, F^{III}_A and F^{III}_B, acting normal to the respective surfaces. This phase begins at the first increment after the flexure tip contacts object B, corresponding to a flexure length of $l'_{III} = l''_{II} + \Delta l$. As the flexure advances, its tip moves upward along the surface of object B, tracing a circular trajectory with radius R_B around its center. The portion of the flexure between objects A and B deforms into a C-shape, while the remaining segment between object A and the base assumes an S-shaped configuration. The orientations of the resulting normal forces are illustrated in Fig. 2.4(a). Phase III concludes when the longitudinal axis of the deflected flexure tip becomes perpendicular to the surface normal of object B for this use-case.

Step 1: PRBM

A representative PRBM for phase III, obtained by combining two original PRBM formulations, is shown in Fig. 2.4(c). This model is constructed by introducing a cut in the flexure at an infinitesimal distance to the right of the load F_A, resulting in two free-body diagrams (FBDs) for the segments l_{oa} and l_{ab}, as illustrated in Fig. 2.4(b).

On the right, the C-shaped segment l_{ab} is loaded by the tip force F_B, and its equilibrium is maintained by an internal force F_{ab} and internal moment M_{ab} at the cut. On the left, the S-shaped segment l_{oa} is loaded by the cut forces F_{ab} and moment M_{ab} (acting in opposite directions), in addition to the external contact force F_A. At its clamped base, the segment is held in equilibrium by an internal force F_o and internal moment M_o, where the component $F_{o,x}$ may be interpreted as the advancing actuation force.

The segment l_{oa} is modeled using the PRBM for a "combined force–moment end load (3R model)," as proposed in [136], refined in [137], and described in Section A.1.9 of [91]. The segment is fixed at its left end and subjected at its free end to the combined force $F_{ab} + F_A$ and moment M_{ab}, resulting in an S-shaped deformation. Its pseudo-rigid-linkage topology consists of the fixed link l_1 followed by three serial links l_2, l_3, and l_4 connected by revolute joints. The lengths of these links are proportional to the total segment length l_{oa}, using the given ratios in (2.9):

$$\begin{bmatrix} l_1 \\ l_2 \\ l_3 \\ l_4 \\ l_5 \\ l_6 \end{bmatrix} = \begin{bmatrix} \gamma_1 l_{oa} \\ \gamma_2 l_{oa} \\ \gamma_3 l_{oa} \\ \gamma_4 l_{oa} \\ (1-\gamma_5) l_{ab} \\ \gamma_5 l_{ab} \end{bmatrix}, \qquad \begin{aligned} \gamma_1 &= 0.125 \\ \gamma_2 &= 0.351 \\ \gamma_3 &= 0.388 \\ \gamma_4 &= 0.136 \\ \gamma_5 &= 0.85 \end{aligned} \tag{2.9}$$

The links rotate by the angles θ_2, θ_3, and θ_4, and torsional springs with stiffnesses K_1, K_2, and K_3 are attached at the joints. These stiffness values are determined by the segment length l_{oa}, the second moment of area I, Young's modulus E, and the given characteristic spring factors K_{Θ_i}:

$$K = \begin{bmatrix} K_1 \\ K_2 \\ K_3 \\ K_4 \end{bmatrix} = \begin{bmatrix} K_{\Theta_1} EI/l_{oa} \\ K_{\Theta_2} EI/l_{oa} \\ K_{\Theta_3} EI/l_{oa} \\ \gamma_5 K_{\Theta_4} EI/l_{ab} \end{bmatrix}, \qquad \begin{aligned} K_{\Theta_1} &= 3.25 \\ K_{\Theta_2} &= 2.84 \\ K_{\Theta_3} &= 2.95 \\ K_{\Theta_4} &= 2.65 \end{aligned} \tag{2.10}$$

The segment l_{ab} is modeled using the PRBM for a "deflecting fixed–free beam loaded at its end," described in Section A.1.3 of [91]. This segment experiences the external tip force F_B, counteracted at the cut by the internal force F_{ab} and internal moment M_{ab}, analogous to clamping forces that ensure static equilibrium. Its pseudo-rigid-linkage topology consists of the links l_5 and l_6, with lengths given by the ratio γ_5 in (2.9). At the cut, the orientation of link l_5 matches the orientation of link l_4, ensuring $\theta_4 = \theta_5$. Link l_6 rotates by angle θ_6, and the torsional spring with stiffness K_4 in (2.10) is affixed at this joint. The undeformed longitudinal and lateral axes of segment l_{ab} correspond to the local axes x_5 and y_5, respectively, note not the horizontal and vertical axes. The angle of the tip load F_B with respect to the x_5-axis, and its components along these axes, are denoted ϕ_B, nP_B, and P_B.

Compared to the classical PRBM formulations, sliders appear at the connection points between links due to the unknown division of the total flexure length l_i into the two segments. In the original models, segment lengths are known a priori, so link lengths follow directly from (2.9). In phase III, however, the location of contact point A—and therefore the partitioning of l_i into l_{oa} and l_{ab}—is unknown. The sliders therefore represent

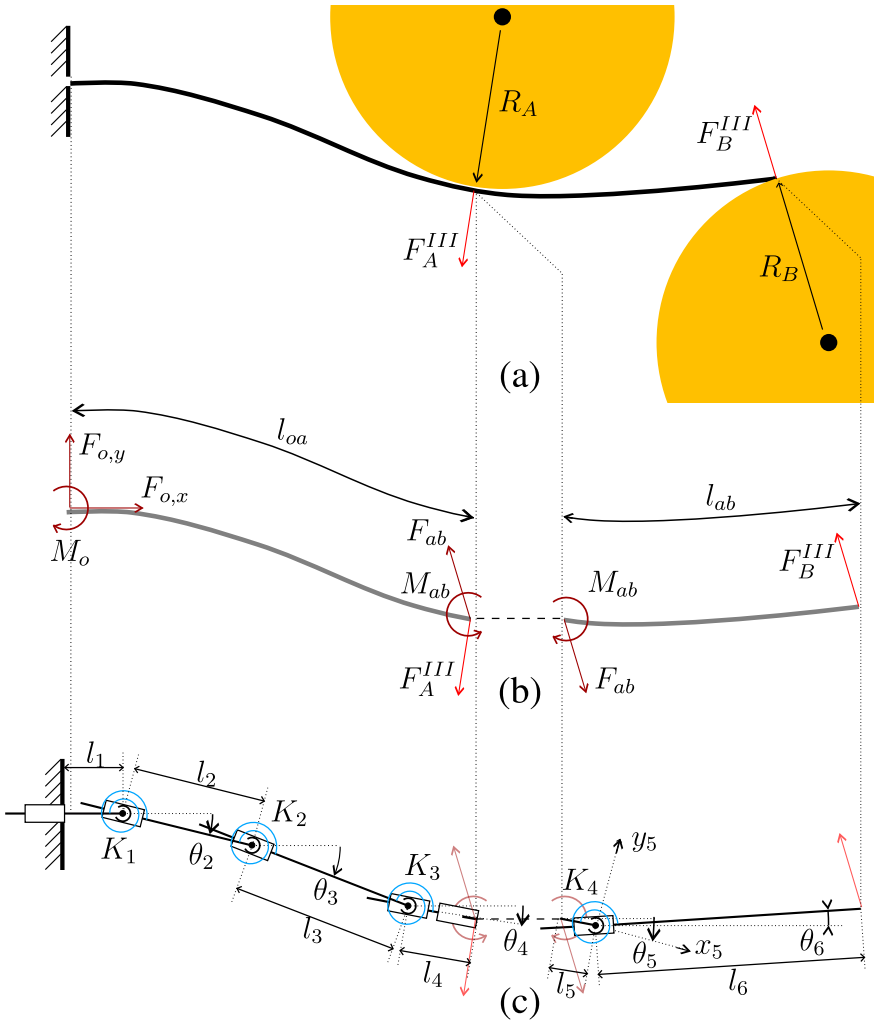


Figure 2.4: Phase III: (a) the flexure deflection and contact forces F_A and F_B during passage between objects, (b) the free-body diagrams of the flexure segments l_{0a} and l_{ab}, derived by cutting just to the right of loads F_A to have loadings at the extremities of the segments, (c) the serial combination of two selected PRB models corresponding to the segments; with on the left a model encompasses l_1 to l_4 along with torsional springs K_1 to K_3, and on the right a model features links l_5 and l_6, and torsional spring K_4. Introducing sliders into the original PRB models reflects the yet undetermined pseudo-link lengths arising from the unknown contact location with object A; their values, which must sum to the flexure length l^i at incremental step i, are determined by minimizing the system's potential energy, subject to the constraint that the pseudo-link lengths within each segment are related through the characteristic length ratios γ of the underlying PRB models.

proportional adjustments of the link lengths. For example, if contact point A shifts to the right, the segment l_{oa} becomes longer while l_{ab} becomes shorter; consequently, links l_1–l_4 extend proportionally and links l_5–l_6 shorten accordingly. These sliders allow the overall PRBM topology and principles to remain intact while accommodating the unknown segment lengths and associated stiffness values.

Finally, the PRBMs of the two segments are combined in series by connecting links l_4 and l_5, producing a unified topology with one external tip load and an additional external load applied along the flexure at the end of link l_4.

Step 2: Kinematic analysis

The kinematic analysis of phase III was performed using the two closed vector loops shown in Fig. 2.5 and defined in (2.11):

$$\begin{aligned} \vec{\mathbf{r_1}}+\vec{\mathbf{r_2}}+\vec{\mathbf{r_3}}+\vec{\mathbf{r_4}} &= \vec{\mathbf{r_7}}+\vec{\mathbf{r_8}}+\vec{\mathbf{r_9}}, \\ \vec{\mathbf{r_5}}+\vec{\mathbf{r_6}}+\vec{\mathbf{r_7}} &= \vec{\mathbf{r_{10}}}+\vec{\mathbf{r_{11}}}+\vec{\mathbf{r_{12}}}. \end{aligned} \tag{2.11}$$

The vectors $\vec{\mathbf{r_1}}$–$\vec{\mathbf{r_6}}$ describe the positions and orientations of the pseudo-rigid links l_1–l_6. The vectors $\vec{\mathbf{r_7}}$ and $\vec{\mathbf{r_{10}}}$ represent the locations of the contact points on objects A and B, while $\vec{\mathbf{r_8}}$, $\vec{\mathbf{r_9}}$, $\vec{\mathbf{r_{11}}}$, and $\vec{\mathbf{r_{12}}}$ specify the relative positions of the object origins with respect to the flexure base and object A. Loop 1 (purple in Fig. 2.5) contains the pseudo-rigid linkage of segment l_{oa} together with the circular motion of its tip around object A, whereas Loop 2 (green) includes the pseudo-rigid linkage of segment l_{ab}, the motion of its tip around object B, the motion of its base over object A at the connection point with vector $\vec{\mathbf{r_4}}$, and the relative offset between the two objects.

To solve (2.11), the vectors were expressed in complex-number form and separated into x- and y-components, yielding the system (2.12). This set of four equations has 13

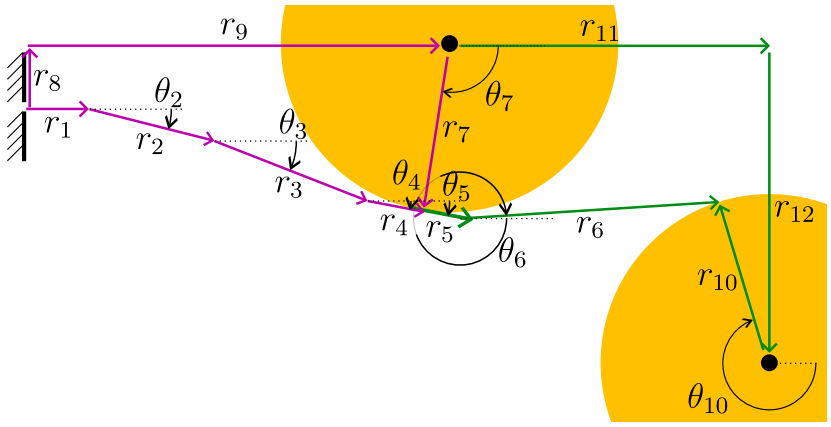


Figure 2.5: The two vector loops of phase III enabling the kinematic analysis. With vector r_1 to r_6 being the links of the serially combined pseudo-linkages, r_7 and r_{10} representing the distance from the object's origin to the point of contact with the flexure, and r_8, r_9, and r_{11}, r_{12}, the relative positions of the object's origin concerning the flexure's base and object's A origin, respectively. The two closed loops are shown in purple and green (also includes r_7).

unknowns after substituting the known lengths and angles $l_7 = R_A$, $l_8 = Q_{A,y}$, $l_9 = Q_{A,x}$, $l_{10} = R_B$, $l_{11} = Q_{B,x} - Q_{A,x}$, $l_{12} = Q_{B,y} - Q_{A,y}$, $\theta_1 = \theta_8 = \theta_{11} = 0$, and $\theta_9 = \theta_{12} = \frac{1}{2}\pi$:

$$\begin{aligned} l_1 + l_2 c_2 + l_3 c_3 + l_4 c_4 - l_7 c_7 - l_8 &= 0, \\ l_2 s_2 + l_3 s_3 + l_4 s_4 - l_7 s_7 - l_9 &= 0, \\ l_5 c_5 + l_6 c_6 + l_7 c_7 - l_{10} c_{10} - l_{11} &= 0, \\ l_5 s_5 + l_6 s_6 + l_7 s_7 - l_{10} s_{10} - l_{12} &= 0. \end{aligned} \tag{2.12}$$

Additional relations follow from the link-length distributions of both PRBM segments, resulting in the expressions in (2.13):

$$L[l_1] = \begin{bmatrix} l_2 \\ l_3 \\ l_4 \\ l_5 \\ l_6 \end{bmatrix} = \begin{bmatrix} (\gamma_2/\gamma_1)\, l_1 \\ (\gamma_3/\gamma_1)\, l_1 \\ (\gamma_4/\gamma_1)\, l_1 \\ (1-\gamma_5)/\gamma_1 \cdot l^i - 1.2\, l_1 \\ \gamma_5\, l^i - 6.2\, l_1 \end{bmatrix}. \tag{2.13}$$

The first three lines of (2.13) follow directly from rewriting the link lengths l_2–l_4 in terms of l_1. This was done by dividing the first four relations in (2.9) by their corresponding γ-values to obtain (2.14), after which l_2, l_3, and l_4 were isolated and expressed explicitly as functions of l_1 resulting in:

$$l_{oa} = \frac{l_1}{\gamma_1} = \frac{l_2}{\gamma_2} = \frac{l_3}{\gamma_3} = \frac{l_4}{\gamma_4}. \tag{2.14}$$

The last two lines of (2.13) were obtained by first rewriting the link lengths l_5 and l_6 in terms of l_1 through dividing the fifth and sixth relations in (2.9) by γ_5, yielding:

$$l_{ab} = \frac{l_5}{1-\gamma_5} = \frac{l_6}{\gamma_5}, \tag{2.15}$$

and rewriting (2.15) to obtain:

$$l_6 = \frac{\gamma_5\, l_5}{1-\gamma_5}. \tag{2.16}$$

Substituting (2.14) and (2.16) into $l^i = l_1 + l_2 + l_3 + l_4 + l_5 + l_6$ yields the final expressions.

Finally, geometric coupling relations arise because the vectors $\vec{\mathbf{r}_4}$ and $\vec{\mathbf{r}_5}$ share the same orientation and are always perpendicular to $\vec{\mathbf{r}_7}$, giving:

$$\theta_4 = \theta_5 = \theta_7 - \frac{1}{2}\pi. \tag{2.17}$$

Thus, using (2.12), (2.13), and (2.17), the original 13 unknowns reduce to six variables—l_1, θ_2, θ_3, θ_6, θ_7, and θ_{10}. These were obtained by minimizing the system's potential energy for each incremental flexure length l^i.

Minimizing the system's potential energy

Fig. 2.6 schematically illustrates the optimization algorithm used to determine the mechanism pose corresponding to the minimum potential energy. The expression for the potential energy is given in (2.18), where $\mathbf{x}$ denotes the vector of optimization variables:

$$\min_{\mathbf{x}=[l_1,\theta_7]} V[\mathbf{x}] = \frac{1}{2}\Big(K_1[\mathbf{x}]\,\theta_2[\mathbf{x}]^2 + K_2[\mathbf{x}](\theta_2[\mathbf{x}] - \theta_3[\mathbf{x}])^2 + K_3[\mathbf{x}](\theta_3[\mathbf{x}] - \theta_4[\mathbf{x}])^2 + K_4[\mathbf{x}](\theta_5[\mathbf{x}] - \theta_6[\mathbf{x}])^2 \Big). \quad (2.18)$$

Starting at the top of Fig. 2.6, for each incremental flexure length l^i, the optimization problem was solved using the *interior-point* algorithm in *fmincon*, enhanced by a multi-start strategy to ensure a robust search for the global minimum. The starting point, bounds of the optimization variables, and initial estimates of the unknown pose variables were denoted by $\mathbf{x}_0$, $\mathbf{x}_{lb}$, $\mathbf{x}_{ub}$, and $\boldsymbol{\theta}_0$, respectively. The optimization variables were chosen as $\mathbf{x} = [l_1, \theta_7]$, and the remaining unknown pose variables $\boldsymbol{\theta} = [\theta_2, \theta_3, \theta_6, \theta_{10}]$ were computed sequentially using the equations defined throughout this section, following the scheme from top to bottom.

At the start of each optimization run j (green box in Fig. 2.6), the variables $\mathbf{x}^j$ and l^i were substituted into (2.13) to obtain the link lengths L^j. These lengths were then inserted into (2.12) to solve for the corresponding angles $\boldsymbol{\theta}^j$. The stiffness values K^j were subsequently computed using (2.10), after which the potential energy was evaluated using (2.18). This process was repeated across all multi-start samples until the global minimum was found at iteration $j = k$.

Once the minimum was found, we exited the green box in Fig. 2.6, and the optimal solution $\mathbf{x}^k$ was again substituted into (2.13) and (2.12) to compute the final geometry L^n, the pose $\boldsymbol{\theta}^n$, and the contact point locations for the flexure of length l^i. For the next incremental length l^{i+1}, the initial values were updated to $\mathbf{x}0 = \mathbf{x}^n$ and $\boldsymbol{\theta}_0 = \boldsymbol{\theta}^n$, after which the same optimization procedure was repeated. This iterative process was performed for all flexure lengths in phase III, from l'_{III} to l''_{III}.

Step 3: Kinetostatic force and moment analysis

The two free-body diagrams shown in Fig. 2.7, comprising pseudo-link l_6 and the connected pseudo-links l_4 and l_5, were used to establish the force equilibrium equations needed to compute the contact force F_A^{III}. Before doing so, the force equations associated with the PRB model of segment l_{ab} were used to evaluate the contact force on object B, F_B^{III}, as expressed in (2.19)–(2.21).

The magnitude of the contact force on object B is given by:

$$F_B^{III} = P_B \sqrt{1 + n_B^2}, \quad (2.19)$$

where P_B is the component of the force acting in the lateral y_5-direction of the undeformed segment l_{ab} (see also Fig. 2.2), and is computed as:

$$P_B = \frac{K_4(\theta_5 - \theta_6)}{l_6\big(\cos(\theta_5 - \theta_6) + n_B \sin(\theta_5 - \theta_6)\big)}. \quad (2.20)$$

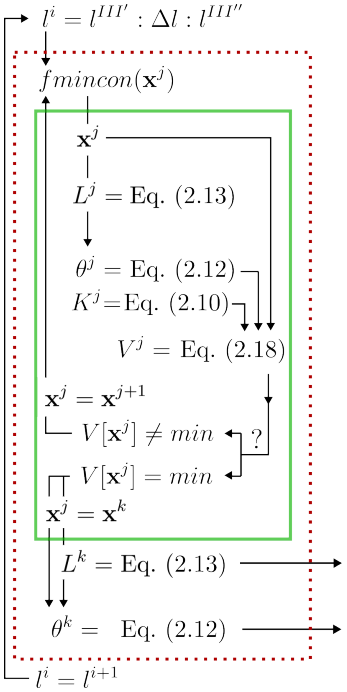


Figure 2.6: Schematic overview of the optimization algorithm for determining the unknown link lengths L^k and angles θ^k of the pseudo-linkage in phase III for each incremental flexure length l^i. The optimization variables $\mathbf{x} = [l_1, \theta_7]$ are used to obtain the remaining pose variables $\theta = [\theta_2, \theta_3, \theta_6, \theta_{10}]$ by minimizing the potential energy using *fmincon*. Each candidate vector $\mathbf{x}^j$ is substituted into the equations boxed in green, resulting in a potential energy value V. When the minimum is reached, the optimal vector $\mathbf{x}^k$ is passed to the red-boxed equations to compute the resulting geometry and pose. This procedure is repeated for every subsequent increment l^{i+1}.

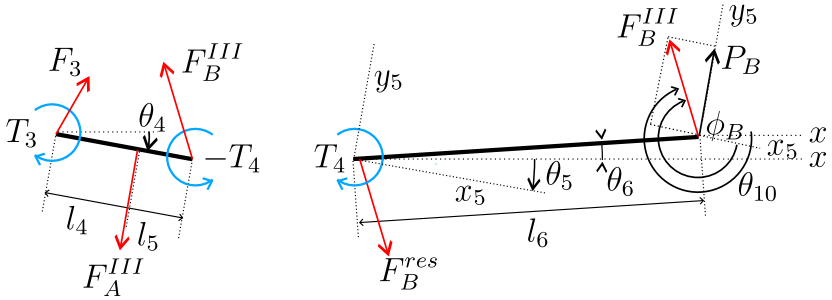


Figure 2.7: Free-body diagrams of pseudo-link l_6 and the combined pseudo-links l_4 and l_5, used to set up the force equilibrium equations for computing F_B^{III} and F_A^{III}. Torques T_3 and T_4 are generated by the torsional pseudo-springs, while F_3 denotes the force applied by link l_3.

The parameter n_B denotes the ratio of longitudinal to lateral force components (i.e., x_5 to y_5):

$$n_B = -\tan(\phi_B) = -\tan(2\phi - \theta_{10} + \theta_5). \tag{2.21}$$

The components of F_B^{III} in the global x- and y-directions follow from:

$$\overrightarrow{\mathbf{F}_\mathbf{B}^\mathbf{III}} = \begin{bmatrix} F_{B,x} \\ F_{B,y} \end{bmatrix} = \begin{bmatrix} c_{10}\,|F_B^{III}| \\ s_{10}\,|F_B^{III}| \end{bmatrix}. \tag{2.22}$$

As illustrated in the right-hand free-body diagram of Fig. 2.7, the contact force F_B^{III} acting on pseudo-link l_6 is balanced by an equal and opposite reaction force F_B^{res} at the pivot, together with the torque generated by the torsional pseudo-spring K_4. This torque is given by:

$$T_4 = K_4\,(\theta_6 - \theta_5). \tag{2.23}$$

To evaluate the contact force on object A, F_A^{III}, the static equilibrium of the combined pseudo-links l_4 and l_5 (left FBD in Fig. 2.7) was applied. On the left-hand side of this system, the torsional pseudo-spring K_3 generates a torque:

$$T_3 = K_3\,(\theta_3 - \theta_4). \tag{2.24}$$

The torque T_3 is balanced by (i) the moment generated by F_B^{III} at a moment arm of $(l_4 + l_5)$ in the direction θ_{10}, (ii) the torque T_4 in the opposite direction, and (iii) the moment induced by F_A^{III}, which always acts normal to the flexure at a lever arm l_4. Rearranging the equilibrium condition yields the expression for F_A^{III}:

$$F_A^{III} = \frac{(-F_{B,x}\,s_4 + F_{B,y}\,c_4)(l_4 + l_5) + T_4 - T_3}{l_4}. \tag{2.25}$$

The global force components of F_A^{III} follow from:

$$\overrightarrow{\mathbf{F}_\mathbf{A}^\mathbf{III}} = \begin{bmatrix} F_{A,x} \\ F_{A,y} \end{bmatrix} = \begin{bmatrix} c_7\,|F_A^{III}| \\ s_7\,|F_A^{III}| \end{bmatrix}. \tag{2.26}$$

Finally, the force $F_{0,x}$ and moment M_0 acting on the flexure base (Fig. 2.4) were computed using:

$$W_o = \begin{bmatrix} F_{o,x} \\ F_{o,y} \\ M_o \end{bmatrix} = \begin{bmatrix} -F_{A,x} - F_{B,x} \\ -F_{A,y} - F_{B,y} \\ M_o \end{bmatrix}, \tag{2.27}$$

where the base moment is:

$$\begin{aligned} M_o = {} & F_{A,x}(l_2\,s_2 + l_3\,s_3 + l_4\,s_4) + F_{A,y}(l_1 + l_2\,c_2 + l_3\,c_3 + l_4\,c_4) \\ & + F_{B,x}(l_2\,s_2 + l_3\,s_3 + (l_4 + l_5)\,s_4 + l_6\,s_6) \\ & - F_{B,y}(l_1 + l_2\,c_2 + l_3\,c_3 + (l_4 + l_5)\,c_4 + l_6\,c_6). \end{aligned}$$

2.3 Experimental validation

To evaluate the model and assess its accuracy, we have built an experimental setup with a test protocol. This setup facilitated the observation of the flexure's trajectory during its forward movement while concurrently measuring the development of interaction forces. Additionally, the setup allowed us to precisely determine the events and instances when the flexure's tip established and lost contact with the object and initiated sliding over it by determining the respective flexure lengths.

2.3.1 Test setup

The experimental setup is shown in Fig. 2.8, where a numeral label identifies each component. The setup involved advancing a straight flexure (1) through a slit (2) and encountering two objects (3). The inset in Fig. 2.8 shows the instrumented object module (4) to measure the force in a single direction per object. The object was mounted on a linear motion stage (5), whose motion was prevented by an in-line placed force sensor (6), allowing us to measure the contact forces in the direction of the stage. In Fig. 2.8, both modules are shown in an orientation to measure the force exerted in the x-direction, i.e. the advancing direction of the flexure, but they can be rotated for force measurement in other directions.

The flexure was made of H&S foil sheet stainless steel 1.4310 material with $E = 195$ GPa and had dimensions 0.4x50x300 mm. The slit was created by employing two right-angle brackets, type Thorlabs XE75A90. The linear motion stage was of type PMB RTS-2065, and the force sensors were a Futek LSB200 load cell rated 10 and 5 lbs (4.54kg and 2.27 kg) for objects A and B, respectively.

The setup included a laser (7), a Micro-Epsilon ILD1420-500, to determine the flexure length protruding from the slit. It measures the distance from the flexure's driven end to the slit. This value was subtracted from the total flexure length to determine the flexure length while moving forward.

The flexure was driven by a spindle (8) using an actuator (9), a Nema17-05GM stepper motor, controlled using an A4988 stepper driver operated by an Arduino board (10) at a rate of 1000 steps per second. Sensor signals were processed using a National Instruments USB 6008 I/O device (11), and data over time from the force sensors and the distance measurement were saved using a Labview script.

The objects are turned aluminum bars, and frictionless contact was emulated by allowing them to rotate freely around their axis, as in [58], indicated by the red arrow.

The mounts (12), constructed through 3D printing with PLA material, interconnect various components: the flexure, the laser, and the spindle; the object and the linear motion stage; the linear motion stage, the load cell, and the ground.

Several additional components were incorporated into the experimental setup to enhance measurement accuracy and minimize potential errors. These included steel plates (13) and 3D printed facets to increase the symmetry and stiffness of the mounts, two linear guides (14) facilitating smooth flexure motion, a wheel (15) to prevent tilting of the object around the translational axis of the slider, and a ball transfer unit (16) fixed at one end of the force sensor to establish unidirectional force loading from the object mount on the load cell. In addition, meticulous attention was paid to aligning all components during construction using gauge blocks.

2.3.2 Test procedure

Two experimental tests were carried out: one measuring the components $F_{A,x}$ and $F_{B,x}$ and the other measuring the $F_{A,y}$ and $F_{B,y}$ of the force exerted by flexure on the object. Both instrumented object modules (4) were rotated 90 degrees with respect to the breadboard to align the force sensor in the x or y directions, respectively.

To validate the developed model, we located the slit at (0,0), object A at $Q_A = (100, 15)$ mm, and object B at $Q_B = (175, -60)$ mm, and ran the simulation with the following settings: $\Delta l = 0.05$ mm, $x_{lb} = 0.9\,x_0$, and $x_{ub} = 1.1\,x_0$, without linear constraints or bounds in the optimization problem. At the onset of phase III, we excluded initial increments with potential-energy values deviating more than 5% from the value reached at the end of phase II. For the transition from phase I to phase II, no increments were excluded.

The validation process consisted of two parts. First, we assessed the kinematics by visually examining whether the chosen PRB models adequately capture the deflection behavior and trajectory of the flexure in the three phases and by quantifying the precision through the error between the simulated and experimentally measured flexure length at events and at the separation between the tip and object. Second, we evaluated the kinetostatics by comparing the shape and trend of the measured and simulated development of the interaction force curves for all four force components, and by computing the error between simulated and measured values at key points in the graph (an occurrence): the peak forces within a phase, the values at an event, and the value when the flexure's tip leaves an object.

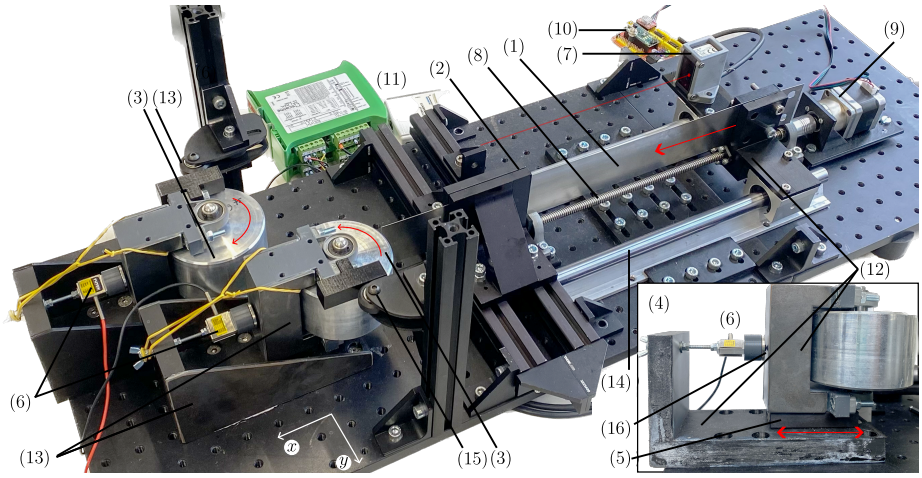


Figure 2.8: The experimental setup: a flexure (1) driven forwards through a slit (2) encountering two objects (3). The inset shows the instrumented object module (4) comprising the object mounted on a linear motion stage (5) whose motion was prevented by an in-line placed force sensor (6). Here it's oriented to measure the force exerted in the x-direction, but a second test is conducted to measure in the y-direction by rotating the modules 90 degrees. The other main components of the setup are a laser (7), slit (8), actuator (9), motor controller (10), data processor (11), mounts (12), plates (13), linear guides (14), wheels (15), and a ball transfer unit (16).

2.4 Results

First, the kinematic results of both the simulation and experiment will be presented, and subsequently the results of the interaction forces.

2.4.1 Kinematic results

The kinematic results are illustrated in Fig. 2.9, with the results of phase II on the left and phase III on the right. At the top is the experimental portrayal of the flexure deflection at the end of each phase shown. At the bottom is the simulated configuration of the pseudo-linkage shown for every fiftieth incremental length.

Starting by comparing the picture and simulation, a similar motion direction can be observed. On the left, the flexure hits object B with an almost perpendicular angle. According to the simulation, the angle between the vector $\vec{\mathbf{r}}_3^{II}$ and the normal of surface B at the initial point of contact was 183.8°, which is just above the junction of 180°. Continuing, the flexure's tip has moved upward, navigating in between the objects, as can be seen on the right.

Continuing by comparing the chosen PRB models with the flexures' deflecting behavior, it can be seen on the left of Fig. 2.9 that the flexure segment between the slit and the contact

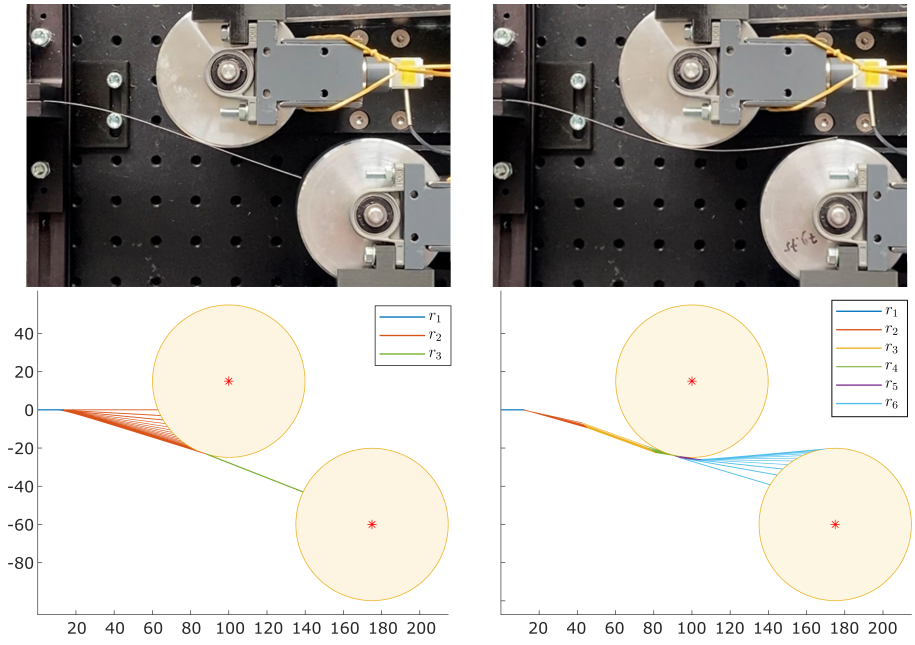


Figure 2.9: The kinematic results, with the outcomes of phase II on the left and phase III on the right. The top half of the figure depicts the experimental setup with the flexure deflection at the end of each phase. At the bottom half, the simulated configuration of the pseudo-linkage is plotted for every fiftieth incremental length. Vector r_1 to r_6 being the links of the pseudo-linkages, all increase proportionally with l^i. The global positioning coordinates are provided along the axis.

point has a C-shaped deflection while the already passed segment remains undeformed. The chosen pseudo-linkage topology, featuring a single rotational joint (1-R), replicated the C-shaped deflection of the clamped cantilever beam in phase II.

While the flexure is advancing, the pose and geometry of the pseudo-linkage progressed naturally along its deflectional behavior. As can be seen, the vectors $\vec{\mathbf{r}}_1^{II}$ and $\vec{\mathbf{r}}_2^{II}$ lengthened as the flexure advanced, while the location of the pseudo-joint slightly shifted forward. Concurrently, the vector $\vec{\mathbf{r}}_2^{II}$ rotated downward until it became perpendicular to the normal of the surface A of the object. Subsequently, the vectors $\vec{\mathbf{r}}_1^{II}$ and $\vec{\mathbf{r}}_2^{II}$ remained unchanged, while the vector $\vec{\mathbf{r}}_3^{II}$ began to increase in length, representing the segment of the flexure that has passed object A. The exit angle, $\theta_3^{II''} = 21.39°$, is larger than the rotation angle of the pseudo-joint, $\theta_2^{II^{\perp}} = 17.25°$.

Similarly, it can be seen on the right of Fig. 2.9, that the flexure's segment between the slit and the contact point with object A has a C-shaped deflection and the segment between the contact point with object A and B has a S-shaped deflection. The chosen pseudo-linkage topology, featuring the 4-R topology, mimicked the intricate flexure deflection in phase III. This entailed a 1-R linkage to capture the C-shaped deflection of the segment l_{ab}, while the 3-R part of the linkage mimics the nonsymmetrical S-shaped deflection of segment l_{oa}.

While the flexure is advancing, the pose and geometry of the pseudo-linkage progressed naturally along its deflectional behavior as both segments increased in length, whereby the C-shaped segment grew notably faster than the S-shaped segment. With this, the simulated angles θ_2, θ_3, and θ_4, and the link lengths l_1 to l_4 of the 3-R linkage exhibited marginal changes, maintaining their S-shaped configuration relative to one another. In contrast, angle θ_6 underwent a more pronounced rotation and link length l_5 and l_6 became significantly longer. Consequently, contact point A and the segment l_{ab} (thus the base of the 1-R pseudo-linkage) underwent a gradual counterclockwise rotation and were moved in the growing direction. Those simulated modifications in link lengths and angles and the movement of the contact point A aligned with the experimental observations of the advancing flexure during the experiment.

Lastly, the kinematic modeling accuracy was assessed by calculating the absolute and percentage error between the flexure length of the simulation and the flexure length of the experimental at specific moments: when the two events occurred (at the end of a phase) and when the flexure tip lost contact with the surface of objects A and B (indicated as lost in the table). These four distinct lengths, denoted as l_I'', l_{II}'', $l_{II}^{\perp}$, and $l_{III}^{\perp} = l_{III}''$ respectively, were assessed for their kinematic modeling accuracy by computing the absolute and percentage error between the simulated and the experimental lengths. The absolute error was calculated by taking the absolute difference between the simulated and experimental values, while the percentage error was computed by dividing the difference between the simulated and experimental values by the experimental value, that is, $e_{\%} = (x_{sim} - x_{exp})/x_{exp}$. The fifth and sixth columns of Table 2.1 present both errors corresponding to the four specific lengths, in addition to force values results that will be discussed later in subsection 2.4.2.

The experimental length values are determined by the measured data shown in the force development graph (Fig. 2.10). This graph plots both the measured (represented by rough lines) and simulated (depicted by smooth lines) contact forces exerted by the flexure on objects A and B in the x- and y-directions. Consequently, four distinct sets of corresponding

Phase	occurrence	mm, N	Sim.	Exp.	$e_{\|\Delta\|}$	$e_{\%}$
I	hit A	l_I''	63.03	62.83	0.2	0.3
II	max. force	$F_{A,x}$	5.05	4.70	0.35	7.4
		$F_{A,y}$	5.01	4.30	0.71	16.5
	lost A	$l_{II}^{\perp}$	91.67	91.07	0.60	0.7
	constant force	$F_{A,x}^{\perp}$	1.46	1.62	0.16	-9.9
		$F_{A,y}^{\perp}$	4.71	4.55	0.16	3.5
	hit B	l_{II}''	146.20	146.19	0.01	0.0
III	max. force	$F_{A,x}$	2.96	2.70	0.26	9.6
		$F_{A,y}$	15.26	15.20	0.06	0.4
		$F_{B,x}$	6.24	5.50	0.74	13.4
		$F_{B,y}$	6.41	6.20	0.21	3.4
	lost B	$l_{III}^{\perp}$	175.60	173.00	2.60	1.5
	constant force	$F_{A,x}^{\perp}$	2.41	2.35	0.06	2.6
		$F_{A,y}^{\perp}$	15.07	15.0	0.07	0.5
		$F_{B,x}^{\perp}$	0.49	0.80	0.31	-38.8
		$F_{B,y}^{\perp}$	5.51	5.50	0.01	0.2

Table 2.1: Modeling accuracy; assessed by computing both the absolute $e_{|\Delta|}$ and percentage errors $e_{\%}$ between simulated and experimental flexure length l and force component F values at particular points (occurrences) in phases I, II, and III. They are obtained using Fig. 2.10 at the end of phases, l'', maximum force peak values reached per phase F, and when the flexure tip lost contact with the object, $l^{\perp}$ and $F^{\perp}$, respectively.

lines emerge: the experimentally measured and simulated force developments of $F_{A,x}$, $F_{A,y}$, $F_{B,x}$, and $F_{B,y}$. Within this graph, the four specific lengths are distinctly identifiable: abrupt increases in force signify instances when the flexure hits an object, at l_I'' and l_{II}'', while the onset of a constant force plateau, called $F^{\perp}$, indicates that the tip lost contact and is moving towards the subsequent object, at $l_{II}^{\perp}$, and $l_{III}^{\perp}$.

As a result, the kinematic aspect of the model exhibits a high degree of accuracy, with the percentage error, $e_{\%}$, consistently confined within 1.5% and the most significant observable absolute error of $e_{|\Delta|} = 2.6$ mm when the flexure length is approximately 174 mm long.

2.4.2 Interaction force results

While the force development graph was previously introduced in subsection 2.4.1, this section aims to analyze the kinematic results depicted in Fig. 2.10. As can be seen, The force components exhibit highly nonlinear behavior, with both simulated and experimental force developments mirroring each other across the entire flexure length for all four components. During phase I, the results indicate zero force, so they have been cropped from the figure. Transitioning into phase II, the force components for object A, $F_{A,x}$ and $F_{A,y}$, rapidly increase upon encountering the object, reaching maximum values, declining, and eventually stabilizing at a constant value as the flexure's tip departs from the object. Notably, the x-component shows a steeper increase and reaches its maximum earlier than

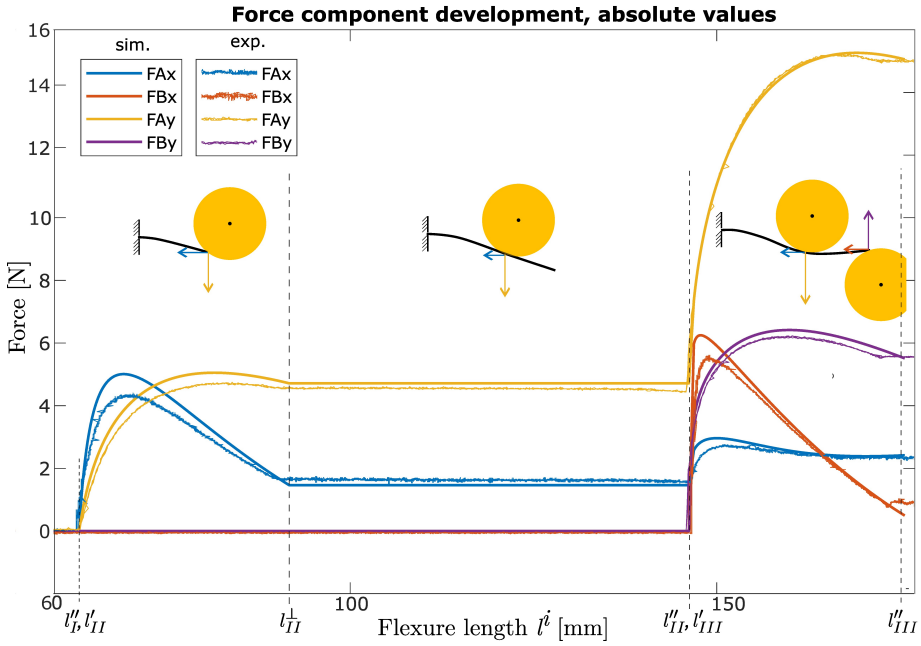


Figure 2.10: Contact force development of the advancing flexure. This graph plots four distinct sets of corresponding lines with the experimentally measured (represented by rough lines) and simulated (depicted by smooth lines) contact forces exerted by the flexure on objects A and B in the x- and y-directions. At the end of phase I, at flexure length of l_I'', the components $F_{A,x}$ and $F_{A,y}$ exhibit a nonlinear increase upon encountering object A, stabilizing once the tip departs from its surface at length $l_{II}^{\perp}$. Then, at the end of phase II, at flexure length l_{II}'', all four components undergo another nonlinear ramp-up upon encountering object B, reaching a steady value at the end of phase III when the tip disengages from the surface at length l_{III}''.

the y-component, albeit experiencing a more significant decrease. The forces remained constant from flexure lengths $l_2^{\perp}$ to l_2'', as expected. The maximum force values are tabulated in Tab. 2.1 as max. $F_{A,x}''$ and $F_{A,y}''$, while the constant values are indicated as $F_{A,x}^{\perp}$ and $F_{A,y}^{\perp}$.

As we move into phase III, the force components acting on object B rapidly increase upon interaction with object B, as expected. Simultaneously, there is an increase in the force exerted on object A, with particular emphasis on its y-component as it increased the most compared to all other components. Similarly to phase II, the x-components peak earlier than their y-components for both forces and show a more substantial decline until all reach a stabilized value as the flexure's tip begins to lose contact with object B. The maximum and constant force values during phase III are also listed in Tab. 2.1.

Assessing the accuracy of the model's kinematic aspect using Fig. 2.10, it becomes evident that the problem was modeled with a high level of accuracy. Although not perfectly overlapping, the measured and simulated force profiles exhibit similar shapes and comparable magnitudes throughout the advancing range of the flexure. The most notable absolute error observed in the overall graph was 0.7 Newton at the peak of the force components $F_{A,y}$

during phase II and $F_{B,x}$ during phase III. This discrepancy represents an overestimation of approximately $e_{F\%} = 15$ % of the measured value. The most substantial percentage error within the table is $e_{F\%} = -38.5\%$, for the component $F_{B,x}$ at the end of phase III, mainly due to the proximity of the force value to zero Newton, resulting in a moderate absolute error. Notably, all other absolute errors within the table fall within the range of 0.3 Newton and maintain a percentage error of around 10%.

2.5 Discussion

2.5.1 Results

Both the kinematic behavior and the force predictions of the model were successfully experimentally validated.

The kinematic aspect demonstrated high accuracy within 1.5%. Although the evaluation was conducted at only four specific points, this accuracy level can reasonably be extrapolated across the entire advancement range of the flexure for several reasons.

Primarily, the model accurately predicted the motion direction of the flexure along the objects. Notably, the chosen object arrangement was challenging as the flexure encounters object B almost in a straight line, i.e. the angle between the vector $\overrightarrow{\mathbf{r_3}}^{II}$, the longitudinal direction of the undeformed part of the flexure protruding over object A, and vector $\overrightarrow{\mathbf{r_{10}}}^{III}$, the direction normal to the surface at the point of contact with object B, having an angle of 183.8° when the flexure encounters object B. Resulting, a slight discrepancy in modeling could have significantly altered the trajectory, as the flexure could have struck object B at a slightly lower point, such that it would have navigated on the other side of object B. Therefore, the results were not immediately obvious; hence, accurate kinematic modeling over the entire motion range was required to correctly predict the motion direction of the flexure alongside the objects.

Furthermore, the pose of the pseudo-rigid linkage was shown to naturally resemble the deflection behavior of the flexure during advancement. The close agreement between the shape and magnitude of the simulated force profiles and the experimental data follows directly from accurately capturing the geometry and pose evolution of the pseudo-linkage over the full range of motion. The model predicted force magnitudes within 10% of the measured values. Despite the strongly nonlinear force development, the simulated and measured profiles closely matched in both shape and magnitude.

The resulting modeling accuracy—supported by experiment—provides a reliable indication of the order of magnitude that can be expected for design purposes. The experiment was not intended to yield a perfect numerical match; small deviations in alignment, friction, or slight curvature variations already have a large influence on the absolute force values. Instead, its primary purpose was to gain insight into the interactive navigation behavior of such a flexure and to validate the trends—the characteristic force shapes, the timing of events, and the effects of topology switches. The close agreement in these trends confirms that the model captures the essential behavior.

Although the results are encouraging and the achieved accuracy is sufficient for design purposes, they are based on a single experimental case. The measured forces are strongly dependent on the assumed stiffness of the model, and the sensitivity of the predicted forces to variations in these stiffness values may be significant. To reduce this uncertainty, we

deliberately selected a straight flexure manufactured from spring steel, allowing us to rely on industrial production standards so that its mechanical properties closely matched the parameters used in the model. In addition, we assumed frictionless contact to avoid uncertainties associated with contact mechanics; together, these choices contributed to a more reliable model validation. Nevertheless, we encourage additional validation in future work, both experimentally—by varying flexure material, geometry, and shape, as well as the size and position of the rigid objects—and through finite element simulations. Although not used in this study, such simulations could efficiently evaluate the model across many parameter variations, enable systematic sensitivity analyses without experimental uncertainties, and provide a broader, more comprehensive validation of the model.

Finally, it is worth noting that, for the study as presented here, we used fixed thumb-rule values for the characteristic radius and normalized torsional stiffness (e.g., $\lambda = 0.85$ and $K = 2.65$ in Phase II). We also ran extended simulations in which these parameters were updated at each incremental step based on the evolving flexure configuration. However, for the presented case, as well as for simulations with different object spacings, this only reduced the modeling error by a few percentage points. For reasons of clarity and brevity, we therefore chose to retain the standard thumb-rule parameters in the main analysis, but incremental updating of these parameters can readily be implemented as an additional substep if higher accuracy is desired.

2.5.2 Case study: phase transitions

To elucidate the phase transitions in our case study, none of the initial increments in phase II were removed, as they did not exhibit unnatural results or force peaks. However, in phase III, the initial increments depicted peaks of both high and low forces, followed by increments that showed gradual force development, beginning with magnitude identical to the last increment of phase II. Those with force peaks had significant fluctuation in potential energy, prompting their removal by choosing that the system's potential energy may not deviate by more than 5% of the value reached at the end of phase II.

The removed increments were notably influenced by the abrupt shortening of link 1 due to switching to another pseudo-linkage topology, transitioning from $l_1^{II''} = 17.25$ mm to $l_1^{III'} = 16.77$ mm at the end of phase II and the onset of phase III, respectively. In an attempt to geometrically fit the new topology between the slit and object B while ensuring contact with object A, the linkage was stretched into a straight configuration, aligning links l_2 to l_6. However, this resulted in an unnatural pose, storing all potential energy in torsion spring K_1. As the system progressed through subsequent increments, it gradually relaxed, leading to the backward rotation of spring K_1 and transferring energy to the other three springs. Once the system's potential energy fell within a 5% range, the force development increased gradually, and the pseudo-linkage's pose began resembling the actual deflection shape of the flexure; hence, this value was chosen as bounds.

2.5.3 Case study: extendability

The modeling framework presented here—developed for a specific case of a straight flexure navigating between two circular rigid objects—readily extends to various scenarios of flexure navigation through interaction, for instance to other flexure designs, different

numbers or shapes of objects, and alternative relative motions between them. The flexure can be interchanged with differently shaped or differently loaded flexures by implementing an alternative Pseudo-Rigid-Body (PRB) model, for example incorporating the topology of precurved flexures or small-length pivots. The environmental conditions can likewise be generalised to a wide range of scenarios, such as including more objects (more loads, e.g. four or five obstacles), allowing loss of contact with intermediate objects while advancing (removing loads), employing differently shaped 2D objects, integrating compliant (soft) objects, or considering movable objects that encounter environmental resistance. Real-world scenarios that exemplify these variations include, for instance, a catheter navigating through tissue in medical applications, or a compliant gripper finger manoeuvring within a pile of food objects that may be rigid or soft, and fixed or movable with respect to the environment.

For analyzing other environmental scenarios, the passage side, the deflection shape of the flexure, and the deflection shape of each segment first need to be specified. In cases with more than two objects, the modeling framework presented here can be extended and a similar procedure can be repeated. Incorporating a third object, for example, requires the introduction of a fourth phase, in which—analogous to Phases II and III—we (i) determine the length at which the flexure first contacts the object, (ii) determine the deflected shape of the flexure between the objects and segment it accordingly, (iii) replace each segment with an appropriate PRB topology and connect these serially while incorporating sliders to determine the contact points, and (iv) solve the resulting system using the minimum potential energy approach.

Differently shaped objects, such as cam-shaped objects, can be incorporated by defining a vector pointing from the object's origin to its surface, whose length is not constant, like vector $\vec{\mathbf{r}_3}$, but is a function of its angle with the x-axis. Similarly, to account for compliant objects, we replaced this vector with a variable-length vector while introducing a linear spring to represent their stiffness. Moreover, a movable or deformable environment can be incorporated by defining a variable-length vector pointing from the flexures' base to the object's origin to its surface while introducing a linear spring between the object and the ground to represent their experienced resistance by the object.

2.5.4 Methodology: contributions and restrictions

Primarily, this paper extends the Pseudo-Rigid-Body Modeling (PRBM) of flexures by covering event-based scenarios. We have effectively demonstrated how to transition between pseudo-linkage topologies when an event occurs, enabling the analysis of subsequent phases. Seamless transitions from the prior phase to the new phase were attained by keeping the system's potential energy within reasonable bounds. This was shown by introducing two new loads as an advancing flexure encountered subsequent objects.

To ensure a seamless transition between phases we need to be more specific, we need to distinguish non-catastrophic and catastrophic events. Non-catastrophic events are accompanied by moderate potential energy changes in the system, with the input force generally being the primary source. An example demonstrated in our use case involved introducing two new loads as an advancing flexure encountered subsequent objects, and when obstructed, the actuator supplies most of the energy required for the next phase. Consequently, potential energy is gradually added in a controlled manner over

an extended period. In contrast, catastrophic events entail abrupt changes in energy, such as sudden object drops or removals from the flexure, or a suspending wire/point of a flexure that suddenly snaps. In these situations, energy is abruptly added to or removed from the environment. Hence, ensuring a smooth transition solely by bounding the system's potential energy might not be guaranteed for catastrophic events.

Secondly, we have successfully enabled and experimentally validated the modeling of flexures with multiple loads along their length using the PRBM approach. This was demonstrated during phase III, where we combined two original PRB models in series, incorporating supplementary prismatic joints with undetermined link lengths. Subsequently, we determined these lengths by minimizing the system's potential energy. As observed during the experiment and supported by the achieved modeling accuracy, it was shown that the presented pseudo-linkage topology exhibited the required degrees of freedom to precisely represent the intricate deflectional shape of the flexure and effectively address the natural increase in the link lengths relative to the total flexure length. This approach can be extended to analyze flexures with more loads along their lengths or with different initial shapes.

The selected use case allowed us to focus on the core mechanics of base-driven flexure navigation—bending under obstruction, switching contact points, progressing through clutter, and the resulting interaction forces—in a setting that was analytically tractable yet still rich enough to reveal the essential behavior. By starting with a straight flexure that sequentially contacted one object and then another, we could incrementally introduce complexity, minimise parametric uncertainties, and obtain a level of experimental validation that would have been impractical with other flexure geometries or materials.

Despite its apparent simplicity, the case was both demanding and representative: the flexure experienced strong and often abrupt interactions, with pronounced nonlinearities that required serial switching of PRBM topologies to analyse loads applied at unknown positions along its length. These topological transitions appeared clearly in both simulation and experiment, demonstrating how the model captures the essential mechanics of event-driven changes in load application. At the same time, the unified vector-loop formulation for the pseudo-linkage and its environment enabled us to resolve these transitions in a generalisable manner and to gain clear insight into the system's behavior.

Together, these elements establish a general modeling framework for event-driven flexure navigation with multiple loads along the flexure's length—a "recipe" that others can follow and readily extend to additional objects, compliant environments, or flexures with different geometries or design parameters. The insights gained here form the foundation for translating these principles into the design and realisation of base-driven advancing flexures as practical advancing mechanisms across different domains, where their predictable trajectories, controlled interaction forces, and strong propagation capabilities can be effectively exploited.

2.6 Conclusion

In this paper, our work extends the application of Pseudo-Rigid-Body Modeling (PRBM) in two significant aspects: (1) first, by enabling seamless transitions between different PRB models, covering event-based scenarios, and second, by analyzing flexures with multiple loads along their length. Both aspects offer versatile applications, independently or in conjunction, for analyzing diverse flexures.

Events marking critical junctures, such as adding or removing load cases from flexures, demand a sudden shift to an alternative pseudo-linkage topology for accurate subsequent modeling. By bounding the system's potential energy, our approach ensures smooth transitions between various pseudo-linkage topologies during non-catastrophic events.

We developed our approach through a detailed case study involving the kinetostatic modeling of a flexure advancing from its base forward, encountering, and maneuvering between two subsequent circular objects. Here, two events are identified once hitting a new obstacle, separating the problem into three distinct phases. Each phase was analyzed through a series of three sequential steps.

It was shown that in cases with two loads traveling along a flexure's length, effective modeling can be achieved by serially combining two pseudo-linkages with undetermined link lengths, resolved by minimizing the system's potential energy. This approach can be expanded to analyze flexures bearing multiple additional loads or to analyze flexures with initial shapes other than straight.

Both the kinematic behavior and the predicted interaction forces of the model were successfully validated experimentally. Our experimental setup involved a flexure driven forward through a slit, interacting with two instrumented object modules to measure contact forces in a specific direction. As a result, our model accurately predicted the direction of motion of the flexure when navigating between these objects. Moreover, it faithfully replicated the deflection behavior of the flexure and demonstrated a high degree of kinematic accuracy within 1.5%. Furthermore, the force development profiles, with their highly non-linear characteristics, matched closely each other, predicting force magnitudes within a margin of 10%.

Therefore, our work extends the PRBM methodology by enabling seamless transitions between pseudo-linkage topologies and facilitating comprehensive analyses of flexures experiencing multiple load cases along their lengths. These advancements pave the way for further research in this domain, promising expanded applications and deeper insight into flexure behavior with the help of relatively simple and physically meaningful models.

II

Design

Towards Finger Design

In Part I, we developed and experimentally validated a kinetostatic model of a straight, base-driven flexure navigating between obstacles. Beyond its contribution to compliant mechanism design, this study plays an important conceptual role in the thesis. In a simplified yet deliberately demanding setting, we tested whether a mechanism that reflects the envisioned finger behavior—moving closely along an object under frictionless contact—can still advance between obstacles when driven only from its base. This provided guidance both at an abstract level, by indicating which manoeuvring strategies from Appendix C are most promising, and at the mechanism level, by confirming that flexures are suitable candidates for motion through dense environments. The insights gained from Part I therefore form a starting point for the explorative design reasoning that underpins Part II, where we design and manufacture gripper fingers that combine precurved flexures with an eversion-based motion mechanism.

From a finger-design perspective, modeling a straight rather than a curved flexure may seem counterintuitive, but it provided a fundamental first step towards using advancing flexures to realise tangential finger motion along the object's surface. The straight-flexure case represents an extreme scenario: without a predefined curvature, the flexure engages more strongly with its environment and often approaches obstacles at near-normal incidence. This amplifies interaction forces and makes the underlying mechanics easier to observe and analyse, turning the model into a useful stress test for flexure-based navigation through clutter. At the same time, the straight-flexure case offered a relatively simple and well-structured testbed for developing the model step by step, drawing on the many existing fundamental PRBM formulations available for different load cases and adding complexity in each new phase. By showing that such a straight, base-driven flexure can still move forward in a predictable and controlled manner, the study strengthened our confidence that flexures can realise the desired motion without resorting to more complex actuation concepts, such as snake-like robots, soft continuum manipulators, or heavily actuated steering mechanisms.

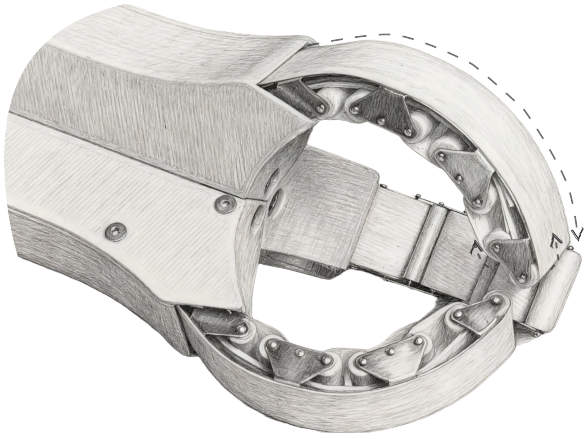
These insights directly informed the selection of manoeuvring strategies for bringing the fingers from the wrist to underneath the object. They support our preferred approach of advancing the fingers tangentially downward along the object, guided by a precurved slider and relying on controlled flexural interaction to handle residual collisions, rather than following more elaborate approach paths around the object as considered in Appendix C. At the same time, the results motivated the move towards precurved flexures in the design: guiding a flexure along a path that already wraps around the object reduces the severity of head-on impacts and promotes grazing interactions by design. This is advantageous both for limiting peak interaction forces—as observed when comparing near-normal and more tangential contacts in Part I—and for passively holding round objects within a gently enclosing cavity. Nevertheless, practical situations will still involve contact due to object

variability, misalignment, or neighbouring items, so the interaction behavior studied in Part I remains essential for making the design robust in realistic environments.

Finally, the work in Part I highlighted the importance of maintaining frictionless, or at least rolling-like, contact to avoid large lateral friction forces and impact peaks. This naturally motivates the use of an eversion mechanism wrapped around a precurved flexure, which approximates frictionless sliding by continuously renewing the contact surface. In Part II, this line of reasoning is translated into concrete finger designs based on precurved flexures and eversion principles, where we investigate in practice whether the favourable navigational behavior observed for the straight flexure can be realised in gripper concepts intended for confined-space grasping.

3

Dual-Belt Curved-Flexure Eversion Mechanism Fingers



Chapter 2 introduced and validated a kinetostatic model for straight advancing flexures, achieving 98% trajectory accuracy and 90% force accuracy. Building on these fundamentals, Part II shifts to precurved flexures, enabling predefined object-following paths and providing intrinsic holding capabilities. Chapter 3 presents the first full finger prototype: a three-finger design based on a Dual-Belt Curved-Flexure Eversion Mechanism (DBCF-EM). Each precurved, base-driven flexure advances along a circular path and is equipped with rollers and two belts that evert at its tip toward its curved sides. Experiments show reliable contour following and a significant reduction in environmental friction, enabling successful grasping from a pile in a robotic setup.

This chapter is based on the MSc thesis work [142] and has been submitted as an article to IEEE Robotics and Automation Letters, titled: Friederich, J.H.B., Huisjes, A.E., and Herder, J.L. (2025). *The DBCF-EM Gripper: Using Dual-Belt Curved-Flexure Eversion Mechanisms as Fingers for Confined-Space Robotic Grasping.*

The DBCF-EM Gripper: Using Dual-Belt Curved-Flexure Eversion Mechanisms as Fingers for Confined-Space Robotic Grasping

3

Abstract *This paper presents a new grasping strategy for confined environments by reorienting the finger-closing motion from a conventional perpendicular approach to an advancing, object-following trajectory. As proof of principle, we introduce the first flexure-driven eversion mechanism—the Dual-Belt Curved-Flexure Eversion Mechanism (DBCF-EM)—and implement it as fingers in a three-fingered prototype gripper, validated through robotic experiments involving the automated removal of tomatoes from a crate by vertical positioning above each target. The DBCF-EM combines advancing pre-curved flexures with a dual-belt eversion system, enabling finger motion tangential to the object surface while suppressing disturbance forces at contact interfaces. Experiments showed that the fingers followed the object contour within their own thickness, with a maximum deviation of 3 mm and a negligible normal disturbance of no more than 0.1 N, while the dual-belt system reduced tangential disturbance forces by 91–97%. In robotic trials, the gripper achieved 100% object pick-up and a 91% damage-free success rate. These results confirm the effectiveness of the DBCF-EM concept for confined-space grasping and highlight its potential beyond food handling for safe, reliable, and easily automated manipulation and navigation in dense, and delicate environments.*

3.1 Introduction

Automating the manipulation of agri-food products is challenging due to their variable shape, softness, and fragility [25]. A wide range of robotic gripper concepts have been developed to address these challenges [35, 143], particularly those using mechanical fingers that achieve secure yet gentle grasps by enclosing objects through form-closure or caging strategies [28, 36, 55, 67, 144, 145]. These fingered grippers perform well when objects are laterally accessible, that is, when there is sufficient space around the object to insert the fingers around it and close them perpendicularly, such as on laboratory tables [98].

However, conventional fingered grippers often fail in practical settings [12, 100, 101] —such as densely packed crates, hanging clusters, or narrow conveyor lanes—because lateral space is limited or absent. In these confined spaces, the use of conventional fingered grippers is challenging, as inserting and closing their fingers often disturbs neighboring items excessively, leading to grasp failures or object damage. To address this, existing solutions often rely on advanced robotic planning or obstacle interaction or avoidance strategies [99, 146, 147], as these issues primarily arise during real-world deployment, i.e., after the gripper design phase. In contrast to control approaches, we propose a mechanical solution that tackles the core problem by redesigning the fingers to inherently limit environmental disturbance during grasping.

In this paper, we introduce and experimentally validate the *Dual-Belt Curved-Flexure Eversion Mechanism* (DBCF-EM) gripper, enabling confined-space robotic grasping. The DBCF-EM fingers consist of a pre-curved flexure that drives two everting belts covering their curved side surfaces during motion. The fingers extend longitudinally from the gripper housing and advance tangentially along the object's curved surface to set the grasp, while the everting belts reduce sliding forces on contacting surfaces. This design enables reliable grasping in confined and cluttered spaces by limiting environmental disturbances and requiring minimal lateral clearance on the order of the finger thickness.

This paper is structured as follows: Section 3.2 describes the DBCF-EM conceptual design, prototype fabrication, and pull-out force estimation. The experimental setups for performance assessment are detailed in section 3.3. Section 3.4 presents the experimental results, including the grasp success rates from robotic tests emptying a crate of tomatoes, followed by mechanical performance measurements. Finally, sections 3.5 and 3.6 discuss the findings and conclusions of this work.

3.2 Method

3.2.1 Conceptual gripper design

Fig. 3.1 shows the three-fingered DBCF-EM gripper in its **open state** (right) and **grasped state** (left), with the finger closing motion illustrated and all primary components labeled. The design consists of three finger modules arranged around a central hub, each storing a DBCF-EM finger in a channeled housing. Each finger combines a pre-curved flexure (grey) with two everting belts: the inner belt (blue) and the outer belt (red). All fingers are connected to a single actuator mounted on top of the hub, which drives their flexures forward from the back, pushing them outward through the channels during the grasp-closing motion.

Fig. 3.2 provides a more detailed 2D cross-sectional sketch of a DBCF-EM finger in both its open state (top) and its final grasped state (bottom), with all components shown. The belts (red and blue) extend from the fingers' interior, pass over the fingertips in opposite directions, and cover the exterior of the inner and outer curved finger surfaces, guided by rollers to follow the flexures' (grey) curvature. Each belt is fixed at the housing while their free ends are attached to a sufficiently preloaded elastic band (yellow) which keeps the belts in tension and takes care of recoiling the belts during the return (opening) motion. The other end of the elastic band is fixed to the actuated end of the flexure.

The DBCF-EM fingers can grasp and release spherical objects in confined spaces by reducing environmental disturbances in two key ways: tangential object-following finger motion while reducing the induced disturbances.

Tangential object-following finger motion

The fingers navigate tangentially along an object's surface, thereby setting or releasing a grasp without requiring the clearance normally necessary for finger-closing/opening motions. This was achieved by **guiding pre-curved flexures** outward through the channel of the housing as illustrated in Fig. 3.1 and Fig. 3.2. From the open state, the fingers are retracted and straightened within the housings, with the flexures bent to conform to the internal channel. During grasp closing, the flexure emerges from the housing, bends back to its original pre-curved shape, and follows a circular path with a radius designed to match the object radius plus the finger thickness, $R_{object} + t$, ensuring tangential finger motion along its surface when setting the grasp. The channeled housing outlets guide the flexures tangentially onto the object's surface so their trajectory aligns with the contour when the gripper is placed against the object with its longitudinal axis normal to the object surface. The outlets are curved to achieve a more compact gripper layout, allowing the finger modules to be positioned closer together. With this tangential object-following finger motion, the required clearance between the object and its environment is limited to the finger thickness, whereas traditional caging grippers pivot or translate their fingers perpendicularly toward the object, demanding additional free space that is often obstructed by adjacent items.

Reduction of tangential disturbances at the contact interfaces

The fingers advance with near-zero shear forces at environmental contact interfaces by combining the flexure with a **dual-belt eversion system**. As shown in Fig. 3.2, the belts generate an everting motion, unwrapping along the flexure's curved contours and maintaining zero relative velocity between the finger and the environment, thereby reducing environmental disturbance. Without these belts, the fingers would introduce sliding friction when advancing between the object and surrounding clutter, potentially causing excessive forces that lead to damage or misgrasps.

The everting dual-belts are inspired by the operating principles of eversion mechanisms (EMs), which are well known for maneuvering through dense and unstructured environments with near-zero slip [113–115]. Conventional EMs consist of a flexible tube or membrane that is turned inside out and inflated by internal overpressure, thereby extending longitudinally through eversion. During this process, material near the central axis is transported forward to the tip at twice the growth speed of the mechanism and

then redirected outward toward the walls, where it becomes stationary. As a result, the outer surface maintains zero relative velocity with the contacting environment, effectively eliminating shear forces.

The dual-belt system of our DBCF-EM finger adopts the mechanics of EMs in a mechanical planar embodiment. Instead of internal overpressure, the belts are driven directly by the advancing flexure. When setting the grasp, rollers at the flexure tip push against the wrapped belts, causing them to unwrap onto the flexure's curved exterior surfaces. In this outward eversion process, the interior belt segments are drawn forward at twice the flexure speed, thereby elongating the elastic bands. The belts are guided by additional rollers along the finger's length to remain snug against the contour; in contrast to straight-propagating conventional EMs, our design follows a curved trajectory, making these rollers essential to prevent the belts from shortcutting directly from fingertip to palm. When releasing the grasp, the process reverses: as the flexure retracts, the elastic bands contract and pull the belts back, unwrapping them from exterior to interior and thus realizing inward eversion.

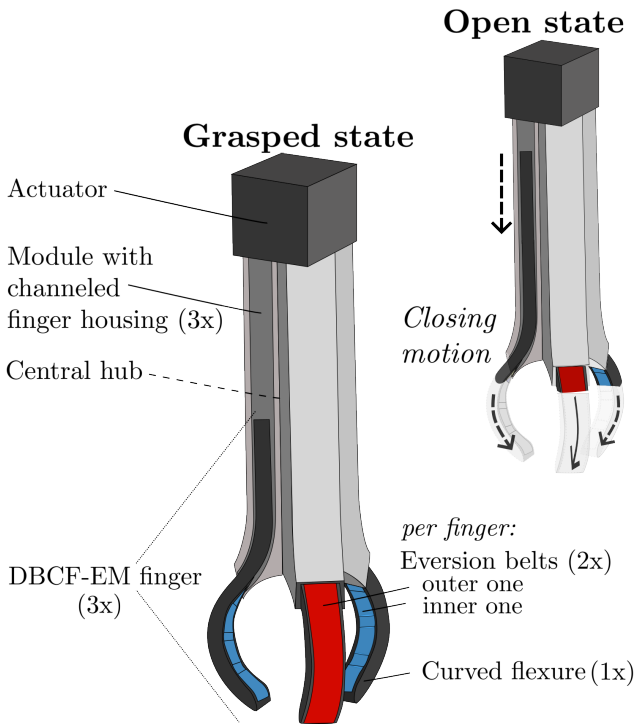


Figure 3.1: Schematic of the three-fingered DBCF-EM gripper in its open (right) and grasped (left) states, with main components labeled. Each finger module contains a pre-curved flexure, straightened within a channeled housing, and two everting belts along its inner (blue) and outer (red) surfaces. During closing, the flexures slide outward, recover their curvature, and trace a circular path matching the object, while the belts unwrap outward to maintain zero relative motion and minimize shear. This design enables grasping in confined spaces with minimal disturbance and clearance limited to the finger thickness.

In both motions, the mechanism maintains zero relative velocity with the environment, thereby eliminating shear forces during finger advancement or retraction.

Beyond these primary features, the gripper concept with DBCF-EM fingers integrates the dual belts, rollers, and flexures into a multifunctional design with characteristics essential for successfully grasping and lifting spherical agricultural products in confined spaces. The flexure acts as the backbone of each finger, providing longitudinal stiffness for propagation and navigation through clutter, while its lateral compliance allows controlled deviation from the intended path when necessary—such as when the gripper or object is misaligned, a finger is obstructed by adjacent items, or when grasping slightly oversized objects—thereby enabling shape adaptivity within elastic limits without damaging the object.

In addition, the flexure serves as a structural caging frame once the object is enclosed, with the gripper's holding force arising from its bending stiffness. The belts further reinforce this capability, as the tensile stiffness of the inner eversion belt functions analogously to tendons in the human hand, resisting finger opening when the object is pulled out. The object remains secured until the cage opening exceeds its size.

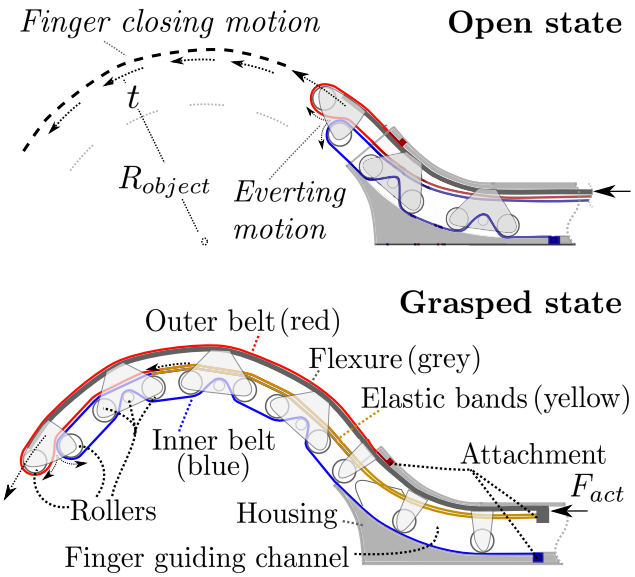


Figure 3.2: Cross-sectional schematic of a DBCF-EM finger in its open (top) and grasped (bottom) states. Two everting belts (red, blue), guided by rollers, follow the pre-curved flexure (grey) and are attached at its base via pre-tensioned elastic bands (yellow) and at the other end to the housing. Driven outward through the guiding channel by the applied actuation force F_{act}, the flexure restores its curvature and drives the belts to unwrap from the finger's interior outward, maintaining near-zero relative velocity—and thus minimizing tangential disturbances—with the environment.

3.2.2 Use case: task and design requirements

To validate the proposed DBCF-EM gripper concept, we designed and built a prototype to empty a crate of 33 piled tomatoes, grasping them one by one. The tomato population had an average mass of 131 g (87–192 g), an average height (from the stem to the blossom end) of 62 mm (48–71 mm), and an average diameter of 60 mm (47–71 mm). Based on these measurements, the gripper was required to reliably grasp nearly spherical tomatoes averaging 60 mm in diameter and 130 g in mass, while remaining flexible enough to handle the smallest (47 mm, 87 g) and largest (71 mm, 192 g) fruits.

Tomatoes were chosen as the validation case because they resemble many spherical fruits such as apples and oranges in size and shape, while being particularly challenging due to their fragility, which requires careful finger motion. In contrast, products like potatoes or melons are more robust but may have less regular geometry or higher mass, demanding greater flexure adaptability or different design dimensions. Still, the tomato-crate case provides a representative, demanding, and practically relevant benchmark for confined-space grasping in agri-food logistics, where fruits are frequently stacked in crates or piled on conveyor belts.

3.2.3 Mechanical design and manufacturing

In this section, the detailed design and manufacturing process of the gripper are illustrated through a series of photos showing the prototype at different stages of assembly. Fig. 3.3 presents both the disassembled and assembled gripper, displaying from top to bottom: the finger components (a, b), the finger module in partially and fully grasped states (c), the central hub with the actuator in its initial state (d), and the assembled gripper in fully grasped state.

The finger

As shown in (a) and (b) the finger comprises: the belts (1) with attached elastic bands (2) and the flexure (3) with rollers (4) and (5) and the actuation block (6). The flexure was CO_2-laser-cut from 0.2 mm thick hardened spring steel sheet (C100S, 1.1274, AISI 1095). Subsequently, the 150-mm-long flexure was pre-shaped into an S-configuration, with final curvatures conforming to the channel outlet contour and to the effective radius of the object plus finger thickness, as seen in the stored and outwardly protruding segment in the fully grasped state, bottom figure of (c). During sliding through the channel exit, the flexure remains within its elastic range, ensuring no plastic deformation occurs.

The roller tabs along the longitudinal sides of the flexure hold the roller axes and require sharp 90° bends with a small radius, which are infeasible in hardened spring steel. To enable plastic deformation without fracture, each tab was locally softened by torch heating followed by slow cooling. The rollers (4) are 3D-printed PLA cylinders with 0.5 mm diameter, 8 mm long steel pins (5) press-fitted at both ends as axles. The pin heads keep the rollers centered in the flexure and serve as sliding surfaces within the housing channel.

The everting belts are 3D-printed from flexible TPU in three layers (0.2, 0.1, 0.1 mm) with alternating ±15° infill orientations, providing longitudinal stiffness and lateral flexibility. The retraction bands are rubber loops with an unstressed cross-section of 1.2 × 1.2 mm and a total length of 56 mm, with tensile force rising from 1.5 N at the 70 mm pre-tensioned length to 4.4 N at 150 mm in the fully grasped state.

The elastic band is attached to the belt via a printed foldable tab that is welded back onto the belt to form a loop through which the band passes (see the right side of the belt). Welding was performed by clamping the folded section between steel strips and gently heating with a soldering iron until fused. On the other end of the belt, upward tabs are formed by adding extra printed layers, enabling them to slide and lock into slots inside the finger housing and thereby secure the belt within the finger (see (c)).

The actuation block (6) provides attachment for the elastic bands, secures the flexure base to the actuator, and guides its motion through the channel (8) of the housing (7).

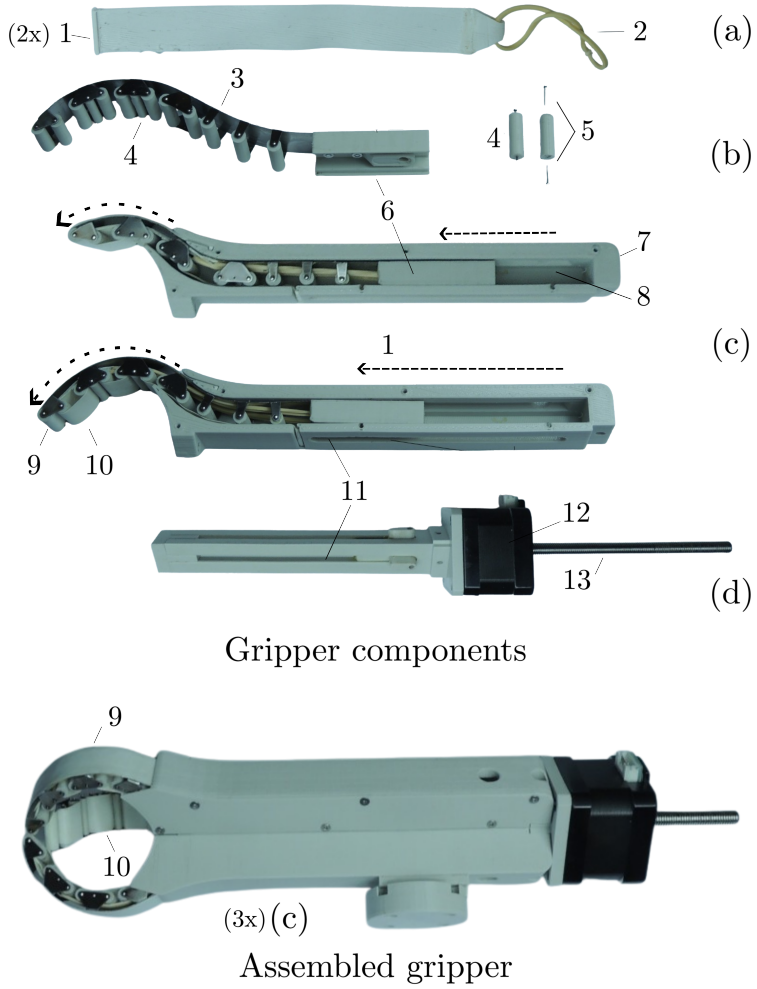


Figure 3.3: Prototype of the three-fingered DBCF-EM gripper in various stages of assembly. From top to bottom: (a,b) the finger components, (c) the finger module in partially and fully grasped states, (d) the central hub with spindle and actuator, and (e) the fully assembled gripper.

The finger module, central hub, & gripper

The finger module (c) consists of a housing (7), which incorporates a channel (8) and a belt-attachment slot, both enclosed by a lid. The lid is shown in place in the assembled gripper, but omitted in (c) to reveal the finger, which is stored in a straight configuration inside the housing in the retracted (open) state. Once extruded, the finger returns to its relaxed, precurved shape and follows a curved trajectory towards its grasped state. The outer (9) and inner (10) belts are also shown in place. The housing includes a longitudinal slot (11) along its side, which aligns with one of the slots along the three faces of the central hub (d) when assembled. Inside the triangular bar of the hub, a slider moves axially back and forth, driven by a spindle (13) rotated through the actuator (12). The slider has three protrusions that pass through the slots and connect to the finger actuation blocks (6), moving them synchronously in and out of their housings.

The fully assembled gripper, including the actuator, is shown at the bottom of Fig. 3.3. The parts are connected with 16 mm M3 screws, and all sliding surfaces were lubricated with bearing grease. In its grasped state, the gripper measures 250 mm in length and 47 mm in width, with a total mass of 431 g, of which 269 g is due to the actuator and spindle. Each finger measures 11 mm in thickness and 15 mm in width. The actuator is a non-captive NEMA 17 spindle motor with a holding torque of 0.26 Nm, equipped with a T6×2 spindle and powered by an A4988 stepper driver connected to an Arduino. Under the chosen operating settings, the gripper opened and closed in approximately 8 s (1 cm/s finger extrusion/retraction), which was sufficient for the validation experiments but could be adjusted in practical applications.

3.3 Experimental performance validation

To evaluate the gripper's effectiveness in confined-space grasping, a set of performance metrics was tested using dedicated experimental setups. The metrics were: (i) tangential object-following finger motion, (ii) reduction of tangential disturbances at the contact interfaces, (iii) holding force, (iv) net disturbance force on the object during grasping, and (v) grasp success rate for the defined use case when integrated on a robotic setup.

3.3.1 Tangential object-following finger motion

The finger should propagate tangentially along the object without measurable deviations (mm), thereby limiting environmental perturbation to the finger thickness. This was evaluated by side-view video recordings of a single finger grasping an object of mean size $D = 60$ mm. Stills at different time points were overlaid to graphically compare deviations from the object surface and the final finger state.

3.3.2 Tangential disturbances at contact interfaces

The reduction of tangential disturbances at the contact interfaces was evaluated to verify the effectiveness of the zero-slip belts, compared against two benchmark fingers without belts. Disturbances from a propagating finger in a pile can appear as shear forces tangential along the object surface, inducing rotation; together these represent the mechanical work exerted on the environment.

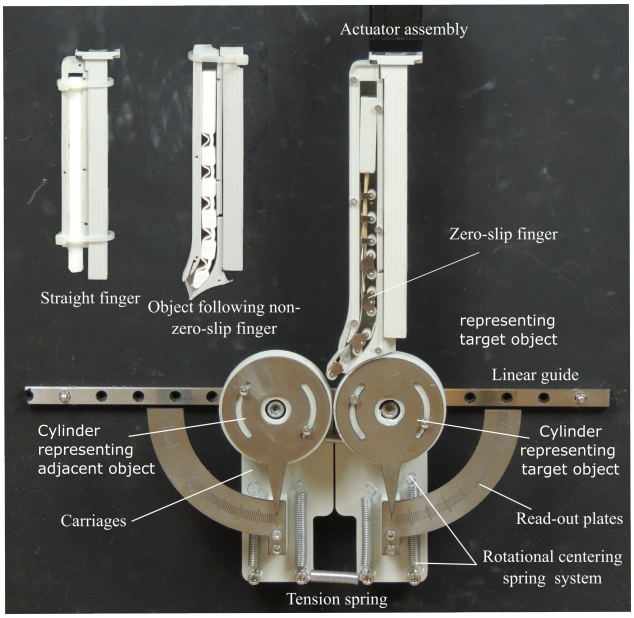


Figure 3.4: Setup for measuring object rotation and tangential disturbance forces during finger insertion. Two cylinders—each representing an object—rotate about their axes and translate along linear guides, with springs between the guides for tangential force measurement. Benchmark fingers without everting belts (top left) were used for comparison.

Fig. 3.4 depicts the dedicated setup that was built to measure the tangential disturbances. A finger was pushed between two cylinders of radius $R_{cyl} = 30$ mm, mounted on ball-bearing axles and placed on free-running carriages along a linear slider, representing the target object and its adjacent object.

To emulate inter-object resistance, the carriages were coupled with an extension spring providing an effective force of 7 N when separated by the nominal finger thickness of 11 mm. The cylinders were kept in neutral position by opposing springs with effective torsional stiffness coefficients of $\kappa_{\text{obj}} = 0.66$ mNm/deg and $\kappa_{\text{obst}} = 0.64$ mNm/deg. Cylinder rotation was read from graduated arcs with $\pm 0.5^{\circ}$ precision.

The maximum angular perturbation was recorded during finger insertion, and the corresponding maximum shear force was calculated as $F_{\text{t}} = T_{\text{cyl}}/R_{\text{cyl}}$, with the torque related to rotation by $T_{\text{cyl}} = \kappa \Delta\theta$. To assess belt effectiveness, ten DBCF-EM measurements were averaged and compared to two benchmark fingers without belts—a solid straight and a pre-curved variant—both matching the DBCF-EM in thickness and made from the same material as the belts, ensuring equal friction coefficients between the objects and the propagating finger for fair comparison.

3.3.3 Pull-out force

The pull-out force is a critical performance metric for grippers, as it determines whether an object can be held reliably once grasped [58]. In this study, the focus was on the removal

of a single object from a pile, for which a holding force sufficient to overcome gravity, plus a small margin for the upward lifting acceleration, was considered adequate. Because the gripper retrieved objects vertically from a pile, the pull-out force along the longitudinal axis of the gripper was measured.

For this, a setup was built in which the gripper was mounted vertically upward and closed around a spherical object with $D = 60$ mm and $m_{obj} = 50$ g. The object was then pulled upward with a spring scale until released from the grasp. From the recorded experiment, the maximum force on the scale was determined with a precision of ±25 g (≈ ±0.25 N). After correcting for the object's weight (≈ 0.5 N), the net holding force exerted by the gripper was obtained.

3.3.4 Net disturbance force on the object

Excessive interaction forces along the gripper's longitudinal axis—the net disturbance force [N]—can push the object away and cause misgrasps. The curved wrist channel and finger radius were designed to guide the fingers tangentially around the object, preventing direct impacts and thereby minimizing this force. To quantify the net disturbance force, the setup as illustrated in Fig. 3.5 was built, consisting of a spherical object with $D = 60$ mm mounted on a linear slider and held in neutral position by two opposing springs with an effective stiffness of $k_{eff} = 0.19$ N/mm. The gripper was aligned with the slider at a 2 mm distance from the object surface, measured from the wrist center. During repeated grasping cycles, the maximum displacement Δu of the object from its initial position was recorded with a precision of ±0.25 mm. The corresponding net disturbance force was then calculated as $|F_{net}| = k_{eff}\Delta u$.

3.3.5 Grasp success rate in a practical robotic set-up

The grasp success rate was evaluated to assess the gripper's overall performance and validate its newly introduced features in a practical setting. For this, it was integrated into a robotic system, as shown in Fig. 3.6, and tasked with removing 33 piled tomatoes one by one. Success was defined as the ratio of successful pick-and-place attempts to total attempts, requiring both removal from the pile and damage-free handling. This metric reflects the gripper's efficiency and reliability in a realistic robotic context, beyond stand-alone testing.

The setup consisted of an ABB IRB 1200 robotic arm controlled via ROS, which performed object recognition and position estimation using stereo image sensing, as developed in [148], but here used without the advanced software implementations presented there. Instead of bin-picking chicken legs, the system performed pick-and-place of piled tomatoes, employing a tomato detection model and our own gripper design installed as the end effector. Apart from the target object position, no higher-level processing such as obstacle recognition or grasp pose planning was applied. In each attempt, the algorithm selected a tomato at the pile's surface based on recognition accuracy—only those roughly free at the top could be picked, though side surfaces could still be obstructed—after which the robot positioned the gripper vertically above the estimated center with an accuracy of ±5 mm in both horizontal and vertical directions. The gripper was manually activated to enclose the object, after which the robot lifted the tomato from the pile and placed it on a deposit table, where release was again manually activated. The grasp success and damage rates were quantified from video recordings and visual inspection.

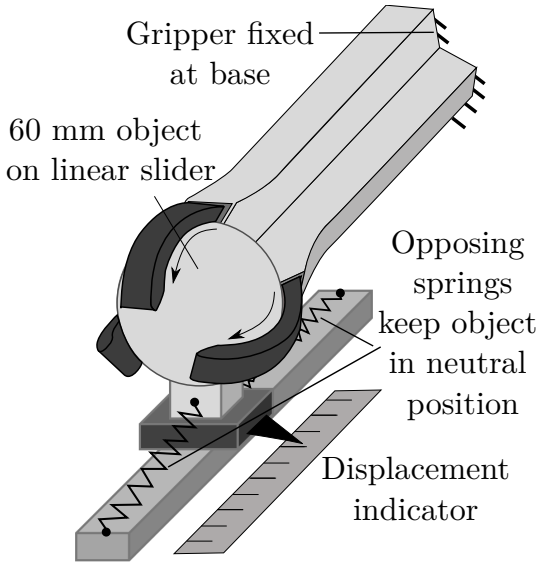


Figure 3.5: Setup for measuring net disturbance force during grasping, derived from object displacement and spring stiffness.

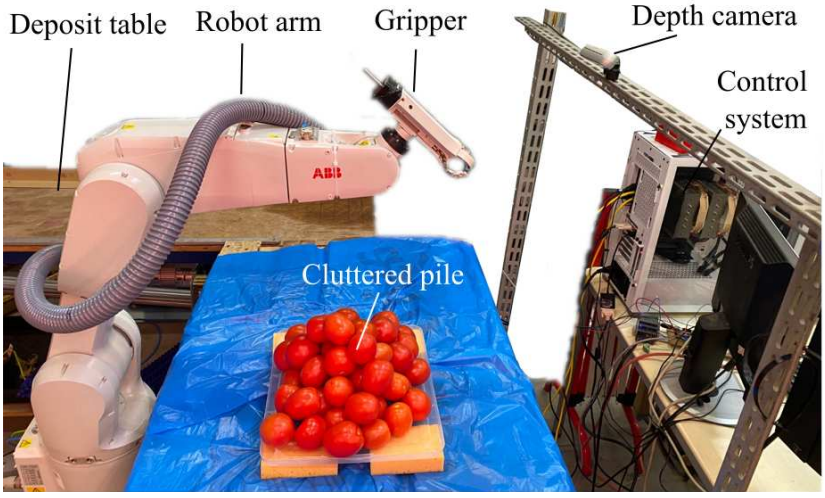


Figure 3.6: Robotic setup for grasp-success-rate evaluation, illustrating automated removal of tomatoes from a crate by vertical positioning of the gripper above each target tomato, without advanced grasp planning.

3.4 Results and implications

This section presents the experimental outcomes for the five defined performance metrics and their implications: (i) tangential object-following motion, (ii) reduction of tangential disturbances at contact interfaces, (iii) holding force, (iv) net disturbance force, and (v) grasp success rate.

3.4.1 Tangential object-following finger motion

Figure 3.7 shows overlaid side-view stills of a finger grasping a spherical object. The finger advanced tangentially with minimal deviation—within 3 mm during the first 10 mm after exiting the wrist—then closely followed the contour until full enclosure. No significant outward bending was observed on contact. These results confirm the suitability of our grasping strategy for confined spaces: tangential, object-following motion achieves full enclosure while requiring only the nominal finger thickness as clearance, the theoretical minimum set by the finger geometry. They further demonstrate that a pre-curved, base-driven flexure guided parallel to the object surface can effectively trace the contour, establishing it as a strong mechanical concept for this strategy. Further refinement could reduce the finger thickness and required clearance.

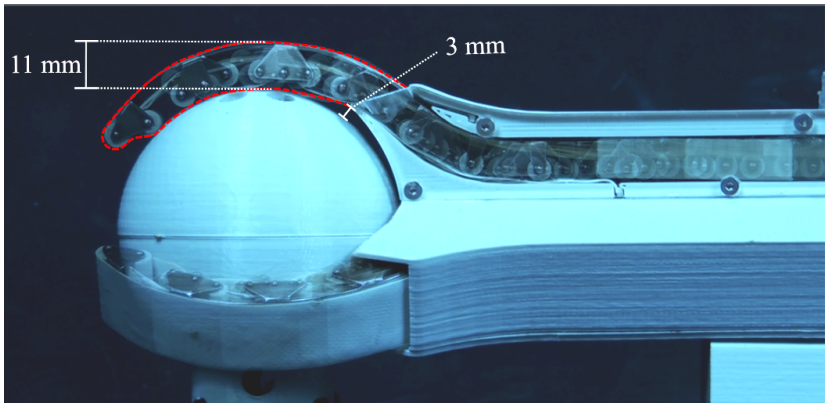


Figure 3.7: Example results of tangential object-following finger motion tests, showing an overlay of intermediate states during grasping. The finger propagated within the bounds of its thickness, with a maximum deviation of 3 mm near the wrist.

3.4.2 Tangential disturbances at contact interfaces

Figure 3.8 presents the tangential disturbances at the contact interfaces of the adjacent (red) and target (blue) objects for the straight benchmark (left), curved benchmark (middle), and DBCF-EM (right) fingers. The left axis shows the maximum angular perturbation $\Delta\theta$ (°) during insertion, and the right axis the corresponding tangential friction force F_t (N), obtained from the measured rotation using the defined stiffness relation in 3.3. The mean rotations of the target / adjacent objects were 35.5°/33.5° for the straight finger, 39.9°/19.1° for the curved finger, and only 3.2°/0.5° for the DBCF-EM finger. This clearly demonstrates

the effectiveness of the dual-eversion belts in suppressing tangential disturbances during finger insertion, showing reductions of at least 91% and 97% compared to the benchmark fingers.

A notable observation is that, for both curved fingers, the rotation of the target object was lower than of the adjacent one, whereas for the straight finger, the rotations of both objects were nearly equal and comparable to the rotation of the adjacent object of the curved dummy finger. This difference may be explained by the contact area distribution, where the inner sides of the curved fingers wrap around the target object, forming a more distributed contact region that tends to result in lower disturbances, whereas the straight finger and the outer sides of the curved fingers contact the neighboring objects along a smaller, roughly line-shaped region, tending to result in higher disturbances.

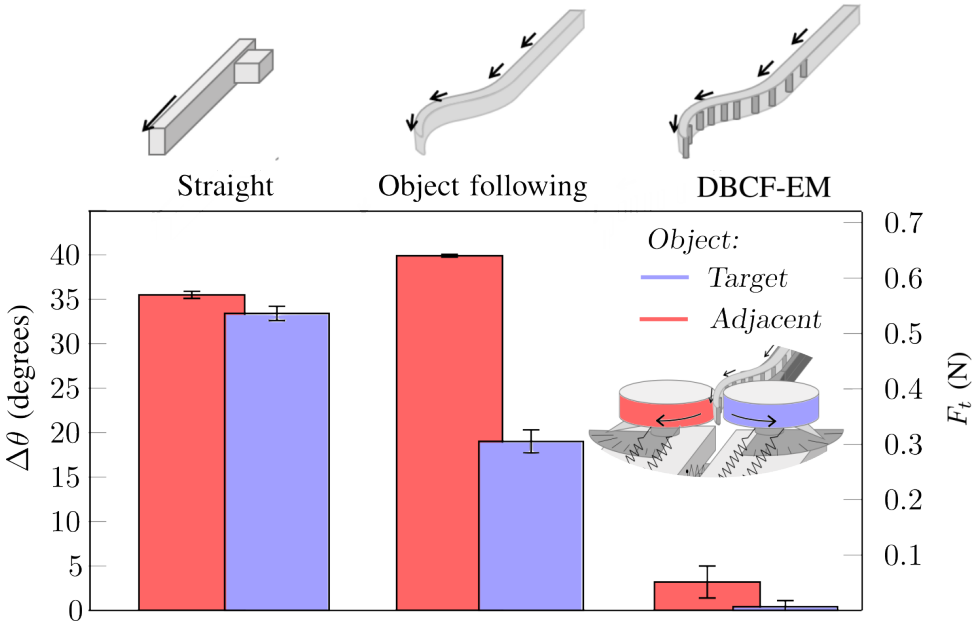


Figure 3.8: Results of tangential disturbances—rotation (left axis) and corresponding force (right axis, derived from rotation)—at the target object (blue) and adjacent objects (red) interfaces, showing reduced disturbances for the DBCF-EM finger compared to the two benchmark fingers.

3.4.3 Pull-out force

The pull-out tests yielded a holding force of $F_h = 3.7 \pm 0.4$ N (95% CI), about twice the heaviest tomato's weight, thus exceeding the minimum requirement for pile removal under moderate vertical accelerations. Although obtained with a PLA dummy whose friction coefficient with the finger differs from that of real tomatoes, the values provide a conservative estimate, as the caging gripper relies mainly on form-closure and tomatoes perceptibly resist sliding more strongly. Our robotic experiments will reveal that the holding

force was sufficient for this specific use case. In general, the reported values provide a reasonable estimate for spherical objects and are particularly useful for benchmarking other grippers due to the experiment's repeatability.

3.4.4 Net disturbance force on the object during grasping

The net disturbance force during grasping was measured as $F_{net} = 0.1 \pm 0.04$ N (95% CI). This force is negligible compared to both the holding force and the object weight, indicating it is unlikely to damage or displace the object outward during grasping. The relatively low forces align with the visual observations in Fig. 3.7, confirming circular tangential motion without notable flexure bending.

3.4.5 Grasp success rate in a practical robotic set-up

The results of the grasp success rate test are presented in Fig. 3.9. In the practical robotic experiment, the gripper successfully grasped, lifted, moved, and placed all 33 tomatoes, yielding a raw grasp success rate of 100% (33/33), defined as the percentage of objects removed regardless of damage. However, post-experiment inspection revealed three damaged tomatoes, resulting in an effective grasp success rate of 90.9% (30/33). The accompanying supplementary video demonstrates the gripper's operation during the robotic experiment, as referenced in Appendix A.1.

Damage consisted of skin punctures, likely caused by sharp uncovered flexure edges (longitudinal sides and fingertip edges) that occasionally slid along neighboring tomatoes like a knife, or by the sharp housing exit when positioned too low by the robot. No bruising was observed, indicating the gripper did not apply excessive squeezing, consistent with the measured disturbance forces.

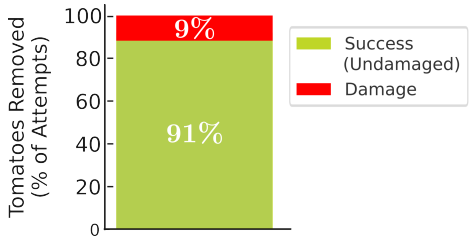


Figure 3.9: Grasp performance of the DBCF-EM gripper in confined spaces. All pick-and-place tasks were completed (100%), with damage occurring in 9% of attempts, yielding a 91% undamaged grasp rate.

3.5 Discussion

This study introduced a novel approach to grasping in confined environments by changing the finger motion from a normal (perpendicular) approach to a tangential trajectory along the object surface. Technical tests confirmed that a finger concept comprising flexure-driven eversion mechanisms can navigate curved paths while minimizing environmental disturbances, with dual-eversion belts yielding a 92–97% reduction in tangential forces.

Practical evaluation further showed that this enabled grasping in confined environments, achieving a raw grasp success rate of 100% and inducing only limited displacements during finger insertion. This positions the mechanism as a distinct and promising alternative within the gripper literature, and since comparable designs with this capability are largely absent and new disturbance metrics were introduced, direct benchmarking is difficult.

More general comparisons can nevertheless be made. Compared to soft grippers, the integration of flexures provides a more defined trajectory, higher lateral stiffness, and the ability to withstand larger forces, while maintaining shape adaptability. Although squeezing forces were not explicitly measured, the fingers are expected to perform favorably relative to fingered grippers with perpendicular closing motion (either soft robotic, continuum, or rigid linkage designs), which rely on object resistance for conformation and shape adaptation.

Unlike conventional fingered grippers, confined-space grasping was achieved without requiring complex world perception or planning algorithms. The design therefore facilitates straightforward robotic integration, easing system requirements for engineers: by simply positioning the gripper vertically above a tomato, the fingers were able to find their way around the object through the clutter.

3.5.1 Damage and limitations

Object damage nonetheless remains a key limitation, underscoring the need for design refinement to eliminate it. The observed damage was not due to malfunctioning of the mechanism, which operated according to the intended principles, but rather to uncovered sharp flexure edges not protected by the belts. This finding, together with the demonstrated reduction of shear forces, highlights the effectiveness of incorporating eversion mechanisms into the finger design, while also pointing to the necessity of further development.

Other limitations relate to the use case: experiments were performed only with tomatoes and at lower accelerations than typical in industry. Additional performance metrics—such as the holding force, mass, volume, closing time, lifetime, robustness, hygiene compliance, and the ability to handle objects beyond tomatoes—were considered during the design process but not further optimized, as the focus of this work was to demonstrate the principle and validate the concept for the selected use case. Direct comparison of these metrics with state-of-the-art grippers is therefore of limited relevance, yet highlights the need for continued design refinement, as such aspects remain critical for industrial acceptance of the DBCF-EM and to justify its added design complexity. Addressing them will be essential for future implementation in food-handling lines.

3.5.2 Holding force requirements

Increasing the holding force is an essential step toward industrial acceptance, as it enables the gripper to withstand higher accelerations and handle heavier objects. Towards the grippers longitudinal direction is generally the easiest escape path, so the tested direction off the pull-out force reflects the minimum holding force. For slower operations or when the gripper is angled from vertical—as in harvesting—this may already be sufficient. However, high-speed bin-picking requires holding forces of at least an order of magnitude higher than those reported here. Also for handling larger objects the challenge grows quickly,

since object mass scales with the cube of diameter; doubling the diameter increases mass by a factor of eight.

Holding capacity can be increased in two principal ways: (i) adding more fingers or (ii) tuning finger parameters to stiffen the caging structure. The lateral stiffness of the flexures is a key contributor and can, as a first approximation, be inferred from linear elastic beam theory. The lateral deflection scales approximately as $\delta \propto PL^3/(EI)$, where the area moment of inertia of a rectangular flexure scales as $I \propto wt^3/12$, and load P scales proportional to object mass $M \sim d^3$. This shows that the flexure width w and thickness t affect stiffness differently: increasing width raises stiffness, but less than mass increases with diameter, while flexure thickness scaling effects cancel out. Increasing flexure stiffness can increase the holding force but reduces the shape adaptability of the finger.

The inner eversion belt also contributes significantly to cage stiffness, being held under pre-tension by elastic bands that act as structural tendons between finger parts, similar to those in the human hand. Analytical and FEA models were developed, as presented in Appendix B.2, to estimate their contribution at approximately 2.7–2.9 N, accounting for over 50% of the total measured holding force (3.7 N). Belt pre-tension is therefore decisive; increasing it—for example, using stiffer elastic bands or tightening the belts after closure—could further raise the holding force. However, higher pre-tension also pulls the fingers inward more strongly, increasing unwanted flexure deflection, which must be compensated by designing a larger finger curvature than the object's.

3.5.3 Future directions and broader applications

Even though specific metrics can be optimized toward industrial acceptance, future work should focus on redesigning the finger architecture, retaining the demonstrated advantages of flexure-driven eversion for low-disturbance tangential grasping, but in a more robust and hygienic form. One promising direction is embedding pre-curved flexures within conventional eversion sleeves to exploit the three-dimensional design space. This would circumferentially cover the fingers while reducing mechanical complexity, moving parts, and dirt accumulation, thereby improving hygiene, durability, and speed.

To the best of our knowledge, the DBCF-EM finger represents the first flexure-driven eversion mechanism, in contrast to conventional designs actuated by internal pressure. Our results illustrate the potential of combining flexures with eversion principles to achieve characteristics well-suited for safe and reliable navigation in dense and delicate environments, while also providing load-carrying capability. Therefore, we encourage engineers to explore alternative implementations and broader applications of flexure-driven eversion mechanisms in future designs. Beyond food handling, the same principles may inspire applications in medical devices (e.g. needles or endoscopic tools), inspection systems, and search-and-rescue robots, where delicate yet reliable interaction in confined spaces is essential.

3.6 Conclusion

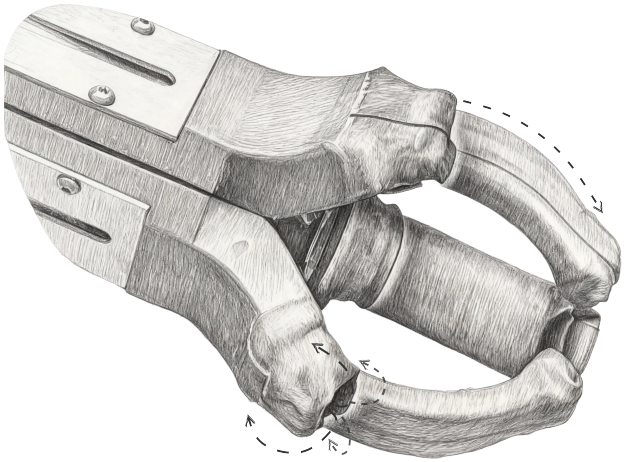
This paper introduced a new grasping strategy for objects located in confined environments by achieving caging grasps with advancing fingers that tangentially follow the object surface to enclose it, while passing between adjacent objects that typically obstruct the perpendicular closing motion of conventional fingered grippers. As proof of principle, a gripper equipped with Dual-Belt Curved-Flexure Eversion Mechanism (DBCF-EM) fingers was designed, built, and validated through robotic experiments involving the automated removal of tomatoes from a crate through simple vertical positioning above each target. The 100% removal rate from the pile confirms the feasibility of this strategy for confined-space grasping through gripper design, although the occurrence of approximately 10% damaged objects—caused by the sharp and open finger structure—indicates that refinements are still needed.

Dedicated experiments quantified the key mechanical behaviors of the DBCF-EM finger design: (1) its tangential, object-following motion enabled by an advancing pre-curved flexure, and (2) the reduction of tangential disturbances through dual-belt eversion. The results showed that the fingers closely followed the object contour with a maximum deviation of 3 mm and minimal bending, inducing a negligible normal disturbance force of $F_{net} = 0.1$ N. Combining the flexure with dual-eversion belts reduced tangential disturbances by 91–97% compared to benchmark fingers, confirming the effectiveness of the eversion-based approach. The measured holding force of $F_h = 3.7$ N was sufficient for the selected use case, exceeding twice the heaviest tomato's weight and meeting the requirement for pile removal under moderate accelerations, as ultimately confirmed by the robotic experiments. Together, these results demonstrate that fingers designed as flexure-driven eversion mechanisms enable confined-space grasping by limiting environmental disturbance.

Finally, this work introduced the first flexure-driven eversion mechanism, illustrating the potential of combining advancing pre-curved flexures with eversion principles. Its characteristics show promise for simple, robust, and easily automated manipulation in dense and delicate environments, while providing structural stiffness compared to conventional pressure-driven eversion mechanisms. Beyond food handling, the same principles may inspire applications in medical devices (e.g., needles or endoscopic tools), inspection systems, and search-and-rescue robots, where delicate yet reliable interaction in confined spaces is essential.

4

Sleeved Concentric-Flexures Eversion Mechanism Fingers



Chapter 3 introduced a gripper using Dual-Belt Curved-Flexure Eversion Mechanisms (DBCF-EM), demonstrating a successful proof of principle but also revealing limitations, including occasional misgrasps, object damage, and hygiene and durability concerns due to its open-sided design. These findings motivated the need for an evolved design. Chapter 4 presents an improved gripper based on Sleeved Concentric-Flexure Eversion Mechanisms (SCF-EM). A stretch-engineered latex sleeve everts outward to fully encapsulate the finger, driven by two concentric curved, base-driven flexures that follow a circular trajectory around the object. Tests show 100% grasp success, low disturbance forces, and sufficient holding forces, while the enclosing sleeve and reduced component count significantly improve durability and hygienic performance in confined-space grasping, addressing many of the limitations observed with the DBCF-EM gripper.

This chapter has been submitted as an article to ASME Letters in Translational Robotics, titled: Huisjes, A.E., and Herder, J.L. (2025). *The SCF-EM Gripper: Using Sleeved Concentric-Flexures Eversion Mechanisms as Fingers for Confined-Space Robotic Grasping.*

The SCF-EM Gripper: Using Sleeved Concentric-Flexures Eversion Mechanisms as Fingers for Confined-Space Robotic Grasping

Abstract *This paper presents the SCF-EM gripper, which employs specially developed Sleeved Concentric-Flexure Eversion Mechanism (SCF-EM) as fingers for grasping in confined spaces, with a focus on food handling applications. The gripper minimizes environmental disturbance by moving its fingers tangentially along an object's surface while setting the grasp, in contrast to conventional grippers that approach perpendicularly. Each SCF-EM finger features an eversion sleeve actuated by two concentrically placed pre-curved flexures between its inner and outer sides, synchronized via a cable-pulley system. This constitutes the first mechanically actuated eversion mechanism—driven not by pneumatic pressure, as in traditional designs, but by advancing an internal flexure from its base to push against the sleeve interior. A prototype gripper, equipped with three SCF-EM fingers, was manufactured for grasping tomatoes piled in a crate. To evaluate its performance, three key metrics were defined and experimentally validated. The results show: (1) a 100% grasp success rate for the specified task, demonstrated on a robotic test setup, (2) low induced disturbance forces—1.7 N normal and 1.5 N tangential—sufficiently gentle to avoid product damage, and (3) a 10.0 N pull-out force, ample for lifting tomatoes, corresponding to 4–10× their weight. These results demonstrate the SCF-EM gripper's effectiveness for delicate object handling in confined environments and highlight the potential of mechanically driven eversion mechanisms.*

4.1 Introduction

The automation of food handling is challenged by the fragile and diverse nature of food products. Ensuring a secure yet gentle grasp—without applying excessive force or introducing contamination—demands advanced and adaptable gripper designs. Various gripper concepts [25, 35, 36, 143, 149, 150] have been developed to address these challenges, and particularly those with mechanical fingers that encompass the object appear fit for purpose, as their grasp is both secure and gentle [34, 36, 55–57, 60, 67, 73, 75, 76]. These fingers often employ shape-adaptive principles, such as underactuated rigid linkages [63, 74, 75, 151], compliant mechanisms [89], or soft robotics [27, 28, 77], which allows them to conform to the shape of the objects they grasp. They are barely sensitive to the variety of structural and surface properties of objects and have shown notable success in handling food items delicately and effectively.

However, despite their success in laboratory settings [96–98], grippers with encompassing fingers have seen limited adoption in industry [12, 99, 100]. In practice, food items—such as chicken pieces, tomatoes, or sweet bell peppers—are often located in confined or cluttered environments, including crates, boxes, or hanging clusters on plants [101–107]. These settings leave little to no free space around the object, which is critical for conventional grippers. As illustrated in Fig.4.1(a), they first position their fingers around the object before closing them inward perpendicularly—an approach that fails in confined environments where lateral access is restricted.

To date, solutions to this problem have largely been sought within the robotics domain, as the issues typically arise during deployment on robotic platforms rather than during gripper development. These solutions rely on advanced path planning, motion control, or obstacle-recognition and avoidance algorithms [99, 146, 147]. Such control-side approaches address the symptoms at the system level but do not resolve the root cause: the incompatibility of conventional finger kinematics with confined environments, which leads to large disturbances during grasping. In contrast, we propose a mechanical solution that tackles the problem at its origin.

In this paper, we present the mechanical design of the SCF-EM gripper, with fingers designed as *Sleeved Concentric-Flexure Eversion Mechanisms* (SCF-EM) that enable grasping in confined spaces, and validate its performance through a series of practical and technical tests. Its working principle is illustrated in Fig. 4.1(b). The fingers advance tangentially along the object's surface by being extruded and retracted from the gripper's housing to establish and release encompassing grasps, thereby reducing environmental disturbance and enabling confined-space grasping.

Each SCF-EM finger comprises an eversion sleeve actuated by two concentrically placed pre-curved flexures between its inner and outer surfaces, synchronized via a cable-pulley system. The flexures define the circular path tangentially along the objects surface, while the eversion mechanism reduces sliding forces on the surroundings during finger motion.

This paper is structured as follows: Section 4.2 details the gripper design, including performance metrics for grasping food in confined spaces, the conceptual design of its fingers, and the mechanical design with manufacturing details. Section 4.3 describes the experimental validation, including the practical and technical tests performed and the experimental setups used. Sections 4.4 and 4.5 present the results, discussing their

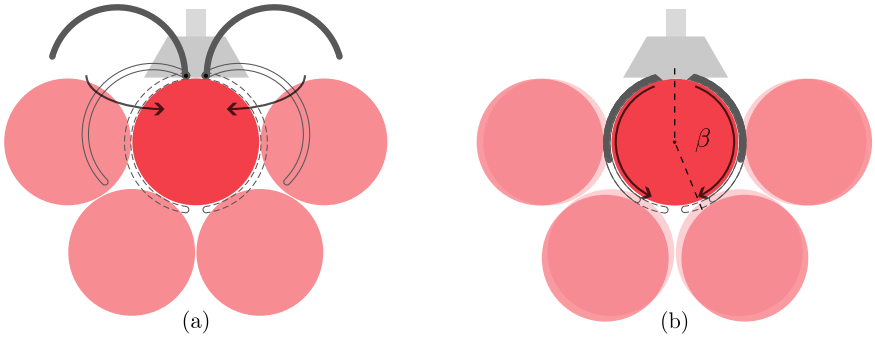


Figure 4.1: (a) Conventional grippers grasp objects by first positioning their fingers beside them, then closing inward perpendicularly—a motion often hindered in confined spaces by adjacent objects, limiting practical use. (b) The proposed solution, explored in this work, enables grasping in confined environments by reducing environmental disturbance through tangential finger motion along the object's surface during grasping. As the fingers advance, they gently displace neighboring items while progressively increasing the enclosure angle up to $\beta = 180^{\circ}$, ultimately enclosing the object with the fingertips underneath. This approach reduces induced disturbances and lateral space requirements, making it well suited for dense environments.

implications, the effectiveness, and limitations of the gripper, and placing this research in a broader context. Finally, the conclusions are presented in Section 4.6.

4.2 Method

The conceptual and mechanical design of the SCF-EM gripper is presented in this section. First, we establish three performance metrics to assess gripper effectiveness in grasping food objects in confined spaces. Then, the conceptual design of the finger is detailed, including the rationale behind it to achieve the desired behavior, followed by the mechanical design and manufacturing process of the gripper for the chosen use case.

4.2.1 Performance metrics

To evaluate a gripper's performance in dense environments, the following performance metrics were established:

1. **Grasp Success Rate**: The percentage of successful pick-and-place actions of the total attempts. This metric indicates the efficiency and reliability of the gripper in securely grasping, lifting, and placing objects in a densely packed environment without dropping or damaging them or the surroundings. The grasp success rate is calculated as the ratio of successful pick-and-place attempts to total attempts.

2. **Disturbance Forces**: The interactional forces exerted by the advancing fingers on objects during grasping, measured in two directions:

   (a) **Normal Forces**: Forces that act perpendicular to the surface of the target object while setting the grasp. Reducing these forces prevents damage, such as

bruises or punctures.

(b) **Tangential Forces**: Forces that act in parallel with the surface of the target object while setting the grasp, i.e. frictional forces. Reducing these forces prevents surface damage such as scraping or tearing and ensures smooth finger movement.

In addition to the fact that excessive disturbance forces can cause damage to the object and surroundings, they can also lead to misgrasping if they are directed away from the gripper and overcome the counteracting forces that keep the object in place.

3. **Pull-Out Force**: The force required to release an object from the gripper once it is grasped. A higher pull-out force indicates a stronger and more reliable grip, ensuring secure handling during lifting and transportation. It reflects the gripper's holding strength, as high holding forces ensure that the gripper can resist external forces and securely hold objects.

In addition to these key metrics, factors such as the gripper's cycle life and maintaining hygienic conditions during operation are also critical for its use in the food industry. These aspects were considered in the design process, but are not the focus of the evaluation in this article.

4.2.2 Finger concept and design rationale

Fig. 4.2 illustrates a planar embodiment of the SCF-EM gripping finger concept. It combines an **eversion sleeve** (yellow) with **two concentrically placed precurved compliant flexures** (grey), linked via a **cable-pulley system**.

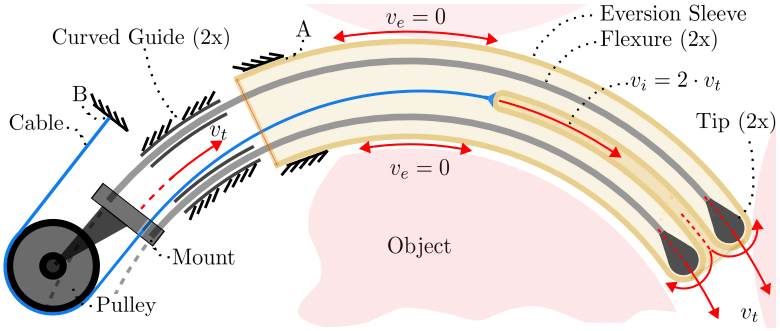
The eversion sleeve is a flexible, fabric-like tube, folded inside out and routed over the tips of two precurved compliant flexures, such that a portion lies within the channel between them while another covers their exterior. The outer part of the sleeve is fixed to the base, whereas the inner portion is connected back to the base via a cable (blue) guided over a rear-mounted pulley (dark grey).

The finger is actuated by pushing the flexures forward. Their tips press against the folded end of the eversion sleeve, dragging the inner portion forward and causing it to evert outward. As the sleeve unfolds around the flexures, it eliminates relative motion with the environment, minimizing friction during advancement.

This principle is inspired by conventional pressure-driven eversion mechanisms [111–114, 152], which use internal over- or underpressure to drive a thin, folded sleeve forward in its longitudinal direction. As shown in Fig. 4.3, material is fed internally at velocity $v_i = 2 \cdot v_t$ and everts at the tip by the pressure inside the tube, resulting in a stationary outer surface ($v_e = 0$) that imposes no shear on its surroundings. These features make them well-suited for low-disturbance advancement through confined spaces.

However, conventional pressure-driven eversion sleeves extend linearly—limiting their compatibility to follow contours of curved objects— and lack lateral load support. To overcome this, we integrate pre-curved compliant flexures as a structural backbone, enabling actuation, curved path following, and load-bearing functionality.

The flexures are pre-curved to match the object's radius, enabling the finger to self-guide along a predefined circular path while setting the grasp. This eliminates the need for active



4

Figure 4.2: 2D cross-sectional sketch of the SCF-EM finger concept illustrating its operating principles. An eversion sleeve (yellow) is wrapped inside-out around the tips of two precurved compliant flexures (grey). The sleeve's ends are anchored to the ground: the outer side at point A, and the interior at point B via a cable (blue) running over a pulley (dark grey) mounted on a bracket behind the flexures, synchronizing backbone and sleeve movement in a 1:2 ratio.The finger encloses the object by advancing the flexures along curved sliders at velocity v_t, pulling the sleeve interior forward at $v_i = 2v_t$ to roll outward around the finger. This results in zero exterior sleeve velocity v_e, thereby mitigating friction with the environment. Upon finger retraction, the cable-pulley system draws the sleeve inward in coordination with the flexures.

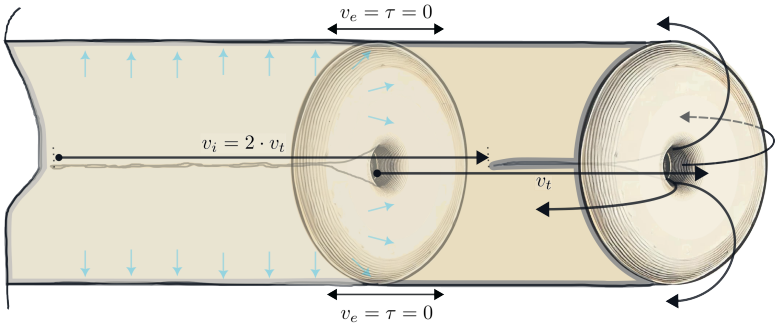


Figure 4.3: 3D sketch of the tip of a conventional eversion mechanism illustrating its operating principles [114]. The mechanism uses an inside-out folded eversion sleeve that advances and retracts at velocity v_t by lengthwise extension and retraction driven by internal overpressure and underpressure, indicated by the blue arrows. The fabric is fed forward at velocity $v_i = 2v_t$ through the sleeve's interior and everted at the tip to its exterior at velocity v_e, resulting in zero relative velocity between the sleeve and the environment. This enables propagation without inducing shear stress on the surroundings.

steering, as the finger naturally advances tangentially around the object's contour when pushed from the base. Longitudinal stiffness is crucial to maintain this propagating motion and to navigate through clutter. Meanwhile, lateral flexibility allows shape adaptation, enabling the finger to accommodate misalignment or variations in object size.

An object is considered grasped when it is form-fitted within a cage of extruded fingers with sufficient stiffness to support its weight, assuming frictionless contact [144, 145, 153, 154]. In our design, the grasp is passive—requiring no continuous actuation—as the holding force arises from the lateral stiffness of the fingers, primarily determined by the flexure thickness and internal friction between finger components sliding past each other during object removal. Combined with the enclosure angle β (typically 90°–180°, see Fig. 4.1) and the number of fingers, this defines the total holding force of the gripper.

To release the grasp, the flexures retract while a 1:2 cable-pulley system simultaneously pulls in the eversion sleeve—which does not retract on its own—ensuring smooth motion between them and a tight fit around the flexures.

By combining the principles of eversion mechanisms with base-driven pre-curved flexures, the SCF-EM finger enables advancement tangentially along the object's surface to set the grasp around it. This motion requires no more lateral clearance than the finger's own thickness, minimizing normal disturbance forces during finger insertion, while the eversion mechanism mitigates tangential disturbances. Additionally, the sleeve encloses the flexures, acting as a hygienic barrier that isolates the finger from its environment.

The next section details the design and construction of a mechanical gripper based on the finger concept, tailored for a specific task and experimentally evaluated.

4.2.3 Use case: task and design requirements

In this article, we validate the proposed SCF-EM finger concept by designing and constructing a gripper tailored to the task of emptying a crate containing a pile of 58 vine tomatoes, grasping them one by one. The gripper must handle tomatoes with diameters ranging from 50 to 75 mm and masses between 60 and 180 g, based on measured data of this specific population.

We selected this use case for its practical relevance in agri-food applications, where tomatoes are often stored in densely packed crates. It presents specific challenges: the unstructured, multi-layered layout limits access—particularly near crate edges—and the tomatoes themselves are fragile, requiring gentle handling to prevent damage from excessive squeezing, puncturing, or scraping during finger motion.

The requirements for the mechanical design of the gripper were established by measuring the mass, height, and diameter of each tomato in the population. These data are summarized in Table 4.1, including mean values, standard deviations, minimum and maximum values, and medians. We determined that the gripper must be capable of grasping and holding objects that are, on average, spherical with a diameter of 60 mm and a mass of 130 g. Furthermore, the gripper must have the flexibility to manipulate both the smallest and the largest objects in the population, that is, those with diameters of 50 mm and 75 mm and masses of 60 g and 180 g, respectively.

Table 4.1: Summary statistics of mass, height, and diameter for the population of 58 tomatoes considered in the use case.

	Mean	Standard Deviation	Minimum	Maximum	Median
Mass (g)	131	20.6	84	183	132
Height (mm)	57.9	3.2	49.6	65.2	58.3
Diameter (mm)	63.7	3.8	52.5	74.2	63.7

4.2.4 Mechanical design and manufacturing

The mechanical design of the gripper is illustrated in Fig. 4.4. Subfigure (a) shows the complete assembly, while subfigure (b) provides a view of the internal components with one finger module removed, whose parts are detailed in subfigure (c). The gripper consists of three finger modules, each housing a gripper finger. The modules are attached to the central hub, which contains the drivetrain components.

The fingers are actuated by a central drive that extends and retracts three precurved compliant fingers from a housing in which they are stored flat. Upon deployment, the fingers follow a circular path with radius $R = 30$ mm, enabling them to glide smoothly along the tomato surface. This reduces normal disturbance forces by avoiding direct squeezing or excessive clearance. Each finger is enclosed by an eversion sleeve that minimizes friction during insertion into the pile. The fingers are symmetrically arranged around the spindle's longitudinal axis, spaced 120 degrees apart to ensure a form-closed grasp.

Driveline

The central driving system consists of a NEMA 17 stepper motor, a spindle, a triangular actuator block, and two mounting brackets located at the top and bottom of the gripper, which secure the finger modules and the actuator. The spindle, a TR8x2 with an 8 mm diameter, is centred with a rotary bearing in the lower mounting bracket and is connected to the actuator. The actuator is powered by a StepStick DRV8825 stepper motor driver, mounted on an Arduino CNC Shield v3 with an Arduino Uno Rev.3, and is operated via a laptop using GRBL software.

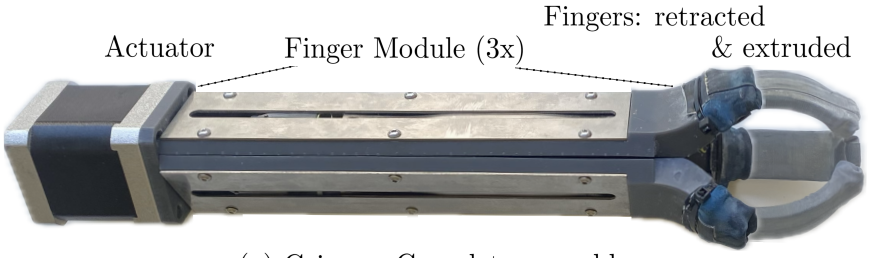
As the spindle rotates, the triangular block translates linearly through the central hub, guided by the elongated triangular channel formed by the inner sides of the finger housings. Attached to the fingers' outer flexure, it drives them in and out of their housings to set and release the grasp.

The finger module

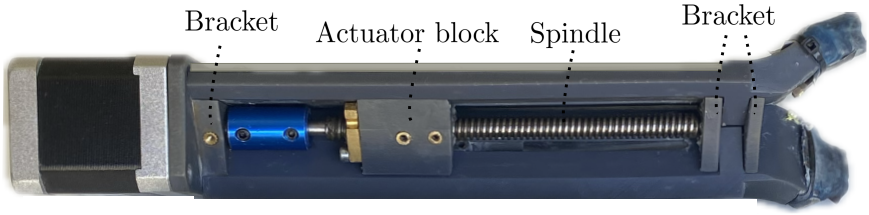
The components of a finger module are illustrated in Fig. 4.4 (c), including the finger, its housing, the cable-pulley system, and mounting. The finger housing contains a passage where the finger is stored, consisting of a linear grooved section covered by a steel plate and a curved channeled outlet. The stored finger is bent from its original curved shape to conform to the passage. When the finger is extruded, the flexures return to their original shape, following a circular trajectory.

The finger housing is 3D printed using SLA technology with Tough 2000 resin material. The curved end of the housing is angled at 45° relative to the straight section, directing

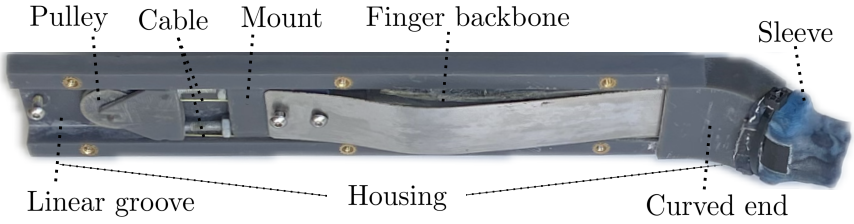
the finger to exit tangentially along the object's surface at a point 45° from the object's vertical axis. A larger exit angle would allow a more compact gripper layout by positioning the modules closer together, but is currently limited by the dimensions of the central hub components and the plastic deformation threshold of the precurved flexures.



(a) Gripper: Complete assembly



(b) Gripper: Disassembled finger module revealing driveline



(c) Finger module

Figure 4.4: Mechanical design of the gripper. (a) Complete assembly; (b) internal components with one finger module removed, revealing the driveline; (c) detailed view of a single SCF-EM finger module. The gripper consists of three finger modules, each housing one gripper finger, arranged 120° apart around the central driveline to enable form-closure grasps. The flexures are elastically straightened and stored in the housing, then driven forward by a central actuator that linearly moves the triangular block through the hub. Upon exiting, the flexures relax into their precurved shape, following a circular path opposite the housing's curved end. The flexures drive the eversion sleeve enclosing the backbone's exterior, with a cable-pulley system synchronizing their motion at a 1:2 ratio.

The finger

The finger and its parts are shown in Fig. 4.5 containing the mechanical design of the backbone and the eversion sleeve.

The finger's backbone consists of two concentric precurved flexures—an inner one with a 30 mm radius and an outer one with a 34 mm radius—each 0.15 mm and 20 mm wide. They are laterally spaced by two C-shaped SBR rubber spacers (4 mm high, 2 mm thick), positioned at their sides, creating a 4 mm × 16 mm central channel through which the eversion sleeve can pass freely. All components are joined at the front using two M1 bolts through the tip elements.

The spacers are glued only to the inner flexure, while only the outer flexure is connected to the driveline. This setup allows the flexures to bend independently and slide relative to each other during extrusion and retraction from the gripper housing—essential to accommodate the arc length mismatch as the backbone transitions from a flat to a curved configuration, which would otherwise cause tension buildup.

For the manufacturing of the precurved flexures, flat spring steel strips (0.15 mm thick, 20 mm wide, and 145 mm / 155 mm long) undergo a two-step rolling process to achieve the intended final curvatures of 30 mm and 34 mm, along with the internal stress profile required to preserve their shape during operation. The 145 mm inner flexure is first bent around an 11 mm roller, resulting in a 15 mm radius after springback—too tight for the intended application. A second, reverse rolling step around a 48.50 mm roller plastically deforms it back to a final radius of 30 mm while embedding the necessary internal stress. This stress ensures the flexure maintains its curvature when passing through the housing's curved exit, where it is bent in the opposite direction with a 48.50 mm radius, thereby preventing plastic deformation during use. In contrast, a flexure rolled only once to 30 mm deforms plastically during operation, increasing its effective radius to approximately 43 mm. The 155 mm outer flexure is produced using the same method, with 10.5 mm and 43.50 mm rollers. In both cases, the first roller diameter was determined experimentally, while the second matches the curvature of the housing's exit.

The eversion sleeve is a custom-made latex tube (130mm long, 0.2mm thick walls), fabricated by gluing the long edges of a latex sheet together with latex glue. Latex was selected for its thin, waterproof, and primarily stretchable properties, which are essential to accommodate the arc length differences between the inner and outer flexures. The tube's circumference is 4% smaller than that of the finger, ensuring a tight fit through circumferential stretching. This minimizes wrinkling and keeps the sleeve snugly aligned with the inner flexure.

A longitudinal strip of tape is applied over the eversion sleeve to prevent stretching along its length during operation. When the finger is assembled in the housing, the tape runs from the attachment point at the base, over the outer flexure and tip, to the internal cable (from point B to A in Fig. 4.2). During extrusion, the fingertip presses against the inner surface of the sleeve via the tape, causing it to roll over and smoothly unroll the eversion sleeve, dragging the rest of the material along. During retraction, the cable pulls on the tape, rolling the sleeve back inwards while maintaining a synchronized 2:1 motion ratio between the sleeve and the flexure. Without this the tape, the sleeve would stretch longitudinally, causing it to wrinkle or wedge into the finger mechanism and block its motion. The tape's tension is adjusted via bolts on the threaded ends, which modify the

distance between the pulley and the mount.

Talcum powder is applied to reduce friction and prevent the eversion sleeve from sticking to itself, ensuring smooth rolling during operation.

The fingertip consists of two identical elements designed to drive the eversion sleeve by enabling smooth rolling and unrolling, preventing it from nesting or jamming during motion. Its rounded end forms a 10 mm wide, 3 mm diameter cylinder that presses against the sleeve's inner surface, promoting smooth outward eversion by sliding over it. The bevelled sides provide clearance for the sleeve to unfold without obstruction.

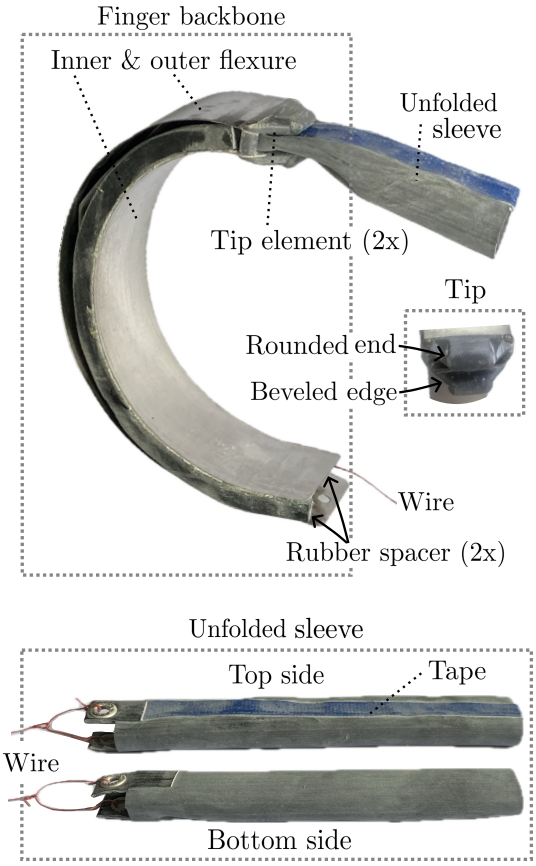


Figure 4.5: Top: SCF-EM finger in its relaxed state, with the eversion sleeve routed through the internal channel of the backbone but not yet folded back over the outer surface. The backbone consists of two spaced, precurved flexures bonded at the tip, with rubber spacer elements attached to the inner flexure. Below: two views of the same stretchable latex sleeve in reversed orientation. Its top side is longitudinally stiffened with tape, enabling it to roll forward over the backbone's outer flexure without stretching in the driving direction, while its bottom side remains circumferentially compliant to achieve a snug fit around the backbone.

4.2.5 Operating principles

Fig. 4.6 summarizes the behavior of the fully assembled gripper finger. Whereas the previous figures separately introduced the housing, flexures, and sleeve routing, this schematic illustrates how these elements interact during actuation and, by depicting the sleeve as if transparent, provides an under-the-hood view of internal motion that would otherwise be hidden. As the flexure pair is driven out of the housing, it relaxes toward its undeformed curved shape along a curved closing trajectory. During this process, it presses against the inner wall of the sleeve and progressively everts it over the fingertip, so that all exterior surfaces of the finger remain continuously covered as the finger advances. This establishes a stationary interface with the environment, decoupling the internal flexure kinematics from external contact. Together, these features are expected to enable low-disturbance, form-closed grasping in dense environments. The flexure elements provide tangential steering along a predefined curved object surface and allow the finger to navigate surrounding clutter, thereby reducing clearance requirements. At the same time, they serve as the structural frame for holding the object once enclosed, while the everting sleeve, in turn, strongly reduces shear forces on the object.

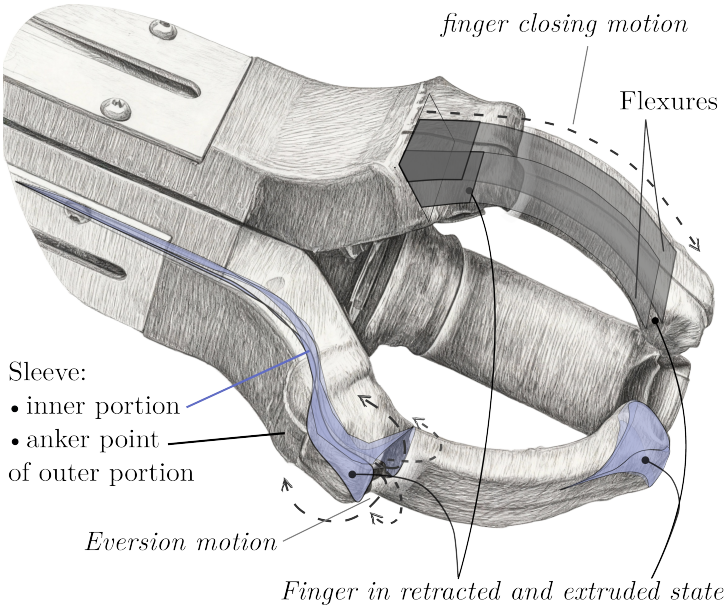


Figure 4.6: Schematic representation of the assembled gripper, emphasizing the finger and sleeve eversion motion, with the finger shown in both its retracted and extended states. During assembly, the sleeve is anchored with its outer portion to the gripper housing, initially following the finger forward before being routed back over the fingertip and folded into the channel between the two flexures (non-everted inner portion shown in blue). Depicting the outer portion of the sleeve as if transparent reveals how, during operation, the flexure pair extends from the housing, relaxes toward its undeformed curved shape along a curved closing trajectory, and presses against the inner wall of the sleeve, thereby everting it over the fingertip toward the exterior finger surfaces, keeping them fully covered and reducing shear forces. This allows for form-closed grasping in confined spaces.

4.3 Experimental performance validation

Multiple tests were conducted using dedicated experimental setups to evaluate the gripper's performance on the three defined metrics.

4.3.1 Grasp success rate for confined-space grasping

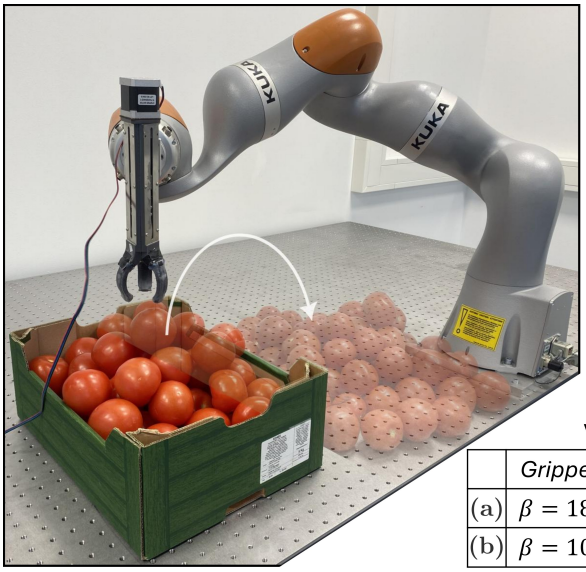
The gripper's grasp success rate was assessed in two different modes of operation, using the robotic setup shown in Fig. 4.7. The gripper was mounted to the end of a KUKA iiwa serial robotic arm and tasked with picking and placing 58 tomatoes, one by one, from a pile in a crate.

Each pick-and-place cycle involved six steps: (1) manually selecting the tomato to be grasped, (2) manually positioning the gripper above it, (3) gathering task-related information, (4) setting the grasp, (5) pick-up and moving the tomato, and (6) releasing.

The tomato selection process (1) was performed manually, mimicking the way humans typically select tomatoes when grasping them by hand, favouring the most accessible ones, such as those with more surrounding space or those positioned highest in the pile. Next (2), the gripper was placed above the selected tomato by manually guiding the robotic arm, which was equipped with gravity compensation and back-drivability software. The configuration was then locked while the gripper was kept in a downward orientation. Following this, (3) relevant task information was collected, including the tomato's mass, height, diameter, orientation (that is, whether the top, side, or bottom is facing upward), the number of contact points with the surroundings, and the number of obstruction points (i.e., the contact points through which the fingers must manoeuvre when setting the grasp). Subsequently, the grasp was set (4), followed by lifting the tomato from the pile (5) and releasing it beside the crate (6). This process was repeated until the crate was emptied.

The grasp success rate is calculated by dividing the number of successful pick-and-place attempts by the total number of attempts and multiplying by 100. A pick-and-place action is considered successful if the following sequential tasks are completed without inflicting damage on the target tomato or the other tomatoes in the pile: (1) setting the grip, by extruding the fingers to encircle the target object; (2) holding the object when being lifted from the pile; (3), releasing the object, by retracting the fingers such that the object falls out. If any gripper task was not completed or damage occurred, the action is deemed unsuccessful and a new attempt is made.

The grasp success rate was evaluated using two test variants on the robotic setup, each operating in a different mode, since this metric is not solely determined by the gripper itself but can also depend on how it is used. The two variants, (a) and (b), illustrated in Fig. 4.8, are described in detail below.



Variants:

	Gripper	*End-e DoF*
(a)	$\beta = 180°$	$3T$
(b)	$\beta = 100°$	$3T + R_z$

Figure 4.7: Robotic setup used to evaluate the gripper's grasp success rate in confined spaces, assessed by emptying a crate of tomatoes in two different tests (see Fig. 4.8), each repeated five times. Two test variants, (a) and (b), were performed, each using different gripper finger enclosing angles, β, and different end-effector (End-e) degrees of freedom (DoF).

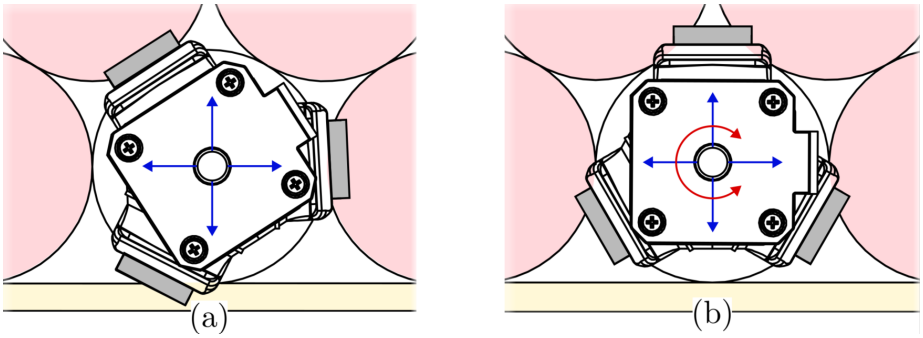


Figure 4.8: Illustration of the two test variants performed on the robotic setup to determine the gripper's grasp success rate, each employing a different operational mode. (a) The *pos gripper with full enclosure* test, where the gripper remains fixed in orientation and the fingers fully enclose the tomato with an enclosure angle of $\beta = 180°$. (b) The *pos-rot gripper with partial enclosure* test, where the gripper is allowed planar rotation and the fingers partially enclose the tomato at an angle of $\beta = 100°$ to align with voids between tomatoes, reducing environmental disturbance.

The two test variants used to evaluate the grasp success rate were:

(a) **The pos gripper with full enclosure test:**

- In this test variant, the gripper secured the object by fully enclosing it with its fingers, achieving an enclosing angle of $\beta = 180^\circ$ (see Fig. 4.1), intending to ensure a robust grip.
- When positioned above the target tomato, the device maintained a fixed orientation relative to the crate throughout the unboxing process to simplify robot operation.

(b) **The pos-rot gripper with partial enclosure test:**

- In this test variant, the gripper partially enclosed the object with its fingers, achieving an enclosing angle of $\beta = 100^\circ$.
- When positioned above the target tomato, the device was allowed to reorient in the horizontal plane above each tomato, aligning the advancing fingers with voids—i.e., clearances between adjacent tomatoes or crate walls—whenever possible.

Compared to the test variant (a), the operational adjustments in variant (b) were intended to reduce environmental disturbances caused by the fingers and thereby minimize the risk of object damage. To achieve this, finger paths through contact points between adjacent objects were avoided where possible, as these induce greater displacement than advancing through existing voids.

4.3.2 Disturbance forces

Figure 4.9 depicts the experimental setup used to evaluate disturbance and pull-out forces. It comprises three components: (1) the gripper, mounted on (2) a linear driveline that enables reciprocating motion towards an object positioned on a measurement module (3) for force acquisition. The components are indicated in white, blue, and yellow, respectively.

The linear driveline consists of a long linear slide and spindle, enabling the gripper—driven by actuator 2—to advance toward the object, while laser 2 measures its position relative to a fixed ground reference. The gripper was positioned for grasping by moving it toward the object until initial contact was detected, indicated by a slight increase in measured force, after which it was retracted by 0.1 mm. This position was kept constant for all ten repeated measurements used to determine a specific force.

The length of the finger extruded from the housing during the grasping process is measured by laser 1. This laser is mounted on actuator 1, which drives the finger, and it measures the distance to a receiver fixed to the mount of the finger module.

The measurement module consists of a dummy object mounted on a linear slider and connected to a load cell. The load cell is aligned with the object's degrees of freedom (DoF), constraining its motion and enabling measurement of the force exerted in that specific direction by the finger(s) during the grasping process. By varying the design of the measurement module, forces can be measured in different directions of interest.

The components included a PMB RTS-2065 linear slider for the measurement module, Futek LSB200 load cells as force sensors, two Micro-Epsilon ILD1420-100 laser sensors, and

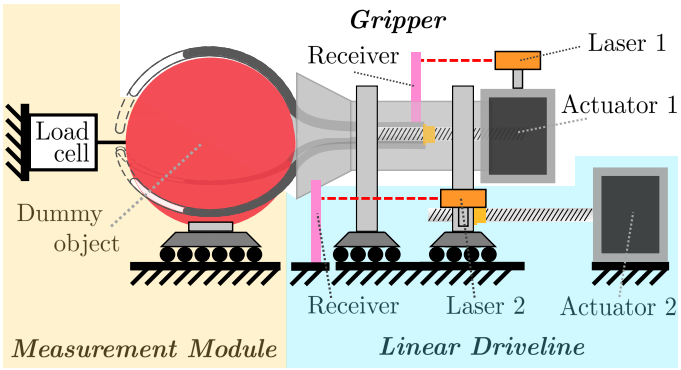


Figure 4.9: Illustration of the general experimental setup used for the technical tests (side view), showing three main components: (1) the gripper, (2) a linear driveline, and (3) a measurement module. The measurement module typically consists of a dummy object mounted on a linear slider and a load cell aligned with the slider's degrees of freedom (DoF), restricting the object's motion and allowing measurement of forces exerted by the finger(s) on the object along that direction during grasping. Variations of this basic setup were used for each specific force test to measure forces in multiple directions of interest.

a NEMA 17 stepper motor as actuator 2, driven using the same control setup as the gripper. All sensor signals were processed via a National Instruments USB-6008, and data from the force and distance sensors were recorded using a LabVIEW script.

To measure the disturbance forces, three variations of the experimental setup were constructed, as shown in Figs. 4.10, 4.11, and 4.13. These are referred to as the setups for experimental tests (exp. test) 1, 2, and 3, respectively. Experimental tests 1 and 2 were used to measure specific components of the normal disturbance forces, while test 3 was designed to measure tangential disturbance forces. As shown by comparing the setups, the main difference lies in the design of the measurement modules and the required 60° rotation of the gripper around its longitudinal axis, achieved by using different mounts on the driveline. Further details are discussed in the respective sections for each test.

Normal disturbance force

The normal disturbance force was determined by measuring the reaction forces exerted by the fingers perpendicular to the object's surface, in both the longitudinal and lateral directions of the gripper, using the setups of experimental tests 1 and 2, shown in Figs. 4.10 and 4.11. Both measurement modules feature a spherical dummy object mounted on a linear slider, with its motion constrained by an inline load cell.

The differences between the two setups lie in the orientation of the load cell—and thus the direction of the measured force—as well as the number of active fingers. In experimental test 1, the load cell was aligned with the longitudinal axis of the gripper and connected to the object and ground via threaded rods. All three fingers were active, and the force exerted on the object along the gripper's longitudinal axis was measured.

In experimental test 2, the load cell was oriented laterally with respect to the gripper and connected to the object via a single threaded rod. On the opposite side, a ball transfer

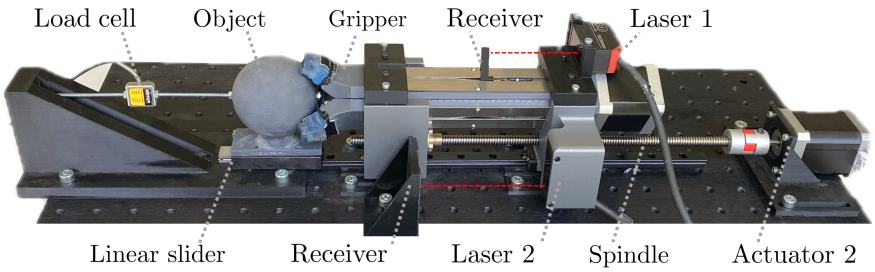


Figure 4.10: Experimental setup of test 1, designed to measure the normal component of the disturbance forces exerted by the gripper on the object along the gripper's longitudinal axis.

unit pressed against a vertical ground wall, allowing vertical displacements and thereby ensuring unidirectional force loading. In this setup, only one finger was active, and the lateral force it exerted on the object was measured.

To enable direct comparison, the force measured in test 1 was divided by three to estimate the contribution of a single finger acting in the longitudinal direction. By employing these measurement modules and monitoring the extrusion length of the finger using laser 1, we quantified the components of the normal disturbance force during grasping.

Measurements were performed on three dummy objects with diameters of 50 mm, 60 mm, and 75 mm, representing the smallest, average, and largest tomato sizes in the population, respectively, since disturbance forces are expected to vary with object size. The dummy objects were 3D printed using SLA technology with Tough 2000 resin and lightly sanded to smooth the surface.

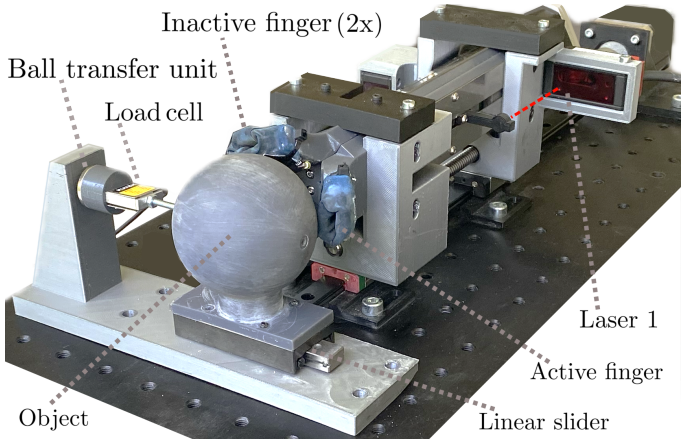


Figure 4.11: Experimental setup of test 2, designed to measure the normal component of disturbance forces exerted by the gripper on the object in the lateral direction.

Tangential disturbance force

The tangential disturbance force was measured in experimental test 3, using the setup illustrated in Fig. 4.12 and shown in Fig. 4.13. This test evaluated the tangential forces exerted on both the target object (red) and an adjacent object (blue) as a single gripper finger passed between them.

The setup included two measurement modules, each featuring a semi-circular dummy object mounted on a linear slider to allow lateral movement during finger passage. The objects could rotate around their vertical axes, but this motion was constrained by load cells positioned 20 mm from the axis of rotation. These load cells contacted the flat back of the objects via ball transfer units and measured the tangential disturbance force by registering the reaction force counteracting the moment induced by the finger. The tangential force was calculated by multiplying the measured force with the ratio of object radius to moment arm.

To emulate inter-object resistance and enable force measurement, two springs were incorporated: a 200 N/m spring connected the target object to the ground, while a 50 N/m spring—pre-stretched by 2 mm—linked the two object modules. The first spring maintained

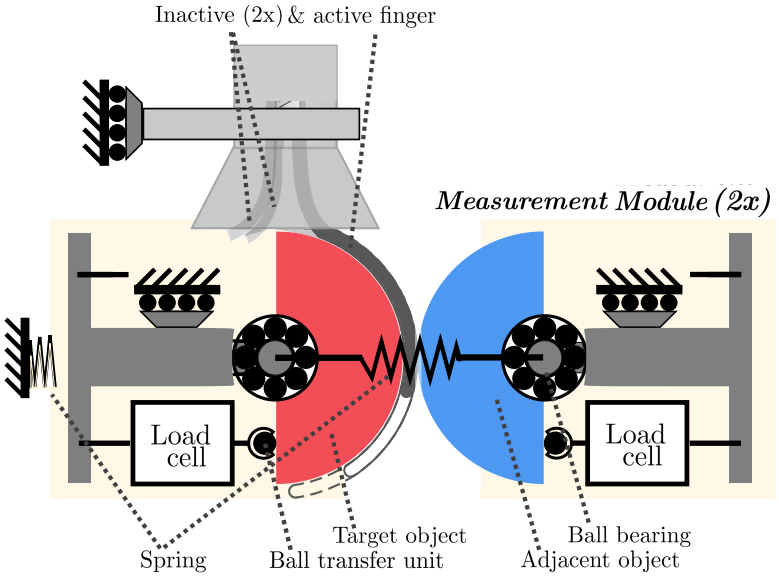


Figure 4.12: Illustration of the experimental setup of test 3: This setup measures the tangential disturbance force exerted by the gripper finger on both the target object (red) and the adjacent object (blue). The objects are mounted on a linear slider allowing lateral movement as the finger passes between them and are connected by springs to emulate inter-object resistance. Although the objects can rotate around their vertical axes, this rotation is restricted by a load cell that measures the tangential disturbance force by detecting the reaction force counteracting the moment caused by the gripper finger's parallel force on the object's surface.

the position of the target object while allowing some mobility, and second ensured mutual contact between the objects. The spring values were chosen based on practical experience.

The initial experiments were performed using the gripper finger equipped with the eversion sleeve, followed by a comparative test in which the finger was replaced by a latex-coated dummy finger to assess the friction-reducing effect of the eversion mechanism. The dummy finger consisted of two circular flexures (32 mm radius) joined at their extremities by tip elements, and coated with the same latex material as the eversion sleeve, affixed using double-sided tape. To replicate the contact pressure from the eversion-finger experiment—despite the absence of the rubber spacer elements in the dummy finger—the spring between the two object modules was stretched an additional 4 mm.

To limit the number of measurements, only 60 mm dummy objects were used in these tests to assess the tangential disturbance forces.

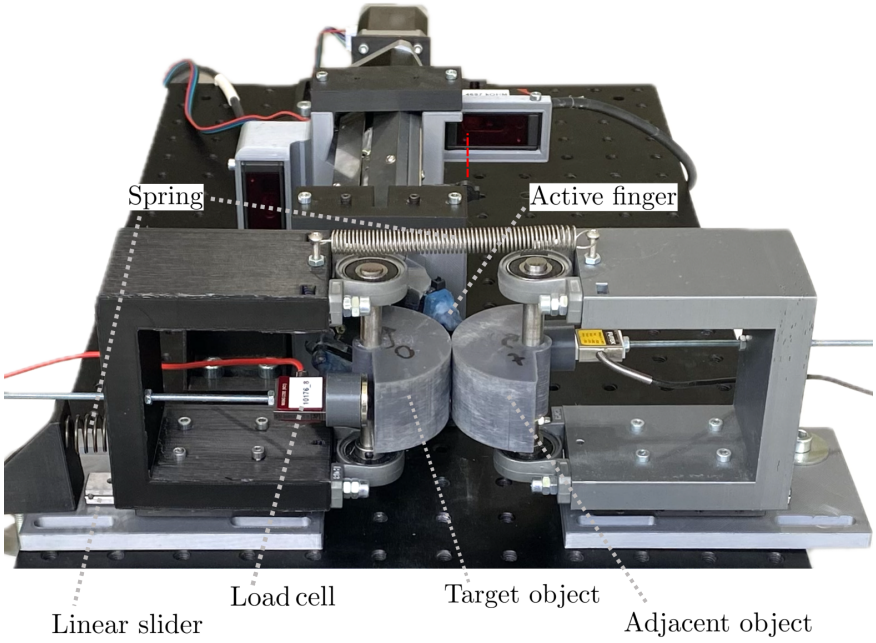


Figure 4.13: Actual setup for experimental test 3, measuring tangential disturbance forces: This photo shows the semi-circular dummy objects mounted on linear sliders, load cells positioned to measure reaction forces, springs providing inter-object resistance, and the active gripper finger. The arrangement and components correspond to the configuration illustrated in the setup of experimental test 3 (see Fig. 4.12)

4.3.3 Pull-out force

To measure the pull-out force required to remove objects from the gripper [58], the setup of experimental test 1 (Fig. 4.10) was used with a modified operating procedure.

First, the object was securely grasped using full-finger enclosure. The measurement started when the gripper, driven by Actuator 2, began moving away from the object, causing the fingers to gradually open as the object was pulled from the grasp—note that the fingers opened due to the object being dislodged, not because of active retraction. This process continued until the object fully escaped the grasp. During this motion, the gripper's position was tracked using Laser 2, while the load cell recorded the force resisting object removal. The peak force measured during this process was taken as the pull-out force, representing the gripper's maximum holding capability.

Two separate tests were conducted to evaluate the gripper's holding performance—one with respect to object size, the other with respect to enclosing angle. In the first test, pull-out forces were measured for spherical dummy objects with diameters of 50 mm, 60 mm, and 75 mm, using a standardized finger length of 100 mm to allow comparison across sizes. For the 50 mm and 60 mm objects, this length enabled near-complete enclosure, whereas the 75 mm object remained only partially enclosed.

In the second test, the relationship between enclosing angle and holding force was examined using the 60 mm object in a partially enclosed configuration. Here, the fingers were extended to enclose the object at angles of 150°, 120°, 90°, and 60°, after which the pull-out force was measured for each case.

4.4 Results and implications

4.4.1 Grasp success rate for confined-space grasping

Fig. 4.14 summarizes the results of the two grasp success rate tests conducted with the gripper mounted on the robotic arm. In test variant (a), the *pos gripper with full enclosure*, a success rate of 92% was achieved, whereas test variant (b), *pos-rot gripper with partial enclosure*, resulted in a 100% success rate for the pick-and-place actions. To provide context for these outcomes, we first describe and analyze the gripper's observed operational behavior—both to evaluate the effectiveness of the design and to clarify the aspects responsible for the high success rates and the performance differences between the two test conditions.

During all tests, the gripper consistently performed its intended function: grasping, holding, and releasing the object. The fingers accurately followed the contours of the tomatoes—regardless of their mass, size, or orientation—without excessive squeezing, while successfully navigating surrounding objects. No misgrasps, drops, or mechanical failures were observed, confirming the reliability of the system. The gripper's performance in the robotic experiments is illustrated in the supplementary video (Appendix A.2).

The eversion sleeve also functioned as intended, exhibiting smooth and synchronized motion with the underlying flexure. During flexure advancement, the sleeve unfolded cleanly over the fingertip and along the outer backbone surfaces without wrinkling. Upon retraction, it was smoothly drawn back into the backbone channel, consistently following the motion of the flexure. Throughout this process, no excessive internal forces were observed between finger components, indicating low friction between the sleeve and the backbone.

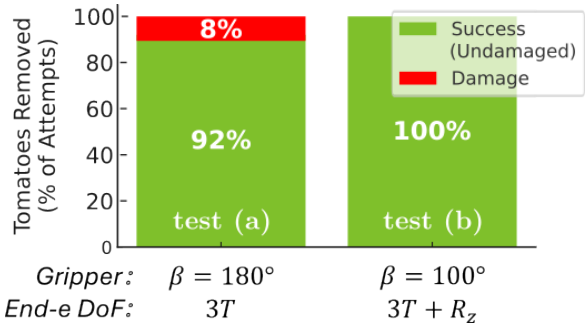


Figure 4.14: Grasp performance in confined-space scenarios for variants (a) and (b). Variant (a), the *pos gripper with full enclosure*, completed 100% of pick-and-place tasks but caused damage in 8% of attempts, yielding 92% undamaged grasps. Variant (b), the *pos-rot gripper with partial enclosure*, completed 100% of tasks with no damage observed, yielding a 100% success rate.

Importantly, the sleeve effectively reduced relative motion between the finger's outer surface and its environment, resulting in no damage due to sliding contact in either test. Even when the sharp outer edges of the finger's backbone came into contact with and pressed against surrounding tomatoes while sliding over them, no damage occurred to either the tomatoes or the finger. This is a noteworthy result, as sharp flexure edges typically pose a risk of causing damage due to their knife-like cutting behavior. However, this was effectively prevented by the well-functioning eversion mechanism, demonstrating the value of incorporating eversion sleeves into the design.

Together, the high success rates and the observed mechanical behavior demonstrate the effectiveness of advancing, precurved compliant fingers with integrated eversion sleeves for handling food items in confined, densely packed environments.

Nevertheless, a closer comparison of both tests reveals that the success rate in variant (a), the *pos gripper with full enclosure*, was slightly lower—92% compared to 100%—due to observable damage in 8% of the attempts. While all pick-and-place actions were successfully completed, some resulted in damage to surrounding tomatoes. This was not caused by grip failure or finger misalignment, but by the displacement required when the thickest part of the fingertip had to pass directly through narrow contact points. In many cases, this caused no issues, as surrounding tomatoes could shift aside. However, damage occurred when two conditions coincided: (1) the fingertip passed through tight contact points, and (2) the adjacent tomatoes were immobile due to dense packing and mechanical constraint. In such cases—especially when picking the first tomato from a new layer or from the bottom of the crate—the fingers had to press into the adjacent tomatoes to forcibly create clearance through deformation, often exceeding their structural limits and causing skin tearing. These scenarios typically occurred when the target was located in a "pocket": a small, enclosed space where the object's top surface lies at or below the level of surrounding tomatoes, further limiting accessibility.

Conversely, variant (b), the *pos-rot gripper with partial enclosure* test, effectively mitigated these challenges by reorienting the fingers above the voids between adjacent objects to make use of the available clearance and by only partially enclosing the target. This

reorientation reduced the additional space required for the fingertips to pass, as some clearance was already present, thereby keeping deformation below harmful limits. Additionally, the partial enclosure diminished the need for clearance beneath the target object, further reducing disturbances. As a result, a 100% grasp success rate was achieved without any damage.

In general, the results highlight the efficiency and reliability of the gripper in securely grasping, lifting, and placing objects in densely packed environments. The tests demonstrate high grasp success rates of 92% and 100%, showing that the gripper can operate without causing damage—even under challenging conditions. While the success rate is influenced by the operational approach, the gripper's limitations in handling immobile objects can be mitigated by reorienting the fingers or, in future designs, by reducing fingertip thickness. At the same time, because the approach angle β and the grasping posture (with or without explicitly aiming for the void) were varied simultaneously, the individual contribution of each factor was not quantified; future experiments that decouple these parameters would help to more clearly establish their respective influence on grasp performance in confined environments.

4.4.2 Disturbance forces

Normal disturbance force

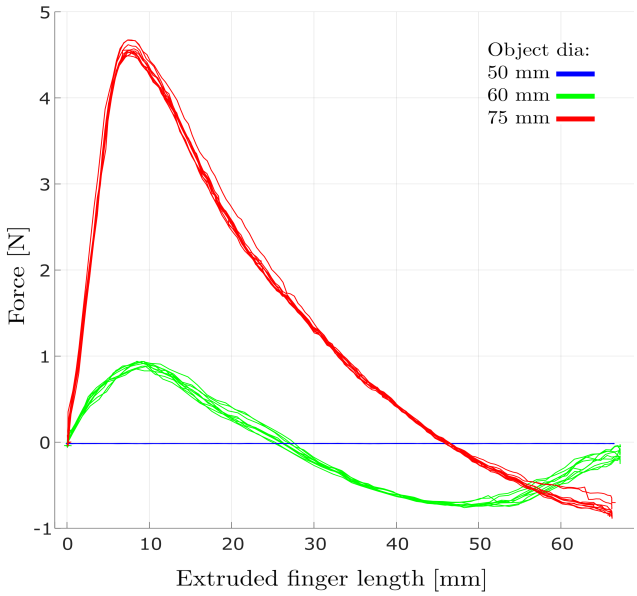
Fig. 4.15a presents the results of experimental test 1, showing the normal disturbance force in the longitudinal direction of the gripper as a function of finger extrusion length. Data are shown for spherical objects of 50 mm, 60 mm, and 75 mm in diameter, represented by blue, green, and red lines, respectively, each based on ten consistent measurements.

As the fingers extend, the force initially increases, then decreases, and eventually turns negative for the 60 mm and 75 mm objects. This indicates that the objects are first pushed outward and then pulled inward against the gripper. The larger object experiences higher forces due to greater finger bending. The peak force occurs early in the process when the flexures are relatively short and stiff. The green line crosses zero earlier than the red one because the 60 mm object is more enclosed at the same finger extension length.

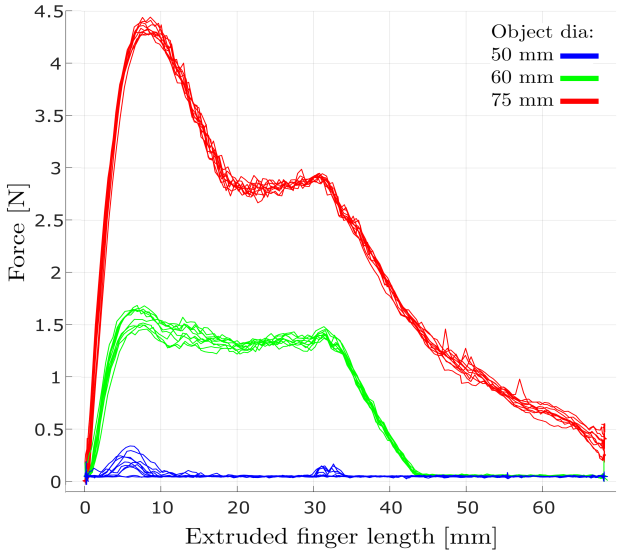
For the 50 mm object, the force is negligible, confirming that the fingers did not make contact—consistent with experimental observations. A similar outcome was expected for the 60 mm object; however, the finite thickness of the fingertip, which was not accounted for in the flexure design, introduced slight outward bending and the resulting force.

Fig. 4.15b shows the results of experimental test 2, depicting the lateral normal disturbance force plotted against finger extension for spherical objects of 50 mm, 60 mm, and 75 mm in diameter, again represented by blue, green, and red lines. As with the longitudinal component, the force increases with finger extension, peaks early, and is greater for larger objects, while remaining near zero for the 50 mm object. Unlike the previous test, the force remains positive throughout, indicating continuous squeezing by the finger. It gradually decreases toward zero as the fingertip moves past the widest part of the object.

In conclusion, the measured peak values for both force components on the average-sized object (60 mm) occurred at a finger extension of approximately 7–9 mm, with peak forces of 0.9 N in the longitudinal direction and 1.5 N laterally. This results in a combined normal disturbance force of approximately 1.7 N applied to the object during grasping—well within the non-damaging range for a tomato, as confirmed by the grasp success rate test.



(a) Normal disturbance force, the longitudinal component (test 1).



(b) Normal disturbance force, the lateral component (test 2)

Figure 4.15: Results of experimental normal disturbance-force tests during grasping of spherical objects with diameters of 50 mm, 60 mm, and 75 mm during finger extension: (a) Its longitudinal component first rises, then falls, and eventually becomes negative (test 1). (b) Its lateral component first increases, then stabilizes and gradually decreases towards zero (test 2). The forces on the smallest objects remain negligible for both tests.

Tangential disturbance force

Fig. 4.16 shows the tangential disturbance force along the surface of adjacent objects as measured in experimental test 3, plotted against the length of the extruded finger. The graph contains four clusters of ten closely grouped lines each, representing individual measurements, with thicker lines indicating the average for each group. The two lower clusters correspond to tests using the gripper finger, while the two upper clusters represent tests using the latex-coated dummy finger. Red and blue lines indicate forces on the target and adjacent objects, respectively; slight color gradients are used to distinguish the individual measurements within each group.

Two distinct phases can be identified in the force profiles for both finger types. The first phase corresponds to the initial part of the grasping process—up to approximately 30–35 mm of finger extension—during which contact primarily occurs between the fingertip and the object, reaching about half enclosure. The second phase begins once the fingertip has passed the point of contact, i.e., from half to full enclosure, where contact primarily involves the backbone of the finger and the object.

The forces measured for the finger equipped with an eversion sleeve were nearly an order of magnitude lower than those recorded for the latex-coated dummy finger. In the first phase, the eversion-sleeved finger generated approximately 1.5 N of tangential force on both the target and the adjacent object, with no measurable force observed in the second phase (as detailed in Fig. 4.17). In contrast, the latex-coated finger produced forces of 9.1 N and 8.3 N in the first phase, and 7.2 N and 2.6 N in the second phase, on the target and adjacent object respectively.

In addition, the force profile of the eversion-sleeved finger was notably smoother. It even showed negative force values on the adjacent object during the first phase, suggesting a tendency for the object to rotate away from the direction of finger motion.

The results demonstrate that the eversion sleeve effectively reduces tangential forces by 84% and 82% during fingertip contact and up to 100% when the backbone contacts the target and adjacent object, respectively. These percentage reductions were calculated per phase by subtracting the peak value recorded for the gripper finger from that of the latex-coated dummy finger, and dividing this by the dummy finger's peak value.

The data suggest that the eversion sleeve performs most effectively around the backbone, where it is fully seated and stable. At the fingertip, where the sleeve is actively unfolding and adapting to the object's contour, its friction-reducing performance is less consistent. This variation is likely due to relative motion between the unfolding sleeve and its surroundings, as the sleeve undergoes significant elongation—up to 50%—before contracting during eversion.

Although the measurements indicate complete force reduction (100%) in the second phase, this should be interpreted with caution. The measurement setup, which used a ball transfer unit, may not have detected small tensile forces. Measurement lines that flatten near zero at approximately 40 mm of finger extension suggest that some residual force could have remained undetected. However, minimal disk rotation and continuous contact with the sensor were observed during the tests, suggesting that any unmeasured forces were very small—particularly for the target object (red line), which remained flat around zero. This supports the conclusion that the eversion mechanism is most effective once the sleeve is fully unfolded and stabilized along the backbone.

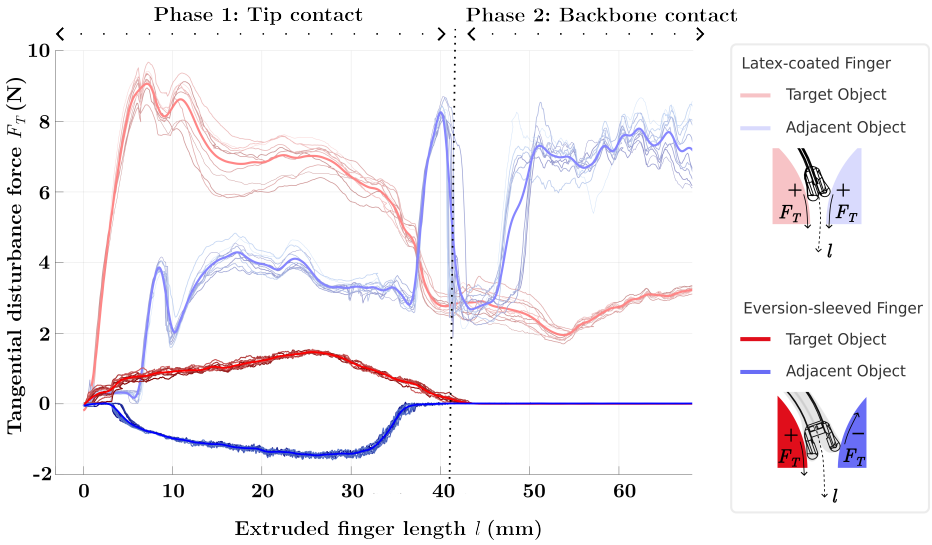


Figure 4.16: Measured tangential disturbance force F_T (test 3) exerted along the surfaces of a target object (red) and an adjacent object (blue) by an advancing finger of length l, comparing eversion-sleeved and latex-coated designs. The lower and upper pairs of lines correspond to the eversion-sleeved and latex-coated fingers, respectively. Thicker lines indicate the average values of ten individual measurements shown as thinner lines.

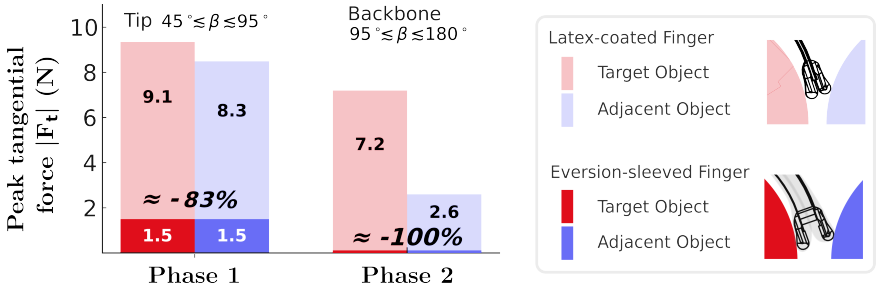


Figure 4.17: Absolute tangential disturbance force peaks measured during Phase 1 (tip-contact, $45^\circ \leq \beta \leq 95^\circ$) and Phase 2 (flexure-contact, $95^\circ \leq \beta \leq 180^\circ$) for the eversion-sleeved finger and the latex-coated dummy finger during confined-space navigation. The eversion principle reduces disturbance-force peaks by approximately 83% in Phase 1 and nearly eliminates them in Phase 2.

Beyond reducing friction, the eversion sleeve also improves finger maneuverability in tight environments. This is evident from the smoother force profiles, which reflect more stable and controlled object interactions. In contrast, the latex-coated dummy finger showed sudden spikes in resistance—indicative of stick-slip behavior—due to frictional buildup and release at localized contact points. Additionally, the measured force on the adjacent object was directed opposite to the finger's motion, suggesting that the eversion sleeve gently pushed the object away from the path of motion rather than pressing into it. This effect supports smoother passage and reduces the likelihood of obstruction or wedging.

Future research could focus on quantifying the reduction in surface stress achieved by the eversion sleeve. While this study measured total tangential forces, surface stress is more directly linked to the potential for object damage, and it is likely that the eversion sleeve, by distributing contact forces more evenly, offers additional benefits over designs with localized contact such as the dummy finger. For practical gripper design, a comparison with a bare steel flexure finger would be more relevant, but in this work we used a latex-coated dummy finger to keep the contact material consistent and isolate the effectiveness of the eversion mechanism's working principle.

4.4.3 Pull-out force

The results of the pull-out tests for different object diameters, using a standardized finger length of 100 mm, are summarized in Fig. 4.18. The pull-out force was found to vary with object size, with the 60 mm object requiring the highest force (10.0 N), followed by the 50 mm (8.5 N) and 75 mm (6.8 N) objects. The mass of a comparable tomato is shown for context.

The pull-out force test results for varying enclosing angles around a 60 mm diameter object are presented in Fig. 4.19. As expected, the pull-out force decreased as the enclosing angle was reduced. At an angle of 150°, the maximum force recorded was 10.0 N. This dropped to 0.7 N at 70°, and became negligible (0.0 N) at 50°.

The results of the pull-out test suggest that the gripper can easily hold tomatoes of various sizes. The force required to hold small, medium, and large objects was 0.82 N, 1.29 N, and 1.80 N, respectively, while the measured holding forces were 8.5 N, 10.0 N, and 6.8 N for the complete finger enclosure, approximately 4 to 10 times the mass of these tomatoes. Additionally, the results show that even with partial enclosure, such as at 90°, the gripper is still capable of reliably holding average-sized objects.

However, caution is warranted when generalizing these results to actual tomatoes. Friction is one of four key aspects influencing the gripper's holding capability, and the frictional characteristics of the test setup may differ from those of real produce. The four grasping aspects identified in the experiments are discussed below to clarify the trends observed in the data and to explain the differences between test outcomes:

(1) In a form-closed grip, releasing an object requires expanding the space between the fingertips to match the object diameter, allowing it to escape the form fit. This expansion necessitates bending the flexures outward, with the force at the fingertips acting normal to the object's surface at the point of contact. The reaction force acting in the opposite direction on the object is in equilibrium with the pull-out force. The component of this reaction force aligned with the gripper's motion direction secures the object in form-closed

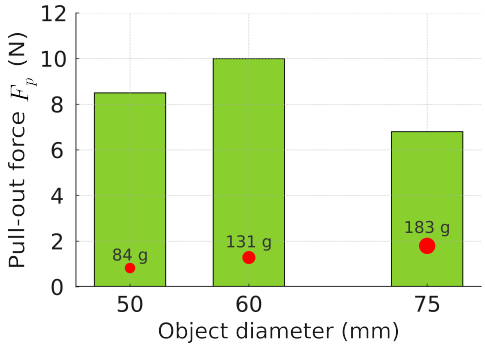


Figure 4.18: Pull-out force for different object diameters with a standardized finger length of 100 mm. Forces measured: 10.0 N (60 mm), 8.5 N (50 mm), and 6.8 N (75 mm). The mass of a comparable tomato is shown for context.

grasps. Smaller objects or smaller enclosing angles require less force to release, as the fingers need to open less. Thus, a 50 mm object requires less force to release than a 60 mm object, and smaller enclosing angles likewise reduce the required release force.

(2) As the enclosing angle decreases, the normal contact force becomes increasingly misaligned with the gripper's motion direction. Consequently, the effective holding force diminishes as more of the contact force acts laterally rather than in the direction resisting pull-out. This explains why the 75 mm object, despite its size, required less force to release than the 60 mm object, and why the pull-out force systematically decreased with smaller enclosing angles.

(3) Although a smaller enclosing angle shortens the flexure and increases its stiffness—which could theoretically raise the pull-out force—the effects described in points **(1)** and **(2)** above appear to be dominant. This is evidenced by the decreasing trend in pull-out force with decreasing enclosure angle, regardless of increased stiffness.

(4) The nonzero holding forces measured at small enclosing angles (e.g., 90° and 70°) indicate that friction also contributes to the gripper's holding performance. In a purely form-closed system with minimal friction, the holding force would approach zero. Therefore, friction between the finger and the object must have played a role in the observed results.

This also implies that the measured values cannot be directly generalized to other objects. The friction coefficient between the finger and real food items may vary from that of the dummy objects used in the tests. For tomatoes specifically, a higher surface friction was observed when sliding the finger over them. This suggests the measured pull-out forces are conservative, with actual holding forces likely higher—making the reported results a safe lower bound.

Although the combined influence of these four factors **(1)-(4)** is evident, quantifying their individual contributions to the holding force would require targeted simulations or dedicated experiments, which are recommended for future work.

Interestingly, despite the complexity of the contact mechanics, the pull-out force showed a strong linear relationship with the enclosing angle in our experiment. Using MATLAB's polyfit function, a linear fit of the form $y = 0.1x - 5.7$ was obtained ($R^2 = 0.98$), with y

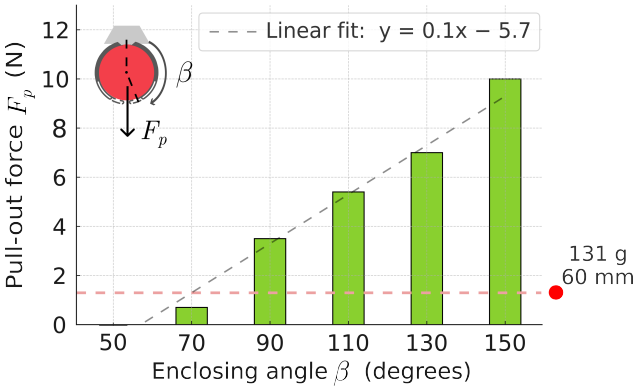


Figure 4.19: Pull-out force measurements for a 60 mm diameter object at varying enclosing angles β. Forces measured: 10.0 N (150°), 7.0 N (130°), 5.4 N (110°), 3.5 N (90°), 0.7 N (70°), and 0.0 N (50°). The mass of a comparable 60 mm tomato is included for context. A linear fit illustrates the approximate relation between β and pull-out force.

representing the pull-out force in newtons and x the enclosing angle in degrees. This suggests a pragmatic rule of thumb for engineers: within the tested range, the enclosing angle shows a simple linear relationship with the holding force, making it a useful first-order estimate during design decisions and a promising direction for future investigation.

4.5 Discussion

4.5.1 Reflection on concept and methods

This study introduced a novel approach to grasping in confined environments by reorienting the finger motion from a traditional normal (perpendicular) approach to a tangential trajectory along the object surface. This proved highly effective in practice: in the *pos-rot gripper with partial enclosure* test (b), the gripper successfully emptied a crate of 58 tomatoes five times without causing any damage. Even in the *pos gripper with full enclosure* test (a), all tomatoes were removed, though minor damage occurred in a few cases.

To prevent such damage, the design specifically aimed to minimize environmental disturbances—both in terms of applied forces and spatial displacements during finger insertion. Technical tests confirmed that interaction forces were kept low. However, practical tests revealed that excessive displacement when navigating tightly packed items can still lead to damage. This underscores the importance of reducing not only forces but also the physical space intruded upon during grasping, validating the chosen focus and approach for reliable operation in confined environments. These insights offer valuable design handles for maneuvering in other densely packed settings where minimal intrusion is equally critical.

These results highlight the critical role of real-world validation. While technical measurements offer controlled insights into specific parameters, practical testing exposes broader interactions that may only become apparent in cluttered, variable environments.

In most existing studies, gripper evaluation tends to focus on one of two perspectives: either technical testing on isolated prototypes to model or measure performance [155]—or system-level demonstrations in which the emphasis lies on the robot as a whole rather than on the gripper itself. However, the combination of both approaches has proven essential—not only for refining the gripper design, but also for thoroughly evaluating its suitability for real-world use. A gripper that performs well under both controlled and practical conditions is far more likely to be successfully integrated into robotic systems later on, with fewer adaptations required.

Since other aspects of the finger design, such as squeezing forces and tangential disturbance forces, were measured to be low and did not appear to limit grasp success, we encourage future research to further minimize the environmental disturbances by reducing the induced displacement, enhancing the gripper's versatility. For instance, by making the fingers thinner, it may be possible to achieve a 100% grasp success rate when operated as in the *pos gripper with full enclosure* test (a), as this would reduce the required clearance during grasping. While tomatoes are already delicate, this refinement could enable the gripper to handle even more fragile or softer products, or objects with less clearance between them, expanding its range of applications.

4.5.2 Versatility, gentle handling through flexural caging

In addition to its success in confined environments, the gripper exhibits grasping characteristics that are beneficial when focusing on the target object. These features enhance its applicability, offering versatility, flexibility, and reliable, gentle handling of objects.

The gripper's flexures demonstrated size adaptability in both technical and practical tests: fingers designed for a 60 mm radius successfully grasped spherical objects ranging from 50 mm to 75 mm in diameter—achieved solely through material bending, without requiring complex shape-adaptive mechanisms, actuators, or force control systems.

The resulting grasp qualifies as a caging grasp: the fingers simply enclose the object within the cavity defined by their shape, securing it through structural stiffness rather than active squeezing or actuation[156]. Unlike other form-closed designs, such as underactuated or compliant fingers [63, 90], which actively apply forces to adapt and hold the object, this approach minimizes grasping forces by design, applying only what is needed to counteract external accelerations. This was confirmed in experimental tests 1 and 2 with a 60 mm object, where low normal disturbance forces measured at the end of the grasp indicated minimal squeezing during grasping, making it a successful caging grasp. The observed forces primarily originated from fingertip thickness rather than from the need to squeeze the object during grasping. The potential benefits of low squeezing forces and, consequently, reduced surface pressure include a lower risk of damaging the object or unintentionally displacing it during grasping, more predictable grasping behavior for soft objects as they retain their original shape with minimal deformation, and reduced energy consumption. These advantages make this approach particularly valuable for handling fragile or easily deformable items. By contrast, most other form-closed designs—including underactuated rigid linkages [63], soft robotics [27], and some compliant systems [95]—require active deformation around the object. As the object resists this motion, the fingers must apply continuous squeezing force, resulting in higher contact pressure and an increased risk of damage compared to the caging approach.

4.5.3 Durability, hygiene, and holding force considerations

In addition to the quantified performance metrics, valuable observational insights were gained regarding critical factors for agri-food grippers, including lifespan, consistency, robustness, and hygiene. After a month of intensive testing, the gripper demonstrated durability by completing approximately 500 operations without plastic deformation or wear. However, for industrial acceptance, dedicated life-span tests are recommended, as required cycle counts are at least three orders of magnitude higher. This may necessitate some redesign and the manufacturing of specific components to industrial standards rather than the manually produced parts used here.

The eversion sleeve effectively protected the internal components from environmental dirt and debris while also preventing contamination of the surroundings by acting as a washable barrier. During operation, it maintained proper alignment without becoming trapped between flexure components, achieved by enclosing the exterior with rubber adhered to the inner flexure rather than the outer one. Friction occurred mainly between the flexure and the housing, with only minimal friction between the eversion sleeve and the flexure. This low friction reduces wear and helps the flexure maintain its intended shape during bending. However, further research into its hygienic performance is recommended, as the sleeve material is critical for both its life span and the prevention of bacterial contamination. The continuous barrier around the finger is promising in this respect, but a minor redesign is needed to also close the open end of the inner portion of the sleeve. For cleaning, we propose a cycle in which the finger is driven beyond its current stroke so that the entire inner portion everts outward and stretches over the fingertip, exposing all surfaces that may come into contact with the environment and thereby simplifying cleaning and sanitation.

Another important step toward industrial acceptance is increasing the holding-force capability to withstand higher accelerations and handle heavier objects. For slower operations, or when the gripper is oriented away from vertical—as in harvesting—the current performance may be sufficient, as indicated by our robotic tests under moderate accelerations, but high-speed bin-picking requires holding forces at least an order of magnitude higher than those reported here. Holding force can be increased by adding more fingers or by increasing their lateral bending stiffness, for instance by widening or thickening the flexures, which under linear elastic beam theory scales roughly linearly with width and cubically with thickness, or by embedding additional wires longitudinally in the sleeve for tendon-based stiffening that resists opening of the cage. Both strategies come at the cost of reduced size adaptability, unless the tendon wires are actively tensioned or locked after grasping, as demonstrated in other gripper designs [157].

4.5.4 Mechanical (flexure) driven eversion mechanism

Beyond the immediate scope of this study, we present the first mechanically driven eversion mechanism actuated not by internal pressure—as is common in most existing designs—but by advancing an internal pre-curved flexure from its base, which presses against the inner surface of an everting sleeve. While some prior works include internal elements within eversion-based systems (e.g., tendons or sensors) for steering or sensing [158–160], these do not drive the eversion itself. A somewhat related design by Takahashi et al. [161] combines eversion with an internal rigid linkage to improve payload and bending, but their

system remains pressure-driven and uses rigid components. In contrast, our system is fully mechanically actuated via a curved flexure acting as an internal skeleton.

To our knowledge, no prior work has demonstrated a purely mechanically actuated eversion mechanism [111–115, 161]. We thus propose a new subcategory—mechanically driven eversion mechanisms—defined as systems where a thin, tip-extending everting sheet (e.g., sleeve or belt) is both actuated and structurally supported by an internal mechanical element. Our implementation couples a pre-curved flexure to a latex sleeve, synchronizing motion via a cable-pulley system at a 1:2 ratio. Alternative configurations, such as belts or serial linkages replacing the sleeve and flexure, are conceivable within this category.

Demonstrated as a gripper finger moving tangentially along an object's surface, the mechanism follows a circular trajectory without active steering by guiding the flexure through a channel. The latex's stretchability compensates for the circumferential length mismatch caused by the C-shaped curvature—a challenge that is uniquely posed by curved eversion systems. While this study focused on a circular trajectory applied in a gripper design, the concept can be adapted to other paths and applications.

This mechanically driven approach to eversion mechanisms opens new possibilities in fields such as minimally invasive surgery and search-and-rescue robotics, where predictable longitudinal path-following of mechanisms, instruments, or devices with minimal sliding forces on the environment, combined with enhanced payload capacity through embedded structural guidance, is highly valuable.

4.6 Conclusion

In this article, we introduced the first mechanically driven eversion mechanism by presenting the Sleeved Concentric-Flexure Eversion Mechanism (SCF-EM): an eversion sleeve actuated by two concentrically placed pre-curved flexures located between its inner and outer sides, synchronized via a cable-pulley system, enabling passive following of a predefined circular trajectory. The flexibility of the flexures allows deviations from the planned path during environmental interactions, while the eversion sleeve unfolds from the interior to cover the outer sides, significantly reducing sliding forces against the environment during propagation by mitigating relative motion.

To demonstrate its potential, we proposed a conceptual gripper solution for handling objects in dense environments using flexure-driven eversion mechanisms as fingers, designed to minimize environmental disturbance. Unlike conventional grippers that approach objects perpendicularly—often obstructed by adjacent items in confined spaces—our design advances the fingers tangentially along the object's surface, simultaneously reducing sliding forces. We developed, detailed, and manufactured the SCF-EM gripper's mechanical design and validated its performance through extensive testing.

Practical tests with the gripper mounted on a robotic setup demonstrated that the SCF-EM gripper enabled grasping in confined spaces by successfully emptying a crate of 58 tomatoes individually, achieving a 100% grasp success rate without causing damage to the objects, environment, or the gripper itself.

Complementary technical experimental setups were built to quantify performance metrics such as the gripper's holding force and the disturbance forces induced on the environment. Results showed a maximum holding force of 10.0 N for an average-sized

tomato—approximately eight times its weight—while disturbance forces remained below harmful thresholds. Specifically, the maximum normal disturbance force measured on the object's surface during grasping was 1.7 N, and the maximum tangential disturbance force was 1.5 N. Additionally, the effectiveness of the eversion sleeve in significantly reducing friction forces with contacting objects was demonstrated, with tangential disturbance forces 83–100% lower than those of a latex-coated dummy finger without the sleeve.

These results collectively demonstrate the SCF-EM gripper's capability to securely handle delicate objects in confined spaces by minimizing environmental disturbance, underscoring the promise of mechanically driven eversion mechanisms for practical applications in agri-food and beyond.

5

Discussion

The primary aim of this thesis was to develop and evaluate mechanical grippers with fingers designed as flexure-driven eversion mechanisms, addressing the challenge of limited clearance around objects. This was achieved in four chapters by identifying the key problem, proposing a grasping strategy, assessing the applicability of base-driven flexures for our concept through a kinetostatic analysis, and presenting two iterative finger designs alongside their performance evaluation based on established metrics.

This chapter summarizes the key contributions of this work, critically reviews the research steps, compares the outcomes of both designs, and discusses the broader implications and future research directions for the field of gripper technology. In addition, we detail the mechanical characteristics of our core technology -specifically, an individual base-driven interacting flexure and the impact of its combination with an eversion mechanism - both of which provide valuable avenues for exploration by designers in a variety of applications in future studies.

5.1 Overview of contributions and sub-goal achievements

Chapter 1 introduced the challenging characteristics of food objects that make them difficult to handle securely and delicately and presented an overview, highlighting current gripper technologies. More importantly, we address the key problem of limited space around target objects in dense environments, which often hinders existing grippers, and robotic systems more broadly, from functioning effectively in the agri-food sector.

To overcome this key issue, we proposed a novel grasping approach to set form-closed grasps and introduced a new finger concept. The core principle of our solution involves a mechanical gripper whose fingers advance tangentially along the surface of an object to establish and release encompassing grasps, a novel approach to current gripper technology. We designed the fingers as mechanically driven eversion mechanisms, our key technology, enabling interactive navigation through dense environments with minimal disturbance through a purely mechanical solution.

Chapter 2 presented the first development step, assessing the applicability of base-driven flexures in our design by investigating their navigation capabilities alongside multiple objects through interaction. To this end, we used a case study and modeled the kinematics and kinetics of a straight base-driven flexure navigating two sequential obstacles through contact using a Pseudo Rigid Body (PRB) model-based approach, analyzing its trajectories and interaction forces.

To enable this analysis, we extended existing PRB modeling techniques with two aspects: firstly, to cover event-based scenarios, and secondly, to enable the analysis of flexures that endure multiple loads along their length at various unknown locations. Events indicate critical junctures that require an immediate change to another PRB model, such as adding or removing an external load, which occurs, for instance, when the flexure encounters a new contact. Moreover, the flexure experienced multiple contact points when passing between the objects, resulting in individual forces at different points along its span. This detailed analysis was presented within a structured framework, where different events were first identified, followed by three successive steps for each analysis.

The results demonstrate that base-driven flexures are well-suited for propagating and navigating through complex, dense environments in a predefined and predictable manner by solely tuning design parameters and leveraging object interactions. In our experiments, the base-driven flexure successfully passed between two sequential obstacles, with its trajectory and interaction forces accurately predicted by our model, confirming the suitability of the flexures to maneuver our finger design through dense surroundings. Although straight flexures were initially used in modeling due to their straightforward design and ease of fabrication, we transitioned to curved flexures for our designs to enhance the performance of the fingers by defining a natural trajectory around the object's surface and obtaining an encompassing cage grasp.

Chapter 3 introduced a preliminary planar finger design as the first proof-of-principle of our proposed concept: the Dual-Belt Curved-Flexure Eversion Mechanism (DBCF-EM) finger. This design featured a curved flexure combined with two belts guided through rollers, representing a planar embodiment of flexure-driven eversion mechanisms. A gripper prototype with a tripod finger arrangement was manufactured and tested according to defined performance metrics in both practical and technical setups. The results showed that transitioning to curved flexures met the expectations of grasping, as the fingers

closely followed the contours of the target objects and were able to pass alongside adjacent obstacles. Moreover, combining flexure with an eversion mechanism significantly reduced the friction forces with the environment. When integrated into a robotic setup, the gripper successfully grasped individual tomatoes from a pile, completing all gripper-related tasks. However, the results also highlighted areas for refinement, as occasional object damage was observed due to sharp edges of the fingers, lowering grasp success rates. Furthermore, the open nature of the design presented limitations in terms of hygiene and durability.

Chapter 4 introduced an advanced finger design - the Sleeved Concentric-Flexures Eversion Mechanism (SCF-EM) finger - featuring a backbone comprising two concentrically placed curved flexures with different radii, fully enclosed by a stretchable eversion sleeve, embodying a spatial variant of flexure-driven eversion mechanisms. With these enhanced fingers, a similarly arranged gripper prototype was produced and tested across both practical and technical setups. Building on progressive insights, this testing and evaluation process incorporated refinements in the definition and terminology of performance metrics for grasping in confined spaces, along with further advancements in the experimental setups compared to those presented in Chapter 3.

Testing achieved a 100% success rate in grasping tomatoes from a pile, fulfilling all tasks, but now without causing damage to the target objects or their surroundings. This damage prevention was largely attributed to the removal of guiding rollers, which previously introduced sharp edges at risk of cutting objects. In addition, the eversion sleeve provided complete circumferential coverage, shielding the remaining edges of the backbone, and eliminating any relative motion between the finger and the environment.

The integration of a three-dimensional design space enhanced multifunctionality, reduced component count, and provided protection against contaminants, leading to improved durability and hygiene compliance. These advancements were achieved while maintaining the intended mechanical function of the system and strengthening its holding capabilities.

5.2 Positioning DBCF- and SCF-EM gripper performance

As discussed in Chapter 4, numerous papers report well-established gripper performance metrics, such as pull-out force, contact forces, and contact locations between the fingers and the object [27, 63, 95]. These studies focus on underactuated, compliant, and soft robotic fingers, which conform to an object's shape through deformation, inherently generating squeezing forces to secure the object and requiring continuous actuation.

In contrast, our design relies on caging grasps, which passively hold the object within the structure, eliminating the need for squeezing forces [144, 145, 153, 154]. Both pull-out force and normal disturbance forces (squeezing forces) were experimentally measured for our designs and briefly compared with SOTA grippers at the beginning of this section. Subsequently, we will compare the measured results of DBCF-EM and SCF-EM fingers, particularly focusing on our most distinctive performance metric—minimizing disturbance forces on the environment while grasping—since no comparable grippers exist for direct evaluation of this metric.

5.2.1 Relating to the state-of-the-art in gripper designs

Experiments confirmed that pull-out and squeezing forces were not limiting factors in our gripper designs, as its successfully lifted tomatoes without causing damage. More importantly, compared to SOTA grippers, pull-out force can be easily scaled by adjusting flexure thickness, as cage stiffness primarily depends on flexure stiffness, without adding significant finger thickness or proportionally increasing squeezing forces.

Scaling the pull-out force does not significantly change the overall finger thickness, since flexures contribute only 3–5% of total finger thickness, while caging stiffness scales roughly with the third power, according to linear beam theory (pull-out force modeling will be discussed later in this chapter). Moreover, unlike SOTA grippers that rely on squeezing forces for object retention—requiring proportional force scaling—our design does not. Experimental results confirmed that normal disturbance forces remain minimal, although still present. Minor disturbances observed during testing can be mitigated through improved fingertip designs and flexure manufacturing.

Therefore, a direct comparison with pull-out and squeezing force values in the literature is of limited relevance, as our gripper can easily scale pull-out force without proportionally increasing squeezing forces. This is a key advantage over SOTA designs, as it allows force adjustment without adding significant finger thickness, increasing the risk of object damage, or reducing grasp stability.

5.2.2 Trend-based comparison between DBCF-/SCF-EM grippers

Comparing the measured results of the DBCF-EM and SCF-EM fingered gripper during experiments reveals notable differences, primarily due to variations in metric definitions and experimental setups. The setups differ in object mobility and force measurement techniques. Chapter 3 primarily relied on linear and torsional spring displacement, while Chapter 4 used load cells and lasers.

The difference between the methods was intended to compare trends rather than direct values, providing insight into the practical performance of the grippers in varying agri-food scenarios, particularly in dense environments, as identified in Fig. 1.3. This distinction helps future designers choose the configurations relevant to their applications.

The setups of Chapter 3 allowed for less constraint object movement, simulating conditions like fruit hanging on a branch, while those of Chapter 4 replicated a more constrained environment, akin to fruit packed in a crate. Direct comparison shows lower net force (0.1 N) and slip force (approx. 0.05 N) of the DBCF-EM design in Chapter 3, versus normal longitudinal disturbance force (0.9 N) and tangential disturbance force (1.4 N) of the SCF-EM design in Chapter 4. This disparity reflects the rigid load cell connection in the setups in Chapter 4 compared to the rail-supported spring-based setup in Chapter 3, rather than indicating performance superiority. Instead, examining trends reveals similar friction reductions (83–100%) and consistently low disturbance forces between setups, affirming the effectiveness of the eversion mechanism in both scenarios.

Success rates also differ due to different damage criteria: Chapter 3 allowed minor object damage, while Chapter 4's criteria were stricter, reducing the effective success rate of the gripper of Chapter 3 to around 90%, however, maintaining a 100% task completion. But, the Chapter 3 setup, being more autonomous, introduced variability through calibration

issues and inconsistent pose planning, which were addressed with a more reproducible and consistent setup in Chapter 4.

For future research, particularly in agri-food applications, a more comprehensive damage assessment is recommended. Our study relied on visual inspection, supported by pre- and post-test photos, to identify visible damage. However, subtler fruit damage, such as bruising, may only become apparent over time, as briefly noted in the chapter presenting the exploratory studies of the banana gripper. Although costly and time-consuming, long-term storage experiments under controlled conditions could provide a more thorough assessment of fruit damage. Storing test tomatoes in conjunction with a reference population manipulated by hand or with an alternative gripper could yield more conclusive information on shelf-life impacts.

Finally, the measured holding force shows a higher value for the SCF-EM gripper (10 N) than the DBCF-EM gripper (3.7 N), amounting to approximately 170%. This difference cannot be explained by flexural stiffness alone. The materials are identical, and the second moment of area for each design differs by only about 13%. As a rough estimate, we apply linear beam theory for straight beams with small deflections. Although this theory does not strictly apply to the curved flexures used in both designs, it serves as a first-order approximation to estimate and compare their relative bending stiffness. Assuming a rectangular cross-section, the second moment of area is given by $I = wt^3/12$. For the SCF-EM finger ($w = 20$ mm, $t = 0.15$ mm), which uses two flexures, this yields $I_{\text{SCF}} \approx 0.01125\ \text{mm}^4$. For the DBCF-EM finger ($w = 15$ mm, $t = 0.20$ mm), consisting of a single flexure, we obtain $I_{\text{DBCF}} = 0.0100\ \text{mm}^4$. Thus, the SCF-EM finger is only about $(I_{\text{SCF}}/I_{\text{DBCF}} - 1) \approx 13\%$ stiffer in bending—far too little to explain the observed 170% difference in holding force.

The difference is more plausibly explained by frictional effects, both external and internal. In the SCF-EM gripper, a latex outer surface contacts a Though2000 object; in the DBCF-EM, TPU contacts PLA — leading to different friction coefficients. Despite talc on the latex, the SCF-EM shows noticeably higher sliding resistance, contributing to increased holding force. Internal friction plays also a role: the SCF-EM's outer flexure rubs against the tight sleeve, the inner flexure presses against the channel wall, and rubber spacers add resistance — all opposing finger opening. In contrast, the DBCF-EM uses elastomer belts over rollers, with only a single sliding interface, resulting in lower internal friction. This shows that internal friction, though often considered a loss, can be beneficially exploited. Combined, these frictional effects likely explain the higher holding force of the SCF-EM gripper, even though both designs operate in the same force range.

5.3 Implications for the gripper field

Zooming out from the core technology to position various components and outcomes of our work within the broader field of gripping, this perspective provides valuable insights for future gripper designers for diverse applications.

5.3.1 Cohesive design process and practical evaluation

Practical real-world testing, though rare in the gripper design literature, is invaluable for uncovering issues that impact gripper and robotic system performance. Most gripper re-

search emphasizes end-effector design tailored to specific individual objects or challenging properties; broader robotics studies often enhance robot capabilities while taking existing grippers for granted and assuming they are sufficient. By integrating realistic testing setups into the design process, designers can gain a fuller understanding of how robots, grippers, objects, and environments interact, revealing complexities that isolated lab tests often miss.

Embedding real-world testing early in the design cycle provides essential insight, enabling the development of more disruptive, adaptable solutions that seamlessly integrate into robotic systems with minimal modifications. A well-integrated end effector ultimately improves the system's overall performance and simplifies the robot's operation because it requires less of it.

In our work, we advanced integration by incorporating environmental factors and performing practical evaluations on a robotic setup. Future steps toward industrial integration include moving toward autonomous systems and realistic environments, such as greenhouses. Not only for gripping applications but in general, we encourage researchers designing devices for complex environments to embrace environmental interactions and prioritize cohesive system integration [162]. Rather than treating robots and grippers as separate sequential units, designing them as a single unified system - with support from the environment, such as for guidance - has great potential.

5.3.2 Mechanical gripper design

In many gripper applications, even without an eversion mechanism, precurved flexures alone offer significant advantages over conventional mechanical fingers, enabling shape-adaptive cage grasps. A cage grasp gently encloses around an object within its structure, creating a physical boundary around it without applying squeezing or compressive forces, relying only on counteracting gravitational force. This method may be beneficial for flexible handling of a wide variety of delicate objects, as it reduces damage risks while making gripper hold and stability inherently independent of many properties of the object, such as surface texture, friction, or structural deformability. Although cage grasping is not a novel concept, this research reinforces its benefits by demonstrating that the integration of curved flexures enhances shape adaptability, allowing for the accommodation of larger or more varied objects through inherent design and bending characteristics.

For sturdier objects that can withstand impact, the added thickness and complexity of eversion mechanisms may be unnecessary, in that case tailored-shaped flexure fingers alone may still prove beneficial. This adaptability makes them widely applicable throughout the food supply chain, offering reliable handling of items such as chicken fillets, regardless of wet or slippery conditions. It is also worth noting that while tangential finger movement is advantageous in dense environments, this is not strictly necessary to achieve a cage grasp; conventional grippers can form a cage grasp by simply closing their fingers toward the object. This straightforward approach may be preferred in certain cases for its simplicity and familiarity. However, as demonstrated in this thesis, in dense environments, tangential movement along the surface of the object is crucial to reliable and successful grasping.

Beyond the navigation advantages detailed in this work regarding the inclusion of eversion mechanisms, the presence of everting belts within the DBCF-EM finger design offers us the opportunity to enhance the dexterity of the gripper relatively easily by using them for in-hand object manipulation. In-hand manipulation, a trending topic in gripper

technology [55, 163–167], allows one to reorient an object within the gripper after it has been grasped. The movable belts already included on the inner side of the DBCF-EM finger design could allow the addition of this function. By adding an independent actuator to drive the belts separately from the finger motion, the object could be rotated in hand, enhancing the versatility of the gripper. So, in-hand manipulation merits future exploration by using eversion mechanisms as it is readily available in the design to enhance the dexterity of the gripper.

5.3.3 Gripper design theory

This thesis was structured into two parts: theory and design. Although the specific design theory for analyzing the behavior and performance of the designs developed with curved flexure fingers of Part II was not the primary focus of this work, it remains essential for future optimization. The theoretical framework established in Part I is well suited for developing a dedicated design theory due to its adaptable, general, and structured approach, which allows flexible modification of individual steps. For example, the trajectories and interaction forces of a precurved flexure finger can be analyzed across different object sizes, flexure dimensions, and numbers of adjacent obstacles by substituting the original 3-R PRB linkage model of a straight flexure from Chapter 2 with a 3-R PRB linkage model for a precurved flexure, requiring only minimal adjustments to other steps in the framework.

Additionally, this framework can be used to estimate pull-out forces in cage grippers with curved flexure fingers, as demonstrated in Appendix B — at least for the contribution of flexural stiffness. As previously discussed, the total holding force also includes internal and external friction components.

The example in Appendix B employs a 3-R PRB model of a precurved flexure that encloses a circular object and contacts it at its tip. As the object is incrementally displaced out of the gripper, the fingers open through bending, generating a tip force that acts normal to the surface when friction is neglected. The maximum value of the force component in the gripper's longitudinal direction represents the lower bound of its pull-out force. Kinematic and kinetic analyses are conducted similarly to Chapter 2 by incorporating the object, displacement vector, and 3-R linkage within a closed vector loop, producing design charts that calculate the required finger thickness based on holding force and wrapping angle. This is particularly beneficial for designers to make a design trade-off between the degree of object enclosure vs the finger thickness to generate a requested amount of holding force, where in some applications full object enclosure is not feasible or a slim-finger profile is preferred.

Overall, this versatile and parameter-based framework supports further research into the design theory and optimization of grippers and base-driven interactive flexure mechanisms in general. It provides a solid foundation for predicting trajectories, interaction forces, holding forces, and environmental adaptability in diverse operational contexts. Compared to FEM, it requires only a very limited number of parameters, all of which have clear physical significance.

5.4 Implications for axially advancing mechanisms

The key technology developed in this thesis is the flexure-driven eversion mechanism, which was implemented in the design of gripper fingers and evaluated within this application. Broadly, this technology can be characterized as an axially advancing mechanism — that is, a mechanism that advances, propagates, moves, or maneuvers along its longitudinal (axial) direction. It operates as a combination of an eversion mechanism propelled by a base-driven flexure.

As this represents a relatively new class of technology, this section first positions it relative to other eversion mechanisms — a comparison not previously elaborated upon, as the thesis primarily focused on gripper applications. We then discuss the mechanical behavior during propagation, considering both flexure-driven eversion mechanisms and standalone base-driven flexures, and conclude by highlighting key aspects related to the manufacturing of flexure-driven eversion systems.

5.4.1 Positioning DBCF-/SCF-EM in eversion mechanism research

The key technological advancement of this thesis lies in the development of flexure-driven eversion mechanisms, in which we integrate a structural mechanism with conventional soft eversion mechanisms. We introduced the DBCF-EM and SCF-EM, representing planar and spatial embodiments, respectively, specifically designed with curved flexures for use as fingers in mechanical food grippers. The structural mechanism within the eversion system serves a dual function: it actively drives the eversion motion while passively providing load-bearing capacity. The curved flexure design inherently constrains the eversion path to a circular trajectory. In this section, we compare our technology with existing eversion mechanisms found in the literature.

Most eversion mechanisms reported in the literature consist of soft, tube-like structures propelled forward by either pneumatic or hydrostatic pressure [168]. Some examples incorporate internal mechanisms—either localized or tendon-driven—primarily for sensing, controlled steering, or mounting inspection cameras at the tip [158–160]. However, these implementations do not actively drive the eversion mechanism itself.

One existing design bears a closer resemblance to ours [161], featuring an eversion mechanism combined with an internal serial rigid linkage system along its entire length. This internal skeleton enhances load-bearing capacity and is employed in a movable support rail for wheelchair users, offering adjustable stabilization beneath the armpits and across the chest. Similar motivations underpin both designs: enhancing load capacity, enabling lifting, and increasing bending motion while reducing sliding forces. This suggests that integrating an advancing structure within an eversion mechanism holds promise for applications requiring these characteristics. However, despite these similarities, this design differs significantly from ours, as it remains pneumatically driven, whereas our design is propelled solely by an internal structural mechanism.

Since, to the best of our knowledge, no other mechanically driven eversion mechanisms have been previously documented in the literature [111–115, 161], we propose the establishment of a new subcategory within the field of eversion mechanisms, termed mechanically driven eversion mechanisms. This category encompasses systems that feature a thin, tip-extending everting sheet (e.g., a sleeve or belt) integrated with an internal mechanism that

simultaneously drives forward motion and provides structural support.

The DBCF-EM and SCF-EM designs presented in this research fall within this new category and introduce a further subdivision: flexure-driven eversion mechanisms. While our implementation relies on flexures, future research may explore alternative mechanical means to drive eversion mechanisms within this category.

Utilizing flexures enables the creation of a monolithic, thin structure that integrates in-plane flexibility for motion with out-of-plane stiffness for load-bearing, providing a more compact and compliant alternative to bulky, rigid serial linkages. These flexure-driven eversion mechanisms offer significant potential for applications requiring devices that must extend and traverse along their axis while interacting with their surroundings with minimal disturbance. Their design combines the structural strength of mechanical systems with the adaptability and near-zero slip of eversion mechanisms. Additionally, the shape of the flexures passively predefine the motion path—in this case, a circular trajectory. Other predefined motion paths could also be considered, as demonstrated in the literature, where pressure-driven eversion mechanisms employ fixed tendon strips to achieve passive screw motions while unwrapping for antenna applications, aside active steering mechanisms, such as bending segments, as mostly seen [169, 170].

A key distinguishing feature of our work is the planar embodiment of the eversion mechanism, as realized in the DBCF-EM finger design. Unlike existing eversion mechanisms, which are predominantly spatial [113–115], no prior planar eversion mechanisms have been reported in the literature. The DBCF-EM mechanism operates differently from conventional designs, resembling two counter-moving caterpillar tracks—though, rather than generating traction, it mitigates it. Its open configuration does not seem feasible for pressure-driven eversion mechanisms, as they rely on internal pressure buildup to function. This likely explains why planar designs are not found in the literature yet.

In contrast, the SCF-EM design is more akin to conventional eversion mechanisms, featuring a circumferentially enclosed eversion sleeve that unfolds inside-out. However, beyond being mechanically actuated, a key distinction is that most spatial designs do not have a tightly fitted sleeve; instead, their sleeves typically bend or kink when navigating curves. In contrast, our design maintains a snug fit with ample wrinkles.

5.4.2 Base-driven flexures in interactive navigation

Across Chapters 2 to 4, we consistently observe that the mechanical behavior of flexures is highly suited for applications where they must maneuver through environments filled with objects, relying on a high degree of interaction. In Chapter 2, this was experimentally validated for a straight flexure passing between sequential obstacles, followed by practical demonstrations in Chapters 3 and 4 using a curved flexure design following the contour of a spherical object passing alongside adjacent contacting objects while interacting. Their slender structure integrates both propagation and steering capabilities in a single design since it combines axial stiffness with lateral flexibility. This axial stiffness enables them to be driven from the base, allowing them to transmit sufficient force to overcome obstacles and maneuver through tight spaces. Meanwhile, their bending flexibility allows the flexures to adapt to surrounding structures, guiding themselves around obstacles by bending without causing significant stress accumulation upon contact.

However, these steering capabilities are not limitless: when paths deviate substantially

from the original trajectory of the flexure, higher curvatures may be required, risking material plastic deformation or even damage to either the flexure or the objects it interacts with. Furthermore, propagation is restricted by the flexure buckling limits, which can be reached if the environmental resistance is too high. However, nearby objects can bolster the propagation capability by providing lateral support, effectively increasing the critical buckling load of the flexure.

The interaction forces and propagation potential are thus closely tied to the bending stiffness of the flexure and the resistance of surrounding objects being in static equilibrium. It was concluded that for the straight-flexure case, its kinematics and kinetics were highly predictable using a PRB model. Hence, by adjusting the design parameters, such as the initial shape, thickness, and material properties that determine bending stiffness, its navigational behavior can be predictably controlled. This suggests that the behavior of differently shaped flexures, like curved ones, can be predicted with high accuracy as well since compliant mechanism motion relies on the elastic deformation of their material, and this force-displacement relationship is well defined by the material properties (like Young's modulus) and the geometry of the mechanism.

Consequently, base-driven flexures are remarkably well-suited for navigating complex and dense environments in a predictable, predefined manner by tuning design elements and leveraging interactions with the surroundings. This makes them highly suitable for applications requiring reliable and predictable movement through confined spaces, extending beyond grippers to areas such as medical instruments that navigate within the human body or tools designed for drilling or rescue operations in debris-filled or soil-laden environments. The flexures provide a slender and predictable mechanism that passively advances, as long as interactions with the environment remain within safe operational limits. For example, a medical instrument could follow the contour of the skull toward a tumor site or navigate between two stiffer internal media, passively guiding the flexure within these limits by leveraging its propagation and self-steering bending capabilities for precise navigation.

5.4.3 Base-driven flexures combined with eversion mechanisms

A flexure combined with an eversion mechanism provides, in addition to the reduction of friction, additional characteristics that affect their steering and propagating capabilities compared to bare, unassisted flexures. Designers must be aware of them to prevent unwanted behavior when designing future flexure-driven eversion mechanisms and use them beneficially.

First, the interaction of assisted flexures with new objects - and their resulting steering direction - is determined by the unwrapping motion of the eversion mechanisms at the tip, governed by the tip design. As observed in certain experimental cases where the gripper fingers encounter an obstacle, they bend in the opposite direction of the mechanism's unwrapping motion at the contact point. In contrast, a bare flexure typically bends away from the obstacle in the advancing direction of the original path, such that the longitudinal axis through its tip aligns with the surface of the object. For symmetrical tip designs, such as for SCF-EM finger design, the eversion sleeve unwraps symmetrically on both the inner and outer sides of the flexure, allowing an even distribution of motion, and its response is similar to that of a bare flexure when encountering an obstacle. In contrast, the DBCF-EM

finger design has an asymmetric tip design, with the inner belt roller positioned behind the outer belt roller, resulting in a predominantly outward-directed motion along the outer contour of the tip. In tests with larger misalignments, it was observed that the DBCF-EM finger design tends to deviate from its intended path due to this directional bias.

For example, when both fingers are slightly above the target object, each makes initial contact with it on the inner side of the tip. Here, the unwrapping motion of the eversion sleeve aligns with the direction of travel of the finger, allowing it to smoothly roll over the surface of the object and bend in the intended direction. In contrast, the DBCF-EM finger design, with the outer belt fully covering the inner side of the tip, encounters an unwrapping motion opposite to its path, causing it to bend sharply inward and curl upward along the surface of the object towards the gripper shaft, as shown in Figure 5.1.

In addition, when increasing the misalignment of the object and the gripper in its lateral direction, a different behavior was observed between the DBCF-EM and SCF-EM finger design, attributed to the symmetry and asymmetry of the tip design: the DBCF-EM finger design overstretches across two adjacent objects, while the SCF-EM finger design maintains its trajectory between them. This distinction illustrates how the symmetrical versus asymmetric tip design affects the flexure steering with the eversion mechanisms. Symmetrical tips respond similarly to that of a bare flexure and aid in stabilizing the trajectory against misalignments, while asymmetrical tips favor one steering direction, enabling sharp turns or even U-turns when hitting obstacles opposite the flexure motion direction or straightening its path depending on the motion direction of the eversion mechanism at the point of contact. Beyond making future designers aware of this effect, it also opens opportunities to actively steer these mechanisms in a relatively straightforward manner. Although our designs use fixed tip elements, incorporating actuation into a single tip element could enable active steering upon contact with objects, thereby enhancing navigation and allowing precise directional control.

Secondly, combining the flexure with an eversion mechanism significantly enhances its propagation capacity. The reduction in friction minimizes susceptibility to buckling by lowering the effective load, while the everting motion at the tip generates a digging action that further facilitates forward movement. The digging action facilitates this rather than simply pushing a flexure or rigid mechanism through a tight space as the unwrapping motion of the eversion mechanism stretches or displaces objects within the gap, creating a path for the device. This effect reduces forces exerted on the environment, enabling smoother passage through high-resistance areas, minimizing permanent damage (as with traditional drilling), and allowing smaller incisions in medical applications by gently displacing tissue laterally to enter it. From a propagation perspective, the lower friction forces combined with the digging action of the eversion mechanism thus enhance the performance while preserving surrounding materials.

This makes it highly suitable for applications requiring navigation through areas that have resistance to overcome. Beyond gripper systems, this behavior holds potential for medical instruments maneuvering through small incisions, rescue robots in earthquake zones, cable-laying tasks, and navigation through pipelines or soil.

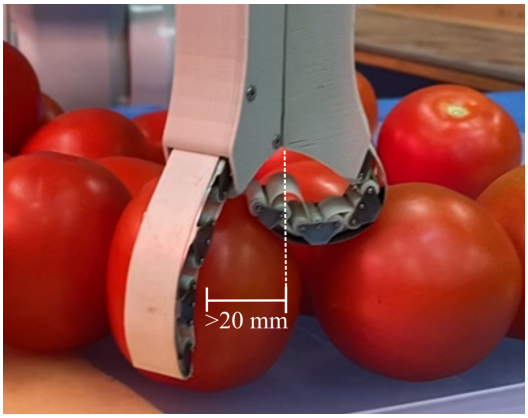


Figure 5.1: Illustration showing how the steering behavior of flexure-driven eversion mechanisms can be controlled through tip design, enabling path formation and potential for active steering. When encountering obstacles, these mechanisms bend in the direction opposite to the motion of the everting component along the outer contour of the tip. With tip asymmetry, as demonstrated in the DBCF-EM finger design, outward-directed motion along the tip becomes dominant. Here, with the gripper positioned slightly offset, the DBCF-EM finger approaches the target object nearly perpendicularly and curls upward along its surface, rather than following the natural forward path typical of bare or symmetrically-tipped flexures, as seen in the SCF-EM finger design.

5.4.4 Manufacturing aspects of flexure-driven eversion mechanisms

Building on our experience and insights from this research, we outline essential design and manufacturing principles to guide the development of future flexure-driven eversion mechanisms. These guidelines aim to assist designers in a field where eversion mechanism technology is still in its early stages, providing some clarity on fabrication techniques. Additionally, combining eversion mechanisms with non-straight flexures presented several challenges, which we further detail to support innovation in this field.

Firstly, using non-straight flexures to drive eversion mechanisms introduces the challenge of tightly guiding the inner radius to maintain proper coverage. This requirement applies not only to the curved examples in this study but also to other flexural shapes, such as S-shaped designs. Without adequate guidance, the inner side of the eversion mechanism may move in a straight line from base to tip. In our DBCF-EM design, guiding rollers were used to prevent this, while in the SCF-EM design, the eversion sleeve was connected to the outer contour, with circumferential stretchability added for a secure fit. This research underscores the importance of proper guidance when designing non-straight mechanisms and offers two strategies (i.e. guiding rollers and circumferential sleeve), although designers may explore alternative approaches to best meet their specific design requirements for future flexure-driven eversion mechanisms.

Secondly, one needs to account for the differing arc lengths on the inner and outer sides, an aspect that proved to be far more challenging than initially anticipated when transitioning from the planar DBCF-EM variant to the spatial SCF-EM finger design. This was relatively straightforward in the DBCF-EM design because the belts were not

connected and could move independently to compensate for the variation in material requirements between the two sides. However, in the SCF-EM finger design, the inner and outer sides of the eversion sleeve are connected circumferentially, requiring more sophisticated coordination of three-dimensional motion. Designers working on similar systems should focus on integrating this eversion sleeve motion, as it plays a key role in ensuring smooth operation. Our primary goal was to demonstrate functionality and hygiene potential, but the design highlights areas for improvement.

For the functionality and hygiene criteria, selecting the right eversion sleeve material is critical and proved challenging. It must be thin, robust, waterproof, flexible for smooth movement, stiff enough to drive, and resistant to self-sticking in the tunnel. Latex emerged as the most effective material in our tests, outperforming alternatives such as silicone and Lycra, which were used for instance in toroidal-hydrostat grippers explored in the final section of the *"Explorative Conceptual MSc Work"*-chapter at the end of this dissertation, from which practical, experience-based insights were obtained. However, given the constraints of our experience and fabric knowledge, collaborating with material specialists could probably reveal better options.

Future development could prioritize materials with higher standards of hygiene, durability, and robustness, along with optimized stretch and constraint properties built into manufacturing. Potential options include homogeneous stretchable materials or woven stretch fabrics with embedded stiffening threads. The stretchability of the material should be carefully designed to adapt to varying lengths around the contour of the finger while supporting smooth eversion. By engaging material experts to develop customized eversion sleeves, this mechanism could move significantly closer to market readiness.

5.4.5 Concluding Remarks

In summary, base-driven flexures excel in interactive navigation, and combining them with eversion mechanisms significantly improves both performance and application potential for compliant mechanisms and soft robotics. Using flexures to drive conventional pressure-driven eversion mechanisms adds axial and lateral stiffness, increasing both propagation and load-bearing capacity while improving the predictability of their motion and interaction. In contrast, integrating eversion mechanisms with base-driven flexures reduces sliding forces exerted on the environment, minimizing damage and enhancing propagation capabilities. This integration also offers steering control opportunities and trajectory adaptability, offering the potential for active and precise steering adjustments.

These capabilities are particularly advantageous for growing devices or robotic applications that require precise long-distance navigation. Examples include medical robotics or instruments for minimally invasive surgery, maneuvering between rigid structures, along vascular pathways, within the skull, or between different tissues, and other fields such as search and rescue, archaeological inspection, burrowing, pipeline repair, trenching, and plant monitoring [114, 152, 171]. Future research should investigate the impact of eversion mechanisms on flexure trajectory and environmental interactions, along with optimizing or actively controlling tip design to improve steering and adaptability. In addition, a specialized manufacturing process tailored to the unique requirements of each application will further expand the potential of these mechanisms.

6

Conclusion

This dissertation presents the stepwise development and evaluation of the first flexure-driven eversion mechanisms, specifically designed as gripper fingers aimed at grasping in confined spaces. The need for such mechanisms arises from the desire to overcome the challenges of limited clearance in confined spaces that prevent traditional grippers from operating successfully, as their grasping process relies on first positioning the fingers around the object and then moving them inward from the sides—a motion that is easily obstructed by adjacent obstacles. To address this challenge, we propose gripper fingers that navigate tangentially along the object's surface while avoiding tangential (sliding) forces at the interface, thereby minimizing environmental disturbance when establishing the grasp, and realize this by designing them as flexure-driven eversion mechanisms.

Before introducing the designs, we evaluated the suitability of base-driven flexures for navigating dense environments in Part I, using a stress-test use case in which the flexure engages more strongly with the environment than envisioned in the curved finger design: the kinetostatic modeling and experimental validation of an advancing straight flexure moving between two consecutive circular obstacles. The results confirmed the compatibility of base-driven flexures with our design, as the flexure was shown to navigate between obstacles by bending when pushed forward, with both trajectory and interaction forces accurately predicted by the analysis to a level sufficient for use in design.

Beyond this assessment, this work makes a significant scientific contribution to compliant mechanism modeling by extending the use of fundamental pseudo-rigid-body (PRB) formulations for beam elements in flexural systems. We enabled PRB modeling of flexures in event-based scenarios and for flexures with multiple loads along their length by implementing switching and stitching of topologies while maintaining the system's potential energy within reasonable bounds. For future flexure designs, this framework offers a versatile tool that can be adapted to model navigating curved flexures or to predict pull-out forces, for example.

In the second part of this work, we introduce and validate two mechanical gripper designs specifically developed to grasp delicate tomatoes piled in a crate. The fingers are implemented as flexure-driven eversion mechanisms, one with two everting belts and the other with a latex eversion sleeve with designed stretchability, both driven by precurved flexures: the Dual-Belt Curved-Flexure Eversion Mechanism (DBCF-EM) finger and the Sleeved Concentric-Flexures Eversion Mechanism (SCF-EM) finger, respectively. We detail the designs of both gripper prototypes and present the practical and technical setups used to validate them against the defined performance metrics.

In both designs, the flexure-driven eversion mechanisms allow the gripper fingers to follow a predefined curved trajectory closely along the object's surface, providing secure grips through structural stiffness, while the everting action significantly reduces friction forces by maintaining a stationary interface, thereby decoupling the internal flexure kinematics from external contact. The experimental results confirmed their effectiveness in confined spaces, achieving grasp success rates of up to 100% when integrated into a robotic systems tasked with emptying a crate of tomatoes one at a time. Low disturbance forces were recorded on both the objects and their surroundings, while the measured pull-out forces were sufficient to securely hold the objects. Comparative studies also show that the integration of eversion mechanisms reduces friction forces by approximately 90%, further highlighting an advantage of this approach.

Throughout this thesis, design refinements were made to enhance the gripper's robustness, lifespan, and hygiene compliance, while resolving issues such as misgrasps and object damage. These improvements ultimately led to the success of the mechanical food grippers in confined spaces. However, more research and advances are needed to meet industry standards, validate performance across a wider range of food products and agri-food environments, and expand design and modeling theory to support future improvements and deepen our understanding of these systems.

For robotic gripper applications in general, this research offers a novel perspective on how to enable reliable grasping in confined spaces. Instead of focusing solely on optimizing the grip or robotic system performance, we re-examined the grasp-setting process, a critical step in most practical applications, and successfully modified it by incorporating obstacles early in the design phase. By exploiting object interactions within safe limits, rather than avoiding them entirely, the design becomes simpler, more reliable, and highly practical for a wide range of applications, facilitating smoother integration into real-world robotic systems. This comprehensive design approach could also be applied to other fields where mechanisms or instruments operate in confined, unstructured environments, provided that some interaction force is acceptable.

Beyond gripper applications, exploring new implementations of flexure-driven eversion mechanisms will be crucial to maximizing their societal impact by extending their success to other domains where navigating confined spaces and interacting with the environment are challenging, such as medical devices, search-and-rescue robotics, and inspection systems for hard-to-reach environments.

A

Supplementary Video Material

Overview

This appendix contains QR codes linking to video recordings of the grippers described in Chapters 3–4, highlighting their operating principles, as well as the robotic gripper experiments conducted to evaluate grasp success rates in confined spaces.

Each QR code provides direct access to the corresponding YouTube video and can be scanned with a smartphone; for convenience, a clickable link is also included in the caption below. All videos can also be found on the YouTube channel[1] , should the direct link service ever become unavailable in the future.

All recordings are additionally archived in the TU Delft Research Data Repository for long-term preservation and have been submitted as supplementary material accompanying the related publications in *IEEE Robotics and Automation Letters (R-AL)* and *ASME Letters in Translational Robotics*.

Figure A.1: QR-code to YouTube channel[1]

[1] https://www.youtube.com/@aehuisjesRD

A.1 Video recordings of DBCF-EM gripper

The QR code links to the video showing the DBCF-EM gripper experiment as performed in real operation. The video can be accessed by scanning the QR code with a smartphone, or via the clickable link: url link to DBCF-EM gripper video[2]. The video is titled *"Compliant Eversion-Mechanism Gripper (DBCF-EM) for Confined-Space Grasping: Piled Tomato Pick Demo"* on YouTube.



A.2 Video recordings of SCF-EM gripper

The QR code links to the video showing the SCF-EM gripper experiment as performed in real operation. The video can be accessed by scanning the QR code with a smartphone, or via the clickable link: url link to SCF-EM gripper video[3]. The video is titled *"Compliant Eversion-Mechanism Gripper (SCF-EM) for Confined-Space Grasping: Piled Tomato Pick Demo"* on YouTube.



[2] https://youtu.be/oapgMvshExw
[3] https://www.youtube.com/@aehuisjesRD

B

Pull-Out Force Models

This appendix presents preliminary analytical approaches to approximate the pull-out force of grippers employing flexure-driven eversion mechanisms as fingers.

The primary focus of this thesis was on the first phase of the grasping process — establishing the grasp in confined spaces — rather than on the subsequent step of maintaining the object once lifted from the pile. Therefore, the modeling of the pull-out force was not performed at the same level of depth as the other work presented in this thesis. Nevertheless, understanding this parameter is essential for future industrial developments and for use in the design phase.

Appendices B.1 and B.2 present simplified models that provide an initial quantitative understanding of how the two main contributors—the bending stiffness of the precurved flexure and the belt pretension—affect the holding capacity of grippers employing flexure-driven eversion mechanisms as fingers. Other influencing factors within the design were neglected, and it was assumed that the easiest direction for the object to escape the grasp is along the longitudinal axis of the gripper, represented here as vertically downward when the gripper itself is orientated vertically upward.

Both appendices are based on MSc theses, (1) and (2), available via the TU Delft repository: http://resolver.tudelft.nl/. Here, they are written as standalone summaries highlighting the main contributions of each work, whereas the original theses contain more extensive derivations and results. Although exploratory in nature, this work provides a practical starting point for more detailed future modeling and validation.

(1) Mark Kuntz, *Pull-out force of grippers with initially-curved fingers based on Pseudo-Rigid Body modeling*, (2024, Feb)

(2) Bart Friederich, *Design and validation of a manoeuvering caging gripper for grasping in cluttered environments*, (2022, April)

B.1 Pull-out force of precurved flexure fingers via PRBM

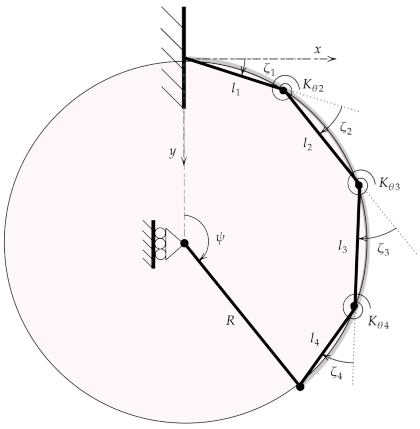
B.1.1 Problem introduction

As successfully demonstrated in Chapter 3 and Chapter 4, grippers with precurved fingers exhibit advantageous properties, such as the ability to passively hold objects by form-closure around the object using their structural stiffness and passive adaptability to various object sizes due to their bending compliance. However, their pull-out force, a key performance metric, has so far only been empirically determined and lacks an established modeling approach. Accurate prediction of pull-out force is critical to ensuring that these grippers can lift and transport objects securely and further optimize their designs.

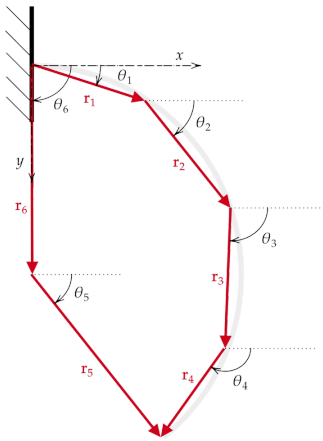
In this work, we specifically focus on the contribution of the bending stiffness of the pre-curved flexures in the finger designs, hereby neglecting the contributions of the eversion mechanism and secondary effects such as tendon forces generated by pretension and elastic stretching of the belts or sleeve, and friction losses along the rollers in the DBCF-EM design or between the sleeve and the finger backbone in the SCF-EM design.

B.1.2 Methodology

This research models the pull-out force of grippers with precurved fingers, assuming a form-closed grasp, using the Pseudo-Rigid Body Model (PRBM) approach, with several steps similar to those in Chapter 2. As shown in Fig. B.1a, the model features an object enclosed by a single finger, with the encompassing angle ϕ, thickness, width, and material properties as design parameters. The finger is modeled using the PRBM for precurved flexures [91], replacing the curved finger with a 3R rigid body linkage consisting of three revolute joints and torsional springs. The link lengths and spring stiffness are derived from the design properties of the fingers.



(a) Gripper finger replaced by a 3R pseudo-rigid body linkage



(b) Closed vector loop for solving the kinematics

Figure B.1: (a) The gripper finger is replaced by a 3R pseudo-rigid body linkage, and (b) the established closed vector loop used to solve the kinematics through the vector loop equations.

To perform kinematic analysis, vector loop equations were established by creating a closed kinematic chain between the rigid-body linkage and the object, as shown in Fig. B.1b. The object was incrementally displaced downward in the y-direction, causing the finger to bend. The system's potential energy was minimized to determine the corresponding linkage angles. The analysis concluded when the object escaped the grasp, that is when the tip of the flexure reached a distance equal to the radius of the object R from the y-axis. The force at the tip of the flexure, aligned with the vector r_5, was calculated using a free-body diagram of the link r_4 for each displacement. The vertical component, which opposes the object's gravitational force, defines the maximum pull-out force during the trajectory.

An experimental setup was constructed to validate the model. This setup included a curved finger mounted on a rail, connected to a load cell, and a drive system to extract the object from the grip while recording displacement and applied forces. The principles and design of the setup share similarities with those in Chapter 2 and Chapter 4. The model was validated through experimental testing with PLA and stainless steel test pieces.

Lastly, a parametric study was conducted in which the required enclosing angle ϕ for a given thickness of the finger h is calculated to achieve the pulling force to hold the weight of a tomato.

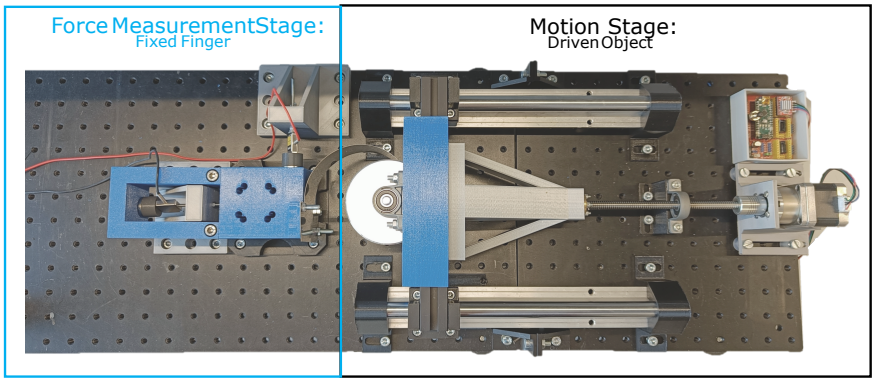


Figure B.2: Experimental setup used to validate the pull-out force model. The setup consists of a curved finger mounted on a rail, connected to a load cell, with a drive system that extracts the object from the grip while measuring the applied forces.

B.1.3 Results and conclusion

The developed model accurately captured the relationship between key design parameters and the pull-out force, enabling reliable predictions of the gripper's ability to hold an object. The experimental results showed reasonable agreement with the theoretical predictions, as similar trends were observed between the force-deflection curves during the displacement of the object, although systematic errors were present (with deviations of 12% for PLA and 32% for stainless steel).

From the parametric study, a design chart was created to aid in gripper design, offering a quick visualization of finger design options for a given holding force, presented in Fig. B.3. The chart reveals a non-linear, decreasing trend between the enclosing angle, ϕ, and the thickness h of the finger that becomes less steep as h increases.

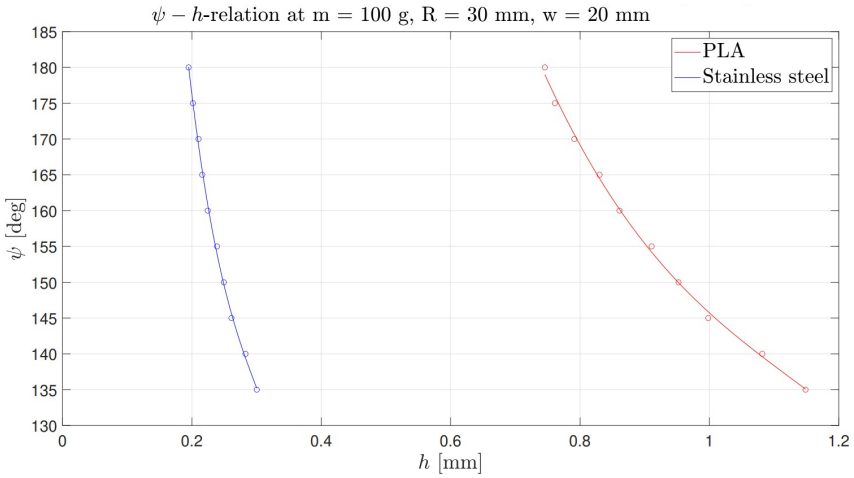


Figure B.3: Design chart from the parametric study showing the required enclosing angle ϕ for a given finger thickness h, calculated to achieve the pull-out force for holding the weight of a tomato. The chart presents results for two different materials, and such graphs can be used as design tools for the selection of finger dimensions

B.2 Pull-out force by DBCF-EM eversion belt pretension

B.2.1 Problem introduction

As presented in Chapter 3, the DBCF-EM gripper achieves object retention through the stiffness of the caging structure of its fingers, which resists opening and prevents the object from escaping. This caging stiffness is mainly provided by the bending stiffness of the pre-curved flexures and by the (pre)tension in the eversion belts. The contribution of the pre-curved flexures has already been analytically approximated in Appendix B.1.

This work focuses on the contribution of the eversion belts to the holding force of the DBCF-EM gripper, as they not only facilitate shear-force reduction with the environment through their eversion motion, but also enhance the gripper's holding capability due to their pretension.

B.2.2 Methodology

The pretentsion in the eversion belts are generated by the elastic bands, which not only facilitate their retraction when the fingers are drawn back into the housing but also generate a tensile load between the moving parts inside the fingers. This comparable to tendons in the human hand—as illustrated in Fig. B.4a, and resists the separation of the flexural tabs once an object is enclosed, thereby contributing to the overall holding force of the gripper.

An approximate analytical estimation was performed to predict the minimum achievable holding force based solely on belt pretension, determined by the equilibrium between the contact reaction force at the fingertip and the tendon tension F_{tendons}. For the case study presented in Chapter 3, a moment balance was used around the point where the flexure emerges from the wrist, defined as pivot point P (Fig. B.4b).

To conservatively estimate the minimum holding force, only a single contact point at the fingertip was considered, modeled as a frictionless contact, and the tendon force acting between the first tab and the wrist. The moment generated by the contact force F_{contact}, acting at a distance R_{contact} from P, was balanced by the tendon force F_{tendons}, acting at a distance R_{tendons} from P, as shown in Fig. B.4a. Considering that the contact force is oriented at 45° relative to the gripper's symmetry axis, the effective component $F_{\text{hold,finger}}$ preventing object extraction is given by Equation B.1.

The pretensioned belts acting as tendons were modeled as constant tensile elements connecting the wrist and finger segments. Other secondary effects such as the bending stiffness of the backbone, the elastic stretch of the belts, and friction losses along the rollers, were neclected in this analytical model.

Substituting the design parameters, namely F_{tendons} = 9 N, R_{tendons} = 6 mm, and R_{contact} = 42 mm, the estimated holding force per finger is $F_{\text{hold,finger}}$ = 0.9 N, resulting in a total gripper holding force of $F_{\text{hold,analytical}}$ = 2.7 N.

$$F_{\text{hold,finger}} = \sin(45^\circ)\frac{F_{\text{tendons}} R_{\text{tendons}}}{R_{\text{contact}}}. \tag{B.1}$$

To refine the estimation, a finite element analysis (FEA) was performed in which all four tendons per finger were modeled as constant attractive forces between the rollers. The object was represented as a rigid half-cylinder with a diameter D = 60 mm and frictionless contact with the finger. Using a non-linear analysis, the tendon tension was increased to F_{tendons} = 9 N, resulting in a simulated holding force of $F_{\text{hold,finger}}$ = 0.97 N or $F_{\text{hold,FEA}}$ = 2.91 N for the gripper in total.

B.2.3 Results and conclusion

The measured holding force of the DBCF-EM gripper was $F_{\text{hold,exp}}$ = 3.7 N, as shown in Fig. B.5. This value exceeds both analytical and FEA estimations by 27% and 13%, respectively. The discrepancy can be explained by the simplifying assumptions in the models, particularly the neglect of friction between the finger and the object and the higher effective belt tension caused by friction in the belt guidance.

For the practical case of manipulating tomatoes, the required total holding force must exceed the object weight of 1.8 N in the vertical direction, meaning that the gripper provides sufficient holding force to which stand static gravitational force.

Overall, the belt tension model provides a reliable lower-bound prediction of the holding force and demonstrates that pretensioned belts substantially enhance the structural stiffness and object retention capability of the DBCF-EM gripper.

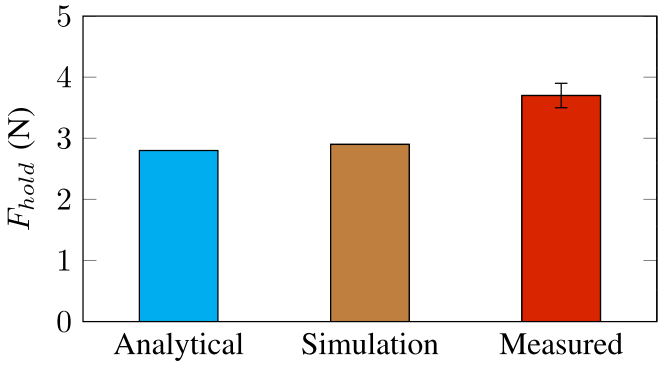
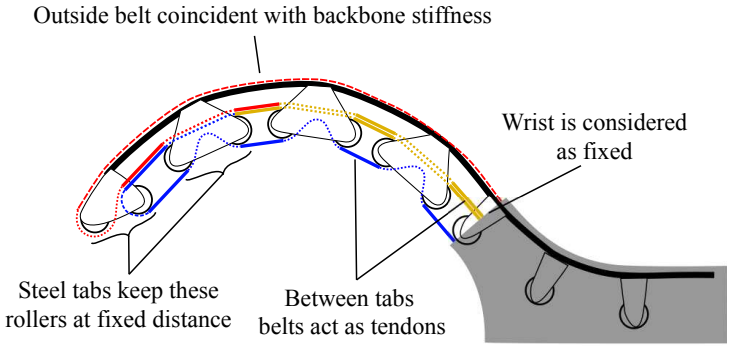
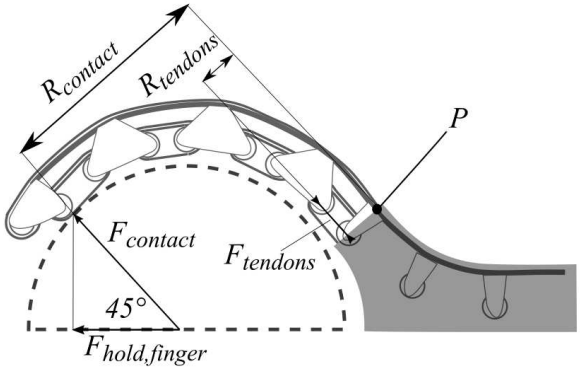


Figure B.5: Measured holding force F_{hold} compared to analytical and FEA estimations. The measured value represents the mean of seven repetitions, with the standard deviation shown as error bars.



(a) Tendon force generation by the pretensioned belts. The pretensioned sections that contribute to the holding force (active) are illustrated with thick lines and resist separation of the steel tabs during object extraction, while the dotted sections (passive) are neglected. Three active belts act in parallel between each tab and the wrist, each exerting 3 N, resulting in $F_{\text{tendons}} = 9$ N.



(b) Relevant geometry and forces used to analytically determine the holding force $F_{\text{hold,finger}}$ of a single gripper finger using a moment balance around pivot point P. R_{tendons} and R_{contact} denote the moment arms of the total tendon force F_{tendons} (acting between the first tab and the wrist) and the contact force, respectively.

Figure B.4: (a) Schematic representation of tendon force generation and (b) analytical model of the holding force contribution by the belts.

C

Design Reasoning

This appendix presents the design reasoning that led to the proposed finger concept developed throughout this thesis: advancing flexure fingers combined with eversion-mechanism principles to reduce environmental disturbances and enable confined-space grasping.

The work originated from the observation that agricultural robotic automation is often limited at the stage of confined-space grasping—situations where objects must be retrieved from cluttered or densely packed environments, which frequently occur in practice. It was also recognized that conventional gripper fingers, which move perpendicularly towards the object, struggle in such settings, as they cannot easily reach underneath or securely enclose the object. To overcome these limitations, we proposed a mechanical redesign of the gripper architecture in which the fingers were intentionally designed to move along the object surface, thereby reducing the clearance required for finger insertion and allowing them to slide underneath and form an enclosing grip. These strategies and their development are presented in this appendix and further elaborated in the work of (2).

In addition, several approaches were explored to reduce friction and tangential disturbance forces at the contact interfaces, since this method of setting the grasp increases the risk of unwanted interactions that may cause damage or misgrasps.

The resulting design selection identified the most promising concept— tangential object-following finger motion enabled by advancing precurved flexures driven from their base, combined with eversion-mechanism principles along their length to minimize tangential disturbances during contact— which is further developed and refined throughout this thesis.

(2) Bart Friederich, *Design and validation of a manoeuvering caging gripper for grasping in cluttered environments*, (2022, April)

C.1 Design rationale towards proposed concept

The advantages of using form-closed grips with mechanical fingers to grasp food objects are explained in Chapter 1.2, followed by the problem statement in Section 1.3, which explains the challenges conventional grippers face in agri-food environments and hence why they are not successful. The environments were dense, cluttered, and unstructured, resulting in a lack of space around the objects. Traditional grippers struggle in these environments because their grasping method, placing the fingers around the object and moving them inward perpendicular to the surface, often leads to collisions with surrounding objects or structures. This results in high forces and displacements that can disrupt both the target object and its environment.

This raises the central question: How can we establish form-closed grasps in confined spaces with minimal disturbance to the surroundings? Although we introduced our solution in Section 1.4, this appendix provides a concise overview of the early stages of the design process. We briefly present the strategies considered to achieve the desired grip and explain the rationale behind the chosen approach and finger concept.

C.1.1 Strategies to set form-closed grasps in dense environments

New maneuvering principles to obtain form-closed grasp with mechanical fingers, rather than grasping the object by enclosing its fingers toward it by moving it perpendicular to its surface. The overview aims to present strategies for reducing the gripper's workspace to minimize disturbance.

When designing grippers for dense cluttered environments, two new challenges arise: limited free space around the object and friction forces caused by surrounding obstacles. To address these, the gripper must closely follow the surface of the object during the grasp maneuver while minimizing disturbances. Several strategies can be applied to set form-closed grasps in such environments, which can be broadly divided into sideways propagation and forward propagation. Fig. C.1 presents different strategies for maneuvering the fingers from the wrist to underneath the object to establish an encompassing grasp around the object's surface:

- S-path propagation involves the gripper structure approaching the object along a single line and following the object's surface with minimal space requirements.
- Helical propagation utilizes a screw-like motion to encircle the object, minimizing the required free space during engagement.
- Building propagation constructs the gripper structure during grasping, effectively building around the object.
- Virtual hinge points allow the caging structure to rotate around the center of the object but require a larger free surface for initial engagement.
- Radial hinging relies on hinges aligned radially from the object, also requiring significant initial free space.

Based on a comparative analysis and some rough prototype tests, object-following motion, such as S-path propagation or building propagation, were found to be the most

potential strategies for maneuvering the fingers around the object with low spatial disturbance, as detailed in (2). They require minimal free surface around the object and can be adapted for various object shapes, making them ideal for cluttered environments.

C.1.2 Strategies to reduce friction

In cluttered environments, friction between the forward-maneuvering gripper fingers and the object and surrounding obstacles is a major source of disturbance during grasping. To address this, several friction reduction strategies were explored, and categorized into three areas:

- Reducing normal forces: Designing the gripper with minimal thickness or wedge shapes can reduce the additional normal forces introduced by the gripper. However, pre-existing normal forces in the clutter cannot be avoided.
- Reducing friction coefficients: Altering the friction coefficient between the gripper and the object could reduce friction, but this approach tends to be object-specific, limiting the universality of the gripper.
- Reducing relative slip: By eliminating the relative motion between the gripper and the object or environment, the work caused by slip is minimized. Strategies such as free-rolling contacts, everting surfaces, and walking contacts to reduce or eliminate slip effectively.

From the analysis, zero-slip surfaces, such as everting surfaces and walking contacts, were identified as the most promising friction reduction strategies. These methods fully eliminate slip and can even convert friction into useful traction during the grasp maneuver, seem to be integrable with object-following motions, and potentially reduce the risk of disturbance or damage during grasping in dense clutter.

C.1.3 Feasible strategies integrable for a conceptual finger

The final step was to combine the most effective strategies for form-closed grasping and friction reduction into a conceptual design of the finger that can operate in cluttered environments with minimal disturbance. Based on the evaluations, a gripper that combined S-path propagation or building propagation with everting surfaces or walking contacts was identified as the optimal solution. This combination minimizes the required space for object engagement and effectively eliminates slip, ensuring gentle and stable grasps.

From the rough prototypes generated, one design stood out with the greatest potential for further development as a prototype. This design integrated an object-following grasp maneuver with zero-slip surfaces. Therefore, we concluded that this concept would be ideal for testing the hypothesis that these combined strategies on a finger can significantly improve the performance of mechanical form-closed grippers in dense environments. This will be thoroughly investigated in this dissertation by developing and evaluating mechanical designs.

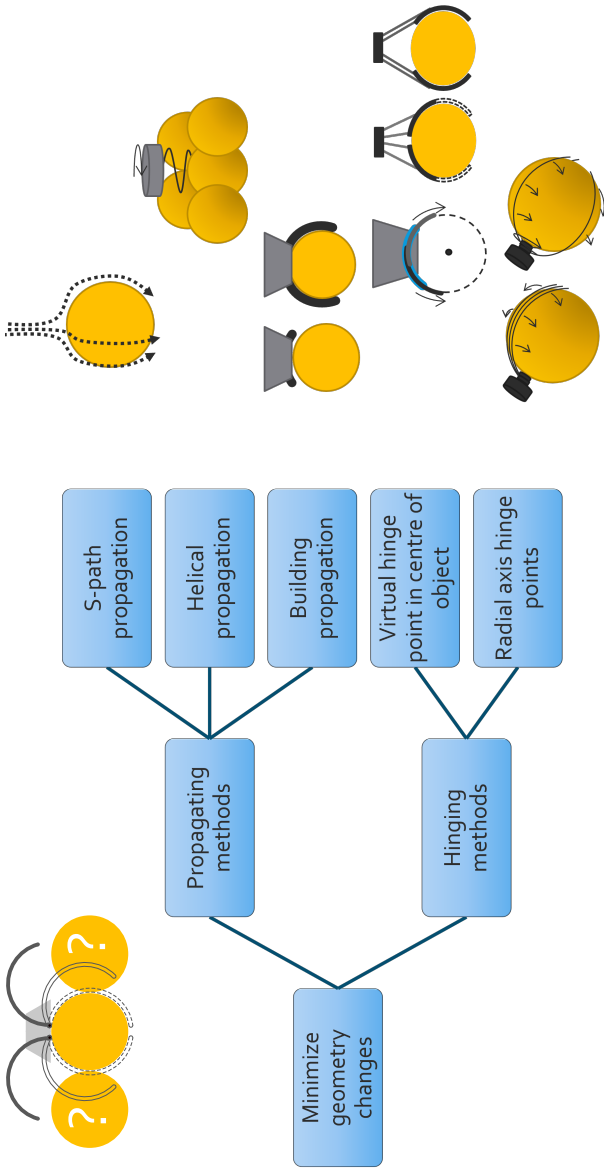


Figure C.1: Different strategies for maneuvering from the wrist to underneath the object to establish a caging structure (2).

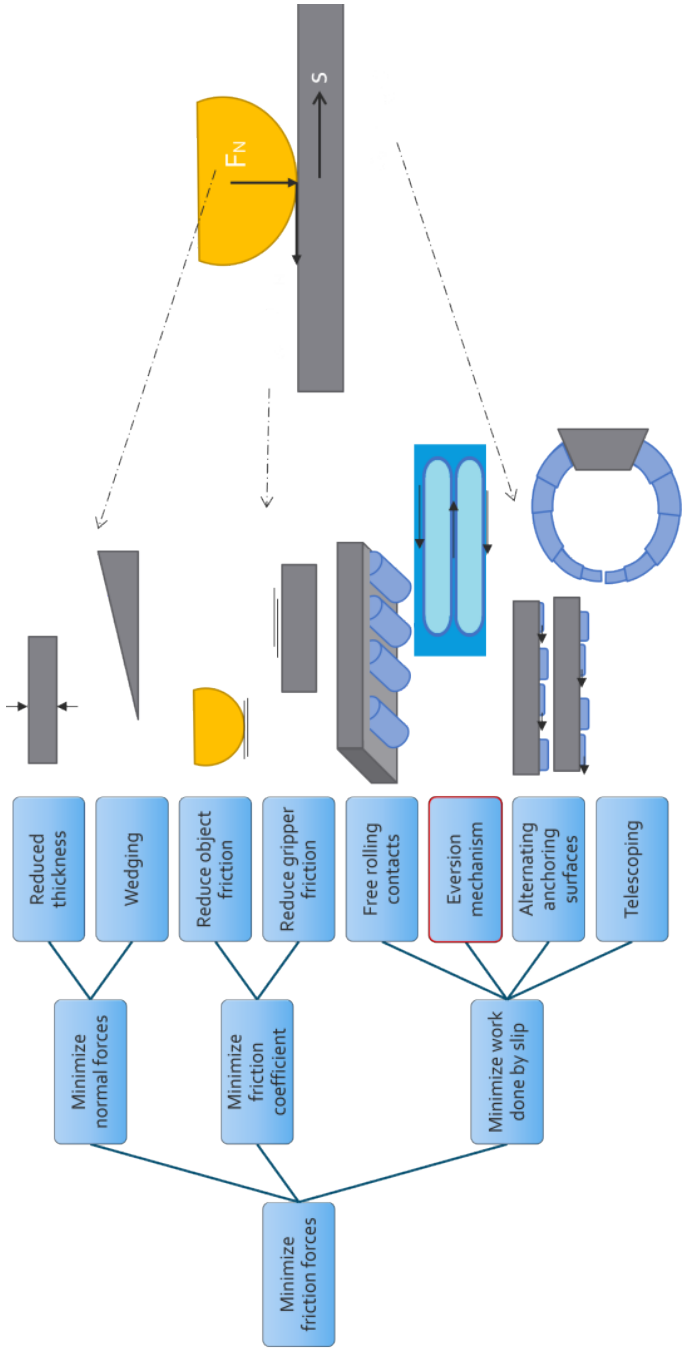


Figure C.2: Different strategies for reducing the effects of friction while maneuvering the caging structure along the object (2).

References

[1] J. Tian, B. C. Bryksa, and R. Y. Yada, "Feeding the world into the future–food and nutrition security: the role of food science and technology," *Frontiers in life science*, vol. 9, no. 3, pp. 155–166, 2016.

[2] L. Christiaensen, Z. Rutledge, and J. E. Taylor, "Viewpoint: The future of work in agri-food," *Food Policy*, vol. 99, p. 101963, Feb. 2021.

[3] G. Kootstra, A. Bender, T. Perez, and E. van Henten, "Robotics in agriculture," in *Encyclopedia of robotics*, pp. 1–19, Springer, 2020.

[4] NOS, "Tweede kamer: groen licht voor aanpak slachthuizen en minder arbeidsmigranten," 2024. https://nos.nl/artikel/2535817-tweede-kamer-groen-licht-voor-aanpak-slachthuizen-en-minder-arbeidsmigranten. Accessed: 10 September 2024.

[5] Daily Mail, "Flop 'pick for britain': Government spent more than £30,000 promoting flop pick for britain scheme that failed to recruit 60,000 willing british volunteers to save country's crops during covid pandemic." https://www.dailymail.co.uk/news/article-9676115/Government-spent-30-000-promoting-flop-Pick-Britain-scheme.html, 2021. Accessed: 11 September 2024.

[6] V. Astrov, S. Leitner, R. Grieveson, D. Hanzl-Weiss, I. Mara, and H. Weinberger-Vidovic, "How do economies in eu-cee cope with labour shortages?," tech. rep., wiiw Research Report, 2021.

[7] L. Christiaensen, Z. Rutledge, and J. E. Taylor, "The future of work in agri-food," *Food Policy*, vol. 99, p. 101963, 2021.

[8] NOS, "Waar werken de arbeidsmigranten en waarom zijn ze volgens bedrijven zo hard nodig," 2023. https://nos.nl/artikel/2501209-waar-werken-de-arbeidsmigranten-en-waarom-zijn-ze-volgens-bedrijven-zo-hard-nodig. Accessed: 10 September 2024.

[9] NOS, "Arbeidsmigratie tot 2040 nodig, daarna mogelijk een probleem," 2023. https://nos.nl/artikel/2501145-arbeidsmigratie-tot-2040-nodig-daarna-mogelijk-een-probleem. Accessed: 10 September 2024.

[10] NOS, "Overheid moet puntensysteem invoeren voor arbeidsmigratie," 2024. https://nos.nl/artikel/2536625-overheid-moet-puntensysteem-invoeren-voor-arbeidsmigratie. Accessed: 10 September 2024.

[11] P. Lin, K. Abney, and G. Bekey, "Robot ethics: Mapping the issues for a mechanized world," *Artificial intelligence*, vol. 175, no. 5-6, pp. 942–949, 2011.

[12] C. W. Bac, J. Hemming, B. van Tuijl, R. Barth, E. Wais, and E. J. van Henten, "Performance Evaluation of a Harvesting Robot for Sweet Pepper: Performance Evaluation of a Harvesting Robot for Sweet Pepper," *Journal of Field Robotics*, vol. 34, pp. 1123–1139, Sept. 2017.

[13] Y. Jin, J. Liu, Z. Xu, S. Yuan, P. Li, and J. Wang, "Development status and trend of agricultural robot technology," *International Journal of Agricultural and Biological Engineering*, vol. 14, no. 4, pp. 1–19, 2021.

[14] Stephen Gossett, "15 agricultural robots and farm robots you should know." https://builtin.com/robotics/farming-agricultural-robots, 2024. Accessed: 12 September 2024.

[15] G. Kootstra, X. Wang, P. M. Blok, J. Hemming, and E. Van Henten, "Selective harvesting robotics: current research, trends, and future directions," *Current Robotics Reports*, vol. 2, pp. 95–104, 2021.

[16] Marel, "Robobatcher flex breast fillets." https://marel.com/en/products/robobatcher-flex-breast-fillets/, n.d. Accessed: 12 September 2024.

[17] A. Bechar and C. Vigneault, "Agricultural robots for field operations: Concepts and components," *Biosystems Engineering*, vol. 149, pp. 94–111, 2016.

[18] D. Rapado-Rincón, E. J. van Henten, and G. Kootstra, "Development and evaluation of automated localisation and reconstruction of all fruits on tomato plants in a greenhouse based on multi-view perception and 3d multi-object tracking," *Biosystems engineering*, vol. 231, pp. 78–91, 2023.

[19] R. Raja, L. A. P. Pacheco, A. K. Burusa, G. Kootstra, and E. Van Henten, "Real-time six degrees of freedom grasping of deformable poultry legs in cluttered bins using deep learning and geometric feature extraction," *Biosystems Engineering*, vol. 253, p. 104134, 2025.

[20] J. Senden, L. Janssen, R. van der Kruk, H. Bruyninckx, and R. van de Molengraft, "Exploiting plant dynamics in robotic fruit localization," *Computers and electronics in agriculture*, vol. 196, p. 106860, 2022.

[21] E. Drijver, R. Pérez-Dattari, J. Kober, C. Della Santina, and Z. Ajanović, "Robotic packaging optimization with reinforcement learning," in *2023 IEEE 19th International Conference on Automation Science and Engineering (CASE)*, pp. 1–7, IEEE, 2023.

[22] C. Morar, I.-A. Doroftei, I. Doroftei, and M. Hagan, "Robotic applications on agricultural industry. a review," in *IOP Conference Series: Materials Science and Engineering*, vol. 997, p. 012081, IOP Publishing, 2020.

[23] D. Xie, L. Chen, L. Liu, L. Chen, and H. Wang, "Actuators and sensors for application in agricultural robots: A review," *Machines*, vol. 10, no. 10, p. 913, 2022.

[24] E. Vrochidou, V. N. Tsakalidou, I. Kalathas, T. Gkrimpizis, T. Pachidis, and V. G. Kaburlasos, "An overview of end effectors in agricultural robotic harvesting systems," *Agriculture*, vol. 12, no. 8, p. 1240, 2022.

[25] B. Zhang, Y. Xie, J. Zhou, K. Wang, and Z. Zhang, "State-of-the-art robotic grippers, grasping and control strategies, as well as their applications in agricultural robots: A review," *Computers and Electronics in Agriculture*, vol. 177, p. 105694, 2020.

[26] Qb Robotics, "Qbrobotics product download area." https://qbrobotics.com/download/, 2024. Accessed: 01 October 2024.

[27] J. M. Krahn, F. Fabbro, and C. Menon, "A soft-touch gripper for grasping delicate objects," *IEEE/ASME Transactions on Mechatronics*, vol. 22, no. 3, pp. 1276–1286, 2017.

[28] J. Hughes, U. Culha, F. Giardina, F. Guenther, A. Rosendo, and F. Iida, "Soft manipulators and grippers: A review," *Frontiers in Robotics and AI*, vol. 3, p. 69, 2016.

[29] G. Fantoni, M. Santochi, G. Dini, K. Tracht, B. Scholz-Reiter, J. Fleischer, T. K. Lien, G. Seliger, G. Reinhart, J. Franke, *et al.*, "Grasping devices and methods in automated production processes," *CIRP Annals*, vol. 63, no. 2, pp. 679–701, 2014.

[30] J. Walker, T. Zidek, C. Harbel, S. Yoon, F. S. Strickland, S. Kumar, and M. Shin, "Soft robotics: A review of recent developments of pneumatic soft actuators," in *Actuators*, vol. 9, p. 3, MDPI, 2020.

[31] J. Shintake, V. Cacucciolo, D. Floreano, and H. Shea, "Soft robotic grippers," *Advanced materials*, vol. 30, no. 29, p. 1707035, 2018.

[32] W. Chen, S. Zhao, S. L. Chow, and A. Nee, "Grippers and end effectors," *Handbook of Manufacturing Engineering and Technology*, pp. 1–32, 2014.

[33] L. Birglen and T. Schlicht, "A statistical review of industrial robotic grippers," *Robotics and Computer-Integrated Manufacturing*, vol. 49, pp. 88–97, 2018.

[34] L. Birglen, T. Laliberté, and C. M. Gosselin, *Underactuated robotic hands*, vol. 40. Springer, 2007.

[35] Z. Samadikhoshkho, K. Zareinia, and F. Janabi-Sharifi, "A brief review on robotic grippers classifications," in *2019 IEEE Canadian Conference of Electrical and Computer Engineering (CCECE)*, pp. 1–4, IEEE, 2019.

[36] J. Hernandez, M. S. H. Sunny, J. Sanjuan, I. Rulik, M. I. I. Zarif, S. I. Ahamed, H. U. Ahmed, and M. H. Rahman, "Current designs of robotic arm grippers: A comprehensive systematic review," *Robotics*, vol. 12, no. 1, p. 5, 2023.

[37] DirectPlant, "Kiwi (actinidia deliciosa) — soorten en snoeien." https://www.directplant.nl/tuintips/kiwi/, 2025. Accessed: 7 January 2025.

[38] Kloeg, "Worker in greenhouse tomato picker." https://www.dreamstime.com/harmelen-netherlands-may-large-tomato-greenhouse-ripe-tomatoes-worker-tomato-picker-worker-greenhouse-tomato-picker-image102807053, 2025. Accessed: 7 January 2025.

[39] Corr. BELTA, "Wit-rusland is van plan om vleeskuikens aan de chinese markt te leveren." https://belta.by/search/findTags/318/page/5/, 2025. Accessed: 7 January 2025.

[40] C. W. Bac, E. J. van Henten, J. Hemming, and Y. Edan, "Harvesting Robots for High-value Crops: State-of-the-art Review and Challenges Ahead: Harvesting Robots for High-Value Crops: State-of-the-Art Review and Challenges Ahead," *Journal of Field Robotics*, vol. 31, pp. 888–911, Nov. 2014.

[41] V.-D. Nguyen, "Constructing force-closure grasps," *The International Journal of Robotics Research*, vol. 7, no. 3, pp. 3–16, 1988.

[42] A. Bicchi, "On the closure properties of robotic grasping," *The International Journal of Robotics Research*, vol. 14, no. 4, pp. 319–334, 1995.

[43] R. M. Murray, Z. Li, and S. S. Sastry, *A mathematical introduction to robotic manipulation.* CRC press, 2017.

[44] P. Y. Chua, T. Ilschner, and D. G. Caldwell, "Robotic manipulation of food products–a review," *Industrial Robot: An International Journal*, vol. 30, no. 4, pp. 345–354, 2003.

[45] Festo, "Vacuümzuiger vas vasb." https://www.festo.com/nl/nl/p/vacuumzuiger-id_VAS_VASB. Accessed: 12 September 2024.

[46] Schunk, "Swg hoekvormige radiale grijper pgr 385." https://schunk.com/be/nl/grijpsystemen/hoekige/radiale-grijper/swg/c/PGR_385. Accessed: 12 September 2024.

[47] Festo, "Bionic learning: Flexshape gripper, based on the archetype of the chameleon's tongue." https://www.festo.com/us/en/e/about-festo/research-and-development/bionic-learning-network/highlights-from-2015-to-2017/flexshapegripper-id_33444/, 2018. Accessed: 12 September 2024.

[48] Fipa, "Needle gripper, 2.5 mm stroke, ee variant gr04-711-25." https://fipa.com/en-EE/variant/gr04-711-25, n.d. Accessed: 12 September 2024.

[49] Robotiq, Alex Owen-Hill, "5 unusual vacuum grippers which innovated robotics." https://blog.robotiq.com/5-unusual-vacuum-grippers-which-innovated-robotics, 2019. Accessed: 12 September 2024.

[50] C. Parlitz, "Hardware for industrial gripping at schunk gmbh & co. kg," in *Grasping in Robotics*, pp. 363–384, Springer, 2012.

[51] Marel, "Marel's new robobatcher box is the world's leading intelligent robotic solution for fish packing." https://marel.com/en/news/marel-s-new-robobatcher-box-is-the-world-s-leading-intelligent-robotic-solution-for-fish-packing/, 2021. Accessed: 12 September 2024.

[52] MTSprout - Management, "Delfts robothandje grijpt groenten." https://mtsprout.nl/leiderschap/management/delfts-robothandje-grijpt-groenten, 2010. Accessed: 11 September 2024.

[53] X. Shan and L. Birglen, "Modeling and analysis of soft robotic fingers using the fin ray effect," *The International journal of robotics research*, vol. 39, no. 14, pp. 1686–1705, 2020.

[54] The Next Web, "Soft robotics will pick fruit with finesse and save your life too." https://thenextweb.com/news/soft-robotics-a-new-breed-of-robots-with-a-softer-touch, 2017. Accessed: 11 September 2024.

[55] Y.-J. Kim, H. Song, and C.-Y. Maeng, "Blt gripper: An adaptive gripper with active transition capability between precise pinch and compliant grasp," *IEEE Robotics and Automation Letters*, vol. 5, no. 4, pp. 5518–5525, 2020.

[56] C. Gosselin, F. Pelletier, and T. Laliberte, "An anthropomorphic underactuated robotic hand with 15 dofs and a single actuator," in *2008 IEEE International Conference on Robotics and Automation*, pp. 749–754, IEEE, 2008.

[57] Z. Wang and S. Hirai, "A soft gripper with adjustable stiffness and variable working length for handling food material," in *2018 IEEE International Conference on Real-time Computing and Robotics (RCAR)*, pp. 25–29, IEEE, 2018.

[58] G. A. Kragten and J. L. Herder, "The ability of underactuated hands to grasp and hold objects," *Mechanism and Machine Theory*, vol. 45, no. 3, pp. 408–425, 2010.

[59] T. Lien, "Gripper technologies for food industry robots," in *Robotics and Automation in the Food Industry*, pp. 143–170, Elsevier, 2013.

[60] A. Bicchi and V. Kumar, "Robotic grasping and contact: a review," in *Proceedings 2000 ICRA. Millennium Conference. IEEE International Conference on Robotics and Automation. Symposia Proceedings (Cat. No.00CH37065)*, vol. 1, pp. 348–353 vol.1, Apr. 2000. ISSN: 1050-4729.

[61] G. J. Monkman, S. Hesse, R. Steinmann, and H. Schunk, *Robot grippers*. John Wiley & Sons, 2007.

[62] D. Prattichizzo and J. C. Trinkle, "Grasping," *Springer handbook of robotics*, pp. 955–988, 2016.

[63] G. A. Kragten, *Underactuated Hands: Fundamentals, Performance Analysis and Design*. Ph.d. dissertation, Delft University of Technology, Delft, The Netherlands, 2011. https://research.tudelft.nl/en/publications/underactuated-hands-fundamentals-performance-analysis-and-design/ (Accessed: 7 January 2025).

[64] I. I. Borisov, O. I. Borisov, V. S. Gromov, S. M. Vlasov, and S. A. Kolyubin, "Versatile gripper as key part for smart factory," in *2018 IEEE Industrial Cyber-Physical Systems (ICPS)*, pp. 476–481, IEEE, 2018.

[65] W. Friedl and M. A. Roa, "Clash—a compliant sensorized hand for handling delicate objects," *Frontiers in Robotics and AI*, vol. 6, p. 138, 2020.

[66] Z. Qiu, H. Paul, Z. Wang, S. Hirai, and S. Kawamura, "An evaluation system of robotic end-effectors for food handling," *Foods*, vol. 12, no. 22, p. 4062, 2023.

[67] L. Birglen, "Enhancing versatility and safety of industrial grippers with adaptive robotic fingers," in *2015 IEEE/RSJ international conference on intelligent robots and systems (IROS)*, pp. 2911–2916, IEEE, 2015.

[68] S. Dontu, E. Kanhere, and P. V. Y. Alvarado, "Starfish-inspired scooping soft gripper for cluster grasping applications," in *2024 IEEE 7th International Conference on Soft Robotics (RoboSoft)*, pp. 1034–1041, IEEE, 2024.

[69] Z. Wang, H. Furuta, S. Hirai, and S. Kawamura, "A scooping-binding robotic gripper for handling various food products," *Frontiers in Robotics and AI*, vol. 8, p. 640805, 2021.

[70] Y. Liu, J. Hou, C. Li, and X. Wang, "Intelligent soft robotic grippers for agricultural and food product handling: A brief review with a focus on design and control," *Advanced Intelligent Systems*, vol. 5, no. 12, p. 2300233, 2023.

[71] L. Kang, S.-H. Kim, and B.-J. Yi, "Modeling, design, and implementation of an under-actuated gripper with capability of grasping thin objects," *Machines*, vol. 9, no. 12, p. 347, 2021.

[72] C. Wang, Y. Zhou, B. Xie, J. Xie, and J. Zhang, "An underactuated universal gripper: Design, analysis, and experiment," *Energies*, vol. 15, no. 23, p. 9151, 2022.

[73] R. A. Stavenuiter, L. Birglen, and J. L. Herder, "A planar underactuated grasper with adjustable compliance," *Mechanism and Machine Theory*, vol. 112, pp. 295–306, 2017.

[74] G. A. Kragten, M. Baril, C. Gosselin, and J. L. Herder, "Stable precision grasps by underactuated fingers," *Transaction on Robotics*, 2011.

[75] H. de Visser and J. L. Herder, "Force-directed design of a voluntary closing hand prosthesis," *Journal of rehabilitation research and development*, vol. 37, no. 3, pp. 261–272, 2000.

[76] W. Sjoerdsma, J. Herder, M. Horward, A. Jansen, J. Bannenberg, and C. Grimbergen, "Force transmission of laparoscopic grasping instruments," *Minimally invasive therapy & allied technologies*, vol. 6, no. 4, pp. 274–278, 1997.

[77] S. Li, J. J. Stampfli, H. J. Xu, E. Malkin, E. V. Diaz, D. Rus, and R. J. Wood, "A vacuum-driven origami "magic-ball" soft gripper," in *2019 International Conference on Robotics and Automation (ICRA)*, pp. 7401–7408, IEEE, 2019.

[78] K. C. Bingham, M. Hessler, S. Lama, and T. Deemyad, "Design and implementation of a compliant gripper for form closure of diverse objects," *Applied Sciences*, vol. 13, no. 17, p. 9677, 2023.

[79] A. Milojević, S. Linß, and H. Handroos, "Soft robotic compliant two-finger gripper mechanism for adaptive and gentle food handling," in *2021 IEEE 4th International Conference on Soft Robotics (RoboSoft)*, pp. 163–168, IEEE, 2021.

[80] A. Agarwal, A. Baranwal, G. Stephen Sugun, and P. K. Agnihotri, "Design and fabrication of a bio-inspired soft robotic gripper," in *Machines, Mechanism and Robotics: Proceedings of iNaCoMM 2019*, pp. 1105–1111, Springer, 2022.

[81] Z. He, B. Lian, and Y. Song, "Rigid-soft coupled robotic gripper for adaptable grasping," *Journal of Bionic Engineering*, vol. 20, no. 6, pp. 2601–2618, 2023.

[82] Y. Yang, Y. Li, Y. Chen, Y. Li, T. Ren, and Y. Ren, "Design and automatic fabrication of novel bio-inspired soft smart robotic hands," *IEEE Access*, vol. 8, pp. 155912–155925, 2020.

[83] A. M. Dollar and R. D. Howe, "The sdm hand as a prosthetic terminal device: a feasibility study," in *2007 IEEE 10th International Conference on Rehabilitation Robotics*, pp. 978–983, IEEE, 2007.

[84] R. Doshi, C. Yeh, and M. LeBlanc, "The design and development of a gloveless endoskeletal prosthetic hand," *Journal of rehabilitation research and development*, vol. 35, pp. 388–395, 1998.

[85] F. Lotti, P. Tiezzi, G. Vassura, L. Biagiotti, and C. Melchiorri, "Ubh 3: an anthropomorphic hand with simplified endo-skeletal structure and soft continuous fingerpads," in *IEEE International Conference on Robotics and Automation, 2004. Proceedings. ICRA'04. 2004*, vol. 5, pp. 4736–4741, IEEE, 2004.

[86] M. C. Carrozza, G. Cappiello, G. Stellin, F. Zaccone, F. Vecchi, S. Micera, and P. Dario, "A cosmetic prosthetic hand with tendon driven under-actuated mechanism and compliant joints: ongoing research and preliminary results," in *Proceedings of the 2005 IEEE International Conference on Robotics and Automation*, pp. 2661–2666, IEEE, 2005.

[87] E. Boudreault and C. m. M. Gosselin, "Design of sub-centimetre underactuated compliant grippers," in *International Design Engineering Technical Conferences and Computers and Information in Engineering Conference*, vol. 42568, pp. 119–127, 2006.

[88] M. Doria and L. Birglen, "Design of an underactuated compliant gripper for surgery using nitinol," *Journal of Medical Devices*, vol. 3, no. 1, p. 011007, 2009. Published Online: March 17, 2009.

[89] W. Crooks, S. Rozen-Levy, B. Trimmer, C. Rogers, and W. Messner, "Passive gripper inspired by *Manduca sexta* and the Fin Ray® Effect," *International Journal of Advanced Robotic Systems*, vol. 14, p. 172988141772115, July 2017.

[90] O. Pfaff, S. Simeonov, I. Cirovic, and P. Stano, "Application of Finray Effect Approach for Production Process Automation," in *DAAAM Proceedings* (B. Katalinic, ed.), vol. 1, pp. 1247–1248, DAAAM International Vienna, 1 ed., 2011.

[91] L. L. Howell, S. P. Magleby, and B. M. Olsen, *Handbook of Compliant Mechanisms*. Hoboken, NJ, USA: Wiley, 2013.

[92] B. Belzile and L. Birglen, "A compliant self-adaptive gripper with proprioceptive haptic feedback," *Autonomous Robots*, vol. 36, pp. 79–91, 2014.

[93] A. Huisjes and V. van der Wijk, "Compliant manipulator design method (comad) for the type synthesis of all serial and parallel multi-dof compliant mechanisms, with example of a schönflies motion generator," *Mechanism and Machine Theory*, vol. 186, p. 105342, 2023.

[94] L. L. Howell, *Compliant mechanisms*. John Wiley & Sons, 2001.

[95] P. Steutel, G. A. Kragten, and J. L. Herder, "Design of an underactuated finger with a monolithic structure and largely distributed compliance," in *International Design Engineering Technical Conferences and Computers and Information in Engineering Conference*, vol. 44106, pp. 355–363, 2010.

[96] G. Zhong, Y. Hou, and W. Dou, "A soft pneumatic dexterous gripper with convertible grasping modes," *International Journal of Mechanical Sciences*, vol. 153-154, pp. 445–456, Apr. 2019.

[97] Z. Wang, Y. Torigoe, and S. Hirai, "A Prestressed Soft Gripper: Design, Modeling, Fabrication, and Tests for Food Handling," *IEEE Robotics and Automation Letters*, vol. 2, pp. 1909–1916, Oct. 2017. Conference Name: IEEE Robotics and Automation Letters.

[98] Z. Wang, K. Or, and S. Hirai, "A dual-mode soft gripper for food packaging," *Robotics and Autonomous Systems*, vol. 125, p. 103427, Mar. 2020.

[99] A. Silwal, J. R. Davidson, M. Karkee, C. Mo, Q. Zhang, and K. Lewis, "Design, integration, and field evaluation of a robotic apple harvester," *Journal of Field Robotics*, vol. 34, no. 6, 2017.

[100] J. R. Davidson, A. Silwal, C. J. Hohimer, M. Karkee, C. Mo, and Q. Zhang, "Proof-of-concept of a robotic apple harvester," in *2016 IEEE/RSJ International Conference on Intelligent Robots and Systems (IROS)*, pp. 634–639, Oct. 2016. ISSN: 2153-0866.

[101] Y. Ge, Y. Xiong, G. L. Tenorio, and P. J. From, "Fruit localization and environment perception for strawberry harvesting robots," *IEEE access*, vol. 7, pp. 147642–147652, 2019.

[102] D. SepúLveda, R. Fernández, E. Navas, M. Armada, and P. González-De-Santos, "Robotic Aubergine Harvesting Using Dual-Arm Manipulation," *IEEE Access*, vol. 8, pp. 121889–121904, 2020. Conference Name: IEEE Access.

[103] C. W. Bac, T. Roorda, R. Reshef, S. Berman, J. Hemming, and E. J. van Henten, "Analysis of a motion planning problem for sweet-pepper harvesting in a dense obstacle environment," *Biosystems Engineering*, vol. 146, pp. 85–97, June 2016.

[104] J. Hemming, C. W. Bac, and E. J. van Henten, "A robot for harvesting sweet-pepper in greenhouses," *International Conference of Agricultural Engineering*, vol. AgEng 2014 Zurich, p. 8, 2014.

[105] O. Khatib, "Real-time obstacle avoidance for manipulators and mobile robots," in *1985 IEEE International Conference on Robotics and Automation Proceedings*, vol. 2, pp. 500–505, Mar. 1985.

[106] D. Popov, A. Klimchik, and N. Mavridis, "Collision detection, localization classification for industrial robots with joint torque sensors," in *2017 26th IEEE International Symposium on Robot and Human Interactive Communication (RO-MAN)*, pp. 838–843, Aug. 2017. ISSN: 1944-9437.

[107] E. J. Van Henten, E. J. Schenk, L. G. van Willigenburg, J. Meuleman, and P. Barreiro, "Collision-free inverse kinematics of the redundant seven-link manipulator used in a cucumber picking robot," *Biosystems Engineering*, vol. 106, pp. 112–124, June 2010.

[108] C. Eppner and O. Brock, "Planning grasp strategies that exploit environmental constraints," in *2015 IEEE international conference on robotics and automation (ICRA)*, pp. 4947–4952, IEEE, 2015.

[109] R. Wang, Y. Miao, and K. E. Bekris, "Efficient and high-quality prehensile rearrangement in cluttered and confined spaces," in *2022 International Conference on Robotics and Automation (ICRA)*, pp. 1968–1975, IEEE, 2022.

[110] T. Boroushaki, J. Leng, I. Clester, A. Rodriguez, and F. Adib, "Robotic grasping of fully-occluded objects using rf perception," in *2021 IEEE International Conference on Robotics and Automation (ICRA)*, pp. 923–929, IEEE, 2021.

[111] B. H. Do, V. Banashek, and A. M. Okamura, "Dynamically Reconfigurable Discrete Distributed Stiffness for Inflated Beam Robots," in *2020 IEEE International Conference on Robotics and Automation (ICRA)*, pp. 9050–9056, May 2020. ISSN: 2577-087X.

[112] E. W. Hawkes, L. H. Blumenschein, J. D. Greer, and A. M. Okamura, "A soft robot that navigates its environment through growth," *Science Robotics*, vol. 2, p. eaan3028, July 2017. Publisher: American Association for the Advancement of Science.

[113] L. Blumenschein, M. Coad, D. Haggerty, A. Okamura, and E. Hawkes, "Design, Modeling, Control, and Application of Everting Vine Robots," *Frontiers in Robotics and AI*, vol. 7, 2020.

[114] S. Al Harthy, H. Sadati, C. Girerd, S. Kim, Z. Wu, B. Saldarriaga, C. Seneci, T. Morimoto, and C. Bergeles, "Tip-growing robots: Design, theory, application," *IEEE Transactions on Robotics*, 2024.

[115] B. Mazzolai, F. Tramacere, I. Fiorello, and L. Margheri, "The bio-engineering approach for plant investigations and growing robots. a mini-review," *Frontiers in Robotics and AI*, vol. 7, p. 573014, 2020.

[116] J. G. Sanchez and J. L. Herder, "Synthesis methods in compliant mechanisms: an overview," in *2009 Design engineering technical conferences & computers and information in engineering conference, IDETC/CIE 2009*, pp. 1–22, ASME, 2009.

[117] J. B. Hopkins and M. L. Culpepper, "Synthesis of multi-degree of freedom, parallel flexure system concepts via freedom and constraint topology (fact)–part i: Principles," *Precision Engineering*, vol. 34, no. 2, pp. 259–270, 2010.

[118] J. B. Hopkins and M. L. Culpepper, "Synthesis of multi-degree of freedom, parallel flexure system concepts via freedom and constraint topology (fact). part ii: Practice," *Precision Engineering*, vol. 34, no. 2, pp. 271–278, 2010.

[119] D. Farhadi Machekposhti, N. Tolou, and J. L. Herder, "A review on compliant joints and rigid-body constant velocity universal joints toward the design of compliant homokinetic couplings," *Journal of Mechanical Design*, vol. 137, no. 3, p. 032301, 2015.

[120] S. Kota, K.-J. Lu, Z. Kreiner, B. Trease, J. Arenas, and J. Geiger, "Design and application of compliant mechanisms for surgical tools," *Journal of Biomechanical Engineering*, vol. 127, no. 6, pp. 981–989, 2005.

[121] A. Lamers, J. A. G. Sánchez, and J. L. Herder, "Design of a statically balanced fully compliant grasper," *Mechanism and machine theory*, vol. 92, pp. 230–239, 2015.

[122] S. P. Timoshenko, "On the correction for shear of the differential equation for transverse vibrations of bars of uniform cross-section," *Philosophical Magazine and Journal of Science*, vol. 41, no. 245, pp. 744–746, 1921.

[123] H. Li and G. Hao, "Constraint-force-based approach of modelling compliant mechanisms: Principle and application," *Precision Engineering*, vol. 47, pp. 158–181, 2017.

[124] S. Awtar, A. H. Slocum, and E. Sevincer, "Characteristics of beam-based flexure modules," *Journal of Mechanical Design*, vol. 129, no. 10, pp. 1029–1049, 2007.

[125] S. Awtar and A. H. Slocum, "A generalized constraint model for two-dimensional beam flexures: Nonlinear load–displacement formulation," *Journal of Mechanical Design*, vol. 135, no. 2, p. 021004, 2013.

[126] N. Lobontiu, "Compliance-based matrix method for modeling the quasi-static response of planar serial flexure-hinge mechanisms," *Precision Engineering*, vol. 38, no. 3, pp. 639–650, 2014.

[127] F. Ma and G. Chen, "Chained beam-constraint-model (cbcm): a powerful tool for modeling large and complicated deflections of flexible beams in compliant mechanisms," in *International Design Engineering Technical Conferences and Computers and Information in Engineering Conference*, vol. 46360, p. V05AT08A027, American Society of Mechanical Engineers, 2014.

[128] L. Campanile and A. Hasse, "A simple and effective solution of the elastica problem," *Proceedings of the Institution of Mechanical Engineers, Part C: Journal of Mechanical Engineering Science*, vol. 222, no. 12, pp. 2513–2516, 2008.

[129] L. L. Howell and A. Midha, "Parametric deflection approximations for end-loaded, large-deflection beams in compliant mechanisms," *Journal of Mechanical Design*, vol. 117, pp. 156–165, 03 1995.

[130] S. Henning, S. Linß, P. Gräser, R. Theska, and L. Zentner, "Non-linear analytical modeling of planar compliant mechanisms," *Mechanism and Machine Theory*, vol. 155, p. 104067, 2021.

[131] M. Ling, L. L. Howell, J. Cao, and G. Chen, "Kinetostatic and dynamic modeling of flexure-based compliant mechanisms: a survey," *Applied Mechanics Reviews*, vol. 72, no. 3, p. 030802, 2020.

[132] L. L. Howell, "Compliant mechanisms," in *21st Century Kinematics: The 2012 NSF Workshop*, pp. 189–216, Springer, 2013.

[133] G. Hao, J. Yu, and H. Li, "A brief review on nonlinear modeling methods and applications of compliant mechanisms," *Frontiers of Mechanical Engineering*, vol. 11, pp. 119–128, 2016.

[134] L. L. Howell and A. Midha, "A method for the design of compliant mechanisms with small-length flexural pivots," *Journal of Mechanical Design*, vol. 116, pp. 280–290, 03 1994.

[135] M. D. Berglund, S. P. Magleby, and L. L. Howell, "Design rules for selecting and designing compliant mechanisms for rigid-body replacement synthesis," in *International Design Engineering Technical Conferences and Computers and Information in Engineering Conference*, vol. 35128, pp. 233–241, American Society of Mechanical Engineers, 2000.

[136] H.-J. Su, "A pseudorigid-body 3r model for determining large deflection of cantilever beams subject to tip loads," *Journal of Mechanisms and Robotics*, vol. 1, p. 021008, 01 2009.

[137] G. Chen, B. Xiong, and X. Huang, "Finding the optimal characteristic parameters for 3r pseudo-rigid-body model using an improved particle swarm optimizer," *Precision Engineering*, vol. 35, no. 3, pp. 505–511, 2011.

[138] V. K. Venkiteswaran and H.-J. Su, "Pseudo-rigid-body models for circular beams under combined tip loads," *Mechanism and Machine Theory*, vol. 106, pp. 80–93, 2016.

[139] V. K. Venkiteswaran and H.-J. Su, "A parameter optimization framework for determining the pseudo-rigid-body model of cantilever-beams," *Precision Engineering*, vol. 40, pp. 46–54, 2015.

[140] F. G. Broeren, V. van der Wijk, and J. L. Herder, "Spatial pseudo-rigid body model for the analysis of a tubular mechanical metamaterial," *Mathematics and Mechanics of Solids*, vol. 25, no. 2, pp. 305–316, 2020.

[141] J. Bastien and L. Birglen, "Variable stiffness soft robotic fingers using snap-fit kinematic reconfiguration," *IEEE Transactions on Robotics*, vol. 39, no. 6, pp. 4567–4580, 2023.

[142] B. Friederich, A. E. Huisjes, and J. L. Herder, "Design and validation of a manoeuvring caging gripper for cluttered environments," Master's thesis, Delft University of Technology, 2022. https://resolver.tudelft.nl/uuid:f20e97b0-97a4-43b7-91ec-1acb3bca72ac.

[143] M. Ciocarlie, F. M. Hicks, R. Holmberg, J. Hawke, M. Schlicht, J. Gee, S. Stanford, and R. Bahadur, "The Velo gripper: A versatile single-actuator design for enveloping, parallel and fingertip grasps," *The International Journal of Robotics Research*, vol. 33, pp. 753–767, Apr. 2014. Publisher: SAGE Publications Ltd STM.

[144] Q. Lei and M. Wisse, "Object grasping by combining caging and force closure," in *2016 14th International Conference on Control, Automation, Robotics and Vision (ICARCV)*, pp. 1–8, IEEE, 2016.

[145] D. Kim, Y. Maeda, and S. Komiyama, "Caging-based grasping of deformable objects for geometry-based robotic manipulation," *ROBOMECH Journal*, vol. 6, pp. 1–13, 2019.

[146] Y. Xiong, Y. Ge, and P. J. From, "Push and Drag: An Active Obstacle Separation Method for Fruit Harvesting Robots," in *2020 IEEE International Conference on Robotics and Automation (ICRA)*, pp. 4957–4962, May 2020. ISSN: 2577-087X.

[147] E. Páll and O. Brock, "Analysis of Open-Loop Grasping From Piles," in *2021 IEEE International Conference on Robotics and Automation (ICRA)*, pp. 2591–2597, May 2021. ISSN: 2577-087X.

[148] R. Raja, A. K. Burusa, G. Kootstra, and E. J. Van Henten, "Advanced robotic system for efficient pick-and-place of deformable poultry in cluttered bin: A comprehensive evaluation approach," *IEEE Transactions on AgriFood Electronics*, vol. 2, no. 2, pp. 355–371, 2024.

[149] G. Mantriota, "Theoretical model of the grasp with vacuum gripper," *Mechanism and Machine Theory*, vol. 42, pp. 2–17, Jan. 2007.

[150] E. Brown, N. Rodenberg, J. Amend, A. Mozeika, E. Steltz, M. Zakin, H. Lipson, and H. Jaeger, "Universal robotic gripper based on the jamming of granular material," *Proceedings of the National Academy of Sciences of the United States of America*, vol. 107, no. 44, pp. 18809–18814, 2010.

[151] C. Meijneke, G. Kragten, and M. Wisse, "Design and performance assessment of an underactuated hand for industrial applications," *Mechanical Sciences*, vol. 2, no. 1, pp. 9–15, 2011.

[152] M. Li, R. Obregon, J. J. Heit, A. Norbash, E. W. Hawkes, and T. K. Morimoto, "Vine catheter for endovascular surgery," *IEEE Transactions on Medical Robotics and Bionics*, vol. 3, no. 2, pp. 384–391, 2021.

[153] E. Rimon and A. Blake, "Caging 2d bodies by 1-parameter two-fingered gripping systems," in *Proceedings of IEEE International Conference on Robotics and Automation*, vol. 2, pp. 1458–1464, IEEE, 1996.

[154] E. Rimon and A. Blake, "Caging planar bodies by one-parameter two-fingered gripping systems," *The International Journal of Robotics Research*, vol. 18, no. 3, pp. 299–318, 1999.

[155] J. Falco, K. Van Wyk, S. Liu, and S. Carpin, "Grasping the performance: Facilitating replicable performance measures via benchmarking and standardized methodologies," *IEEE Robotics & Automation Magazine*, vol. 22, no. 4, pp. 125–136, 2015.

[156] A. Rodriguez, M. T. Mason, and S. Ferry, "From caging to grasping," *The International Journal of Robotics Research*, vol. 31, no. 7, pp. 886–900, 2012.

[157] A. Shiva, A. Stilli, Y. Noh, A. Faragasso, I. De Falco, G. Gerboni, M. Cianchetti, A. Menciassi, K. Althoefer, and H. A. Wurdemann, "Tendon-based stiffening for a pneumatically actuated soft manipulator," *IEEE Robotics and Automation Letters*, vol. 1, no. 2, pp. 632–637, 2016.

[158] D.-G. Lee, N. G. Kim, and J.-H. Ryu, "High-curvature consecutive tip steering of a soft growing robot for improved target reachability," in *2023 IEEE/RSJ International Conference on Intelligent Robots and Systems (IROS)*, pp. 6477–6483, IEEE, 2023.

[159] J. D. Greer, T. K. Morimoto, A. M. Okamura, and E. W. Hawkes, "A soft, steerable continuum robot that grows via tip extension," *Soft robotics*, vol. 6, no. 1, pp. 95–108, 2019.

[160] A. M. Kübler, S. U. Rivera, F. B. Raphael, J. Förster, R. Siegwart, and A. M. Okamura, "A multi-segment, soft growing robot with selective steering," in *2023 IEEE International Conference on Soft Robotics (RoboSoft)*, pp. 1–7, IEEE, 2023.

[161] T. Takahashi, M. Watanabe, K. Abe, K. Tadakuma, N. Saiki, M. Konyo, and S. Tadokoro, "Inflated bendable eversion cantilever mechanism with inner skeleton for increased stiffness," *IEEE Robotics and Automation Letters*, vol. 8, no. 1, pp. 168–175, 2022.

[162] J. D. Greer, L. H. Blumenschein, R. Alterovitz, E. W. Hawkes, and A. M. Okamura, "Robust navigation of a soft growing robot by exploiting contact with the environment," *The International Journal of Robotics Research*, vol. 39, no. 14, pp. 1724–1738, 2020.

[163] R. R. Ma and A. M. Dollar, "In-hand manipulation primitives for a minimal, underactuated gripper with active surfaces," in *International Design Engineering Technical Conferences and Computers and Information in Engineering Conference*, vol. 50152, p. V05AT07A072, American Society of Mechanical Engineers, 2016.

[164] N. Rahman, L. Carbonari, M. D'Imperio, C. Canali, D. G. Caldwell, and F. Cannella, "A dexterous gripper for in-hand manipulation," in *2016 IEEE International Conference on Advanced Intelligent Mechatronics (AIM)*, pp. 377–382, IEEE, 2016.

[165] B. Khulan and Y. Dongwon, "Soft robotic gripper with chambered fingers for performing in-hand manipulation," *Applied Sciences*, vol. 9, no. 15, p. 2967, 2019.

[166] Q. Lu, N. Baron, A. B. Clark, and N. Rojas, "Systematic object-invariant in-hand manipulation via reconfigurable underactuation: Introducing the ruth gripper," *The International Journal of Robotics Research*, vol. 40, no. 12-14, pp. 1402–1418, 2021.

[167] A. Pagoli, F. Chapelle, J. A. Corrales, Y. Mezouar, and Y. Lapusta, "A soft robotic gripper with an active palm and reconfigurable fingers for fully dexterous in-hand manipulation," *IEEE Robotics and Automation Letters*, vol. 6, no. 4, pp. 7706–7713, 2021.

[168] T. Takahashi, K. Tadakuma, M. Watanabe, E. Takane, N. Hookabe, H. Kajiahara, T. Yamasaki, M. Konyo, and S. Tadokoro, "Eversion robotic mechanism with hydraulic skeletonto realize steering function," *IEEE Robotics and Automation Letters*, vol. 6, no. 3, pp. 5413–5420, 2021.

[169] W. McMahan, B. A. Jones, and I. D. Walker, "Design and implementation of a multi-section continuum robot: Air-octor," in *2005 IEEE/RSJ international conference on intelligent robots and systems*, pp. 2578–2585, IEEE, 2005.

[170] A. Ataka, T. Abrar, F. Putzu, H. Godaba, and K. Althoefer, "Model-based pose control of inflatable eversion robot with variable stiffness," *IEEE Robotics and Automation Letters*, vol. 5, no. 2, pp. 3398–3405, 2020.

[171] M. Al-Dubooni, C. Wong, and K. Althoefer, "Hybrid continuum-eversion robot: Precise navigation and decontamination in nuclear environments using vine robot," in *Proceedings of the 2024 IEEE/RSJ International Conference on Intelligent Robots and Systems (IROS)*, (Abu Dhabi, United Arab Emirates), pp. 12443–12449, IEEE, 2024.

Overview of Author Contributions

This chapter provides a concise overview of the author's contributions to all chapters. Chapters 2–4 follow a journal format with co-author contributions listed accordingly. For the remaining chapters, only supervisory and collaborative input is summarised. Unless stated otherwise, all research was carried out by the author. Additional context on the research environment and collaborations is provided in the Preface, Acknowledgements, and the next chapter.

Chapter 1: Introduction

A. E. Huisjes (Dissertation Author): Performed the problem analysis through literature review, collaboration within the multidisciplinary consortium, and initial tests with commercial grippers. Reformulated the problem statement and defined the revised research direction. Proposed the confined-space grasping strategy by sketching and conceptualizing the desired finger behavior at an abstract level for navigation in dense environments with minimal impact, establishing the top-level concept. Selected and refined the most promising strategies into a mechanical finger concept together with the MSc research in Appendix B.2. Defined the overall research objective, subgoals, and thesis outline.
J. L. Herder: Acquired funding for the PhD position and authored the original project proposal. Provided supervision and high-level conceptual guidance, including the shift toward exploiting contact and using flexure-based navigation for load-bearing capacity.

Chapter 2: PRBM

A. E. Huisjes (First author): Led conceptualization and methodology. Developed the analytical framework, including the event-based PRBM, unified flexure–object topology, and switching/serial-topology modeling under potential-energy constraints. Designed and executed all experiments and analyses. Prepared all figures and wrote the full manuscript.
V. van der Wijk: Contributed to methodology refinement by suggesting alternative modeling approaches, supported experimental design by providing technical feedback.
J. L. Herder: Provided supervision and high-level conceptual guidance. Advised to first model straight-flexure navigation before curved configurations combined with eversion principles and suggested rotating objects in experiments. Reviewed the manuscript and contributed to structure, clarity, and positioning.

Chapter 3: DBCF-EM Gripper

J. H. B. Friederich (First author): Conducted the MSc thesis research on which this article is based. Led conceptualization and methodology for exploring alternative closing motions along the objects surface and friction reduction strategies. Developed the DBCF-EM gripper to realise the top-level concept principles of the envisioned gripper finger for confined space grasping, including detailed design, manufacturing, and testing. Prepared the initial article draft.
A. E. Huisjes (Second author): Contributed through prior problem investigation, conceptualization of top level concept, and and high-level methodology. Brought earlier research on navigational flexures that guided concept choice and experimental validation strategies. Integrated the FlexCRAFT robotic experiment. Wrote the complete article based on the MSc thesis for journal submission, substantially restructuring and refining the text, figures, definitions, video, and scientific positioning.
J. L. Herder: Served as supervisor, provided high-level conceptual guidance, and offered recommendations during development. Reviewed the final manuscript.

Chapter 4: SCF-EM Gripper

A. E. Huisjes (First author): Led the entire investigation, including conceptualization, methodology, design, manufacturing, and experimental validation. Designed and fabricated all prototypes (flexure, sleeve, pulley system, housing), developed the experimental setups, conducted all experiments, and interpreted the results. Prepared all figures, supplementary video material, and wrote the full manuscript.
J. L. Herder: Supervisor. Offered conceptual guidance and advice during key design and manufacturing stages. Reviewed the manuscript and contributed to structure, clarity, and scientific positioning.

Chapter 5: Discussion

A. E. Huisjes: Fully responsible for writing the Discussion chapter. Synthesised results across chapters, formulated forward-looking insights and design implications, and structured the chapter to guide future research. Work was carried out with feedback from J. L. Herder and V. van der Wijk.

Chapter 6: Conclusion

A. E. Huisjes: Written by the author, with occasional advice from J. L. Herder on scientific positioning.

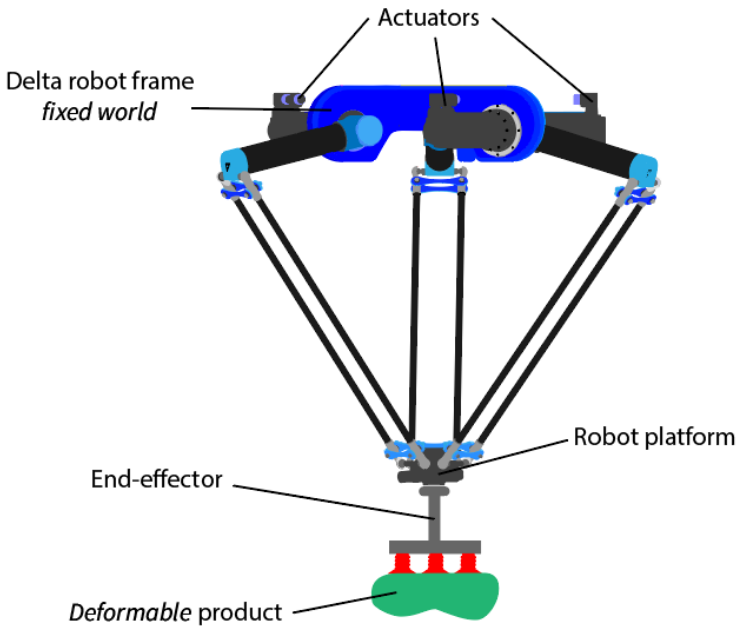
Contextual Exploratory Studies

This chapter presents an overview of six of the eight MSc projects conducted under our supervision, highlighting related work within our research group that explored agri-food gripping challenges using different approaches. In contrast to the two MSc studies presented in Appendix B and Appendix B.2, these exploratory projects are not directly related to the technology developed in this dissertation, but were conducted prior to or in parallel with it. Some of these projects helped identify industrial challenges and inspired the initial ideas behind our concept, while others were conducted in parallel to address different aspects or to solve application-specific problems within the research consortium—such as handling objects like bananas, for which the proposed technology was not the most suitable solution. Together, they illustrate the broader research context from which the concept of advancing flexure fingers was inspired and evolved—a context we wish to briefly highlight here as the closing reflection of this dissertation.

Payload F/M sensor for pneumatic grasping

Problem introduction

In the high-speed case of packaged food products, the detachment of objects from suction cup grippers has become a significant issue, particularly during rapid robotic movements. The ability to measure the dynamic forces and moments that act on the suction cups during these operations is crucial to addressing this challenge. However, traditional six-axis force sensors face performance limitations due to stiff vacuum hoses that must bypass the sensor, inducing unwanted parasitic loads, and affecting measurement accuracy.



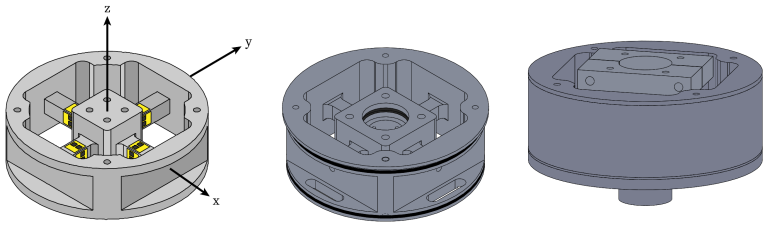
Figuur C.3: A high-speed delta robot grasping a product using suction cups. The interaction forces between the object and the suction cup are difficult to measure directly at the contact point. Therefore, a sensor is placed between the gripper and the robot to measure the forces acting during high-speed movements [1].

Methodology

To solve this problem, a six-axis force moment sensor was developed that integrates the airflow passage directly through its structure, eliminating the need for the vacuum hose to bypass the sensor and preventing parasitic load interference [1]. Strain gauges were selected as the sensing mechanism, arranged in a Maltese cross-sensor structure. The final sensor design was optimized using advanced techniques to meet the specific requirements of the high-speed case packing industry, ensuring accurate force measurement without

compromising suction performance.

Figure C.4 presents the design of the six-axis force moment sensor. The figure illustrates how airflow is routed through the sensor, preventing any interference with the measurement of forces during robot pick-and-place operations. The strain gauge layout and the compact sensor structure are also highlighted in the figure.



Figuur C.4: Design of the six-axis force moment sensor. On the left, the 6-DOF sensor with strain gauges is shown. The middle section illustrates the airflow throughput mechanism integrated into the sensor. On the right, the complete sensor with its protective coverage is displayed [1].

Results and conclusion

The sensor was successfully fabricated and tested in a case-packing system. The integration of airflow through the sensor did not affect the detachment limits of products from the suction cups, confirming that the sensor maintained suction performance. Validation testing revealed that the sensor achieved a maximum cross-coupling of 25.6%, and the measurement error in the Fz direction was 8%, slightly above the targeted 5%. Although the Fz error exceeded the design goals, the errors in all other directions were below 5%, and the sensor was deemed suitable for dynamic load measurements in high-speed case packing applications. Airflow integration is not limited to suction cup grippers and could benefit other pneumatic grippers in similar high-speed applications.

Using this sensor, it was revealed that the primary cause of peeling in suction cups is the moment generated by the swinging of the product during high-speed pick-and-place operations. This provides valuable insights for improving their design, such as incorporating a rotational degree of freedom between the gripper and the robot to reduce the moment at the gripper-object interface.

Mattress-FRE finger: spatial form-closure grip

Problem introduction

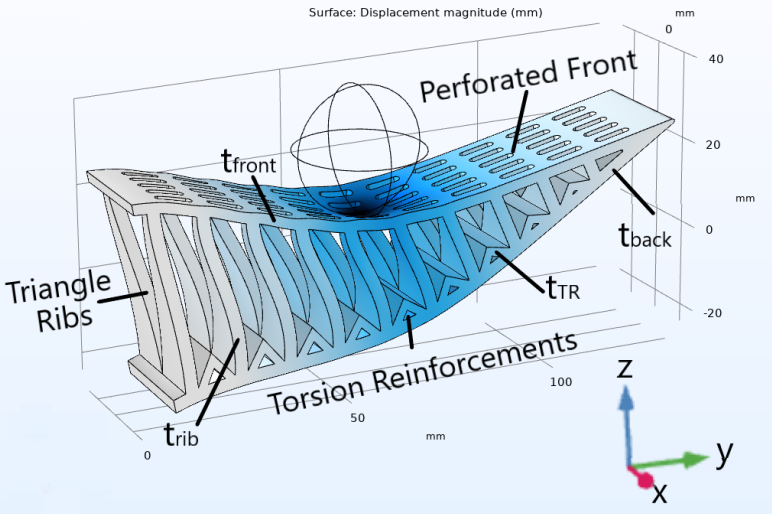
Traditional Fin Ray Effect (FRE) fingers are well regarded for their versatility and effectiveness in pick-and-place automation, thanks to their soft grasp and adaptive shape-conforming capabilities. These grippers passively enclose objects through deformation, forming a planar closed grip in their longitudinal direction. However, they encounter major difficulties when grasping spherical or laterally round objects. The current 2D planar design results in unstable grips, as it relies heavily on lateral friction, and when objects are positioned off-center, they risk slipping away as the structure tends to open sideways due to bending. Although adding extra fingers in a tripod configuration improves stability, it also increases the size and precision requirements for positioning, making this approach impractical for dense agri-food environments.

Methodology

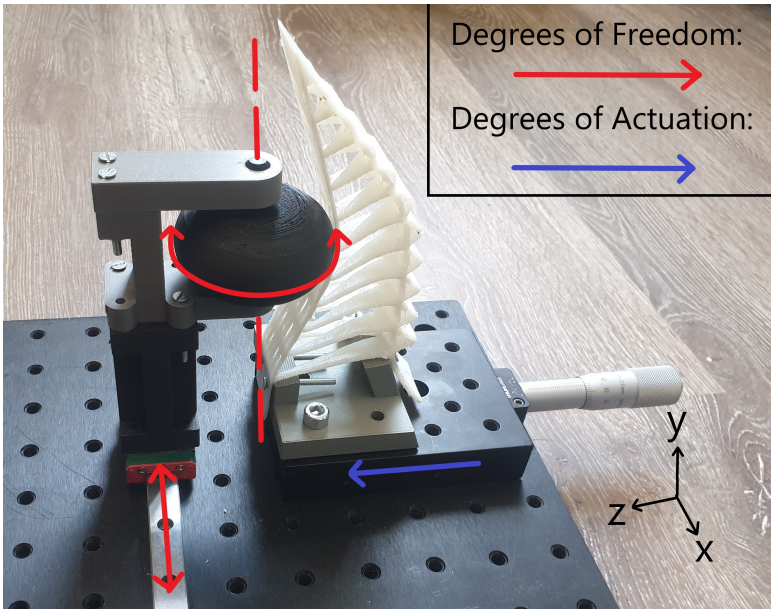
This research [2], sought to redesign the FRE finger to achieve a 3D form-closure grip, providing stability from all directions, both longitudinal and lateral. The new design envisioned a "mattress-like"structure that allows the object to sink into the finger through deformation, and the edges of the fingers provided stiffness to secure it. To realize this design, the FACT method was used to define and eliminate unnecessary constraints in the rib and front facet structure of the finger. Key modifications included adjusting the rib structure to create space for the object and establishing compliant rotation points on the sides. In addition, the front facet was perforated to allow better deformation. Finally, reinforcements are added on the back facet to enhance the torsional stiffness. These changes resulted in the "mattress-FRE finger,ä compliant structure that allows objects to sink into the finger while maintaining a secure grip without relying on friction. The design dimensions were optimized to ensure that the structure could effectively hold objects in place.

Results and conclusion

The redesigned FRE finger was fabricated and tested, demonstrating its ability to securely grasp spherical objects with just one finger pressing it against a supporting surface, achieving complete form-closure from all directions. The new design also exhibited excellent centering capabilities, even when objects were misaligned by up to 16 mm, a substantial improvement over the basic FRE design, which failed to hold the test object with misalignments as small as 8 mm. This advancement highlights the enhanced performance of the mattress-FRE finger in the safe handling of spherical objects in challenging environments.



Figuur C.5: The design of the Mattress-FRE finger. The compliant structure allows the object to sink into the finger, providing a stable form-closed grasp from all directions [2].



Figuur C.6: The manufactured Mattress-FRE finger in the experimental setup, testing grasp stability with a spherical object. The object was constrained longitudinally but free to move laterally. A stable grasp was achieved when the object remained stationary or centered itself, while instability occurred if the object moved sideways or away, measured for different off-sets [2].

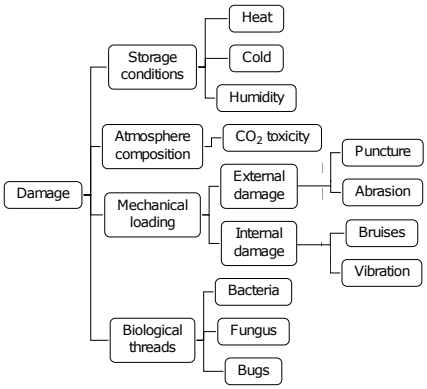
Hooked fingered gripper for bunches of bananas

Problem introduction

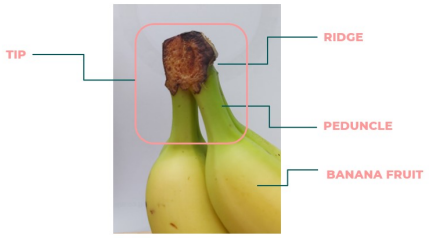
Grasping bunches of bananas poses a significant challenge for mechanical grippers due to the variability in the size, shape, and sensitivity of the fruit to damage. Although previous research focused on gripping single bananas with pinching or granular grippers, these methods proved inadequate to grip entire bunches without causing harm or loss. The need for a gripper that can handle bunches of bananas effectively, while minimizing damage, led to the development of a new strategy to enable robotic automation in supermarket environments.

Methodology

The gripper was designed to grip the banana bunch at its sturdy connecting tip, which is less prone to damage and easily detectable by robotic systems. This location was chosen based on a review of the literature on post-harvest damage, of which an overview is shown in Fig. C.7a, and practical testing of stable grasping points during this research.



(a) Sources of post-harvest fruit damage in the industry. External mechanical damage includes puncturing (skin penetration) or abrasion (skin friction), while internal damage results from impacts or compression, causing bruising or vibrations during transport. [3]

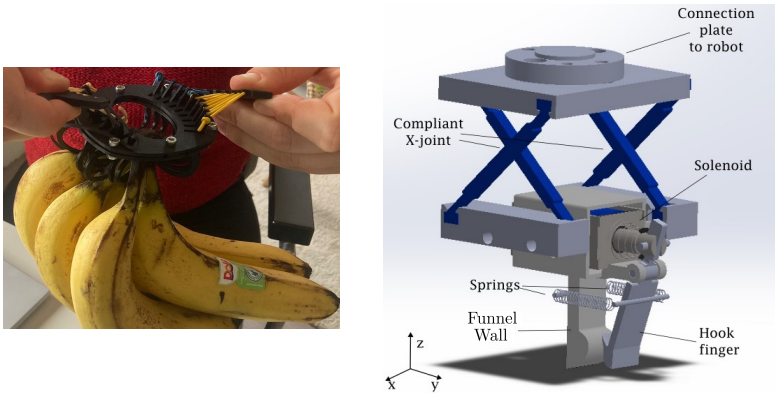


(b) Overview of banana-bunch-tip related terminology, highlighting parts such as the peduncle, ridge, and tip used to determine the grasping location.[3]

Figuur C.7: (a) Sources of post-harvest fruit damage, and (b) banana bunch-tip terminology used to determine optimal grasping points.

The tip of the bunch consists of several parts: the individual banana peduncles, a ridge (the breaking point of the plant), and the rigid part above the ridge, as shown in Fig. C.7b. To grasp at those locations, different grasper concepts were explored and tested, including ao multi-finger and pinch grip designs, but also the final design used a hook to lift the bunch by supporting it under the ridge, as shown on the right side of Fig. C.9.

The hook-based concept features a static nudge and an actuated hook finger, which scoops under the ridge to lift the bunch while allowing for rotation to reduce the need for



Figuur C.8: Two variations of banana bunch tip grippers: on the left, the multi-fingered concept, where each finger moves independently to hook between the banana peduncles; on the right, the final chosen design, which lifts the bunch by placing a hook under the ridge and gently clamping. The gripper is attached to the robot via a compliant X-joint, allowing flexibility during operation.[3]

high grasping forces since the bunch tends to rotate when being lifted. The nudge gently clamps the bunch to keep it on the hook, preventing lateral movement, while the funnel-shaped tip guides the gripper into position, compensating for shape variations and robotic positioning errors. The gripper is mounted to the robot via a compliant X-joint, which enhances self-alignment and allows the bunch to swing freely, reducing the holding forces required. This concept mirrors the proposed solution to prevent the "peel-off"problem in suction cups, where lateral robot movements create a critical moment by the swing of the object's center of gravity, leading to detachment.

Results and conclusion

The gripper successfully picked up 19 out of 19 banana bunches, withstanding a maximum positioning error of 4.9 cm. It demonstrated excellent compensation for misalignment in all directions, achieving a 95% grasping success rate. Minimal damage was observed, limited to minor abrasions on the peduncle, with no damage to the fruit. In practical tests, the gripper performed effectively both manually and when mounted on a pre-programmed robot arm. The hook mechanism and compliant X-joint allowed for stable, damage-free grasping, even as the bunch swung like a pendulum. More research is recommended to refine the design for use in the real world in agri-food and supermarket applications.

Inherently dynamically balanced 2-DoF gripper

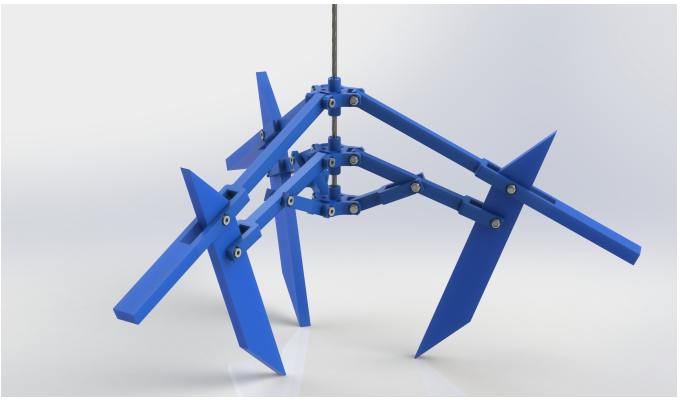
Problem introduction

The increasing demand for high-speed automation has driven innovations in gripper design, particularly for tasks such as pick-and-place operations. Traditional grippers often create reaction forces and moments on their base during operation due to changes in the center of mass and acceleration as a result of the inward-outward motion of their fingers while grasping. This can destabilize the system to which they are attached, especially in dynamic environments such as drones, or induce movement of the robot arms. Dynamically balanced mechanisms address this by eliminating reaction forces and moments, decoupling the motion of the mechanism from its base, and simplifying control requirements.

This research aims to develop a dynamically balanced 2-degree-of-freedom (2-DoF) gripper capable of handling a variety of objects [4]. The gripper was designed using inherent dynamical balancing techniques, avoiding the need for heavy counter masses typically added to achieve balance. A 2-DoF gripper was chosen to handle a larger variety of object sizes.

Methodology

The functional components of the gripper were arranged to naturally counterbalance each other. Two pantograph mechanisms were stacked, with the long arms of the upper and lower pantographs connected by beams acting as gripper fingers. This configuration ensured that the center of mass remained stationary at the base. The gripper design was made axisymmetric, ensuring that the moments generated by one finger were counteracted by others, eliminating the need for rotating counter masses. The finger configuration allowed for a geometric locking grip, where the object was constrained in movement, reducing contact forces compared to friction-based grips. To prevent interference between the pantographs, the small beams of the upper pantograph were removed, simplifying the design without affecting its motion. The size ratios of the beams were optimized to allow geometric locking with 60-degree angles in the widest configuration.



Figuur C.9: 2-DoF gripper with three inherently dynamically balanced fingers

The final 2-DoF gripper design was validated through simulations and experimental testing. Using SPACAR, a multibody simulation software, the dynamic balance of the mechanism was confirmed by analyzing the forces and moments at the base during actuation, along with evaluating the kinematic and geometric locking behavior for various configurations. Experimentally, the gripper prototype was tested by actuating its 2-DoF with a linear induction actuator to assess force reduction during motion compared to an imbalanced version and to assess its ability to securely grip a range of objects using geometric locking or friction-based grips.

Results and conclusion

This research successfully developed and validated a partially balanced 2-DoF gripper. Simulations confirmed complete internal balance, while real-world tests showed a 50% reduction in actuation force during most movements and a 10% reduction at peak forces compared to an imbalanced design. These results indicate that the gripper achieves the balance of the shaking force for internal motions but remains partially coupled to its base, lacking full dynamic balance, resulting in rotation around its axis.

The adaptability of the gripper allows it to handle objects 11% to 100% of its width, with scalability and customizable finger designs for various applications.

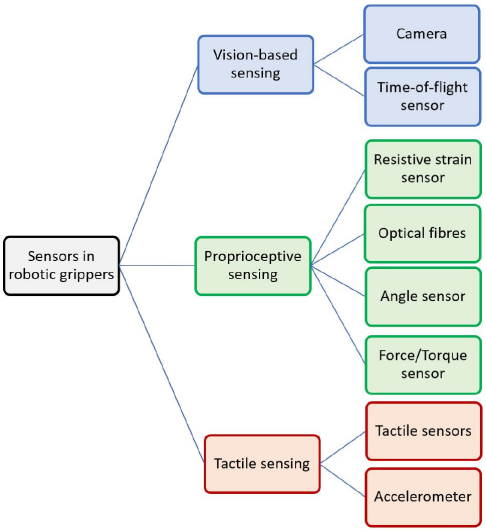
The findings highlight the effectiveness of incorporating inherently balanced principles into the gripper design process. This strategy not only reduces base and actuation forces but also vibrations and simplifies control, enabling efficient high-speed automation in dynamic environments.

Indirect force & contact sensing for compliant fingers

Problem introduction

Compliant grippers are ideal for handling delicate, irregularly shaped food items, as they passively adapt to the shape of the object, providing a soft, damage-free grip. However, this flexibility introduces uncertainty about the contact location and applied force, which is critical to ensuring a stable and secure grasp. To address this, sensor integration is crucial for real-time contact location and force data, allowing early detection of misgrasps or potential damage. Various sensing methods, as shown in Fig. C.10, include tactile sensors, vision-based systems, and proprioceptive sensing, each with its advantages and limitations. Compliant grippers, due to their force transparency, are particularly suited to leverage an indirect sensing method that offers accurate feedback while minimizing the impact on performance and shielding the sensors from environmental factors.

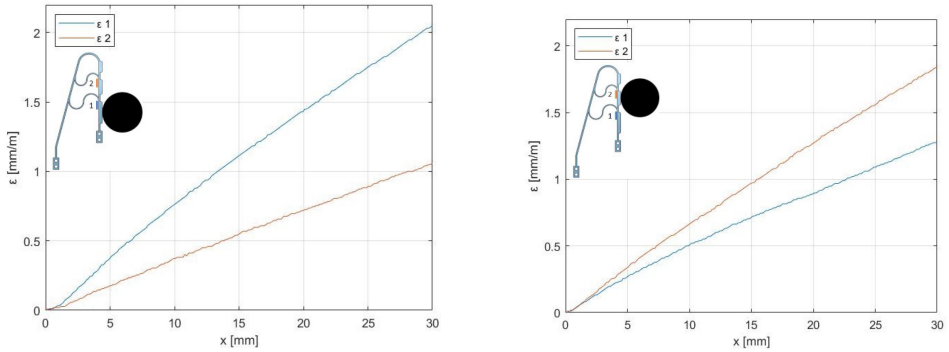
In this research [5], we explore this approach by embedding strain gauges within the gripper structure to infer contact location and force without compromising its performance.



Figuur C.10: Categorization of different sensing methods utilized in gripper literature.

Methodology

The proposed method involves measuring strain at two key locations within a selected compliant finger design [6]. The finger was modeled using Finite Element Analysis (FEA) to simulate deformation while grasping the object located at a variety of different locations along its length. First, simulation data from all load cases were analyzed to select suitable sensor locations by identifying regions with significant strain in different grasp scenarios. During operation, the location of contact and the force were determined by mapping the measured strain to a comparable curve simulated in the data set, associated with a particular



(a) Object located at the bottom (lower phalange)

(b) Object located in the middle (middle phalange)

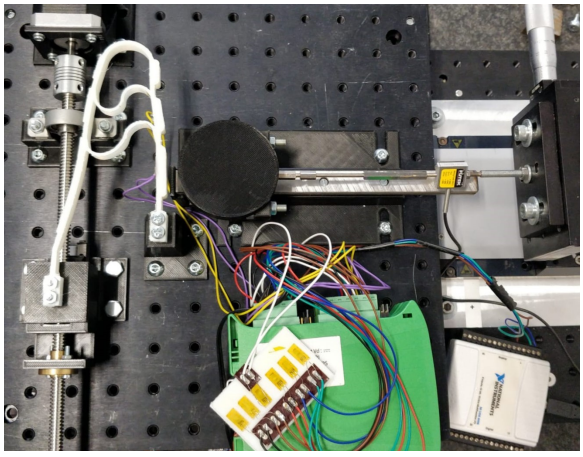
Figuur C.11: Strain curves at the location of sensor 1 (blue) and 2 (red) for two different object locations

load case. Fig. C.11 illustrates how these strain curves differ for two object locations while grasping, shown as a function of the actuation distance x.

An experimental setup, shown in Fig. C.12, was built to validate the method. The compliant finger embedded with strain gauges was fabricated and the strain measurements were collected under various load conditions, with the applied force on the object measured using a load cell.

Results and conclusion

The proposed sensing method accurately estimated contact forces with a precision of up to 0.1 N and successfully identified the contact point along the finger. Although the results



Figuur C.12: Experimental setup used to validate the sensing method and measure its impact on the grasping performance

showed that one sensor seemed sufficient for the scenarios tested, the use of two strain gauges provides a more reliable solution in complex cases where overlap in strain curves might occur. The embedded sensors had minimal effect on gripper performance, causing only a slight increase in actuation force (up to 6% or 0.07 N) and no noticeable impact on mobility when comparing the sensor-equipped finger with one without sensors in our experimental setup. The results of this research open new possibilities for more intelligent and adaptable robotic systems by demonstrating that our method effectively approximates contact location and force with minimal impact on gripper performance.

Parametric model for toroidal gripper performance

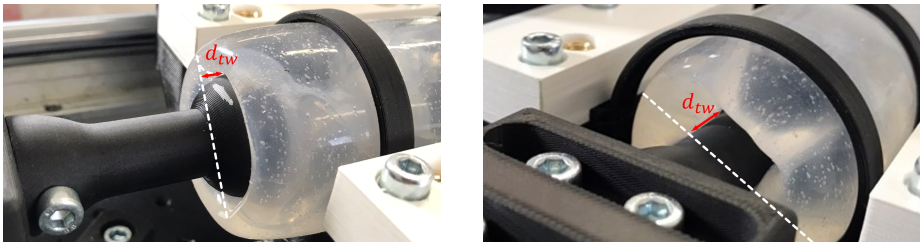
Problem introduction

The toroidal hydrostat gripper is a soft robotic device consisting of a flexible toroidal membrane (doughnut-shaped) pressurized by fluid. It grips objects by rolling the outer membrane over them while the inner membrane remains stationary, providing high holding forces and a gentle grip by setting the grasp through a rolling contact and evenly distributed pressure over the object's surface. Although the holding force for objects with constant radii has been established [7], predicting it for objects with variable radii is crucial to accommodate naturally shaped objects. Additionally, understanding the disturbance force, the force exerted on the object during grasping it, is vital, as exceeding opposing forces, such as surface friction of the object with the ground, can displace the object and push it out of the gripper.

This research aims to develop a parametric model to determine both disturbance and holding forces for objects with variable radii. It also includes the manufacturing details for a toroidal hydrostat gripper and the validation of the model through experimental testing. More details can be found in [8].

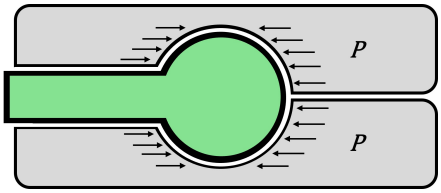
Methodology

We build on the formula by Root et al. [7] for holding forces, using a stepwise procedure that discretizes the total distance that the object is swallowed by the gripper. Radial and axial forces are computed incrementally at each step as functions of the new radii of the toroid and the cross-sectional area of the object. The model incorporates a non-linear stress-strain relationship, with hydrostatic pressure determined using the thin-walled hoop equation. A tuning factor is introduced, with its value determined experimentally, to correct inaccuracies in the prediction of holding and disturbance forces by accounting for membrane deformation, potential vacuum forces, uncertainties in material properties, and geometric assumptions. At the end of each incremental step, the disturbance force (equal to the axial force) and the holding force (equal to the friction coefficient times the radial force minus the axial force) are obtained.

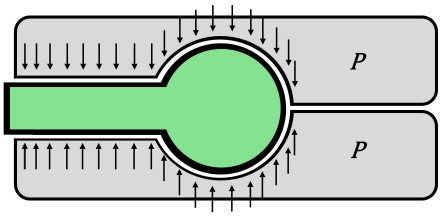


Figuur C.13: Hydrostatic gripper grasping a test object by rolling over it as its exterior surface is moved linearly forward using the black rings. The left subfigure shows the grasping process halfway through, while the right subfigure depicts the process completed.

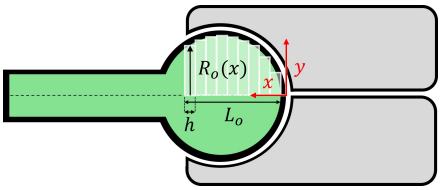
The model was validated using an experimental setup similar to that in Chapter 4, but adapted for the hydrostat gripper. Five different dummy objects were tested: a 19.2 mm,



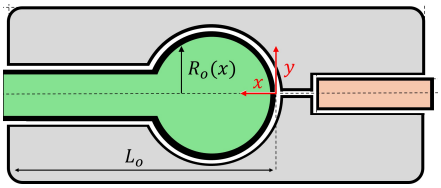
(a) Forces in axial direction



(b) Forces in radial direction



(c) Numerical interpretation of the cross-sectional area as function of R_0 for increasing swallow distance L_0 with step h



(d) Depiction of the object and the rod in the test setup

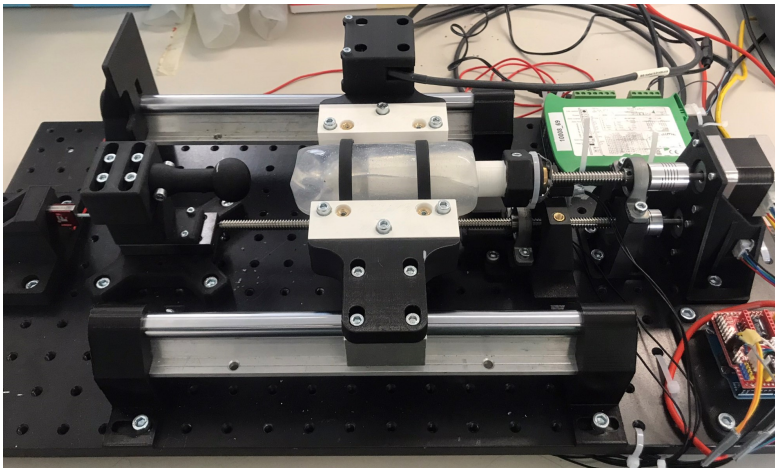
Figuur C.14: Schematic cross-sectional view of the hydrostatic gripper (grey) grasping an object (green) and the actuation rod (orange).

24 mm and 28.8 mm sphere, a 16 mm diameter cylinder, and a 32 mm wide cone with a 15-degree angle. Both push and pull tests were performed to measure the axial disturbance and holding forces during actuation.

The hydrostat was fabricated by coating a rotating PVC pipe with layers of SORTA-CLEAR 12 liquid silicone, ensuring uniform distribution and preventing dripping. Once cured, the ends were cut and the tube inverted to form a pocket, which was filled with water under pressure until the desired radius was reached and sealed with a zip tie. This end and a rod were tucked inside the hydrostat to connect it to an actuator, which completed the gripper.

Results and conclusion

The model accurately predicted the holding forces, with a maximum deviation of 15% at the maximum actuation distance. However, disturbance forces were overestimated by a factor of 2.5, although normalized force curves showed good agreement with experimental data. A high tuning parameter (1.45) was identified, suggesting the presence of an additional vacuum force acting on smooth surfaces. Dimensional limits for the gripper were also identified, including optimal pressure-to-elasticity ratios and constraints on membrane thickness and initial radius.



Figuur C.15: Experimental setup for testing the hydrostatic gripper's disturbance force and holding force capabilities, similar to the setup used in Chapter 4. The gripper is actuated by the top spindle and mounted on a linear guide, while the bottom spindle moves the gripper back and forth. The measurement module, including the test object, is mounted on a linear stage with a force sensor, visible as the red device on the left side of the image

Bibliografie

[1] B. Cleijpool, A. E. Huisjes, and J. L. Herder, "Experimental quantification of gripper limits determined by product detachment in a practical set-up," Master's thesis, Delft University of Technology, 2021. https://resolver.tudelft.nl/uuid:32ef3d3e-974c-42c8-9137-33ca69d06239.

[2] N. Smit, A. Huisjes, and J. Herder, "The fre gripper with planar grasp stability, using spatial form-closure," Master's thesis, Delft University of Technology, 2022. https://resolver.tudelft.nl/uuid:5c38480b-b9c7-4c1a-9f19-8df072355989.

[3] A. van der Start, A. Huisjes, and J. Herder, "Design and evaluation of a gripper for bunches of bananas in a supermarket environment," Master's thesis, Delft University of Technology, 2022. https://resolver.tudelft.nl/uuid:0771c8dd-de37-4152-a6fd-a82ba6a2d03e.

[4] H. Hofland, A. Huisjes, and J. Herder, "Design of a fully actuated dynamically balanced 2-dof gripper," Master's thesis, Delft University of Technology, 2024. https://resolver.tudelft.nl/uuid:49fcc648-8a75-4b0d-ba39-cf6caa4567ac.

[5] L. de Rooij, A. Huisjes, and J. Herder, "Indirect sensing method for contact location and force in a compliant finger," Master's thesis, Delft University of Technology, 2023. https://resolver.tudelft.nl/uuid:272dd5a4-523e-4417-8497-790b512e47cf.

[6] P. Steutel, G. A. Kragten, and J. L. Herder, "Design of an underactuated finger with a monolithic structure and largely distributed compliance," in *International Design Engineering Technical Conferences and Computers and Information in Engineering Conference*, vol. 44106, pp. 355–363, 2010.

[7] S. E. Root, D. J. Preston, G. O. Feifke, H. Wallace, R. M. Alcoran, M. P. Nemitz, J. A. Tracz, and G. M. Whitesides, "Bio-inspired design of soft mechanisms using a toroidal hydrostat," *Cell Reports Physical Science*, vol. 2, no. 9, 2021.

[8] S. van Overbeeke, A. Huisjes, and J. Herder, "Parametric model of the holding and disturbance forces involved with a toroidal hydrostat gripper during gripping and grasping," Master's thesis, Delft University of Technology, 2024. https://resolver.tudelft.nl/uuid:9aca3c0b-ce33-4a28-8f34-ffa2f201ea63.

Acknowledgments

Looking back at this dissertation, I feel a deep sense of pride—not only because of the technical outcomes, but also because the journey behind them - held mostly in my own memories and of which only a small part made it onto these pages, was just as exciting. This book presents only the final scientific results, but for me the past four years were shaped by exploration, learning, and collaboration. They made this a deeply rewarding journey, full of personal growth, new experiences, creativity, and meaningful teamwork.

The colourful layout of this dissertation is more than a stylistic choice to clarify its structure; it mirrors the colourful moments that defined this journey. The thesis is already filled with illustrations and figures, but even the plain text pages deserve a touch of colour, because there were hardly any dull or monotone moments in these years. When I think back to my first year, I could never have predicted where this work would eventually lead. And that is exactly what I love about science—the way a vague idea you envision in your head can, with enough curiosity, persistence, and a bit of courage, grow into something unforeseen, new, and real. I'm deeply grateful that PhD positions exist, and that we live in a society that gives people the space to explore ambitious ideas—ideas that will hopefully give something back in return, sooner or later.

While my name appears on the cover, this dissertation is anything but a one-man show. The autonomy I was given, and the many people I had the privilege to work with, made this journey feel supported from beginning to end—even during the isolation of COVID-19. Being part of the PME department and the FlexCRAFT consortium has been truly special. Many of the insights, motivation, and energy I carried through this PhD came directly from interdisciplinary teamwork, from collaborations with our industrial partners, and from the dedicated gripper-research group of MSc students I had the privilage to have supervised.

Although words fall short, I'd like to thank everyone who made this journey possible, meaningful, and unforgettable.

A heartfelt thank you to my promotor, **Just**. Thank you not only for giving me the opportunity to join this project, but even more for the steady support, freedom, and trust you have shown me over the years. I learned so much from you—about design, about research, and about what it means to be a great teacher and supervisor: calm, thoughtful, and able to put people in positions to bring out the best in themselves.

I'm especially grateful for the trust you placed in me, Just—giving me the autonomy and backing to follow "high-risk paths," even when tangible results took time to appear. You gave me the *degrees of freedom* to move in that direction, allowing me to step away from the original proposal and explore an alternative solution to the problem. The moment we deliberately committed to exploring this new path, you allowed me to pursue it without resistance or pressure. That space made it a natural *compliant* (and exciting) direction to follow, fully aligned with my own reasoning. You helped me let go of the idea that the "first design must be right" and instead embrace going earlier and more often through the build–break–learn–and-try-again cycle. Even though it initially felt more like "beunen

en spelen," I quickly realised that this approach guided me far better than my old belief that science should be created solely from theory and books. You helped me see that this is exactly how meaningful ideas grow—something I genuinely enjoy, and a lesson I will carry with me for the rest of my life. Thank you, Just, for your trust, your patience, calm guidance, and long-term vision. You created the space in which this work—and I—could grow. I am sincerely grateful for that.

To my copromotor, **Volkert**, whose sharp insights always brought clarity and helped me refocus. Whenever I found myself caught up in many other interesting things or meetings, that metaphor of yours would return to mind—the empty desk with a taped-down dissertation on it—reminding me of the goal we needed to work toward. What ultimately had to go into that dissertation was never fully prescribed beforehand; it was up to us to shape it ourselves. You always knew exactly when to give a gentle push, creating the space to move forward and get things done. I truly appreciated that you chose to stay involved even after moving on to Kinetic Art—as I genuinely consider you a great scientist and mechanical engineer. I learned a great deal from you, both during my master's thesis and throughout my PhD, and your guidance has been an important part of my development into an independent researcher.

To my **committee members**, thank you for critically reviewing this dissertation. Without diminishing the contributions of the others, I am especially grateful to Prof.dr. L.E. **Birglen** for his extensive feedback, which sharpened several sections and refined the final details.

A warm thanks to the **FlexCRAFT** consortium—what a privilege it has been to work within this group. **Akshy, David, Xin, Rekha, Robbert, Rick, Rodrigo, Thomas, Tomas, Peter, Jordy, Bastiaan, Boi, Jimmy, Eldert, and Gert**: thank you. Thanks also to our industrial partners, especially Marel (**Laurens**) and Festo (**Jan**), and to the many universities and companies that broadened both the scope and relevance of this work. Collaborating with you was truly enriching. Our meetings were always energizing and often led to impressive robotic demonstrators showcasing our collective research efforts. This research path was possible only because flexibility was embraced not just within the robotic systems themselves, but equally within the FlexCRAFT environment—allowing me to explore directions beyond the original plan and patiently supporting the development of new grippers, prototypes, and results.

To **Akshy and Rekha**: thank you for your hands-on help with the robotic setup—from testing commercial grippers in the original poultry-case configuration to validating the DBCF-EM gripper together with Bart as the system transformed into a tomato-handling setup. And Rodrigo, for your support during the validation of the SCF-EM gripper on the robotic setup of COR. To **Jordy**: thank you for the insights that helped steer our conversations toward system-level approach in the early days, and for the late-evening discussions afterwards.

And although everyone in FlexCRAFT truly deserves their own thank-you sentence, I would like to close by highlighting **Gert** in particular—thank you for your boundless enthusiasm and warm, connecting personality, always emphasising collaboration and bringing people together through workshops and shared initiatives. The enthusiasm you showed during our very first conversation at Hotel de Wageningsche Berg, back when I was still a "PhD-candidate-candidate," energized me to join the project, dive into the

challenges of agri-food robotics, and collaborate with the many inspiring people involved. Thank you once again for being part of my committee; with your expertise in agricultural robotics, you are a highly valuable addition.

I'm sincerely thankful to the **master's students** I had the pleasure of supervising: **Bram**, **Neil**, **Bart**, **Anne**, **Rik**, **Rens**, **Mark**, and **Sander**. Your work was integral to this project, and I truly enjoyed our brainstorming sessions and teamwork. It often felt as if we had our own little gripper research group—something I'm still proud of—and each of your contributions added meaningful value to my research. I therefore included parts or summaries of your work in this dissertation, not only to showcase what we accomplished together, but also to place my own research in a broader context. Beyond the technical contributions, working with each of you on a personal level was a rewarding and educational experience for me as well.

Thank you to the **PME department staff** for making everything run smoothly. In particular, Patrick, Bradley, Spiridon, Gideon, and Damian—your technical support was essential for the achieved quality of the experimental set ups and prototypes. Also thanks to Eveline, Annemieke, Sylviane, Marli, Marianne, Gaby, and Lisette for your ongoing help. Special thanks to senior researchers Davood, Andres, Ron, Hassan, Giuseppe, Jo, Peter, Jaap, Hans, and Regine for your guidance.

To my fellow **PME PhD colleagues**, with whom I shared the office and many lunches: Nima, Malte, Gerben, Abdullah, Marcin, Ali, XinXin, Francesco, and many others including Stijn, Werner, Freek, Jelle R, Thijs, Reinier, Joep, Stefan, Frederike, Pierre, Sifeng He, Ata, Andrea, Ruben, Thomas, Pieter, Maarten, Lucas, Endre, Inge, Hava, Paula, Vincent, and Nick. Thank you for the chats, the brainstorms, the shared struggles and laughs, and for being part of memorable outings, and trips to ICRA in London and the summer school in Lithuania. A special thanks to **Ali** and **Jelle** for the many COVID walks and talks during the early days of our PhD journey and for being my **paranymphs** on the concluding day of my PhD. Ali, thank you not only for all the brainstorming sessions we had, but even more for the many social and cultural conversations that meant a lot to me. Jelle, you have truly been my PhD partner in crime—starting and defending within a month of each other, and sharing all the joys and struggles of every phase of the process. To Dave, for the never-ending sports discussions and for running a marathon together, and to Malte, who was always open to questions and genuinely interested. Thank you all.

En natuurlijk, naast alle collega's en vrienden die ik tijdens mijn PhD heb ontmoet, zijn er ook veel andere mensen die mijn vrije tijd ontzettend leuk hebben gemaakt. Dankzij jullie had ik altijd de nodige afleiding van mijn PhD wanneer dat nodig was—en soms ook wanneer dat níét nodig was. Sommige vrienden ken ik al sinds de basisschool, anderen pas sinds mijn studententijd, maar samen zorgen jullie ervoor dat er altijd genoeg gezellige avonden en weekendjes weg zijn om over van alles te kletsen. Aan iedereen die interesse toonde in mijn project: jullie gesprekken hielpen me uitzoomen, reflecteren en weer opladen. En aan iedereen die dat niet deed: geeft niks—het was juist heerlijk om het er soms níet over te hebben, het werk los te laten en gewoon te genieten van gezelligheid, hobby's of sport. Daarom: bedankt vrienden van **'t Schuurtje**, **Venlo**, **Delft** en **Sprint Breda**, voor alle fijne momenten en plezier naast het werk.

Pap & **Mam**, **Tessa** & **Bram**, **Paul** & **Nadine**, en natuurlijk mijn hele **schoonfamilie**, jullie verdienen uiteraard ook een paar lieve dankwoordjes hier. Net als de mensen hierboven maakten jullie niet alleen deel uit van mijn vrije tijd, maar ook de vaste basis waar ik altijd op kon terugvallen, of uren heb kunnen thuiswerken. Bedankt voor jullie interesse in mijn project; daardoor werd ik regelmatig gedwongen om het in behapbare taal — en soms in gebarentaal met mijn handen — uit te leggen, cruciaal voor het vertellen van de core van dit verhaal. Maar vooral pap en mam: bedankt voor het altijd blijven steunen tijdens de dyslectische struggles op de middelbare school, en ook toen ik daardoor twijfelde of naar de universiteit gaan wel mijn plek zou zijn — *'Wat word ik dan?'*, *'Moet ik niet wat praktischer gaan doen?'* — zonder jullie steun was ik niet gegaan. Guess what: ruim tien jaar later zit ik er nog steeds — en nog met plezier ook — en vraag je je misschien af of ik er ooit nog vanaf kom.

Tot slot, lieve **Loes**, bedankt dat je er altijd voor me bent en me eindeloos steunt. Of het nou was door te luisteren, problemen helpen te reflecteren en relativeren, zeggen dat ik goed bezig ben, of door er simpelweg even te zijn: het gaf me het vertrouwen om door te gaan en daardoor heb ik het allemaal sowieso positiever ervaren dan zonder jouw steun. Je gaf me de ruimte en balans om zowel te genieten van het werk als van het leven, en daarmee het beste in me naar boven te krijgen. En om af en toe een nachtje doorslapen, want de deadline om te promoveren voor we een kleine zouden krijgen heb ik niet gehaald… lieve **Noa** was sneller dan ik. Zelfs haar kleine grijpertjes kunnen inmiddels al dingen vastpakken, en wanneer zij mij tijdens een pauze beetpakt, dan vergeet je even dat er nog werk te doen is.

Ad Huisjes
Breda, Nov 2025

MSc Projects Supervised

Thesis list:

1. Bram Cleijpool, *Experimental quantification of gripper limits determined by product detachment in a practical set up: applied on high-speed case packing of packaged food*, (2021, Sep)

2. Neil Smit, *The FRE Gripper with planar grasp stability, using spatial form-closure*, (2022, July)

3. Bart Friederich, *Design and validation of a manoeuvering caging gripper for grasping in cluttered environments*, (2022, April)

4. Anne van der Star, *Design and evaluation of a gripper for bunches of bananas in a supermarket environment*, (2022, Sep)

5. Rik Hofland, *Design of a fully actuated dynamically balanced 2-DoF gripper*, (2024, Sep)

6. Rens de Rooij, *Indirect sensing method for contact location and force in a compliant finger*, (2023, Jan)

7. Mark Kuntz, *Pull-out force of grippers with initially-curved fingers based on Pseudo-Rigid Body modeling*, (2024, Feb)

8. Sander van Overbeeke, *Parametric model of the holding and disturbance forces involved with a toroidal hydrostat gripper during gripping and grasping*, (2024, July)

Curriculum Vitæ

Albert Eddy Huisjes

1992/01/29 Born in Hardenberg, The Netherlands

Education

2011-2016 *BSc in Mechanical Engineering*
Department of Mechanical Engineering
Delft University of Technology, Delft, The Netherlands
Thesis: *FEA model of the human eye movement*
Supervisor: *Prof.dr.ir. A. (Fred) van Keulen*

2016-2019 *MSc in Mechanical Engineering - Mechatronic System Design*
Department of Mechanical Engineering
Delft University of Technology, Delft, Netherlands
Thesis:
Compliant manipulator design method (COMAD) for the type synthesis of all serial and parallel multi-DoF compliant mechanisms, with example of a Schönflies motion generator
Supervisor: *Prof. dr. ir. Just L. Herder*
Daily-Supervisor: *Dr. ir. Volkert van der Wijk*

2020-2024 *PhD in Mechanical Engineering - Mechatronic System Design*
Department of Precision and Microsystems Engineering
Delft University of Technology, Delft, The Netherlands
Thesis:
Development of Flexure-Driven Eversion Mechanisms, for confined-space grasping
Promotor: *Prof. dr. ir. Just L. Herder*
Copromotor: *Dr. ir. Volkert van der Wijk*

Experience

2024– *Postdoctoral Researcher*
Delft University of Technology, Delft, The Netherlands
Development of a mechanical system for clipless and accurate ocular tumor alignment in proton therapy.

List of Publications

Journal publications

1. **A.E. Huisjes**, V. van der Wijk (2023). *Compliant manipulator design method (COMAD) for the type synthesis of all serial and parallel multi-DoF compliant mechanisms, with example of a Schönflies motion generator.* Mechanism and Machine Theory 186: 105342

In Preparation

3. **A.E. Huisjes** and J.L. Herder (2025). *The SCF-EM Gripper: Using Sleeved Concentric-Flexures Eversion Mechanisms as Fingers for Confined-Space Robotic Grasping.* Submitted as an article to ASME Letters in Translational Robotics 📄

2. J.H.B. Friederich, **A.E. Huisjes**, and J.L. Herder (2025). *The DBCF-EM Gripper: Using Dual-Belt Curved-Flexure Eversion Mechanisms as Fingers for Confined-Space Robotic Grasping.* Submitted as an article to IEEE Robotics and Automation Letters 📄

1. **A.E. Huisjes**, V. van der Wijk, and J.L. Herder (2024). *Pseudo-rigid-body modeling of flexures in event-based scenarios with multiple loads along their length.* Resubmitted as an article to Journal of Mechanisms and Robotics 📄

📄 Included in this thesis.

